

AD-777 989

ANALYSIS OF ON-AIRCRAFT ANTENNA
PATTERNS

Walter Dennis Burnside

Ohio State University

Prepared for:

Naval Air Development Center

August 1972

DISTRIBUTED BY:

NTIS

National Technical Information Service
U. S. DEPARTMENT OF COMMERCE
5285 Port Royal Road, Springfield Va. 22151

NOTICES

When Government drawings, specifications, or other data are used for any purpose other than in connection with a definitely related Government procurement operation, the United States Government thereby incurs no responsibility nor any obligation whatsoever, and the fact that the Government may have formulated, furnished, or in any way supplied the said drawings, specifications, or other data, is not to be regarded by implication or otherwise as in any manner licensing the holder or any other person or corporation, or conveying any rights or permission to manufacture, use, or sell any patented invention that may in any way be related thereto.

ACCESSION No.	
NTIS	White Section <input checked="" type="checkbox"/>
DGC	Red Section <input type="checkbox"/>
UNANNOUNCED	<input type="checkbox"/>
JUSTIFICATION	
BY	
DISTRIBUTION/AVAILABILITY CODE	
U.S.	AVAIL. RES./GT. SPECIAL
A	

18

Walter Dennis Burnside

Contract N62269-72-C-0354

Naval Air Development Center
Warminster, Pa. 18974

DDC
RECEIVED
MAY 7 1974
RECEIVED
D

UNCLASSIFIED, DISSEMINATION UNLIMITED

ic

UNCLASSIFIED

Security Classification

AD-777989

DOCUMENT CONTROL DATA - R&D		
(Security classification of title, body of abstract and indexing annotation must be entered when the overall report is classified)		
1. ORIGINATING ACTIVITY (Corporate author) The Ohio State University ElectroScience Laboratory Department of Electrical Engineering, Columbus, OH		2a. REPORT SECURITY CLASSIFICATION Unclassified
		2b. GROUP
3. REPORT TITLE ANALYSIS OF ON-AIRCRAFT ANTENNA PATTERNS		
4. DESCRIPTIVE NOTES (Type of report and inclusive dates) Technical Report		
5. AUTHOR(S) (Last name, first name, initial) Burnside, Walter Dennis		
6. REPORT DATE August 1972	7a. TOTAL NO. OF PAGES 221	7b. NO. OF REFS 55
8a. CONTRACT OR GRANT NO. Contract N62269-72-C-0354	9a. ORIGINATOR'S REPORT NUMBER(S) ElectroScience Laboratory 3390-1	
b. PROJECT NO.		
c. TASK		
d.	9b. OTHER REPORT NUMBER(S) (Any other numbers that may be assigned this report)	
10. AVAILABILITY/LIMITATION NOTICES Approved for Public Release; Distribution Unlimited		
11. SUPPLEMENTARY NOTES	12. SPONSORING MILITARY ACTIVITY Naval Air Development Center Warminster, Pa. 18974	
13. ABSTRACT High frequency radiation patterns of on-aircraft antennas are analyzed using ray optics techniques. This is a basic study of aircraft-antenna pattern performance in which the analytic aircraft is modelled in its most basic form. The fuselage is assumed to be a perfectly conducting convex surface. The wings are simulated by arbitrarily many sided flat plates and the jet engines are treated as finite circular cylinders. The three principal plane patterns are analyzed in great detail with measured results taken to verify each solution. A volumetric pattern study is initiated with the fuselage modelled by an arbitrary convex surface of revolution. NATIONAL TECHNICAL INFORMATION SERVICE SP-11-11-VA		

DD FORM 1473
1 JAN 64

UNCLASSIFIED

Security Classification

UNCLASSIFIED

Security Classification

14. KEY WORDS	LINK A		LINK D		LINK C	
	ROLE	WT	ROLE	WT	ROLE	WT
On-Aircraft Antennas Radiation Patterns Roll Plane Elevation Plane Azimuth Plane Volumetric Patterns Geometric Theory of Diffraction Modal Solutions Experimental Verification						

INSTRUCTIONS

1. ORIGINATING ACTIVITY. Enter the name and address of the contractor, subcontractor, grantee, Department of Defense activity or other organization (if separate author, issuing the report).

2a. REPORT SECURITY CLASSIFICATION. Enter the overall security classification of the report. Indicate whether "Restricted Data" is included. Marking is to be in accordance with appropriate security regulations.

2b. GROUP. Automatic downgrading is specified in DoD Directive 5200.10 and Armed Forces Industrial Manual. Enter the group number. Also, when applicable, show that optional markings have been used for Group 3 and Group 4 as authorized.

3. REPORT TITLE: Enter the complete report title in all capital letters. Titles in all cases should be unclassified. If a meaningful title cannot be selected without classification, show title classification in all capitals in parentheses immediately following the title.

4. DESCRIPTIVE NOTES: If appropriate, enter the type of report, e.g., interim, progress, summary, annual, or final. Give the inclusive dates when a specific reporting period is covered.

5. AUTHOR(S): Enter the name(s) of author(s) as shown on or in the report. Enter last name, first name, middle initial. If military, show rank and branch of service. The name of the principal author is an absolute minimum requirement.

6. REPORT DATE: Enter the date of the report as day, month, year, or month, year. If more than one date appears on the report, use date of publication.

7a. TOTAL NUMBER OF PAGES: The total page count should follow normal pagination procedures, i.e., enter the number of pages containing information.

7b. NUMBER OF REFERENCES: Enter the total number of references cited in the report.

8a. CONTRACT OR GRANT NUMBER. If appropriate, enter the applicable number of the contract or grant under which the report was written.

8b, 6c, & 8d. PROJECT NUMBER: Enter the appropriate military department identification, such as project number, subproject number, system numbers, task number, etc.

9a. ORIGINATOR'S REPORT NUMBER(S). Enter the official report number by which the document will be identified and controlled by the originating activity. This number must be unique to this report.

9b. OTHER REPORT NUMBER(S): If the report has been assigned any other report numbers (either by the originator or by the sponsor), also enter this number(s).

10. AVAILABILITY/LETTATION NOTICES: Enter any limitations on further dissemination of the report, other than those imposed by security classification, using standard statements such as:

- (1) "Qualified requesters may obtain copies of this report from DDC."
- (2) "Foreign announcement and dissemination of this report by DDC is not authorized."
- (3) "U. S. Government agencies may obtain copies of this report directly from DDC. Other qualified DDC users shall request through _____."
- (4) "U. S. military agencies may obtain copies of this report directly from DDC. Other qualified users shall request through _____."
- (5) "All distribution of this report is controlled. Qualified DDC users shall request through _____."

If the report has been furnished to the Office of Technical Services, Department of Commerce, for sale to the public, indicate this fact and enter the price, if known.

11. SUPPLEMENTARY NOTES: Use for additional explanatory notes.

12. SPONSORING MILITARY ACTIVITY: Enter the name of the departmental project office or laboratory sponsoring (paying for) the research and development. Include address.

13. ABSTRACT: Enter an abstract giving a brief and factual summary of the document indicative of the report, even though it may also appear elsewhere in the body of the technical report. If additional space is required, a continuation sheet shall be attached.

It is highly desirable that the abstract of classified reports be unclassified. Each paragraph of the abstract shall end with an indication of the military security classification of the information in the paragraph, represented as (TS), (S), (C), or (U).

There is no limitation on the length of the abstract. However, the suggested length is from 150 to 225 words.

14. KEY WORDS. Key words are technically meaningful terms or short phrases that characterize a report and may be used as index entries for cataloging the report. Key words must be selected so that no security classification is required. Identifiers, such as equipment model designation, trade name, military project code name, geographic location, may be used as key words but will be followed by an indication of technical context. The assignment of links, rules, and weights is optional.

UNCLASSIFIED

Security Classification

ia

ACKNOWLEDGMENT

Professor R. C. Ruddick, the author's advisor, deserves special thanks for his guidance that he provided countless times throughout the author's stay at the ElectroScience Laboratory.

Professor L. Peters, Jr. and Professor C. H. Walter have been most helpful in analyzing the author's manuscript. Their comments and critical review are incorporated through this report.

Several colleagues deserve recognition: Professor R. Kouyoumjian, for his extremely helpful guidance, suggestions, and discussions; L. Yu and R. Marhefka, for their special effort in providing suggestions and computations necessary to complete such a report; R. Lee, for providing aircraft models and measured results.

ABSTRACT

High frequency radiation patterns of on-aircraft antennas are analyzed using ray optics techniques. This is a basic study of aircraft-antenna pattern performance in which the analytic aircraft is modelled in its most basic form. The fuselage is assumed to be a perfectly conducting convex surface. The wings are simulated by arbitrarily many sided flat plates and the jet engines are treated as finite circular cylinders. The three principal plane patterns are analyzed in great detail with measured results taken to verify each solution. A volumetric pattern study is initiated with the fuselage modelled by an arbitrary convex surface of revolution.

ILLUSTRATIONS

Figure		Page
1	Plane wave incident on an infinitely long cylinder of radius (a).....	7
2	Arbitrarily oriented slot on cylinder.....	8
3	Geometry for three-dimensional wedge diffraction problem.....	12
4	Two-dimensional wedge diffraction geometry.....	15
5	Diffraction by a smooth curved surface.....	17
6	Diffraction by a smooth closed cylindrical surface.....	21
7	Antenna mounted on a circular cylinder· GTD solution.....	22
8	Contours for complex plane integrations.....	24
9	Principal plane patterns with a circumferential slot mounted on an elliptical cylinder.....	28
10	Near field flat plate geometry.....	31
11	Geometry for diffraction point along the mth edge.....	32
12a	Edge diffraction geometry.....	35
12b	Edge coordinate system at point of diffraction.....	36
13a	Geometry for location of image source.....	38
13b	Intersection of image ray with flat plate.....	40
14a	Reflections occur.....	42
14b	Reflections do not occur.....	42
15	Reflected field geometry.....	43
16	Geometry for flat plate measurements.....	46

Figure		Page
17	E_θ radiation pattern for a small dipole mounted above a rectangular plate for $\theta_s = 90^\circ$ and $0^\circ \leq \phi_s \leq 360^\circ$	47
18	E_θ radiation pattern for a short dipole mounted above a rectangular plate for $\theta_s = 90^\circ$ and $0^\circ \leq \phi_s \leq 360^\circ$	48
19	E_ϕ radiation pattern for a short dipole mounted above a rectangular plate for $\theta_s = 90^\circ$ and $0^\circ \leq \phi_s \leq 360^\circ$	49
20a	Geometry of flat plate treated.....	50
20b	Radiation pattern of a stub on a ground plane.....	51
20c	Radiation pattern of a stub on a ground plane.....	52
21	Near field finite cylinder geometry.....	53
22	Plane wave field incident on finite cylinder end cap.....	55
23	Near field specular scatter by rear cylinder end cap.....	59
24	Diffracted field geometry for finite cylinder edge.....	64
25a	Far field radar cross-section from a finite cylinder.....	72
25b	Far field radar cross-section from a finite cylinder.....	73
26	Cylindrical specular region for near zone cylinder.....	74
27a	Short dipole illuminating a finite cylinder.....	76
27b	Radiation pattern of a horizontal dipole (E_θ) with $-180^\circ \leq \theta \leq 180^\circ$	77
27c	Radiation pattern of a vertical dipole (E_ϕ) with $-180^\circ \leq \theta \leq 180^\circ$	78
28	Simplified aircraft model.....	80
29	Two-dimensional model for the roll plane with engines.....	81
30	Various scattering terms in two-dimensional problem.....	83

Figure		Page
31a	E_z radiation pattern for an axial slot on a fuselage with finite length wing.....	84
31b	E_z radiation pattern for a circumferential slot on a fuselage with finite length wing.....	85
31c	E_z radiation pattern for a $\pi/4$ monopole on a fuselage with finite length wing.....	86
32a	E_z radiation pattern for an axial slot on a fuselage with dominant engine and finite length wing.....	87
32b	E_z radiation pattern for a circumferential slot on a fuselage with dominant engine and finite length wing.....	88
32c	E_z radiation pattern for a $\pi/4$ monopole on a fuselage with dominant engine and finite length wing.....	89
33a	Reflection problem in x-y plane.....	91
33b	Reflection problem in y-z plane.....	91
34a	Diffraction problem in x-y plane.....	94
34b	Diffraction problem in y-z plane.....	94
35a	Roll plane pattern of monopole (E_z).....	96
35b	Roll plane pattern of circumferential slot (E_θ).....	97
35c	Roll plane pattern of axial slot (E_z).....	98
36a	Roll plane pattern of monopole (E_y).....	99
36b	Roll plane pattern of circumferential slot (E_θ).....	100
36c	Roll plane pattern of axial slot (E_z).....	101
37a	Roll plane pattern of monopole (E_ϕ).....	102
37b	Roll plane pattern of circumferential slot (E_θ).....	103
37c	Roll plane pattern of axial slot (E_z).....	104
38	Geometry used to find junction edge diffracted fields....	106

Figure		Page
39a	Roll plane pattern of monopole (E_z).....	107
39b	Roll plane pattern of circumferential slot (E_z).....	108
39c	Roll plane pattern of axial slot (E_z).....	109
40a	Elevation plane patterns.....	110
40b	Elevation plane patterns.....	111
40c	Elevation plane patterns.....	112
41	Numerical description of convex surface.....	114
42	Geometry describing the arc length computation.....	117
43a	Principal plane patterns with a circumferential slot mounted on a circular cylinder.....	119
43b	Principal plane patterns with an axial slot mounted on a circular cylinder.....	120
43c	Principal plane patterns with an infinitesimal monopole mounted on a circular cylinder.....	121
44a	Elevation plane patterns with a circumferential slot mounted on an elliptical cylinder.....	123
44b	Elevation plane patterns with a circumferential slot mounted on an elliptical cylinder.....	124
45	Elevation plane patterns with an axial slot mounted on an elliptical cylinder.....	125
46	Elevation plane pattern with an infinitesimal monopole mounted on an elliptical cylinder.....	126
47a	Elevation plane pattern with a circumferential slot mounted on a composite ellipse model.....	127
47b	Elevation plane pattern with a circumferential slot mounted on a composite ellipse model.....	128
47c	Elevation plane pattern with a circumferential slot mounted on a composite ellipse model.....	129
48a	Elevation plane pattern with an axial slot mounted on a composite ellipse model.....	130

Figure		Page
48b	Elevation plane pattern with an axial slot mounted on a composite ellipse model.....	130
48c	Elevation plane pattern with an axial slot mounted on a composite ellipse model.....	131
49a	Elevation plane pattern with an infinitesimal monopole mounted on a composite ellipse model.....	132
49b	Elevation plane pattern with an infinitesimal monopole mounted on a composite ellipse model.....	133
49c	Elevation plane pattern with an infinitesimal monopole mounted on a composite ellipse model.....	134
50a	Elevation plane pattern with a circumferential slot mounted on a composite ellipse model.....	135
50b	Elevation plane pattern with an axial slot mounted on a composite ellipse model.....	136
50c	Elevation plane pattern with an infinitesimal monopole mounted on a composite ellipse model.....	137
51	Azimuth plane geometry with engine added.....	139
52	Geometry of source field incident on rear end cap.....	140
53	Cylinder section scattered field.....	142
54a	Azimuth plane pattern of monopole (E_z) with and without engine.....	143
54b	Azimuth plane pattern of circumferential slot (E_ϕ) with and without engine.....	144
54c	Azimuth plane pattern of circumferential slot (E_ϕ) with and without engine.....	145
54d	Azimuth plane pattern of axial slot (E_z) with and without the engine.....	146
55a	Azimuth plane pattern of monopole (E_z) with and without wing.....	148
55b	Azimuth plane pattern of circumferential slot (E_ϕ) with and without wing.....	149

Figure		Page
55c	Azimuth plane pattern of circumferential slot (E_z) with and without wing.....	150
55d	Azimuth plane pattern of axial slot (E_z) with and without engine.....	151
56	Surface of revolution described by a finite set of points.....	154
57	Geodesic curves on a sphere with the source at $\theta_0 = 90^\circ$, $\phi_0 = 0^\circ$	156
58a	Geodesic curves on a $4\lambda \times 2\lambda$ prolate spheroid with the source at $\theta_0 = 90^\circ$, $\phi_0 = 0^\circ$	157
58b	Geodesic curves on a $4\lambda \times 2\lambda$ prolate spheroid with the source at $\theta_0 = 45^\circ$, $\phi_0 = 0^\circ$	158
59	Comparison of geodesic paths using tensor analysis and calculus of variations solutions.....	161
60	Comparison of tangent direction (θ_t, ϕ_t) using the geodesic solutions.....	162
61	Starting direction of geodesic path which is defined by the angle (γ).....	165
62	Set of test geodesic tangent direction curves on a prolate spheroid.....	166
63	Curvilinear coordinate along a geodesic path.....	167
64	Illustration of the spread factor ($\sqrt{d\psi_0/d\psi}$) terms.....	172
65	Geometry of monopole problem.....	173
66	The four dominant GTD terms that radiate at ($\theta = 90^\circ$, $\phi = 145^\circ$).....	175
67	Rotation of convex surface in order to obtain off-principal plane patterns.....	176
68	Principal plane pattern of monopole (E_{ϕ_1}) with $\xi = 0^\circ$	177
69a	Off-principal plane pattern of monopole (E_{ϕ_1}) with $\xi = 20^\circ$	178

Figure		Page
69b	Off-principal plane pattern of monopole ($E_{\theta,1}$) with $\xi=20^\circ$	179
70a	Off-principal plane pattern of monopole ($E_{\theta,1}$) with $\xi=40^\circ$	180
70b	Off-principal plane pattern of monopole ($E_{\theta,1}$) with $\xi=40^\circ$	181
71	Finite slot geometry.....	182
72	Principal plane pattern of circumferential slot ($E_{\theta,1}$) with $\xi=0^\circ$	185
73	Off-principal plane pattern of circumferential slot ($E_{\theta,1}$) with $\xi=20^\circ$	186
74	Off-principal plane patterns of circumferential slot ($E_{\theta,1}$) with $\xi=40^\circ$	187

TABLES

Table		Page
I	Generalized Diffraction Coefficients and Attenuation Constants.....	25
II	Airy Functions and Roots.....	26
III	Radiation Field in Ray Form in Principal Plane of a General Cross-sectional Shaped Cylinder.....	29
IV	Clairaut's Constant on a Spheroid Using Tensor Analysis Solution.....	160
V	Clairaut's Constant on a Spheroid Using Calculus of Variation Solution.....	163
VI	Radiation Directions Desired Versus Actually Computed Tangent Direction of Given Geodesic Curve Using Interpolation Procedure.....	167
VII	Comparison of Actual and Computed Values of Longitudinal and Transverse Radii of Curvature.....	171
VIII	TE and TM Fields Separable in the Cylindrical Coordinate System.....	203

CONTENTS

	Page
ACKNOWLEDGMENTS.....	ii
VITA.....	iii
ILLUSTRATIONS.....	iv
TABLES.....	xi
 CHAPTER	
I INTRODUCTION.....	1
II THEORETICAL BACKGROUND.....	4
A. Introduction	4
B. Modal Solutions for Infinite Circular Cylinders	4
C. Wedge Diffraction	10
D. Curved Surface Diffraction	17
III NEAR FIELD SCATTERING BY FINITE STRUCTURES.....	30
A. Introduction	30
B. Near Field Scattering by a Finite Plate	30
C. Near Field Scattering by a Finite Cylinder	53
IV ON-AIRCRAFT ANTENNA PRINCIPAL PLANE PATTERN STUDY.....	79
A. Introduction	79
B. Roll Plane Analysis	79
C. Elevation Plane Analysis	105
D. Azimuth Plane Analysis	122
V VOLUMETRIC PATTERNS OF ANTENNAS MOUNTED ON CONVEX SURFACES OF REVOLUTION.....	152
VI CONCLUSIONS.....	189
REFERENCES.....	191
 APPENDIX	
I	197
II	204

CHAPTER I

INTRODUCTION

Radiation pattern analysis of on-aircraft antennas at high frequencies is the object of this research. It is a basic study of aircraft-antenna pattern problems in which the antenna is mounted on the fuselage near the top or bottom. Since it is a study of general-type aircraft, the analytic aircraft is modelled in its most basic form. The fuselage is assumed to be a perfectly conducting convex surface. Thus, the effects of the cock-pit and radome are neglected at present. However, based on the advances made on metallic radomes, the radomes used in future aircrafts may to a good approximation be perfectly conducting. The wings and horizontal stabilizers are modelled by "n" sided flat plates which lie in a plane that is parallel to the fuselage axis. The engines are approximated by finite circular cylinders. This is a rather crude approximation; yet, it is shown that the engines have little effect on the overall pattern. Thus, it is not necessary at present to consider a more general engine model.

The need for this type of solution is basically two fold. First, there are upwards to 200 antennas mounted on a single aircraft. If these antennas can be located on the aircraft at the design stage, then one can expect better performance in that optimum locations and necessary structural changes can be anticipated. Secondly, antenna systems are normally added or changed in the course of an aircraft's useful lifetime. Such relocation or addition of antennas has always required a great deal of engineering time and money. For example, it is not uncommon for one to spend six months building a model and a second six months measuring radiation patterns for antennas mounted at various locations around the structure. On the other hand, it is not inconceivable that one could accomplish the same result in a fraction of the time (perhaps a day) using computer simulated models of the aircraft. Once an optimum region is determined, the antenna can simply be flight tested to ascertain its actual performance. Not only can these computer simulated results be used to determine the location, but they can, also, determine the optimum antenna design for a given application. Note that these analyses consider the three mutually orthogonal delta function sources which can be used to solve for the pattern of an arbitrary fuselage mounted antenna simply by integrating over the equivalent aperture currents.

One of the first solutions used to compute on-aircraft antenna patterns were the modal solutions for infinitely long circular[1,2] and elliptical[3] cylinders. The fuselage was modelled by a cylinder whose elliptical cross-section approximated the fuselage cross-section at the antenna location. Arbitrary antennas were considered and the antenna could be mounted on or above the fuselage. Results were quite adequate provided the aircraft structure was not illuminated too strongly. In fact, these solutions have been the primary high frequency analysis to date. However, with the desire to improve system performance, versatility, and coverage the antenna pattern must be shaped for the desired application in such a way that it can actually illuminate the structure quite strongly. In fact, in many cases the system's performance is dependent on the pattern effects of the secondary contributors. For example, too strong a ripple in a pattern may cause a system to function on a secondary lobe rather than the desired main beam. Consequently, the demands of modern sophisticated applications require that the analytic model represent the actual aircraft in more detail than assumed by the modal solutions alone.

With the advent of modern digital computers, one has been able to obtain integral equation solutions for antenna patterns and impedance using moment methods. Using this approach the surface currents are assumed to be of a given form which in turn radiate in all directions. The values of the complex currents are found by forcing the tangential component of the electric field to vanish on the surface. One of the first moment solutions applied to aircraft antenna problems used the wire grid technique which incorporates a point matching scheme[4]. This solution requires approximately 100 unknown currents per square wavelength to be found in order that the wire grid adequately model a perfectly conducting surface. A more sophisticated approach has been developed by Richmond[5] which uses a reaction technique to solve for the unknown currents. Yet this solution still requires the wire grid model of the aircraft with approximately 100 unknown currents per square wavelength. An exhaustive study of this approach has been made by Lin[6] in which he actually treated the bistatic scattering problem; however, the same conclusions apply for the antenna problem. A third approach might be to divide the surface into patches with each patch having two unknown complex currents. Using this approach perhaps 20 unknown currents per square wavelength need to be found. However, all of these solutions are restricted to lower frequencies based on the fundamental limitation on the size of matrices which modern computers can invert without excessive loss of accuracy.

Another approach that has found great success at solving this type of problem is the Geometrical Theory of Diffraction (GTD). GTD is basically a high frequency solution which is divided into two basic problems; these being wedge diffraction and curved surface diffraction. The wedge diffraction solution has been applied to determine the radiation patterns of such basic antennas as parallel plate antennas[7,8,9], parallel plate arrays[10,11] horns

antennas[12,13], parabolic reflectors[14,15], and rectangular waveguide antennas[16]. Both these diffraction solutions have been applied in computing the patterns of antennas mounted on cylinders[17,18,19], rockets[20], and wings[21]. The only limitation of these solutions is that the source and various scattering centers be separated by at least a wavelength. In some cases even this requirement can be relaxed. Using this approach one applies a ray optics technique to determine the fields incident on the various scatterers. The fields diffracted are found using the GTD solutions in terms of rays which are summed with the geometrical optics terms in the far field. The rays from a given scatterer tend to interact with the other structures causing various high-order terms. In this way one can trace out the various possible combinations of rays that interact between scatterers and determine and include only the dominant terms. Thus, one need only be concerned with the important structural scattering components and neglect all other higher-order terms. This makes the GTD approach ideal for a general high frequency study of on-aircraft antennas in that only the most basic structural features of the aircraft need to be modelled.

The basic approach applied here is to break the aircraft up into its simplest structural forms. Analyze these structures using ray optics techniques with numerical values obtained using modal solutions, physical optics, and GTD. Once the scattering from these structures is found and verified by measured data, they are adapted to the aircraft model simply by adjusting the incident field. In this way the aircraft begins to grow out of simple forms into a structure that actually resembles a modern aircraft in a general way.

Using these theoretical models the radiation patterns of arbitrary antennas mounted on the fuselage of various aircraft shapes are computed. The principal plane patterns of Chapter IV include only those structural components whose scattering was predetermined to be of some consequence in the resulting pattern. In the volumetric pattern study of Chapter V only the fuselage, which is approximated by an arbitrary convex surface of revolution, is considered. However, based on the principal plane studies the fuselage shape plays the dominant effect on the resulting radiation pattern with the wings and/or horizontal stabilizers being the strongest secondary contributors. As a result of these studies, various near field scattering problems and associated numerical techniques have been developed which may find application elsewhere.

CHAPTER II

THEORETICAL BACKGROUND

A. Introduction

As stated in the introduction the modal solutions for the radiation patterns of an antenna mounted on or near a fuselage have previously been the primary tool for high frequency analyses of on-aircraft antenna problems. In fact, these solutions can be quite adequate provided the source does not illuminate much of the aircraft structure. Consequently, the approach of this research is not to replace the modal solutions for fuselage mounted antenna problems but to improve the solutions by adding modelled aircraft scattering structures in the analysis. This is accomplished by using the ray optics technique which allows one to apply various high frequency solutions in its format by casting these solutions into ray form.

The modal solutions for a plane wave field incident on a perfectly conducting circular cylinder are presented and used, frequently, for numerical computations. The ray optics techniques will provide insight into the actual mechanisms involved as the rays interact with the cylindrical structures. Wedge and curved surface diffraction solutions, which constitute the Geometrical Theory of Diffraction (GTD), are presented in that they provide the solutions necessary to introduce the additional structures needed to improve the analyses. Each of these solutions are presented in basic terms in this chapter and applied to specific structural scattering problems in the following chapters.

B. Modal Solutions for Infinite Circular Cylinders

The modal solutions for the total field at any point in space for a plane wave field incident on a perfectly conducting infinitely long circular cylinder are presented in Appendix I. These solutions are divided into the problems of perpendicular and parallel polarizations incident on the cylinder as illustrated in Fig. 1. For the perpendicular polarization case the total field at any point is given by

$$E_{\perp z}^t = \frac{e^{jkz \cos \theta_i}}{k_z \sin \theta_i} \sum_{n=1}^{\infty} 2nj^{n+1} [J_n(k_z \sin \theta_i) - \frac{J_n'(ka \sin \theta_i)}{H_n^{(2)'}(ka \sin \theta_i)}]$$

$$H_n^{(2)}(k_z \sin \theta_i) \sin n(\phi - \phi_i)$$

$$E_{\perp z}^t = -je^{jkz \cos \theta_i} \sum_{n=0}^{\infty} \epsilon_n j^n [J_n'(k_z \sin \theta_i) - \frac{J_n'(k_z \sin \theta_i)}{H_n^{(2)'}(ka \sin \theta_i)}]$$

$$(1) \quad H_n^{(2)'}(k_z \sin \theta_i) \cos n(\phi - \phi_i)$$

$$E_{\perp z}^t = 0$$

$$H_{\perp z}^t = -\frac{j \cos \theta_i e^{jkz \cos \theta_i}}{Z_0} \sum_{n=0}^{\infty} \epsilon_n j^n [J_n'(k_z \sin \theta_i) -$$

$$\frac{J_n'(ka \sin \theta_i)}{H_n^{(2)'}(ka \sin \theta_i)} H_n^{(2)}(k_z \sin \theta_i) \cos n(\phi - \phi_i)]$$

$$H_{\perp z}^t = -\frac{\cos \theta_i e^{jkz \cos \theta_i}}{k_z Z_0 \sin \theta_i} \sum_{n=1}^{\infty} 2nj^{n+1} [J_n(k_z \sin \theta_i) -$$

$$\frac{J_n'(ka \sin \theta_i)}{H_n^{(2)'}(ka \sin \theta_i)} H_n^{(2)}(k_z \sin \theta_i) \sin n(\phi - \phi_i)]$$

$$H_{\perp z}^t = -\frac{\sin \theta_i}{Z_0} e^{jkz \cos \theta_i} \sum_{n=0}^{\infty} \epsilon_n j^n [J_n(k_z \sin \theta_i) -$$

$$\frac{J_n'(ka \sin \theta_i)}{H_n^{(2)'}(ka \sin \theta_i)} H_n^{(2)}(k_z \sin \theta_i) \cos n(\phi - \phi_i)]$$

where

$$\epsilon_n = \begin{cases} 1 & n = 0 \\ 2 & \text{otherwise.} \end{cases}$$

For the parallel polarization case the total field is given by

$$E_{u\rho}^t = -j \cos \theta_i e^{jkz \cos \theta_i} \sum_{n=0}^{\infty} \epsilon_n j^n [J_n'(k\rho \sin \theta_i) -$$

$$\frac{J_n(ka \sin \theta_i)}{H_n^{(2)}(ka \sin \theta_i)} H_n^{(2)'}(k\rho \sin \theta_i)] \cos n(\phi - \phi_i)$$

$$E_{u\phi}^t = - \frac{\cos \theta_i e^{jkz \cos \theta_i}}{k\rho \sin \theta_i} \sum_{n=1}^{\infty} 2n j^{n+1} [J_n(k\rho \sin \theta_i) -$$

$$\frac{J_n(ka \sin \theta_i)}{H_n^{(2)}(ka \sin \theta_i)} H_n^{(2)}(k\rho \sin \theta_i)] \sin n(\phi - \phi_i)$$

$$E_{uz}^t = -\sin \theta_i e^{jkz \cos \theta_i} \sum_{n=0}^{\infty} \epsilon_n j^n [J_n(k\rho \sin \theta_i) -$$

$$(2) \quad \frac{J_n(ka \sin \theta_i)}{H_n^{(2)}(ka \sin \theta_i)} H_n^{(2)}(k\rho \sin \theta_i)] \cos n(\phi - \phi_i)$$

$$H_{u\rho}^t = - \frac{e^{jkz \cos \theta_i}}{k\rho Z_0 \sin \theta_i} \sum_{n=1}^{\infty} 2n j^{n+1} [J_n(k\rho \sin \theta_i) -$$

$$- \frac{J_n(ka \sin \theta_i)}{H_n^{(2)}(ka \sin \theta_i)} H_n^{(2)}(k\rho \sin \theta_i)] \sin n(\phi - \phi_i)$$

$$H_{uz}^t = \frac{j}{Z_0} e^{jkz \cos \theta_i} \sum_{n=0}^{\infty} \epsilon_n j^n [J_n'(ka \sin \theta_i) -$$

$$\frac{J_n(ka \sin \theta_i)}{H_n^{(2)}(ka \sin \theta_i)} H_n^{(2)'}(ka \sin \theta_i) \cos n(\phi - \phi_i)]$$

$$H_{uz}^t = 0.$$

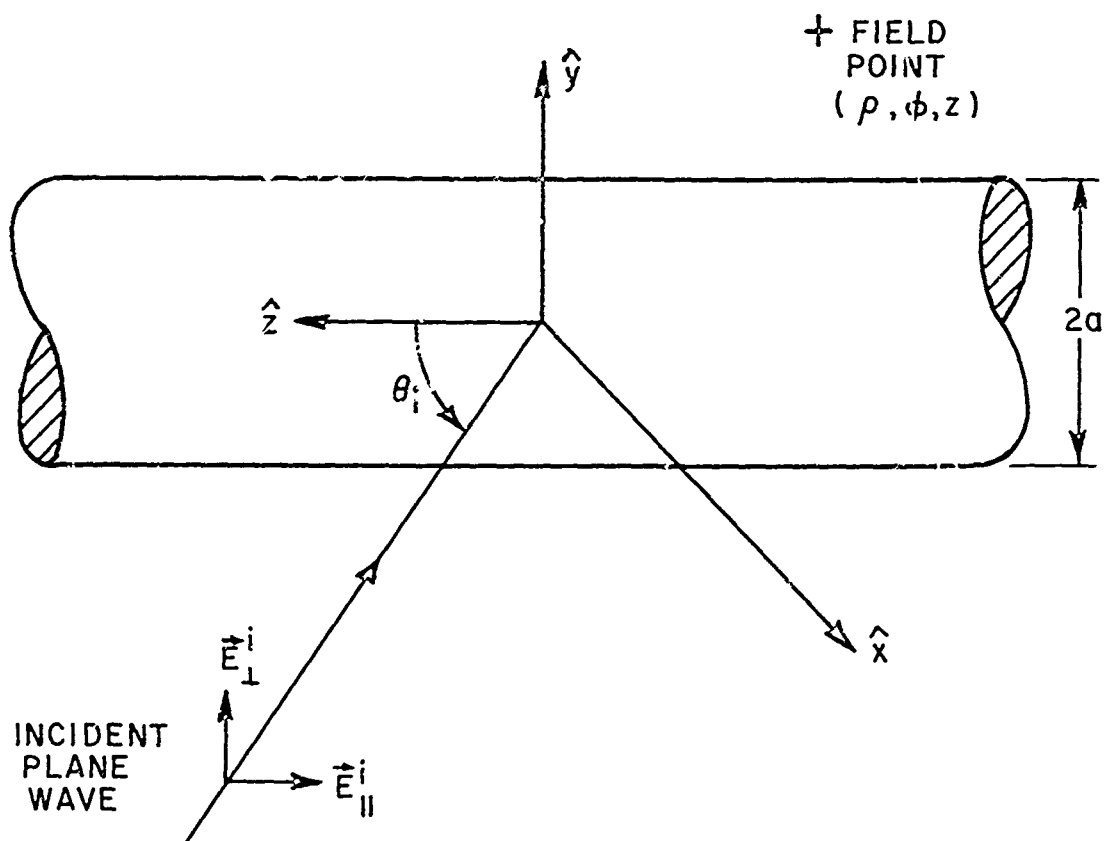


Fig. 1--Plane wave incident on an infinitely long cylinder of radius (a).

The patterns of small antennas mounted on a cylinder (fuselage) can be found using the previously derived solutions. The antennas considered are a radial monopole and an arbitrarily oriented slot. All have dimensions that are small in terms of the wavelength. The radial monopole and slot are considered to receive, respectively, an open circuit voltage and a short circuit current, so that they will cause negligible distortion to the field which would exist there with the antenna absent. Thus, the antenna response is directly related to the total field component at that point.

For the radial monopole, the open circuit voltage is equal to the product of the effective height of the monopole times the component of electric intensity parallel to its axis (E_{ρ}^t). For the slot the short circuit current is equal to the product of the effective height times the component of magnetic intensity parallel to its axis ($\cos \alpha H_z^t + \sin \alpha H_{\phi}^t$) with the slot orientation defined by α as illustrated in Fig. 2.

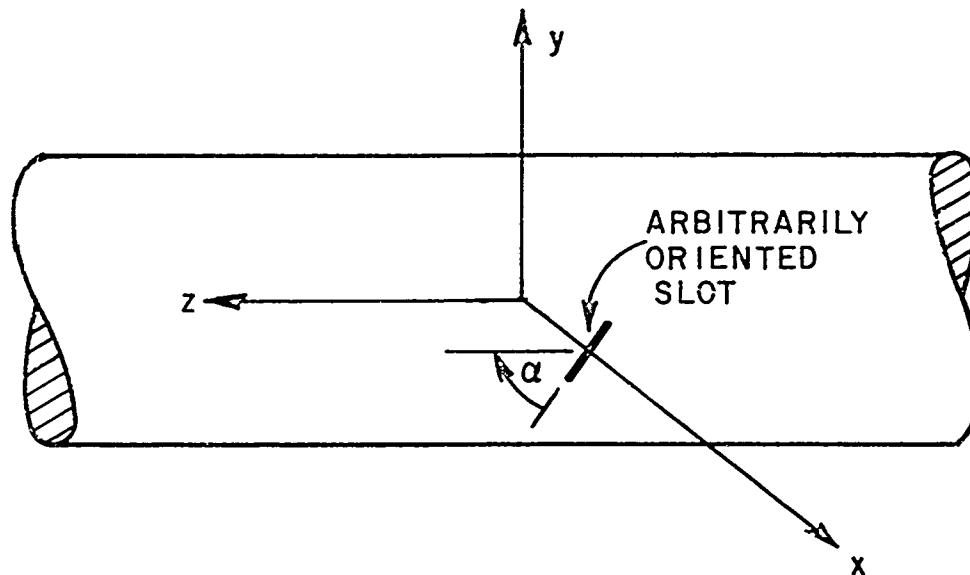


Fig. 2--Arbitrarily oriented slot on cylinder.

It is shown in Ref. 1 that the effective height of the radial monopole for arbitrary plane wave incidence (θ_i, ϕ_i) is given using Eqs. (1) and (2) by

$$(3) \quad h_{\text{monopole}} = \hat{\theta} [E_{\parallel \rho}^t(\rho=b)] + \hat{\phi} [E_{\perp \rho}^t(\rho=b)]$$

where z is the effective length of the monopole without the cylinder present and b is the distance of the radial monopole from the center of the cylinder.

The effective height of the slot can be written similarly as

$$(4) \quad \vec{h}_{\text{slot}} = z(\hat{\theta} H_{0z}^t(\rho=a) \sin \alpha + \hat{\phi} [H_{1z}^t(\rho=a) \sin \alpha + H_{1z}^t(\rho=a) \cos \alpha]).$$

Note that in each case the antenna is located at ($\phi=0, z=0$) and the phase is referred to the center of the cylinder.

The transmitted field, when the antenna elements are used for transmission, is [1]

$$(5) \quad \vec{E}(r, \theta_i, \phi_i) = \frac{jZ_0 I_m e^{-jkr}}{2\lambda r} \vec{h}(\theta_i, \phi_i)$$

which can be cast into ray form using

$$\vec{E}(r, \theta_i, \phi_i) = \vec{R}(\theta_i, \phi_i) \frac{e^{-jkr}}{r}.$$

It is convenient now to consider a new current (I_m') such that

$$(6) \quad \vec{R}(\theta_i, \phi_i) = I_m' \vec{h}(\theta_i, \phi_i)$$

where

$$I_m' = \frac{jZ_0 I_m}{2\lambda}.$$

Applying the above solution to a $\lambda/4$ radial monopole it was determined that the series converged for practical purposes (three significant figures) after summing ($7a \sin \theta_i + 8$) terms. The solutions for the slot antenna converged after summing ($7.5a \sin \theta_i + 10$) terms.

Since these expressions for the distant fields radiated are based on infinitesimal elements of electric and magnetic currents, the far fields of an arbitrary antenna can be determined by integrating across equivalent aperture currents. This is done numerically by

superposition of discrete elements which approximate the actual aperture distribution. This technique can be shown to be valid provided the element spacing is much smaller than the wavelength[22], that is, one may write

$$(7) \quad \vec{R}^{\text{total}}(z_i, z_i) = \sum_{n=1}^N I_n \vec{h}_n(z_i, z_i - z_n, z_n)$$

where I_n is the current of the n th element, (z_n, z_n) defines its position, and \vec{h}_n is the appropriate effective height. For example, some of our slot measurements were taken using open-ended waveguide whose aperture distribution can be adequately approximated by six infinitesimal sources. Note however that an infinitesimal antenna is considered in each case except where it is stated otherwise.

These solutions (Eqs. (1) and 2)) are not just limited to finding the radiation patterns of antennas mounted on or near an aircraft fuselage as used previously. They are applied in Chapters III and IV to determine the near scattered fields by aircraft engines which are modelled as infinite cylinders in Section IV-B and finite cylinders in Section III-C. In addition, they are used to compute the currents on an infinite cylinder and then integrated over a finite length to obtain an approximate solution for the far field specular scatter of a finite cylinder. Consequently, these solutions are used extensively throughout this report.

C. Wedge Diffraction

It has been shown in the last section that a cylindrically shaped fuselage can be analyzed using conventional modal solutions. However, aircraft shapes are, in general, quite complex involving many complicated structures. Thus, to improve the radiation pattern over that simply obtained using the modal solutions, one must take these various scattering structures into account. Based on past performance, the geometrical theory of diffraction has proven itself well suited to this type of analytical study. Not only does this approach fit nicely in terms of the ray optics format but it also provides a means for analyzing the effect of three-dimensional structures. Consequently, a brief description of the wedge diffraction problem is presented here. The diffraction by a curved surface is treated in the following section. Note that these two basic diffraction problems constitute the geometrical theory of diffraction (GTD).

An asymptotic solution for the diffraction from a conducting wedge was first solved by Sommerfeld[23]. Originally, GTD[2] as applied to diffraction by a wedge was based on plane wave diffraction coefficients; however, as shown in Ref. [25] the use of diffraction

of cylindrical waves has been found necessary in the treatment of antennas. Consequently, different formulations of wedge diffraction were substituted for the plane wave diffraction coefficient which is the basis for wedge diffraction theory. Pauli[26] introduced the V_B function as a practical formulation to the solution for a finite-angle conducting wedge. Recently, however, Hutchins and Kouyoumjian[27,28] presented a formulation for the diffracted field (V_B), which significantly improves the accuracy over that obtained from Pauli's form.

This improved diffraction solution[27,28] is better in the transition regions (near the incident and reflected shadow boundaries). It can be written in the form

$$(8) \quad V_B(L, \beta, n) = I_{-\pi}(L, \beta, n) + I_{+\pi}(L, \beta, n)$$

where

$$I_{\pm\pi}(L, \beta, n) \sim \frac{e^{-j(kL + \pi/4)}}{jn\sqrt{2\pi}} \sqrt{a} \cot\left(\frac{\pi \pm \beta}{2n}\right) \times \\ e^{jkLa} \int_{\sqrt{kLa}}^{\infty} e^{-j\tau^2} d\tau + [\text{higher order terms}]$$

and where the higher order terms are negligible for large kL and with n defined from the wedge angle $WA = (2-n)\pi$, also $a = 1 + \cos(\beta - 2n\pi N)$ and N is a positive or negative integer or zero, which ever most nearly satisfies the equations

$$\begin{aligned} 2n\pi N - \beta &= -\pi & \text{for } I_{-\pi} \\ 2n\pi N - \beta &= +\pi & \text{for } I_{+\pi} \end{aligned}$$

The variables L and β are defined later.

The three dimensional wedge diffraction problem is pictured in Fig. 3. A source whose radiated E field is given by $E^i(s)$ is located at point $s'(\rho', \phi', z')$. It can be an arbitrary electric or magnetic source causing plane, cylindrical, conical, or spherical wave incidence on the wedge tip. The diffracted vector field at point $s(\rho, \phi, z)$ can be written in terms of a dyadic diffraction coefficient. Kouyoumjian and Pathak[29] have given a more rigorous basis for the GTD formulation and have shown that the diffracted fields may be written compactly if they are in terms of a ray-fixed coordinate system. The ray-fixed coordinate system is centered at the point of diffraction Q_E , (or points of diffraction in the case of plane wave incidence). Q_E is a unique

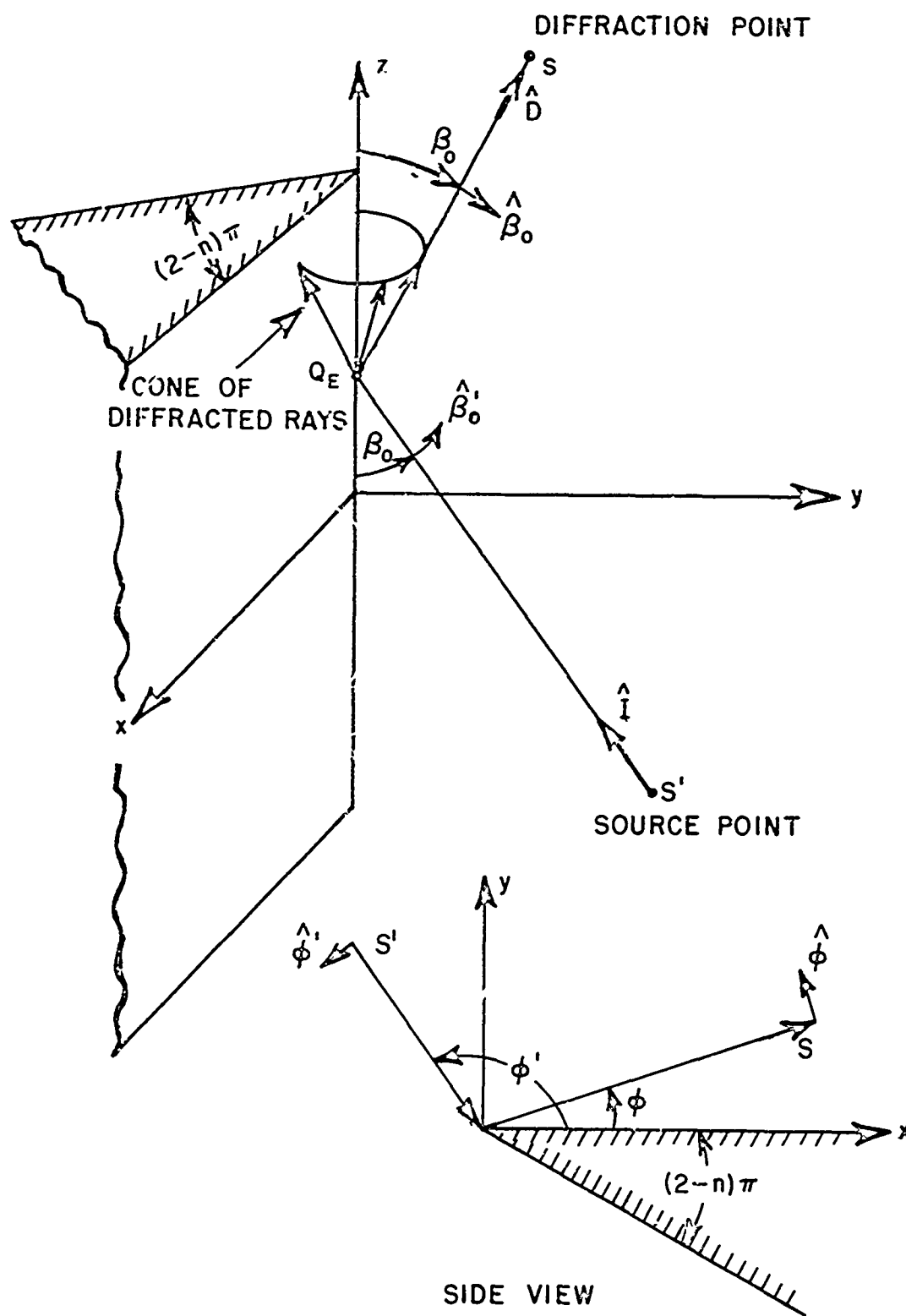


Fig. 3--Geometry for three-dimensional wedge diffraction problem.

point or points for a given source and observation point. The incident ray diffracts as a cone of rays such that $\hat{z}_0 = \hat{z}_0^1$ (see Fig. 3).

The relationships between the orthogonal unit vectors associated with these coordinates $(\hat{s}', \hat{z}_0^1, \hat{z}^1; \hat{s}, \hat{z}_0, \hat{z})$ are given by

$$\hat{I} = -\hat{s}'$$

$$\hat{I} = \hat{z}_0^1 \times \hat{z}^1$$

$$\hat{s} = \hat{z}_0 \times \hat{z},$$

where \hat{I} is the incident direction unit vector, and \hat{s} is the diffraction direction unit vector. The diffracted field is now given by

$$\bar{E}^d(s) = \bar{E}^i(Q_E) \cdot \bar{D}_E(\hat{s}, \hat{I}) A(s) e^{-jks}.$$

For our purpose, it is more convenient to write the diffracted field in terms of the V_B function in Eq. (1) as,*

$$(9) \quad \begin{bmatrix} E_{||}^d(s) \\ E_{\perp}^d(s) \end{bmatrix} = \begin{bmatrix} -V_B^- & 0 \\ 0 & -V_B^+ \end{bmatrix} \begin{bmatrix} E_{||}^i(Q_E) \\ E_{\perp}^i(Q_E) \end{bmatrix} \frac{\sqrt{L} e^{jkl}}{\sin \beta_0} A(s) e^{-jks}$$

where

$$V_B^{\mp} = V_B(L, \beta^{\mp}, n) \mp V_B(L, \beta^{\pm}, n).$$

The minus sign (V_B^-) applies for the \bar{E} -field component parallel to the edge with boundary condition

$$(\bar{E}|_{\text{wedge}}) = 0.$$

The plus sign (V_B^+) applies for the \bar{E} -field vector perpendicular to the edge with boundary conditions

*If a fixed coordinate system is used Eq. (9) takes the form of a 3 x 3 matrix.

$$\left(\frac{\partial \bar{E}}{\partial n} \right)_{\text{wedge}} = 0.$$

The angular relations are expressed by

$$\beta = \beta^{\pm} = \pm \beta_0,$$

where the minus sign (β^-) is associated with the incident field and the plus sign (β^+) with the reflected field. The quantity $A(s)$ is a ray divergence factor given by [29]

$$A(s) = \begin{cases} \frac{1}{\sqrt{s}} & \text{plane, cylindrical (s=s'),} \\ & \text{and conical wave incidence} \\ \sqrt{\frac{s'}{s(s'+s)}} & \text{spherical wave incidence} \end{cases}$$

and L is given by [29]

$$L = \begin{cases} s \sin^2 \beta_0 & \text{plane wave incidence} \\ \frac{\rho' \rho}{\rho + \rho'} & \text{cylindrical wave incidence} \\ \frac{s' s \sin^2 \beta_0}{s + s'} & \text{conical and spherical wave incidence.} \end{cases}$$

For the two-dimensional wedge problem, illustrated in Fig. 4, where there is cylindrical wave incidence with $\beta_0 = 90^\circ$, Eq. (9) reduces to give

$$\begin{bmatrix} E_{||}^d(\rho, \phi) \\ E_{\perp}^d(\rho, \phi) \end{bmatrix} \sim \begin{bmatrix} -V_B^- & 0 \\ 0 & -V_B^+ \end{bmatrix} \begin{bmatrix} E_{||}^i(\rho', \phi') \\ E_{\perp}^i(\rho', \phi') \end{bmatrix} \sqrt{\frac{\rho'}{\rho + \rho'}} e^{jk\rho'} e^{-jk\rho}.$$

In the far field ($\rho \gg \rho'$) this becomes

$$\begin{bmatrix} E_{||}^d(\rho, \phi) \\ E_{\perp}^d(\rho, \phi) \end{bmatrix} \sim \begin{bmatrix} -V_B^- & 0 \\ 0 & -V_B^+ \end{bmatrix} \begin{bmatrix} E_{||}^i(\rho', \phi') \\ E_{\perp}^i(\rho', \phi') \end{bmatrix} \frac{\sqrt{\rho'}}{\sqrt{\rho}} e^{jk\rho'} e^{-jk\rho}.$$

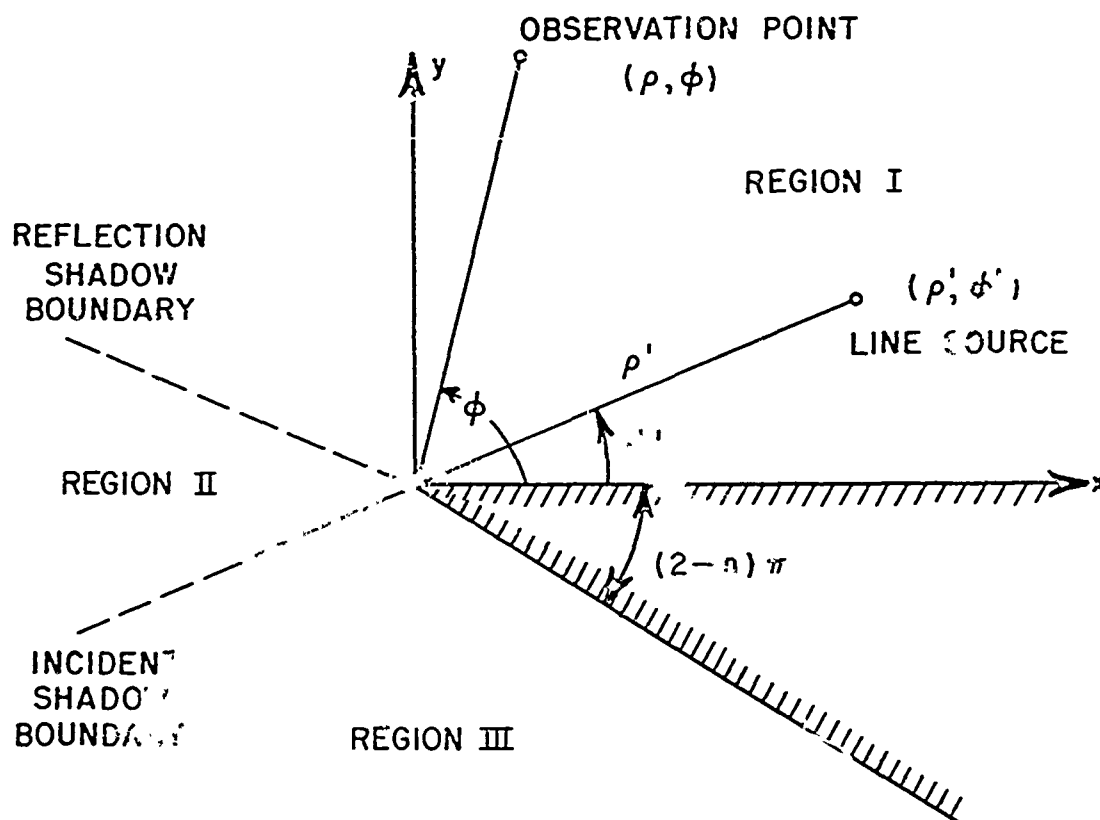


Fig. 4--Two-dimensional wedge diffraction geometry.

Putting this in ray form and factoring out $\frac{e^{-jk\rho}}{\sqrt{\rho}}$, we have

$$(10) \quad \begin{bmatrix} R_{II}^c(\phi) \\ R_{II}^d(\phi) \end{bmatrix} \sim \begin{bmatrix} -V_B^- & 0 \\ 0 & -V_B^+ \end{bmatrix} \begin{bmatrix} R_{II}^i(\phi') \\ R_{II}^i(\phi') \end{bmatrix}$$

The ray form used here is given by

$$\bar{E}(\rho, \phi) = \bar{R}(\phi) \frac{e^{-jk\rho}}{\sqrt{\rho}}.$$

Thus, $\bar{R}(\phi)$ is related to the far field pattern function.

For the three-dimensional wedge problem where there is spherical wave incidence, Eq. (9) reduces to give

$$\begin{bmatrix} E_{||}^d(s, \beta_0, \phi) \\ E_{\perp}^d(s, \beta_0, \phi) \end{bmatrix} = \begin{bmatrix} -V_B^- & 0 \\ 0 & -V_B^+ \end{bmatrix} \begin{bmatrix} E_{||}^i(s', \beta_0', \phi') \\ E_{\perp}^i(s', \beta_0', \phi') \end{bmatrix} \frac{s'}{s+s'} e^{\left(\frac{jks's \sin^2 \beta_0}{s+s'} \right)} e^{jks}.$$

In the far field ($s \gg s'$), we have

$$\begin{bmatrix} E_{||}^d(s, \beta_0, \phi) \\ E_{\perp}^d(s, \beta_0, \phi) \end{bmatrix} = \begin{bmatrix} -V_B^- & 0 \\ 0 & -V_B^+ \end{bmatrix} \begin{bmatrix} E_{||}^i(s', \beta_0', \phi') \\ E_{\perp}^i(s', \beta_0', \phi') \end{bmatrix} s' e^{jks' \sin^2 \beta_0} \frac{e^{-jks}}{s}$$

Putting this in ray form and factoring out $\frac{e^{-jks}}{s}$, it is seen that

$$(11) \quad \begin{bmatrix} R_{||}^d(\beta_0, \phi) \\ R_{\perp}^d(\beta_0, \phi) \end{bmatrix} \sim \begin{bmatrix} -V_B^- & 0 \\ 0 & -V_B^+ \end{bmatrix} \begin{bmatrix} R_{||}^i(\beta_0', \phi') \\ R_{\perp}^i(\beta_0', \phi') \end{bmatrix} e^{-jks' \cos^2 \beta_0}.$$

It is interesting to note that in the principal plane ($\beta_0 = 90^\circ$) the ray form of the three-dimensional case takes on the same form as the two-dimensional problem.

The total ray value at the observation point s is given by the sum of the geometrical optics terms and the diffracted terms

$$\bar{R}^T(s) = \bar{R}^{G.O.}(s) + \bar{R}^d(s)$$

where

$$\bar{R}^{G.O.}(s) = \begin{cases} \bar{R}^i(s) + \bar{R}^r(s) & \text{incident and reflected region I} \\ \bar{R}^i(s) & \text{incident region II} \\ 0 & \text{shadowed region III} \end{cases}$$

and $\bar{R}^r(s)$ may be determined from the image of the source term using basic geometrical optics techniques. These three regions are illustrated in Fig. 4 for a two-dimensional wedge diffraction problem.

D. Curved Surface Diffraction

When an incident ray strikes a smooth, curved perfectly conducting surface at grazing incidence, i.e., at the shadow boundary, a part of its energy is diffracted into the shadow region. To describe this phenomenon Keller[30] introduced a class of curved surface diffracted rays. These ray paths include the points Q_1 and Q_2 which form a curve on the diffracting surface as illustrated in Fig. 5. However, the actual concept of creeping waves was introduced by Franz and Depperman.[31,32] The basic concept as presented in the following discussion is basically taken from "Asymptotic High-frequency Methods" by Kouyoumjian.[33]

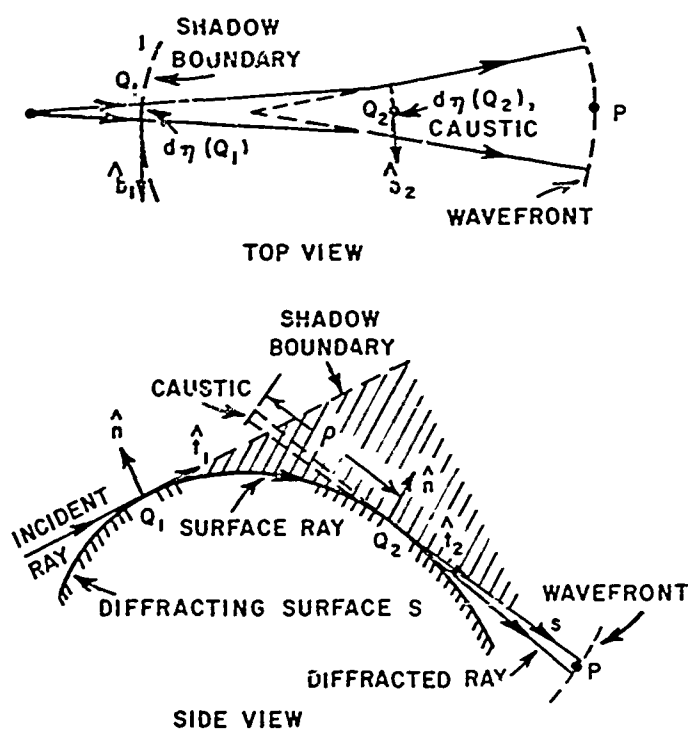


Fig. 5--Diffraction by a smooth curved surface.

The diffraction by a smooth curved surface is shown in Fig. 5 in which O is the source point and P is the observation point in the shadow region. Applying Fermat's principle, the line OQ_1Q_2P is the shortest distance between O and P which does not penetrate the surface. In detail, a ray incident on the shadow boundary at Q_1 divides; one part of the incident energy continues straight on

as predicted by geometrical optics, a second part follows the surface s into the shadow region as a surface ray shedding diffracted rays tangentially as it propagates. With \hat{t} , \hat{n} and \hat{b} being the unit vectors in the direction of incidence, normal to the surface s and binormal to the surface ($\hat{b} = \hat{t} \times \hat{n}$), respectively, the incident field $\vec{E}^i(Q_1)$ may be resolved into its normal and tangential components ($\hat{n} \cdot \vec{E}^i(Q_1)$ and $\hat{b} \cdot \vec{E}^i(Q_1)$). It is assumed that these two components induce surface ray fields which propagate independently of each other along the geodesic arc between Q_1 and Q_2 . From Reference [33] the surface ray field $Ae^{j\phi}$ at Q_1 is related to the incident fields at Q_1 by

$$(12) \quad A(Q_1) e^{j\phi(Q_1)} = D_s(Q_1) \hat{b}_1 \cdot \vec{E}^i(Q_1)$$

where $D_s(Q_1)$ is the scalar diffraction coefficient for a soft surface. The amplitude of the surface ray is assumed to be governed by the conservation of energy between a pair of adjacent surface rays. Hence, the amplitude behavior of the fields is given as

$$(13) \quad A(Q_2) = A(Q_1) \sqrt{\frac{dn_1}{dn_2}} e^{\left[-\int_{Q_1}^{Q_2} \alpha(t') dt' \right]}$$

where

dn_1 and dn_2 = the separation between a pair of rays at Q_1 and Q_2 , respectively.

$\alpha(t)$ = the attenuation constant which is a function of t , the coordinate along the surface ray, because it depends on the local radius of curvature and its derivatives.

The attenuation constant $\alpha(t)$ is introduced due to the tangential shedding of rays as the surface ray propagates. It is seen from Fig. 5 that Q_2 is a caustic of the diffracted field and the second caustic is located at a distance ρ from Q_2 . Thus, the tangential component of the diffracted field which radiates from Q_2 towards P can be found, as in the previous edge diffraction case, with one of the caustics used as a reference point and is given by

$$(14) \quad \hat{b}_2 \cdot \vec{E}^d(P) = D_s(Q_2) A(Q_2) e^{j\phi(Q_2)} \sqrt{\frac{\rho}{s(\rho+s)}} e^{-jks}.$$

From Eqs. (12), (13) and (14) there results

$$(15) \quad \hat{b}_2 \cdot \bar{E}^d(P) = \left[\hat{b}_1 \cdot \bar{E}^i(Q_1) \right] D_s(Q_1) D_s(Q_2) \sqrt{\frac{d\eta_1}{d\eta_2}} \sqrt{\frac{\rho}{s(\rho+s)}} e^{-j \left[k(t+s) + \int_{Q_1}^{Q_2} \alpha(t') dt' \right]}$$

It is found that $b_1 \cdot \bar{E}^i(Q_1)$ excites an infinity of surface ray modes each with its own diffraction coefficient and attenuation constant. Thus, the expression in Eq. (15) is replaced by

$$(16) \quad \hat{b}_2 \cdot \bar{E}^d(P) = \left[\hat{b}_1 \cdot \bar{E}^i(Q_1) \right] \sqrt{\frac{d\eta_1}{d\eta_2}} \sqrt{\frac{\rho}{s(\rho+s)}} e^{-j[k(t+s)]} \left[\sum_m^{\infty} D_{sm}(Q_1) D_{sm}(Q_2) e^{-\int_{Q_1}^{Q_2} \alpha_m(t') dt'} \right]$$

Equation (16) relates the diffracted field at P to the incident field at Q_1 for the soft surface boundary condition.

An expression similar to Eq. (16) is also obtained for the normal component of the incident field; in this case, the scalar diffraction coefficients and attenuation constants for the hard surface replace those of the soft surface. Therefore, the vector diffracted field at P can be written in terms of the electromagnetic field incident at Q_1 as

$$(17) \quad \bar{E}(P) = \left[\hat{n}_2 \hat{n}_1 v(1,2) + \hat{b}_2 \hat{b}_1 u(1,2) \right] \cdot \bar{E}^i(1) \sqrt{\frac{\rho}{s(\rho+s)}} e^{-jks}$$

in which $v(1,2)$, $u(1,2)$ are equal to

$$(18) \quad \sqrt{\frac{d\eta_1}{d\eta_2}} e^{-jkt} \sum_m^{\infty} D_m(1) D_m(2) e^{-\int_1^2 \alpha_m(t') dt'}$$

with the subscripts h, s, respectively, added to D_m and α_m . Note that Q_1 and Q_2 have been replaced by 1 and 2 for the sake of brevity.

Finding dn_1 , dn_2 , and ρ is simply a matter of differential geometry involving the rays and surface; this is discussed at length in Levy and Keller[30]. The generalized diffraction coefficient and attenuation constant can be found in Reference [34].

The diffraction thus far discussed is applied to the open curved surface. For a closed surface, each surface ray mode produced at Q_1 encircles the surface an infinite number of times. The length of the surface ray path for the n -th encirclement is $t + nT$ where T is the circumference of the closed surface. These multiple-encircling rays may be summed to contribute

$$\left[1 - e^{-jkT - \int_0^T \alpha_m(t') dt'} \right]$$

to the denominator of the diffracted field. It is interesting to note that there must be another pair of diffraction points Q_3 and Q_4 for the closed surface as shown in Fig. 6. Therefore, the field at any point P in the shadow region is the sum of these two diffracted fields from Q_1 - Q_2 and Q_3 - Q_4 . The total field at any point in the illuminated region is, by the superposition principle, the sum of incident, reflected and diffracted fields. A detailed discussion of this subject can be found in Reference [34].

An important special case of this GTD solution is the one in which the antenna is mounted directly on the curved surface. This problem has been studied by Kouyoumjian[35] in which he analyzed by asymptotic methods the far field patterns of various antennas mounted on an infinitely long perfectly conducting circular cylinder. In this solution the reciprocity theorem is employed so that the radiation pattern is derived from the plane wave scattering by a cylinder. The physical optics approximation for the surface current is used to describe the field in the region in which the source is directly illuminated by the incident plane wave (the lit region). The Fock approximation[36] is used for the penumbra (transition) region; whereas, in the deep shadow region of the cylinder the geometrical theory of diffraction solution is applied to give the far field expression. It is noted that a launch coefficient, which relates the creeping wave (GTD field) to the actual surface field or current, is introduced so that the GTD solution can be properly employed. This launch factor is deduced from the exact solution for the surface current on the circular cylinder; and, in its asymptotic form, involves the well-known Airy function.

The far-zone principal plane* pattern for an infinitesimal slot mounted on an infinitely long perfectly conducting circular

*The principal plane being a plane cutting across the cross-section of the cylinder.

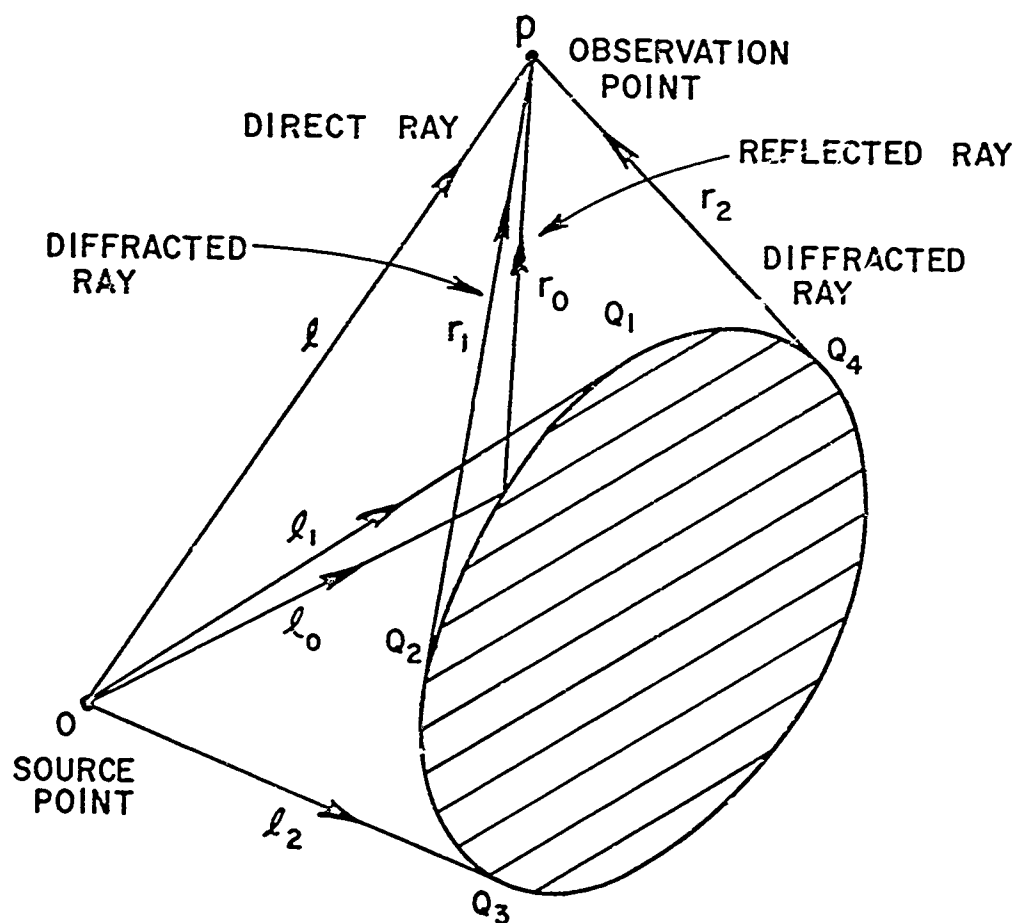


Fig. 6--Diffraction by a smooth closed cylindrical surface.

cylinder, equivalent to a magnetic line source $k\hat{y}$, with radius "a" as shown in Fig. 7 can be obtained by employing the aforementioned GTD asymptotic expressions for the various regions and is given by [35]

1) Lit Region: Geometrical Optics Description

$$(19) \quad R_y(\rho, \theta) = 2 e^{jka \cos(\theta_0 - \theta)}$$

2) Transition Region: $M^{-1} \leq \phi < \pi - M^{-1}$

$$(20) \quad R_y(\rho, \theta) = [g^*(\xi_1) e^{-jka\psi_1} + g^*(\xi_2) e^{-jka\psi_2}]$$

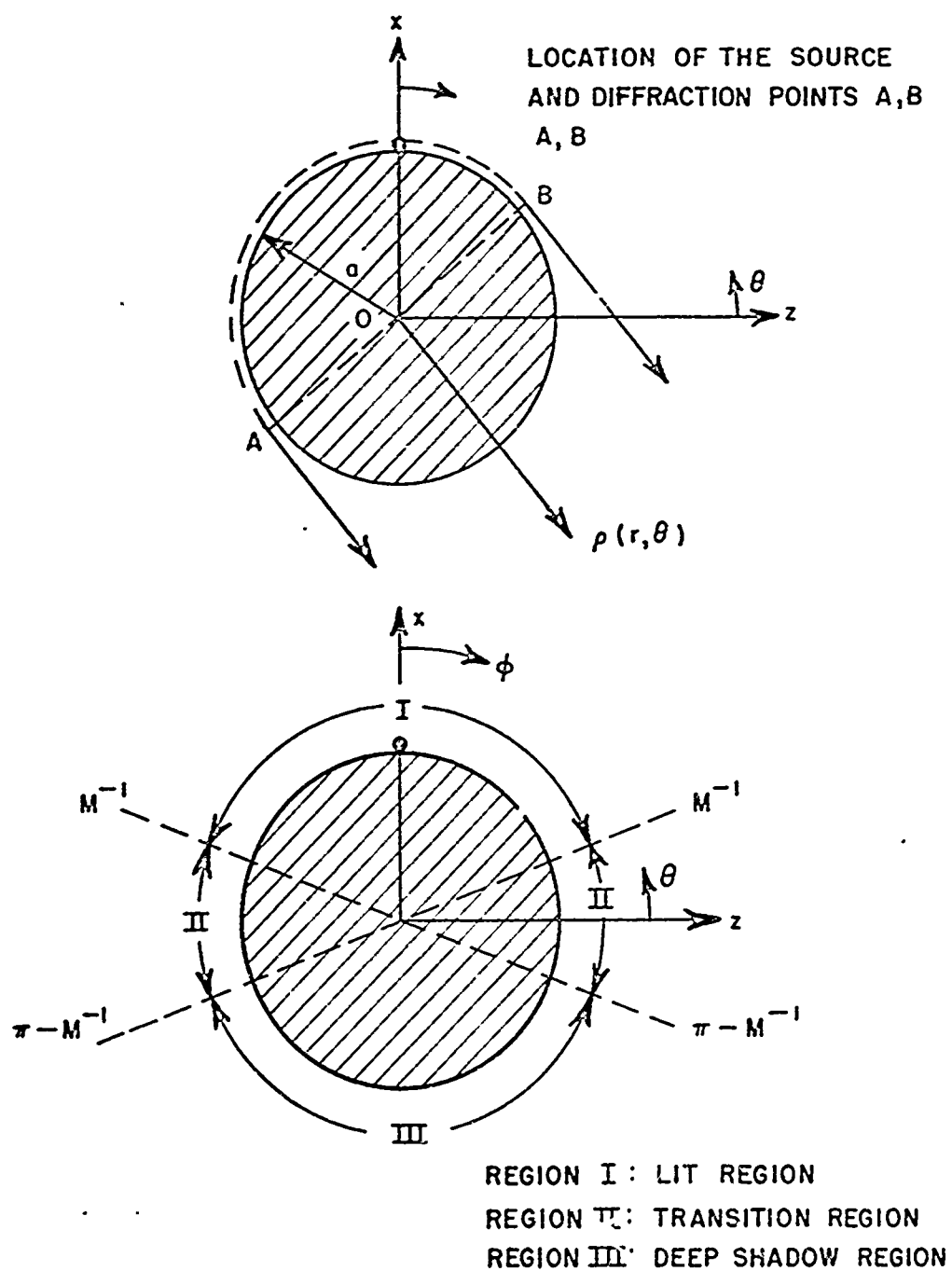


Fig. 7--Antenna mounted on a circular cylinder: GTD solution.

where

$$\psi_1 = \psi_0 - \psi' - -/2$$

$$\psi_2 = \frac{3-}{2} - |\psi_0 - \psi'|$$

$$M = \left(\frac{ka}{2} \right)^{1/3}$$

$$\psi = \psi_0 - \psi_0 \quad -/2 < \psi < 3-/2$$

$$\xi_1 = \left(\frac{ka}{2} \right)^{1/3} \psi_1$$

$$\xi_2 = \left(\frac{ka}{2} \right)^{1/3} \psi_2$$

The functions $g^*(\xi_1)$ and $g^*(\xi_2)$ are the conjugate of $g(\xi_1)$ and $g(\xi_2)$, respectively. The function $g(\xi)$ is the so called Fock's function for hard boundary condition ($\partial u / \partial n = 0$) and is given as

$$g(\xi) = \frac{1}{\pi} \int_{\Gamma_1} \frac{e^{-i\xi\tau}}{w_2(\tau)} d\tau,$$

where

$$w_2(\tau) = \frac{1}{\pi} \int_{\Gamma_2} e^{\tau t - t^3/3} dt$$

and Γ_1 and Γ_2 are contours in the complex plane as shown in Fig. 8. The magnitude and phase of the Fock function $[g(x)]$ are given in Reference [36].

3) Deep Shadow Region: Surface Ray Description

$$(21) \quad R_y(\rho, \theta) = (-2\pi) \left(\frac{ka}{2} \right)^{-1/3} e^{j \frac{\pi}{12}}.$$

$$\sum_{m=0}^{\infty} \{ [D_m^h(a)]^2 \text{Ai}(-\bar{q}_m) e^{-[\alpha_m^h(a)] s_1} e^{-jks_1} \\ + [D_m^h(a)]^2 \text{Ai}(-\bar{q}_m) e^{-[\alpha_m^h(a)] s_2} e^{-jks_2} \}$$

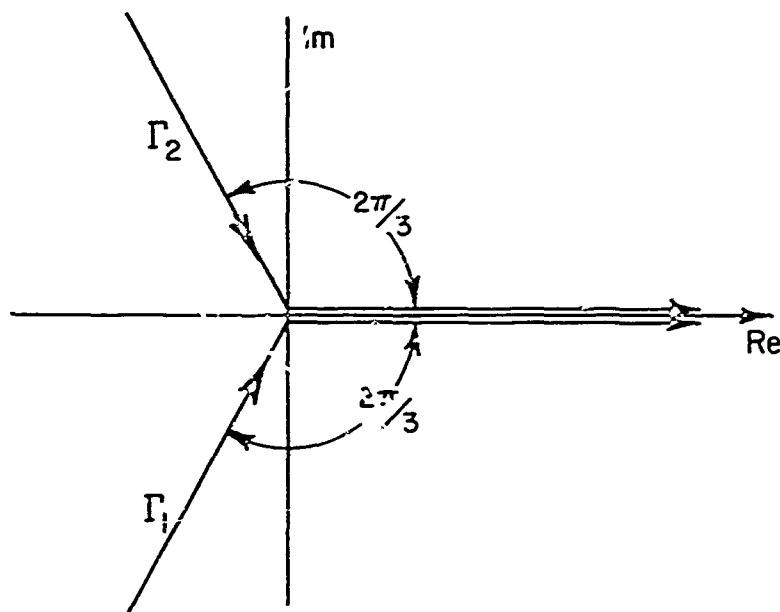


Fig. 8--Contours for complex plane integrations.

where

$$s_1 = a\psi_1$$

$$s_2 = a\psi_2$$

and ψ_1 and ψ_2 were defined earlier and \bar{q}_m is the root of $Ai'(-\bar{q}_m)$, that is, $Ai'(-\bar{q}_m) = 0$. The diffraction coefficient $[D_m^h(a)]^2$ and the surface attenuation constant $\alpha_m^h(a)$ are given in Table I. The roots \bar{q}_m and $Ai(-\bar{q}_m)$ are given in Table II. It is noted that the surface ray expression in Eq. (21) can be rewritten in the following way

$$(22) \quad R_y(\rho, \theta) = (-2\pi) \left(\frac{ka}{2} \right)^{-1/3} e^{j \frac{\pi}{12}} \sum_{m=0}^{\infty} \{ [D_m^h(a)]^2 Ai(-\bar{q}_m) e^{-\gamma(a)s_1} \\ + [D_m^h(a)]^2 Ai(-\bar{q}_m) e^{-\gamma(a)s_2} \}$$

where $\gamma(a) = \alpha_m^h(a) + jk_s$, propagation constant of the surface ray.

TABLE I
GENERALIZED DIFFRACTION COEFFICIENTS AND ATTENUATION CONSTANTS

Surface	Square of Diffraction Coefficient $D_m^2 = (\text{Column A}) \cdot (\text{Column B})$		Attenuation Constant $\alpha_m = (\text{Column C}) \cdot (\text{Column D})$	
	A. Keller's Result	B. Correction Terms	C. Keller's Result	D. Correct. in Terms
Soft Acoustic and S-ft EH	$\pi^{-1/2} 2^{-5/6} \frac{1/3 e^{-j\pi/12}}{k^{1/6} A_1 (-q_m)^2}$	$1 + \left(\frac{2}{k\rho_g}\right)^{2/3} q_m \left(\frac{1}{30} + \frac{\rho_g}{4\rho_{tn}} + \frac{\rho_g^2}{180}\right) e^{-j\pi/3}$	$\frac{q_m}{\rho_g} e^{j\pi/6} \left(\frac{k\rho_g}{2}\right)^{1/3}$	$1 + \left(\frac{2}{k\rho_g}\right)^{2/3} q_m \left(\frac{1}{60} - \frac{2}{45} \rho_g^2 + \frac{4}{135} \rho_g^2\right) e^{-j\pi/3}$
		$1 + \left(\frac{2}{k\rho_g}\right)^{2/3} \left(q_m \left(\frac{1}{30} + \frac{\rho_g}{4\rho_{tn}} + \frac{\rho_g^2}{180}\right) - \frac{1}{2} \left(\frac{1}{10} + \frac{\rho_g}{4\rho_{tn}} - \frac{\rho_g^2}{60}\right) \right) e^{-j\pi/3}$		$1 + \left(\frac{2}{k\rho_g}\right)^{2/3} \left(q_m \left(\frac{1}{60} - \frac{2}{45} \rho_g^2 + \frac{4}{135} \rho_g^2\right) + \frac{1}{2} \left(\frac{1}{10} + \frac{\rho_g}{4\rho_{tn}} - \frac{\rho_g^2}{60}\right) \right) e^{-j\pi/3}$
Hard Acoustic	$\pi^{-1/2} 2^{-5/6} \frac{1/3 e^{-j\pi/12}}{k^{1/6} q_m (A_1 (-q_m))^2}$	$1 + \left(\frac{2}{k\rho_g}\right)^{2/3} \left(q_m \left(\frac{1}{30} + \frac{\rho_g}{4\rho_{tn}} + \frac{\rho_g^2}{180}\right) - \frac{1}{2} \left(\frac{1}{10} + \frac{\rho_g}{4\rho_{tn}} - \frac{\rho_g^2}{60}\right) \right) e^{-j\pi/3}$	$\frac{q_m}{\rho_g} e^{j\pi/6} \left(\frac{k\rho_g}{2}\right)^{1/3}$	$1 + \left(\frac{2}{k\rho_g}\right)^{2/3} \left(q_m \left(\frac{1}{60} - \frac{2}{45} \rho_g^2 + \frac{4}{135} \rho_g^2\right) + \frac{1}{2} \left(\frac{1}{10} + \frac{\rho_g}{4\rho_{tn}} - \frac{\rho_g^2}{60}\right) \right) e^{-j\pi/3}$
		$1 + \left(\frac{2}{k\rho_g}\right)^{2/3} \left(q_m \left(\frac{1}{30} + \frac{\rho_g}{4\rho_{tn}} + \frac{\rho_g^2}{180}\right) - \frac{1}{2} \left(\frac{1}{10} + \frac{\rho_g}{4\rho_{tn}} - \frac{\rho_g^2}{60}\right) \right) e^{-j\pi/3}$		$1 + \left(\frac{2}{k\rho_g}\right)^{2/3} \left(q_m \left(\frac{1}{60} - \frac{2}{45} \rho_g^2 + \frac{4}{135} \rho_g^2\right) + \frac{1}{2} \left(\frac{1}{10} + \frac{\rho_g}{4\rho_{tn}} - \frac{\rho_g^2}{60}\right) \right) e^{-j\pi/3}$

TABLE II
AIRY FUNCTIONS AND ROOTS

MODE	BOUNDARY CONDITION			
	SOFT		HARD	
m	q_m	$A_i(-q_m)$	\bar{q}_m	$A_i'(-\bar{q}_m)$
0	2.33811	0.70121	1.01879	0.53566
1	4.08795	-0.83011	3.24820	-0.41902
2	5.52056	0.86520	4.82010	0.38041
3	6.78671	-0.91085	6.16331	-0.35791
4	7.94413	0.94734	7.37218	0.34236

The calculated radiation patterns using Eqs. (19) to (22) in the xz-plane (principal plane) of Fig. 7 for various cylinders have been shown to agree very favorably with those obtained from the modal solution, especially for $ka \geq 3.0$. These formulations also predict the radiation pattern fairly well for small cylinders with radii down to the range from $1/3$ to $1/4$ wavelength.[37]

The results for the circular cylinder are extended to cylinders with general cross-sectional shape in which the curvature varies along the ray path. This variable curvature has a strong effect on the attenuation constant which in turn affects the energy propagation quite significantly. Thus, the representations for fields in the lit, transition, and deep-shadow region are modified to include the variable curvature effect and again are given by

1) Lit Region:

$$(23) \quad R_y(\theta) = 2 e^{jkr_s \cos(\theta - \theta_p)}$$

2) Transition Region:

$$(24) \quad R_y(\theta) = \{g^*(\xi_A) e^{-j \int_A^P k ds} \cdot F(A) + g^*(\xi_B) e^{-j \int_B^P k ds} \cdot F(B)\}$$

3) Deep-Shadow Region:

$$\begin{aligned}
 (25) \quad R_y(\cdot) = & -2-j \left[\left(\frac{k}{2} g \right)^{-1/3} \right]_{r=r_p} e^{j \frac{\pi}{3}} \left(\frac{jk}{2} \right)^{1/2}, \\
 & \cdot \sum_{m=0}^{\infty} \left\{ D_m^h(P) D_m^h(A) \text{Ai}(-\bar{q}_m) e^{-j \int_A^P \gamma_m^h(s) ds} \cdot F(A) \right. \\
 & \left. + D_m^h(P) D_m^h(B) \text{Ai}(-\bar{q}_m) e^{-j \int_B^P \gamma_m^h(s) ds} \cdot F(B) \right\}
 \end{aligned}$$

where A and B are the points that the surface rays diffract toward the direction of the observation point, \cdot ; $(r_{s,p})$ defines the source locations; and ρ_g is the radius of curvature of the curved surface;

$$\xi_A = \int_A^P \left(\frac{k}{2\rho_g} \right)^{1/3} ds$$

and

$$\xi_B = \int_B^P \left(\frac{k}{2\rho_g} \right)^{1/3} ds.$$

The increment of the arc length along the ray trajectory is ds ; $F(A)$, $F(B)$ are the phase correction factors at the tangent points A and B; $g^*(\xi_A)$, $g^*(\xi_B)$ are the conjugates of $g(\xi_A)$ and $g(\xi_B)$, the Fock function as defined previously; and $D_m^h(P)$, $D_m^h(A)$, and $D_m^h(B)$ are the diffraction coefficients at the source location, and points A and B, respectively. The propagation constant is $\gamma_m^h(s) = \alpha_m^h(s) + jk$, where α_m^h is the ray trajectory attenuation factor for the hard boundary case and k is $2\pi/\lambda$. The general expressions used for the diffraction and attenuation constants are given in Table I. Note that the phase reference point for these formulations is at the origin. Some calculated radiation patterns in xz-plane (the elevation plane) employing these formulations for an elliptical cylinder are also given in Reference [37]. These results compare fairly well with the exact solution obtained by Sinclair[1] as shown in Fig. 9.

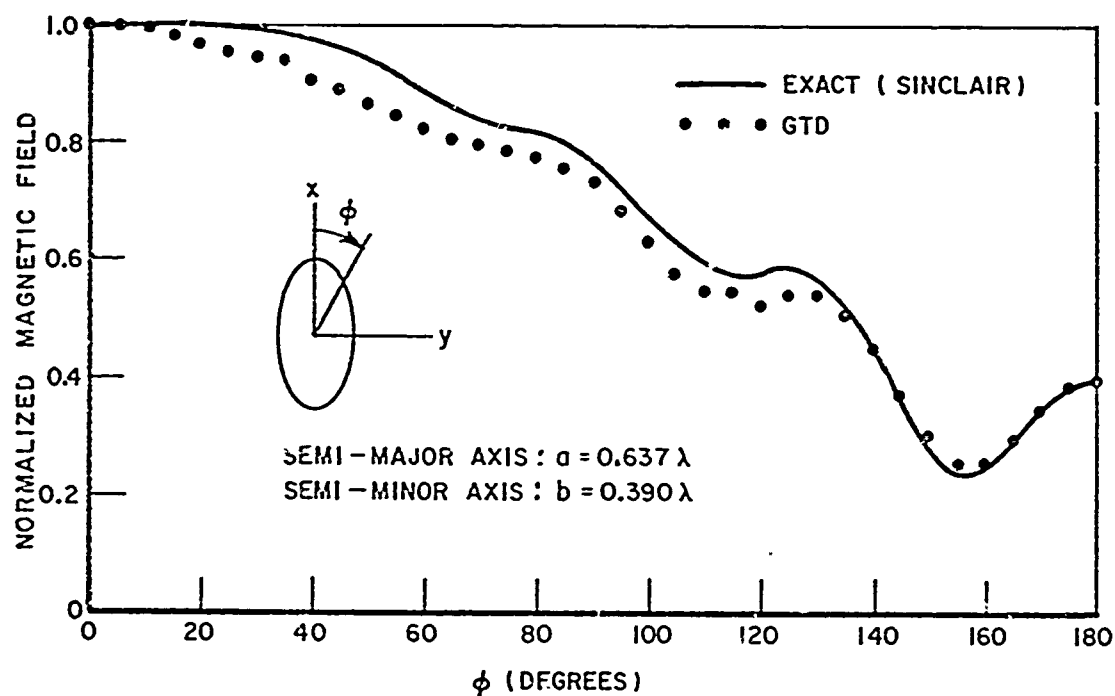


Fig. 9--Principal plane patterns with a circumferential slot mounted on an elliptical cylinder.

The same technique is also employed to derive the generalized expressions for a slot antenna with soft boundary condition and infinitesimal monopole antenna. The equations again contain the Fock functions. A summary of the far field expressions for the circumferential slot, axial slot and infinitesimal monopole are presented in Table III[35].

TABLE III
RADIATION FIELD IN RAY FORM IN THE PRINCIPAL PLANE
OF A GENERAL CROSS-SECTIONAL SHAPED CYLINDER

ANTENNA	LIT REGION	TRANSITION REGION	DEEP SHADOW REGION
Slot Antenna (Hard Boundary)	$-2 e^{jkr_s \cos(\theta-\theta_0)}$	$\left\{ g^*(\epsilon_A) e^{-j \int_0^P k ds} \cdot f(A) \right. \\ \left. + g^*(\epsilon_B) e^{-j \int_0^P k ds} \cdot f(B) \right\}$	$-2 e^{-j \left[\frac{k_0 a}{2} \right]^{-1/3}} \int_{\theta=\theta_0}^{\theta_0} e^{j \frac{k_0}{2} \left(\frac{h}{2} \right)^{1/2}} \sum_{m=0}^{\infty} \left\{ \phi_m^h(P) \phi_m^h(A) \right. \\ A_1(-\bar{q}_m) e^{-j \int_0^P \gamma_m^h(s) ds} \cdot f(A) \\ \left. + \phi_m^h(P) \phi_m^h(B) A_1(-\bar{q}_m) e^{-j \int_0^P \gamma_m^h(s) ds} \cdot f(B) \right\}$
Slot Antenna (Soft Boundary)	$-\frac{2}{\epsilon_0} \cos(n-\theta_0) e^{jkr_s \cos(n-\theta_0)}$	$-\frac{1}{\epsilon_0} \left[\frac{k_0}{2} \right]^{1/3} \left\{ \tilde{g}^*(\epsilon_A) e^{-j \int_0^P k ds} \cdot f(A) \right. \\ \left. + \tilde{g}^*(\epsilon_B) e^{-j \int_0^P k ds} \cdot f(B) \right\}$	$-\frac{2}{\epsilon_0} \left[\frac{k_0}{2} \right]^{-2/3} \int_{\theta=\theta_0}^{\theta_0} e^{-j \frac{k_0}{2} \left(\frac{h}{2} \right)^{1/2}} \sum_{m=0}^{\infty} \left\{ \phi_m^s(P) \phi_m^s(A) \right. \\ A_1'(-\bar{q}_m) e^{-j \int_0^P \gamma_m^s(s) ds} \cdot f(A) \\ \left. + \phi_m^s(P) \phi_m^s(B) A_1'(-\bar{q}_m) e^{-j \int_0^P \gamma_m^s(s) ds} \cdot f(B) \right\}$
Infiniteesimal Monopole	$-2 \sin(n-\theta_0) e^{jkr_s \cos(n-\theta_0)}$	$\sin^{3/2} \theta_0 \left\{ g^*(\epsilon_A) e^{-j \int_0^P k ds} \cdot f(A) \right. \\ \left. + g^*(\epsilon_B) e^{-j \int_0^P k ds} \cdot f(B) \right\}$	$-2 e^{-j \left[\frac{k_0 a}{2} \right]^{-1/3}} \int_{\theta=\theta_0}^{\theta_0} e^{j \frac{k_0}{2} \left(\frac{h}{2} \right)^{1/2}} \sum_{m=0}^{\infty} \left\{ \phi_m^0(P) \phi_m^0(A) \right. \\ A_1(-\bar{q}_m) e^{-j \int_0^P \gamma_m^0(s) ds} \cdot f(A) \\ \left. + \phi_m^0(P) \phi_m^0(B) A_1(-\bar{q}_m) e^{-j \int_0^P \gamma_m^0(s) ds} \cdot f(B) \right\}$

CHAPTER III

NEAR FIELD SCATTERING BY FINITE STRUCTURES

A. Introduction

Two relatively new near field scattering problems are considered in this chapter using various high frequency approximations. In these problems the antenna is in the near field of a finite three-dimensional scattering body; whereas, the observation point is in the far field. However, it is assumed that any point on the scattering body is in the far field of the source. Thus, if a large antenna illuminates one of these scattering bodies, one must integrate over the equivalent aperture currents using the equivalence principle to obtain the currents and the radiation integrals to compute the far field pattern. However, as shown in Ref. [22], this integration can be accomplished numerically using a finite number of discrete infinitesimal sources. This point was discussed in Section II-B.

The scattering body is defined in terms of its location and dimensions in a general coordinate system, and the antenna is defined by its location and far field pattern. Note that some assumptions are made in terms of the geometry so that these results ultimately find application in terms of our approximate on-aircraft antenna problem.

These analyses are applications of the fundamental problems considered in the previous chapter. Similar types of studies have been made previously such as the near field scattering by various geometric bodies considered by Lentz[38]. Near field scattering effects must be included in an analysis of radomes such as the plane wave spectrum analysis done by Wu[39]. Thus, near field scattering problems are of recent interest and can have application beyond the on-aircraft antenna problem considered here.

B. Near Field Scattering by a Finite Plate

The near field scattering by a finite flat plate is a relatively new topic at higher frequencies where the plate is large in terms of the wavelength. The solution presented here is a practical application of the three-dimensional wedge diffraction theory given earlier. The flat plate geometry is illustrated in Fig. 10. The source is defined by its location and far-field pattern. The far-field pattern of the source is appropriate in that the plate is located at least $2D^2/\lambda$ away from the source where D is the maximum dimension of the

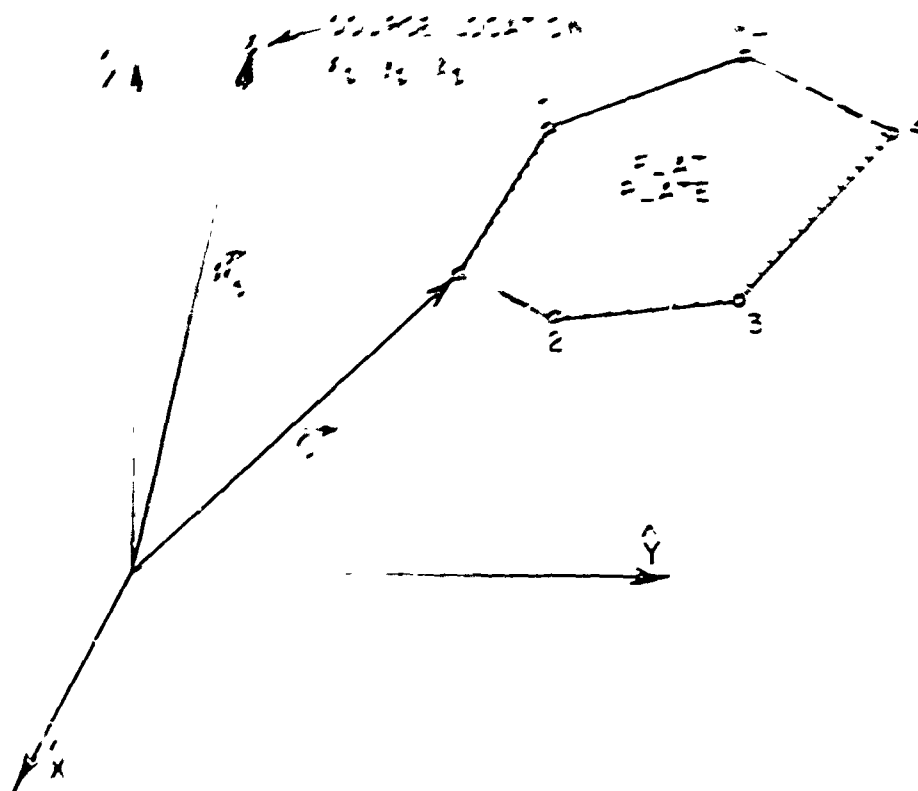


Fig. 10 Rear field flat plate geometry.

source. The flat plate is simply specified by the location of its n corners.

It is known that for a given scatter direction there is only one point along an infinitely long straight edge at which the diffracted field can emanate for a near zone source. Thus, this point must be found if it exists for each of the n edges that describe the flat plate.

Let us now consider a general m th edge using the geometry illustrated in Fig. 11. The expressions necessary to find the diffraction point are given below:

$$\begin{aligned}
 (1) \quad & \vec{r}_m = (x_m - x_0)\hat{x} + (y_m - y_0)\hat{y} + (z_m - z_0)\hat{z} = r \hat{e}_r \\
 & \vec{r}_{10} = x_1\hat{x} + y_1\hat{y} + z_1\hat{z} = r_{10}\hat{e}_{10} \\
 & \vec{r}_{20} = x_2\hat{x} + y_2\hat{y} + z_2\hat{z} = r_{20}\hat{e}_{20} \\
 & \vec{r}_{30} = x_3\hat{x} + y_3\hat{y} + z_3\hat{z} = r_{30}\hat{e}_{30}
 \end{aligned}$$

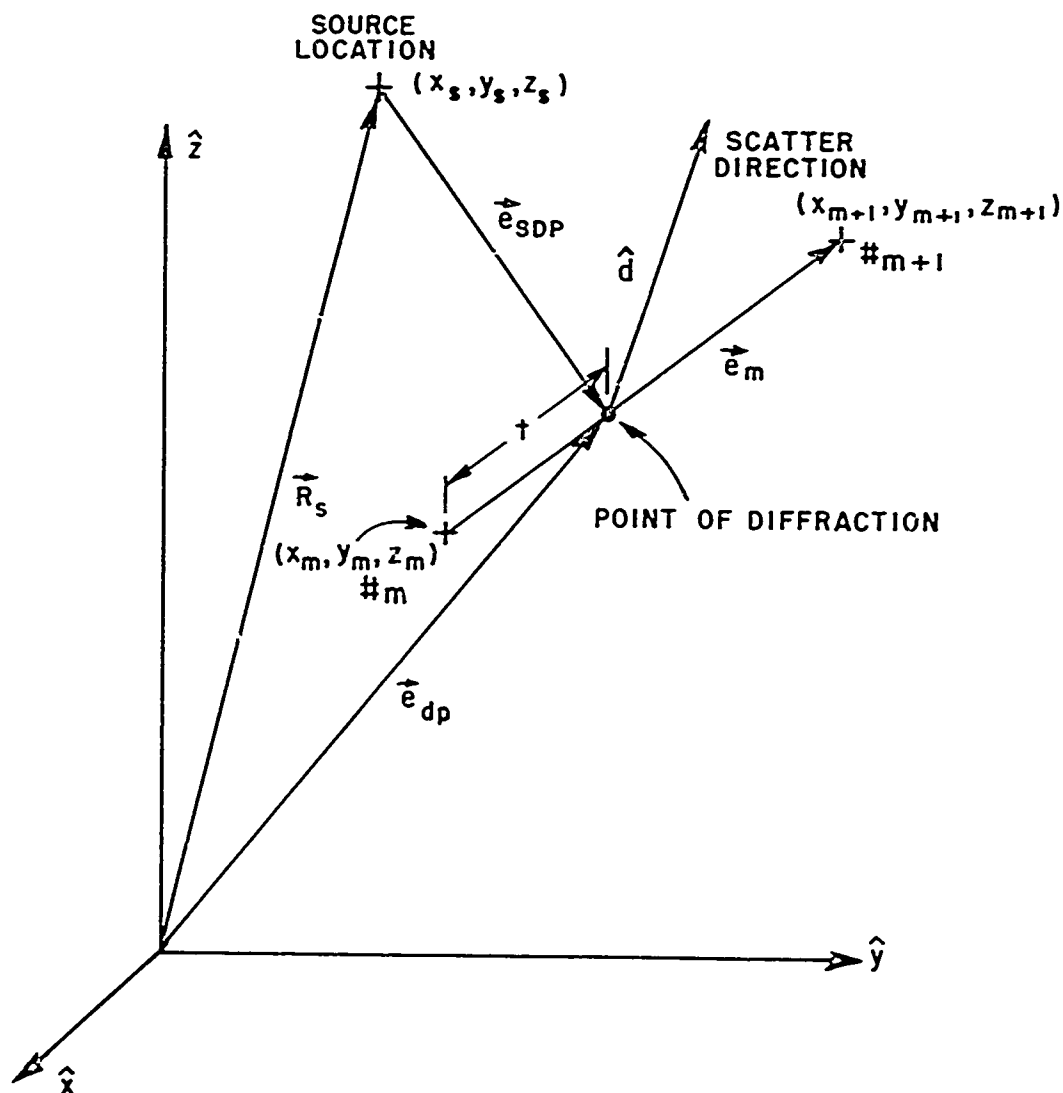


Fig. 11--Geometry for diffraction point along the mth edge.

It is known that the angle of incidence (β'_0) is equal to the angle of diffraction (β_0), which in turn is defined by the given scatter direction which is given by

$$\hat{d} = \sin \theta_s \cos \phi_s \hat{x} + \sin \theta_s \sin \phi_s \hat{y} + \cos \theta_s \hat{z} .$$

Since these angles are equal ($\beta'_0 = \beta_0$) the cosines of these angles must be equal which implies

$$(27) \quad \hat{e}_{sdp} \cdot \hat{e}_m = \hat{d} \cdot \hat{e}_m$$

where

$$\begin{aligned} \hat{e}_{sdp} \cdot \hat{e}_m &= \frac{x_{sdp}(x_{m+1}-x_m)}{AM} + \frac{y_{sdp}(y_{m+1}-y_m)}{AM} + \frac{z_{sdp}(z_{m+1}-z_m)}{AM} \\ \hat{d} \cdot \hat{e}_m &= \frac{\sin \theta_s \cos \phi_s (x_{m+1}-x_m)}{M} + \frac{\sin \theta_s \sin \phi_s (y_{m+1}-y_m)}{M} + \\ &\quad \frac{\cos \theta_s (z_{m+1}-z_m)}{M} \end{aligned}$$

Thus, one finds that

$$\begin{aligned} \left(x_m + \frac{t(x_{m+1}-x_m)}{M} - x_s \right) (x_{m+1}-x_m) + \left(y_m + \frac{t(y_{m+1}-y_m)}{M} - y_s \right) \cdot \\ (y_{m+1}-y_m) + \left(z_m + \frac{t(z_{m+1}-z_m)}{M} - z_s \right) (z_{m+1}-z_m) = A\gamma \end{aligned}$$

or

$$(28) \quad t = \frac{1}{M} [A\gamma - (x_m - x_s)(x_{m+1} - x_m) - (y_m - y_s)(y_{m+1} - y_m) - (z_m - z_s)(z_{m+1} - z_m)]$$

where

$$M = \sqrt{(x_{m+1}-x_m)^2 + (y_{m+1}-y_m)^2 + (z_{m+1}-z_m)^2}$$

$$\gamma = \sin \theta_s \cos \phi_s (x_{m+1}-x_m) + \sin \theta_s \sin \phi_s (y_{m+1}-y_m) + \cos \theta_s (z_{m+1}-z_m)$$

and

$$\begin{aligned} A = \sqrt{\left(x_m - x_s + \frac{t(x_{m+1}-x_m)}{M} \right)^2 + \left(y_m - y_s + \frac{t(y_{m+1}-y_m)}{M} \right)^2 + \\ + \left(z_m - z_s + \frac{t(z_{m+1}-z_m)}{M} \right)^2} \end{aligned}$$

An iteration technique can now be applied using the above equations by placing the present (or assumed) value of t in the above equation for A and then proceed to solve for a new value for t using Eq. (28). It can be shown analytically that this iteration approach will always converge to the desired value of t , which locates the point along the edge. However, iteration techniques often are not efficient in numerical computations as was found in this case. It was found that in certain regions too many iterations were required which resulted in a loss of numerical accuracy. Consequently, a search approach has been developed in which the values of $\hat{e}_{sd} \cdot \hat{e}_m$ are determined at the end points of an edge of the plate and at its midpoint. These values are then compared with $\hat{d} \cdot \hat{e}_m$ for which one can easily determine whether the diffraction point falls within the limits of the finite edge and if so which side of the midpoint. These tests are all based on the dot product comparisons. For example, if the value of $\hat{d} \cdot \hat{e}_m$ does not fall between the values of $\hat{e}_{sd} \cdot \hat{e}_m$ for the two end points, then a diffraction does not occur from the m th edge for that scatter direction. If the scatter direction dot product falls between an end point and the mid point, one then determines $\hat{e}_{sd} \cdot \hat{e}_m$ for the midpoint of the new region within which a diffraction occurs. From these values one finds a smaller region within which a diffraction must occur. This process continues until the diffraction point is found within certain minimum limits.

Once the diffraction point is located, one must find the diffracted field value from the m th edge. The far field pattern of the source can in general be written as

$$(29) \quad \vec{E}_s(\theta, \phi) = [\hat{\theta} F(\theta, \phi) + \hat{\phi} G(\theta, \phi)] \frac{e^{-jks'}}{s'} = \vec{R}(\theta, \phi) \frac{e^{-jks'}}{s'}$$

where s' is the range from the source to the field point. Using the geometry illustrated in Fig. 12a and applying the results presented in Section II-C one finds that

$$(30) \quad \begin{bmatrix} R_{||}^d \\ R_{\perp}^d \end{bmatrix} = \begin{bmatrix} -V_B^- & 0 \\ 0 & -V_B^+ \end{bmatrix} \begin{bmatrix} R_{||}^i \\ R_{\perp}^i \end{bmatrix} e^{-j[k(s' - \gamma) - k_{\rho}\rho]}$$

where

$$R_{||}^i = \vec{R}(\theta_i, \phi_i) \cdot \hat{\beta}'_0$$

$$R_{\perp}^i = \vec{R}(\theta_i, \phi_i) \cdot \hat{\phi}_0$$

$$k_{\rho}\rho = ks' \sin^2 \beta_0$$

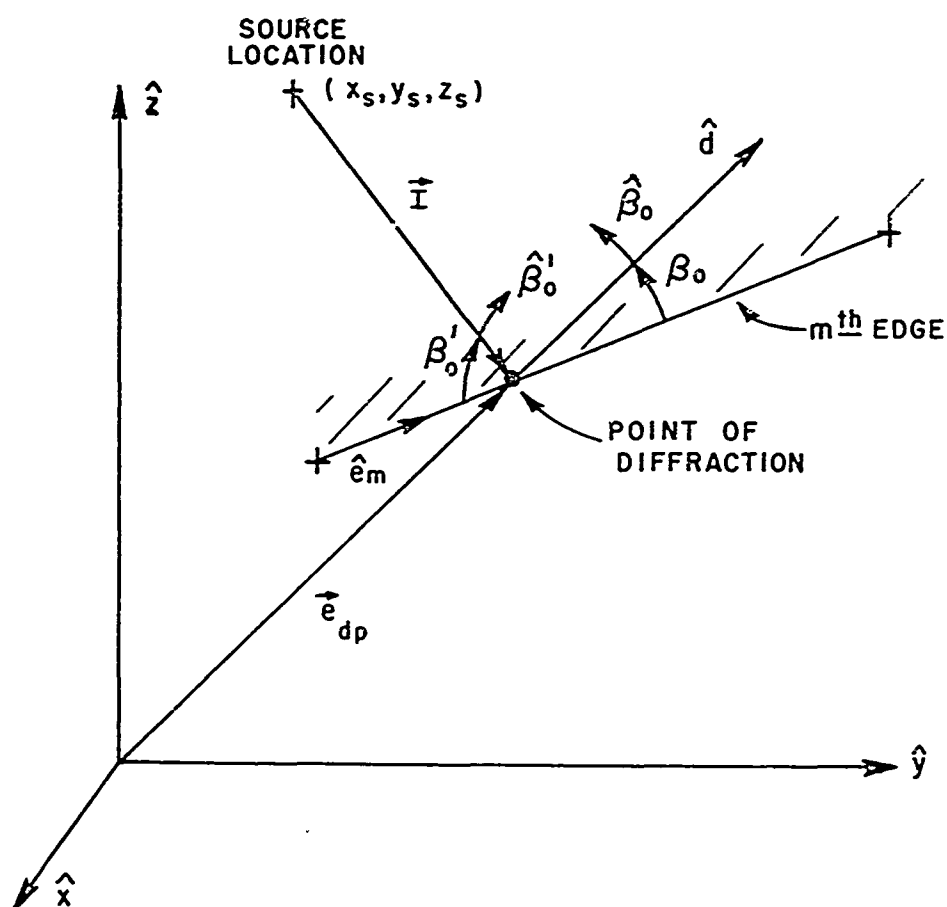


Fig. 12a--Edge diffraction geometry.

$$\gamma = x_{dp} \sin \theta_s \cos \phi_s + y_{dp} \sin \theta_s \sin \phi_s + z_{dp} \cos \theta_s$$

$$V_B^{\mp} = V_B(k_\rho, \psi - \psi_0, 2) \mp V_B(k_\rho, \psi + \psi_0, 2).$$

The incident field direction (θ_i, ϕ_i) from the source to the point of diffraction is defined by

$$\theta_i = \tan^{-1} \left(\sqrt{\frac{x_{sdp}^2 + y_{sdp}^2}{z_{sdp}^2}} \right), \text{ and}$$

$$\phi_i = \tan^{-1} \left(\frac{y_{sdp}}{x_{sdp}} \right).$$

Note that these angles as well as all others are defined in terms of an arctangent in that for numerical results the Fortran arctangent routines define the angle between -180° and 180° . It is easily shown that

$$\sin \beta_0 = |\hat{d} \times \hat{e}_m|$$

where

$$0^\circ \leq \beta_0 \leq 180^\circ.$$

In order to find the diffraction angles it is necessary to define a coordinate system at the diffraction point as illustrated in Fig. 12b.

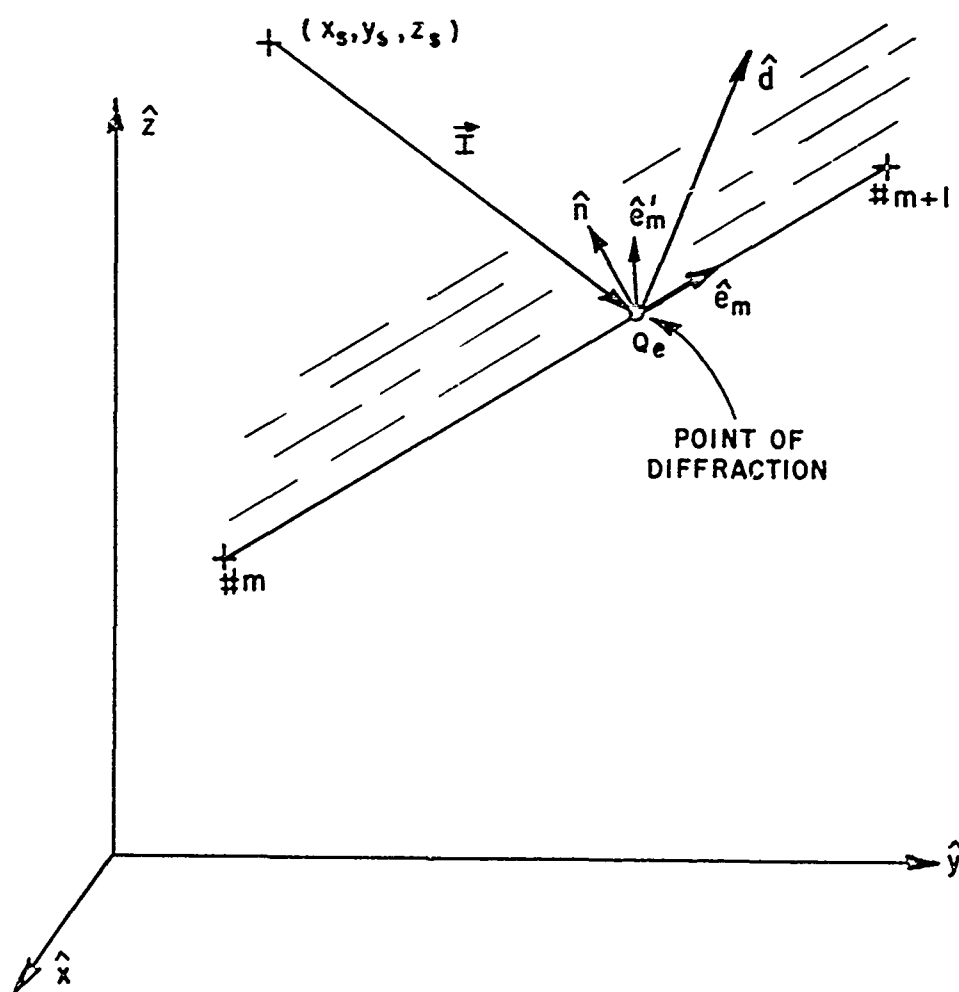


Fig. 12b--Edge coordinate system at point of diffraction.

The three orthogonal unit vectors are \hat{e}_m the unit vector along the edge, \hat{n} the normal to the surface, and $\hat{e}_m' = \hat{n} \times \hat{e}_m$. The incident vector direction can now be written in terms of this coordinate system as

$$-\hat{I} = \hat{e}_m' \sin \theta_0 \cos \phi_0 + \hat{n} \sin \theta_0 \sin \phi_0 + \hat{e}_m \cos \theta_0.$$

Using the above expression one finds that

$$\psi_0 = \phi_0 = \tan^{-1} \left(\frac{-\hat{I} \cdot \hat{n}}{-\hat{I} \cdot \hat{e}_m'} \right).$$

The scatter direction unit vector can, also, be decomposed in terms of this coordinate system by

$$\hat{d} = \hat{e}_m' \sin \theta \cos \phi + \hat{n} \sin \theta \sin \phi + \hat{e}_m \cos \theta$$

which results in giving

$$\psi = \phi = \tan^{-1} \left(\frac{\hat{d} \cdot \hat{n}}{\hat{d} \cdot \hat{e}_m'} \right).$$

The vector directions of the diffracted field are defined by the following expressions:

$$\hat{\phi}_0 = -\hat{e}_m' \sin \phi_0 + \hat{n} \cos \phi_0$$

$$\hat{\phi} = -\hat{e}_m' \sin \phi + \hat{n} \cos \phi$$

$$\hat{\beta}_0' = \hat{\phi}_0 \times \hat{I} \quad \text{and} \quad \hat{\beta}_0 = \hat{\phi} \times \hat{d}.$$

Once these terms are determined the total diffracted field from a general m th edge is given (Eq. (30)) by

$$(31) \quad \vec{R}_m^d(\theta_s, \phi_s) = R_{||}^d \hat{\beta}_0 + R_{\perp}^d \hat{\phi}.$$

Using the superposition principle the total singly diffracted field by the n edges of the flat plate is given using Eq.(31) by

$$(32) \quad \vec{R}^d(\theta_s, \phi_s) = \sum_{m=1}^n \vec{R}_m^d(\theta_s, \phi_s) .$$

The reflected field from the flat plate is considered next. The first step in this calculation is to find the location of the image source, which is uniquely determined once the plane of the flat plate is defined relative to the source location. In fact, the image is located along a line which is orthogonal to the plate and positioned an equal distance on the opposite side of the plate. This location can be found analytically using the geometry illustrated in Fig. 13a.

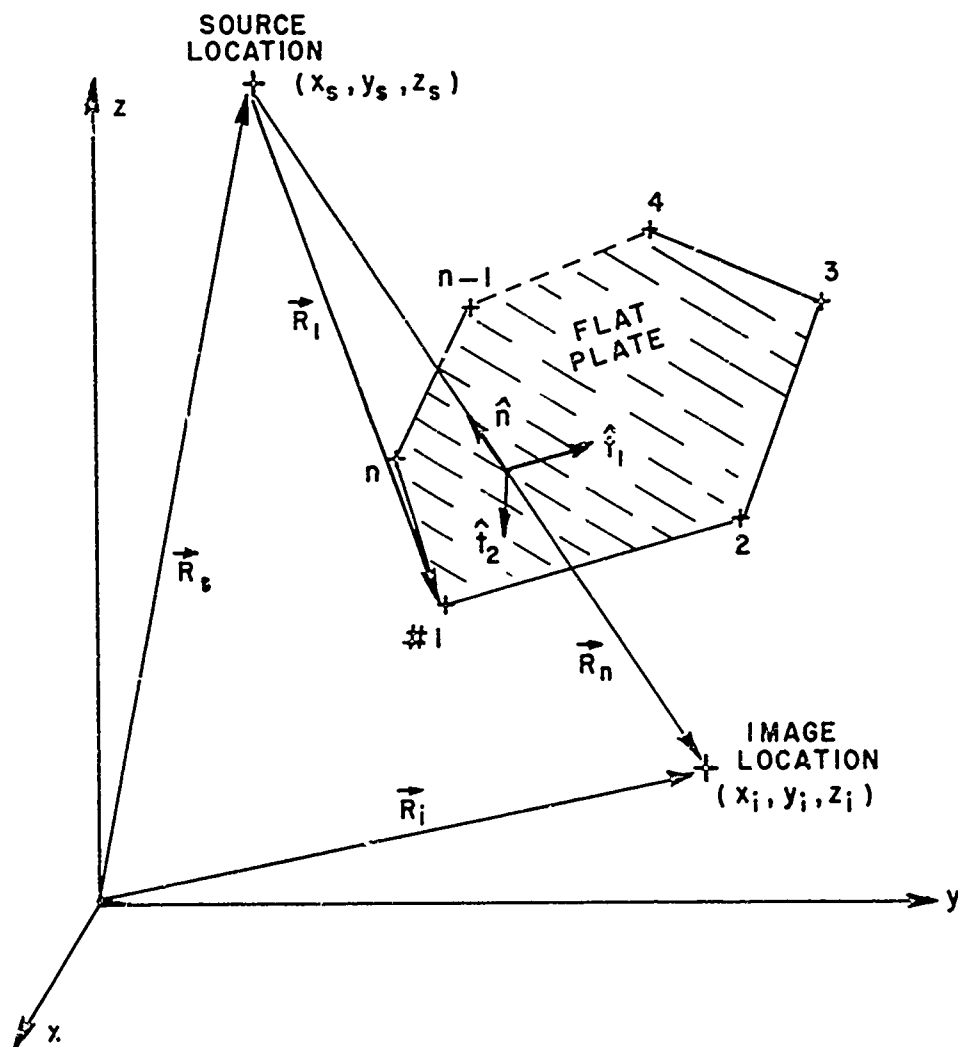


Fig. 13a. Geometry for location of image source.

The image position vector (\vec{R}_i) can be determined using the following expressions:

$$(33) \quad \vec{R}_i = -\alpha_n \hat{n} = 2[\alpha_1 \hat{t}_1 + \alpha_2 \hat{t}_2]$$

$$\vec{R}_1 = (x_1 - x_s)\hat{x} + (y_1 - y_s)\hat{y} + (z_1 - z_s)\hat{z}$$

$$\hat{n} = n_x \hat{x} + n_y \hat{y} + n_z \hat{z}$$

$$\hat{t}_1 = t_{1x} \hat{x} + t_{1y} \hat{y} + t_{1z} \hat{z}$$

$$\hat{t}_2 = t_{2x} \hat{x} + t_{2y} \hat{y} + t_{2z} \hat{z}$$

which result in the following matrix equation

$$\begin{pmatrix} -\frac{n_x}{2} & -t_{1x} & -t_{2x} \\ -\frac{n_y}{2} & -t_{1y} & -t_{2y} \\ -\frac{n_z}{2} & -t_{1z} & -t_{2z} \end{pmatrix} \begin{pmatrix} \alpha_n \\ \alpha_1 \\ \alpha_2 \end{pmatrix} = \begin{pmatrix} x_1 - x_s \\ y_1 - y_s \\ z_1 - z_s \end{pmatrix}.$$

Note that \hat{n} , \hat{t}_1 , and \hat{t}_2 are, respectively, the unit normal and tangent vectors associated with the plane of the flat plate. The above matrix can now be inverted giving the values of α_n , α_1 , and α_2 which in turn defines \vec{R}_i . Knowing the vector (\vec{R}_i), the image vector location is simply defined using Eq. (33) by

$$\vec{R}_i = \vec{R}_s + \vec{R}_n,$$

where

$$\vec{R}_s = x_s \hat{x} + y_s \hat{y} + z_s \hat{z}.$$

With the image position known, one needs to determine if the reflected field contributes to the total scattered field using the geometrical optics approach. If the reflected field is a contributor, the ray from the image source in the scatter direction must pass through the finite plate limits. Thus, one must find the location of the intersection point of this ray and the plane

containing the flat plate. This is accomplished using the geometry illustrated in Fig. 13b. The relationship necessary to find this point is

$$\gamma_1 \hat{t}_1 + \gamma_2 \hat{t}_2 - \gamma_d \hat{d} = \vec{R}_i - \vec{C}_1$$

which results in

$$\begin{pmatrix} t_{1x} & t_{2x} & -\sin \theta_s \cos \hat{\phi}_s \\ t_{1y} & t_{2y} & -\sin \theta_s \sin \hat{\phi}_s \\ t_{1z} & t_{2z} & -\cos \theta_s \end{pmatrix} \begin{pmatrix} \gamma_1 \\ \gamma_2 \\ \gamma_d \end{pmatrix} = \begin{pmatrix} x_i - x_1 \\ y_i - y_1 \\ z_i - z_1 \end{pmatrix}$$

Again the above matrix can be inverted to solve for the point of intersection.

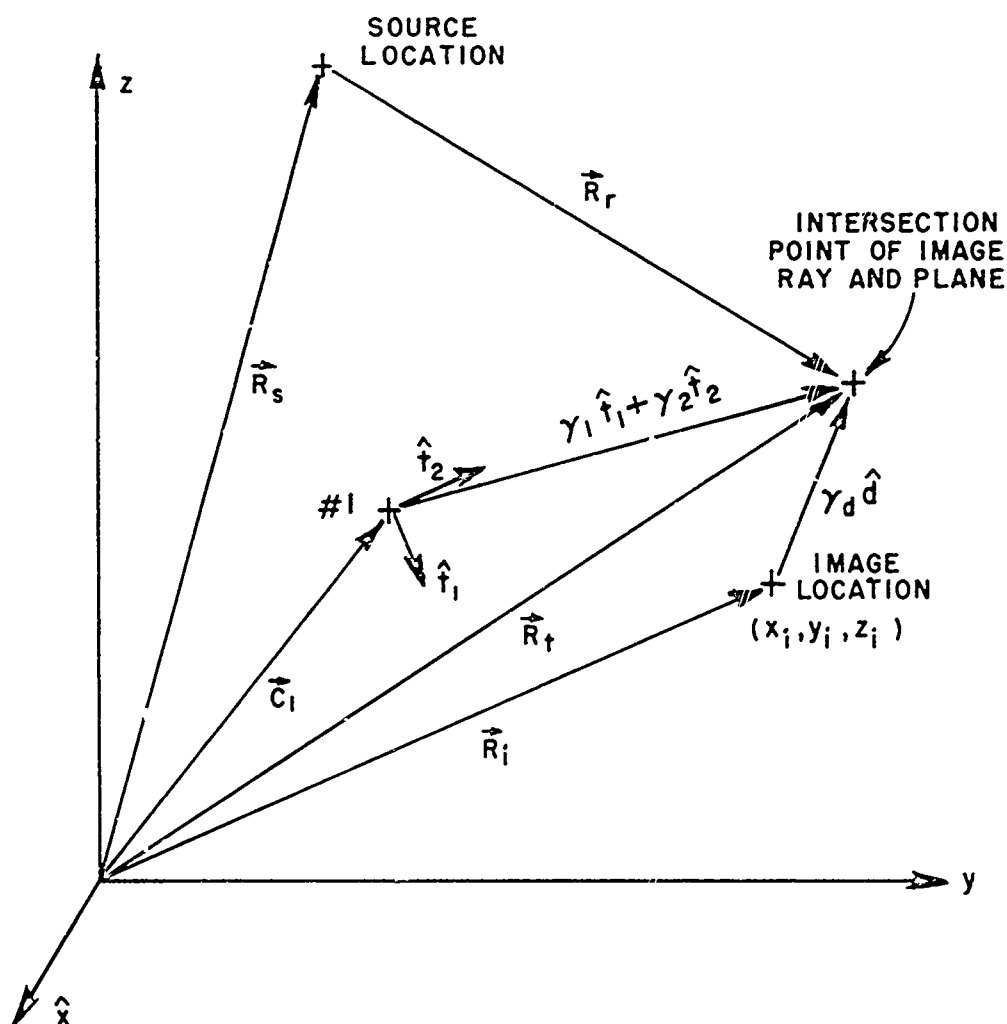


Fig. 13b--Intersection of image ray with flat plate.

One must now decide if this point falls within the finite limits of the flat plate, which can be accomplished many ways. The scheme used here is simply to determine if the angle (θ_{mi}) between one of the edges of a general corner and a line going from the general corner to the intersection point is greater than the angle (θ_m) between the edges making up the corner. If θ_{mi} is greater than θ_m for any of the corners, then reflections do not occur. Examples of this technique are shown in Fig. 14. Note that reflections occur for the geometry of Fig. 14a since $\theta_{mi} < \theta_m$ for all m ; whereas, reflections do not occur in Fig. 14b since $\theta_{mi} > \theta_m$ at the m th corner.

Once it is determined that reflections do occur, it is necessary to find the value of the reflected field. It is known that the reflected field from the image source can be written as

$$(34) \quad \vec{E}^r(\theta_s, \phi_s) = [\hat{\theta}^r F^r(\theta_s, \phi_s) + \hat{\phi}^r G^r(\theta_s, \phi_s)] \frac{e^{-jkr_i}}{r_i}$$

using the geometry illustrated in Fig. 15. The ray form of the reflected field is given simply by

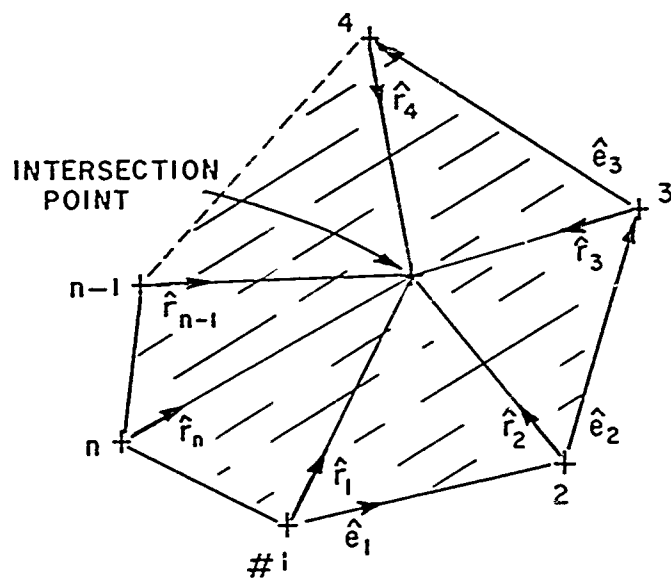
$$(35) \quad \vec{R}^r(\theta_s, \phi_s) = [\hat{\theta}^r F^r(\theta_s, \phi_s) + \hat{\phi}^r G^r(\theta_s, \phi_s)] \cdot e^{jk[x_i \sin \theta_s \cos \phi_s + y_i \sin \theta_s \sin \phi_s + z_i \cos \theta_s]}$$

with $\hat{\theta}^r$ and $\hat{\phi}^r$ being related to the image source coordinate system. The above quantities can be found from the boundary conditions that must be satisfied on the flat plate and which are given by

$$(36) \quad \begin{aligned} \hat{n} \cdot \vec{E}^r \text{ (on plate)} &= \hat{n} \cdot \vec{E}^s \text{ (on plate)} \\ \hat{t}_1 \cdot \vec{E}^r \text{ (on plate)} &= -\hat{t}_1 \cdot \vec{E}^s \text{ (on plate)} \\ \hat{t}_2 \cdot \vec{E}^r \text{ (on plate)} &= -\hat{t}_2 \cdot \vec{E}^s \text{ (on plate)}. \end{aligned}$$

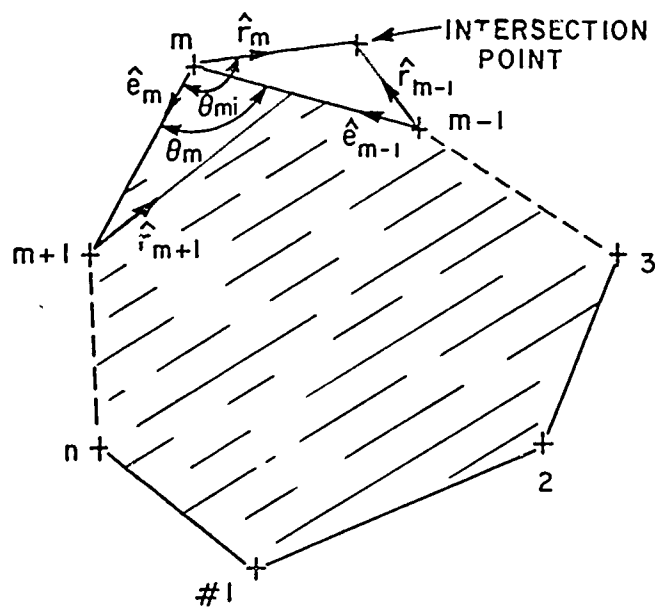
Note that \vec{E}^r and \vec{E}^s are, respectively, the image and source field values at the point of intersection on the flat plate. The geometry used to define these various terms is shown in Fig. 13b with

$$\vec{R}_r = \vec{R}_t - \vec{R}_s = (x_t - x_s)\hat{x} + (y_t - y_s)\hat{y} + (z_t - z_s)\hat{z}$$



(a)

Fig. 14a--Reflections occur.



(b)

Fig. 14b--Reflections do not occur.

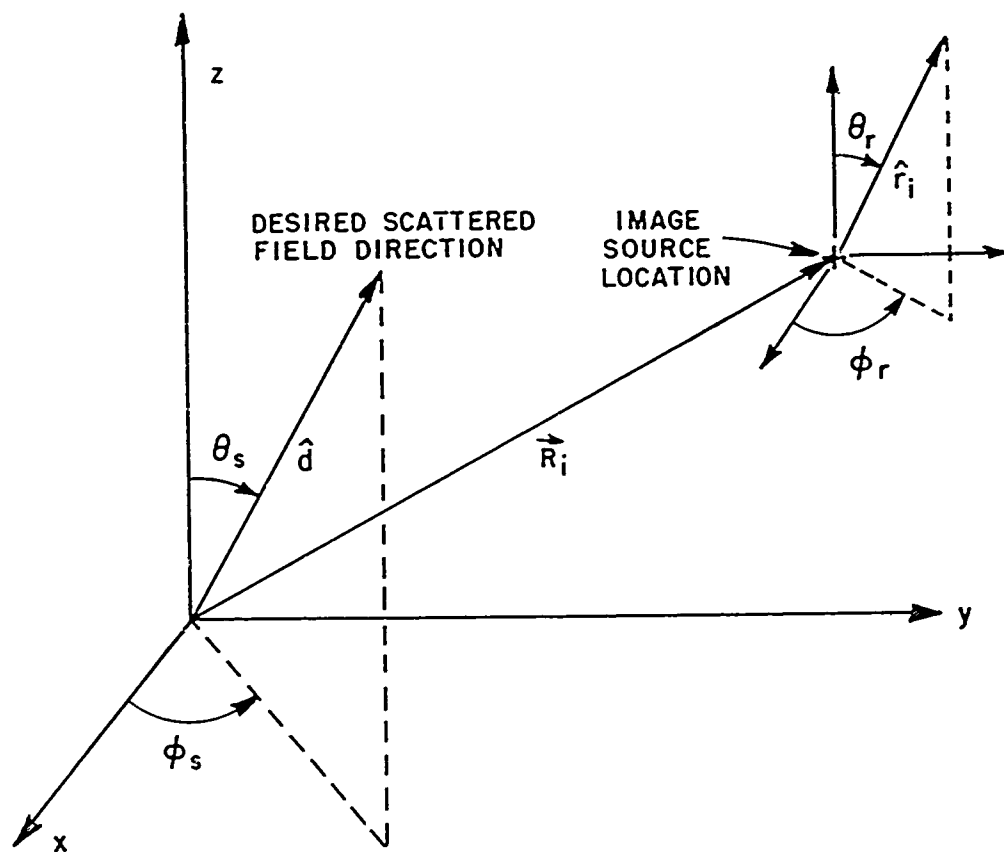


Fig. 15--Reflected field geometry.

and

$$\hat{R}_r = \sin \theta_i \cos \phi_i \hat{x} + \sin \theta_i \sin \phi_i \hat{y} + \cos \theta_i \hat{z}$$

which results in the incident field direction defined by

$$\theta_i = \tan^{-1} \left(\frac{\sqrt{(x_t - x_s)^2 + (y_t - y_s)^2}}{(z_t - z_s)} \right)$$

$$\phi_i = \tan^{-1} \left(\frac{y_t - y_s}{x_t - x_s} \right) .$$

Thus, at the point of intersection one finds that

$$(37) \quad \begin{aligned} \vec{E}^S \text{ (on plate)} &= [\hat{\theta}^S F(\theta_i, \phi_i) + \hat{\phi}^S G(\theta_i, \phi_i)] \frac{e^{-jkr_s}}{r_s} \\ \vec{E}^r \text{ (on plate)} &= [\hat{\theta}^r F^r(\theta_r, \phi_r) + \hat{\phi}^r G^r(\theta_r, \phi_r)] \frac{e^{-jkr_i}}{r_i} \end{aligned}$$

with

$r_s = r_i$. Substituting the above expressions into Eq. (36) one finds that

$$\begin{aligned} \hat{n} \cdot \vec{E}^S &= [F \hat{\theta}^S \cdot \hat{x} + G \hat{\phi}^S \cdot \hat{x}] n_x + [F \hat{\theta}^S \cdot \hat{y} + G \hat{\phi}^S \cdot \hat{y}] n_y + [F \hat{\theta}^S \cdot \hat{z} + \\ &\quad G \hat{\phi}^S \cdot \hat{z}] n_z \\ \hat{n} \cdot \vec{E}^r &= [F^r \hat{\theta}^r \cdot \hat{x} + G^r \hat{\phi}^r \cdot \hat{x}] n_x + [F^r \hat{\theta}^r \cdot \hat{y} + G^r \hat{\phi}^r \cdot \hat{y}] n_y \\ &\quad + [F^r \hat{\theta}^r \cdot \hat{z} + G^r \hat{\phi}^r \cdot \hat{z}] n_z \end{aligned}$$

with

$$\begin{aligned} \hat{\theta}^S &= \hat{x} \cos \theta_i \cos \phi_i + \hat{y} \cos \theta_i \sin \phi_i - \hat{z} \sin \theta_i \\ \hat{\phi}^S &= -\hat{x} \sin \phi_i + \hat{y} \cos \phi_i \\ \hat{\theta}^r &= \hat{x} \cos \theta_s \cos \phi_s + \hat{y} \cos \theta_s \sin \phi_s - \hat{z} \sin \theta_s \\ \hat{\phi}^r &= -\hat{x} \sin \phi_s + \hat{y} \cos \phi_s \end{aligned}$$

One can also write similar equations for $(\alpha_1 \hat{t}_1 + \alpha_2 \hat{t}_2) \cdot \vec{E}^S$ and $(\alpha_1 \hat{t}_1 + \alpha_2 \hat{t}_2) \cdot \vec{E}^r$. The resulting equations can be summarized by

$$\begin{aligned} \hat{n} \cdot \vec{E}^r &= F^r C_{11} + G^r C_{12} \\ \hat{n} \cdot \vec{E}^S &= F C_{13} + G C_{14} \\ (\alpha_1 \hat{t}_1 + \alpha_2 \hat{t}_2) \cdot \vec{E}^r &= F^r C_{21} + G^r C_{22} \\ (\alpha_1 \hat{t}_1 + \alpha_2 \hat{t}_2) \cdot \vec{E}^S &= F C_{23} + G C_{24} \end{aligned}$$

which can be written in matrix form using Eqs. (36) and (37) as

$$\begin{pmatrix} C_{11} & C_{12} \\ C_{21} & C_{22} \end{pmatrix} \begin{pmatrix} F^r \\ G^r \end{pmatrix} = \begin{pmatrix} F C_{13} + G C_{14} \\ -F C_{23} - G C_{24} \end{pmatrix}.$$

The above matrix can be easily inverted to give

$$F^r(\phi_s, \psi_s) = \frac{[-F C_{13} + G C_{14}]C_{22} + [F C_{23} + G C_{24}]C_{12}}{C_{11} C_{22} - C_{12} C_{21}}$$

and

$$G^r(\phi_s, \psi_s) = - \frac{[F C_{23} + G C_{24}]C_{11} + [-F C_{13} + G C_{14}]C_{21}}{C_{11} C_{22} - C_{12} C_{21}}.$$

These solutions can then be substituted into Eq. (35) to give the reflected field component of the scattered field. The total scattered field from the flat plate is then given, using Eqs. (32) and (35), by

$$(38) \quad \vec{R}^s(\phi_s, \psi_s) = \vec{R}^d(\phi_s, \psi_s) + \vec{R}^r(\phi_s, \psi_s).$$

This solution has been compared with measured results using a short dipole antenna mounted above a flat square plate as shown in Fig. 16. In Fig. 17 a dipole is mounted above the center of a square plate with resultant patterns shown for $0^\circ \leq \psi_s \leq 360^\circ$ and $\theta_s = 90^\circ$. In Fig. 18 the dipole is mounted near one edge of the plate. In Fig. 19 the geometry is the same as the last case except the dipole is now rotated by 90° . Note that good agreement is obtained in each case between the calculated and measured results even through the back lobe region.

In order to illustrate the versatility of this solution, it is used to approximate the scattering effect of a disc. This is done by computing the pattern of a monopole mounted on plates with increasingly many sides. In Fig. 20 the calculated results for plates with 4, 6, 8 and 10 sides are illustrated and compared with the measured result taken on the disk[40]. Note that as the number of sides is increased the closer the computed and measured results agree.

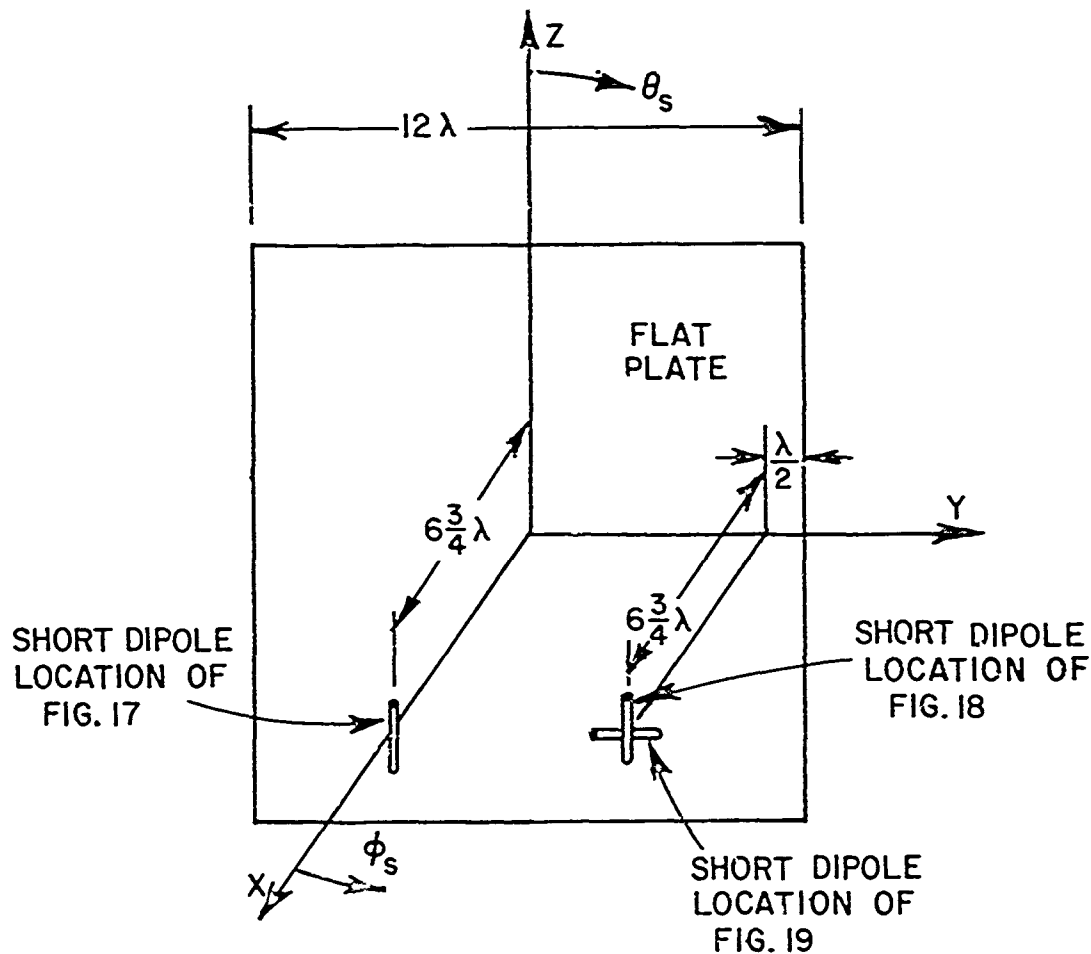


Fig. 16--Geometry for flat plate measurements.

Even though the above results show good agreement one must realize the inherent approximations in this solution. It is based on edge diffraction with just singly diffracted edge rays being considered. Thus, it has been assumed that the plate is large in terms of the wavelength such that double diffraction is normally negligible. However, neglecting double diffraction may cause some error especially when the pattern is computed in the plane of the flat plate. Secondly, a diffraction term from each of the corners should be included but is not available in practical form at present. Nevertheless, it has little effect on the overall pattern except when the diffraction point approaches a corner. In these two cases our solution can be somewhat in error although only a small angular region is involved.

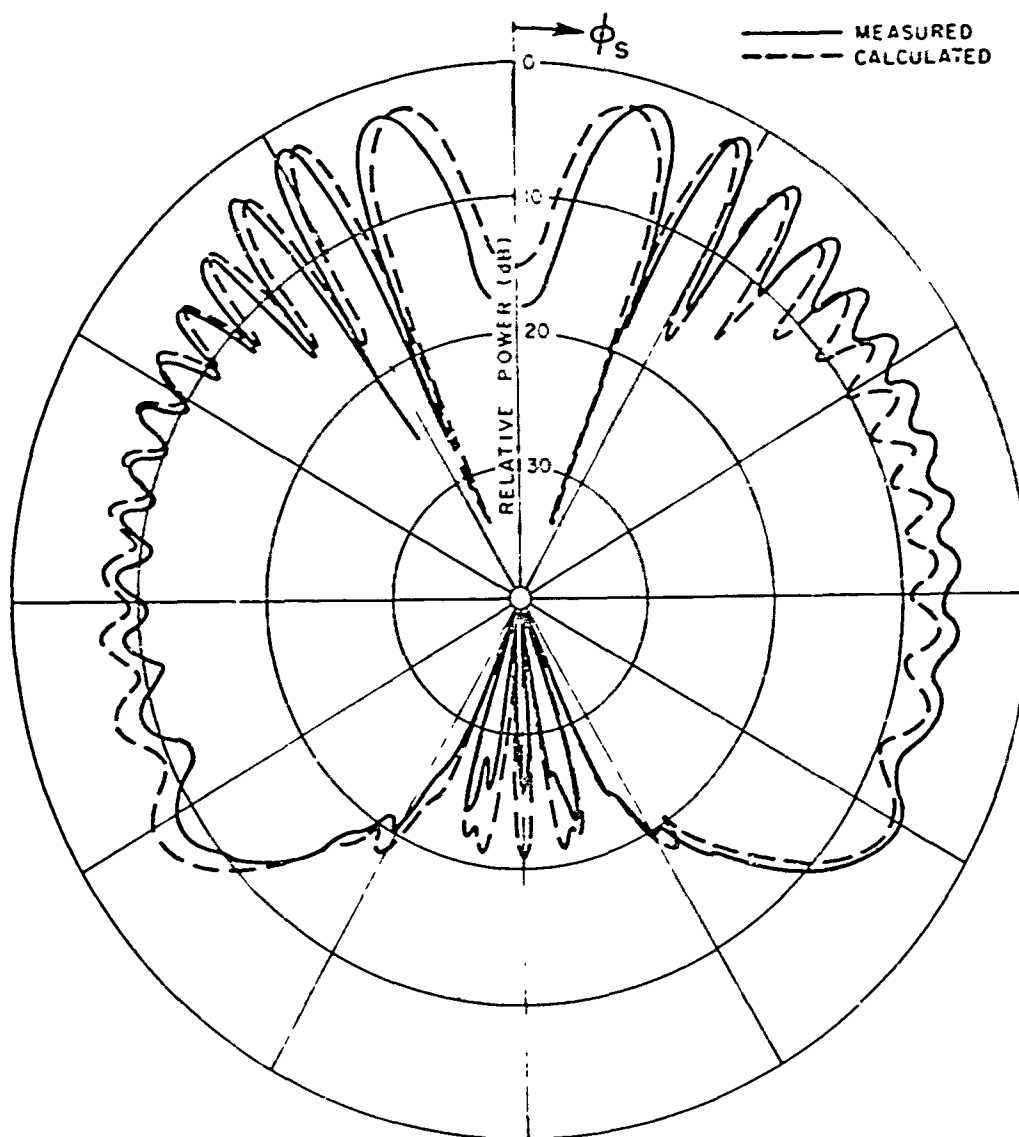


Fig. 17-- E_θ radiation pattern for a small dipole mounted above a rectangular plate for $\theta_s = 90^\circ$ and $0^\circ < \phi_s \leq 360^\circ$.

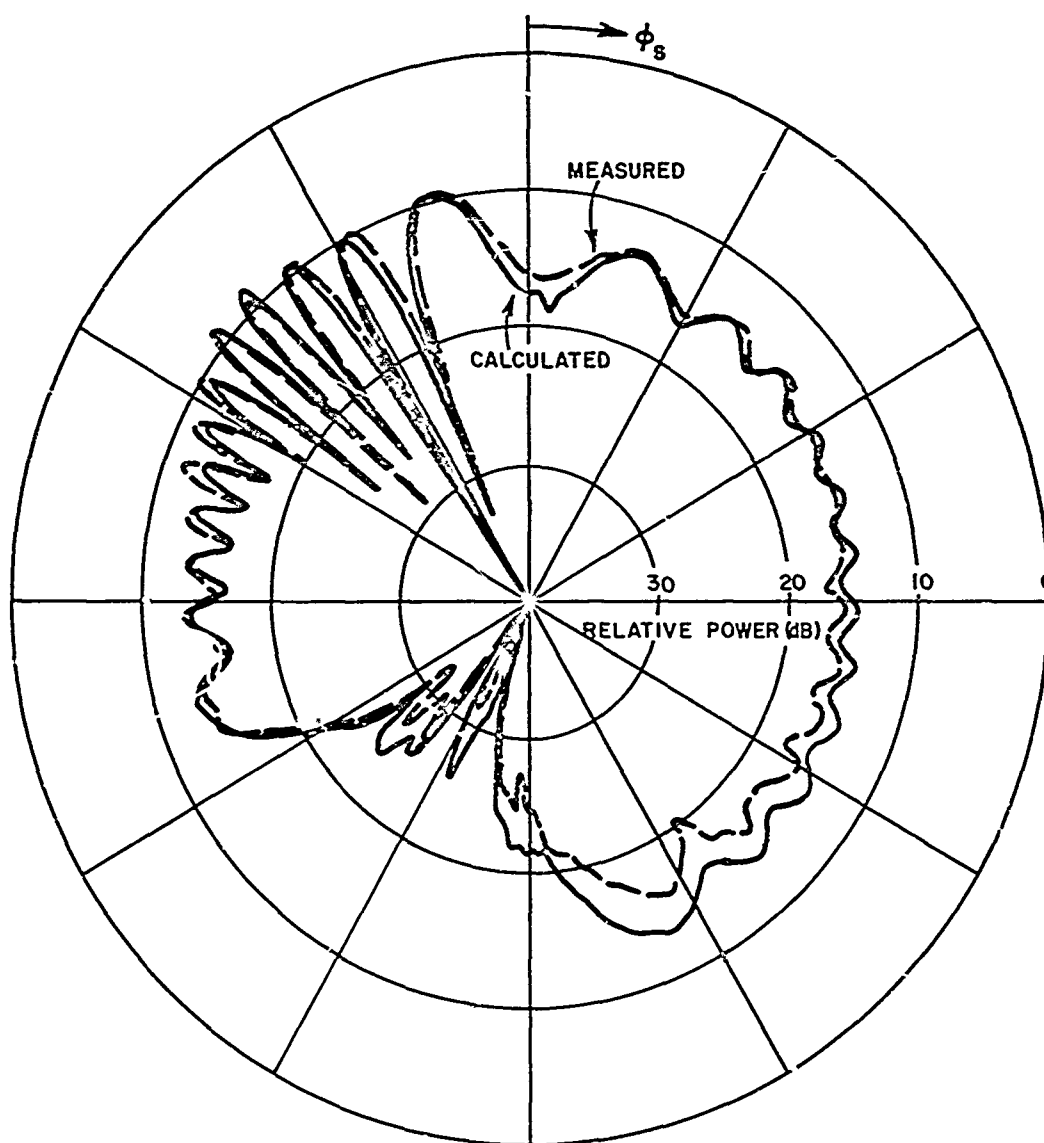


Fig. 18-- E_θ radiation pattern for a short dipole mounted above a rectangular plate for $\theta_s = 90^\circ$ and $0^\circ \leq \phi_s \leq 360^\circ$.

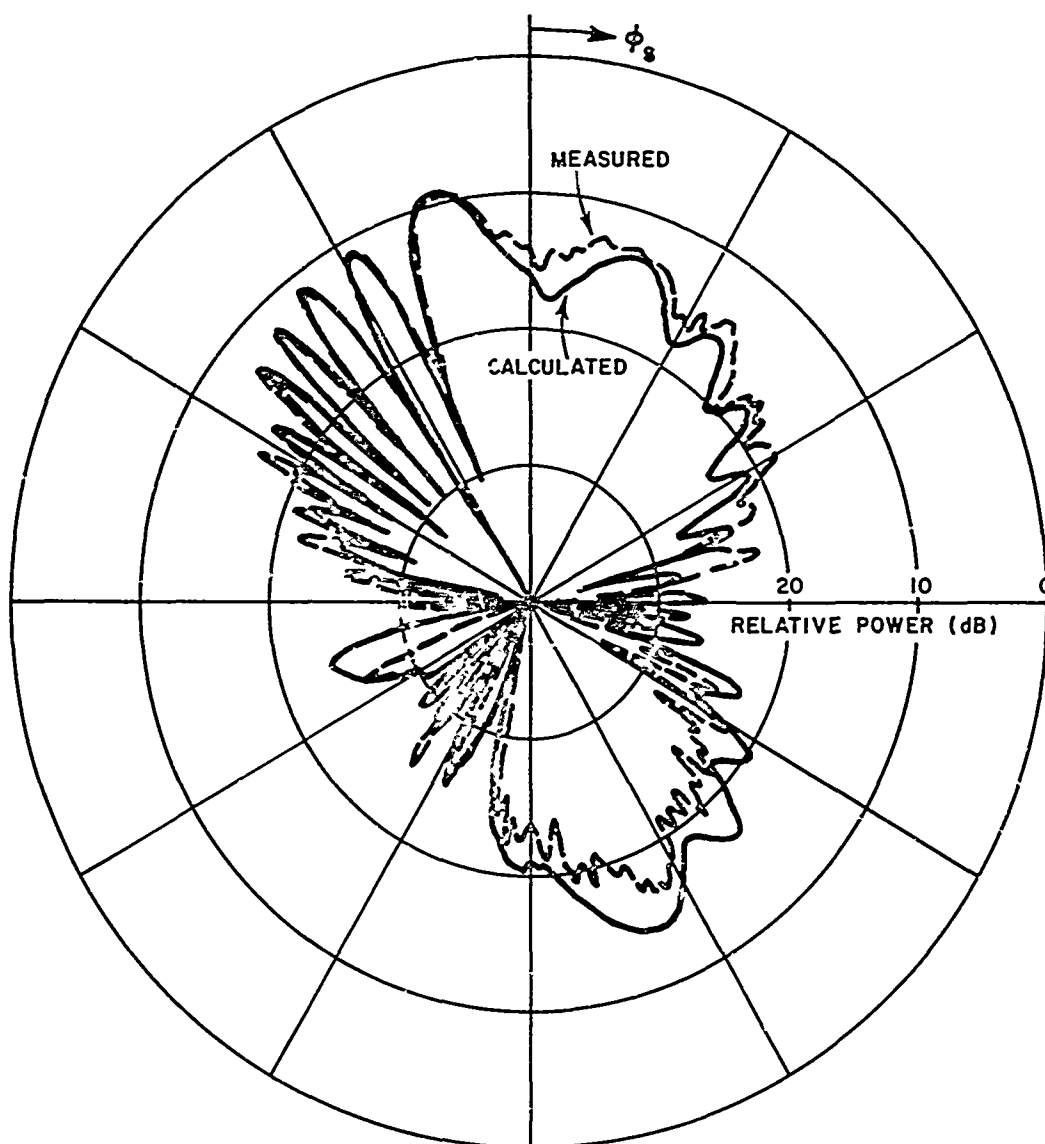


Fig. 19-- E_ϕ radiation pattern for a short dipole mounted above a rectangular plate for $\theta_s = 90^\circ$ and $0^\circ \leq \phi_s \leq 360^\circ$.

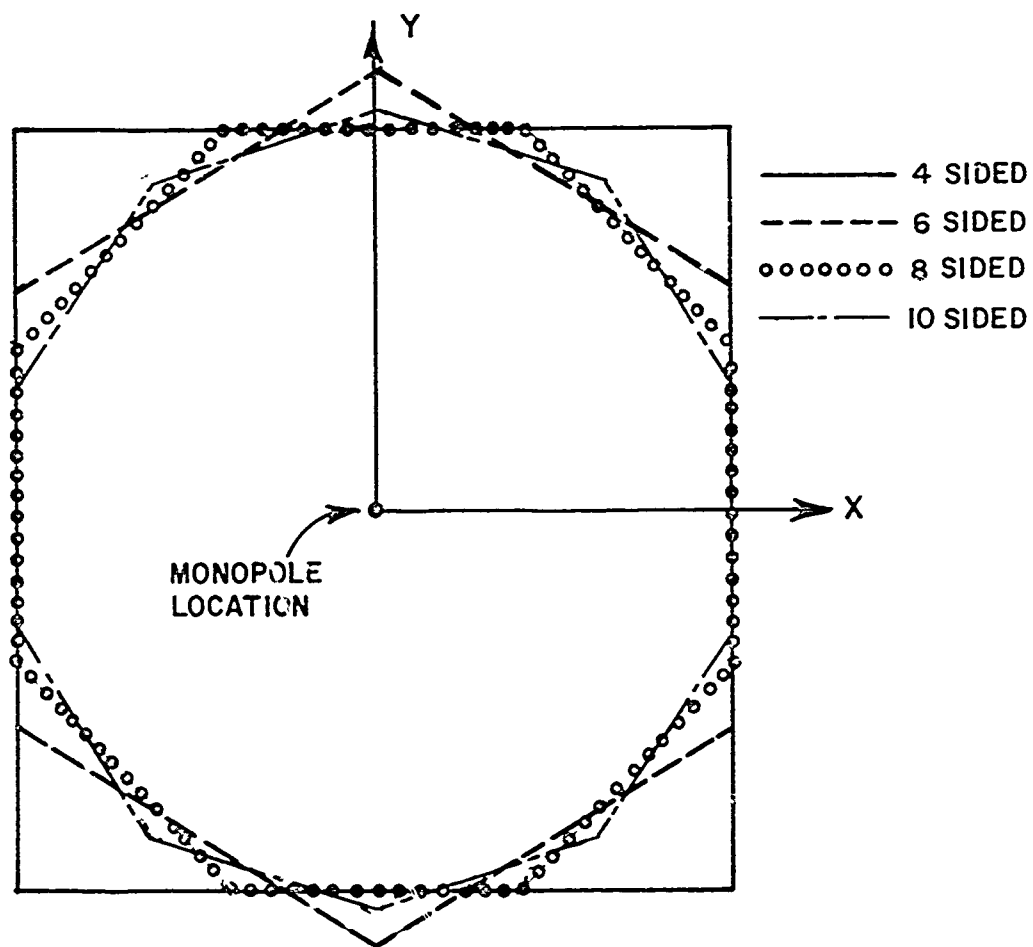


Fig. 20a--Geometry of flat plate treated.

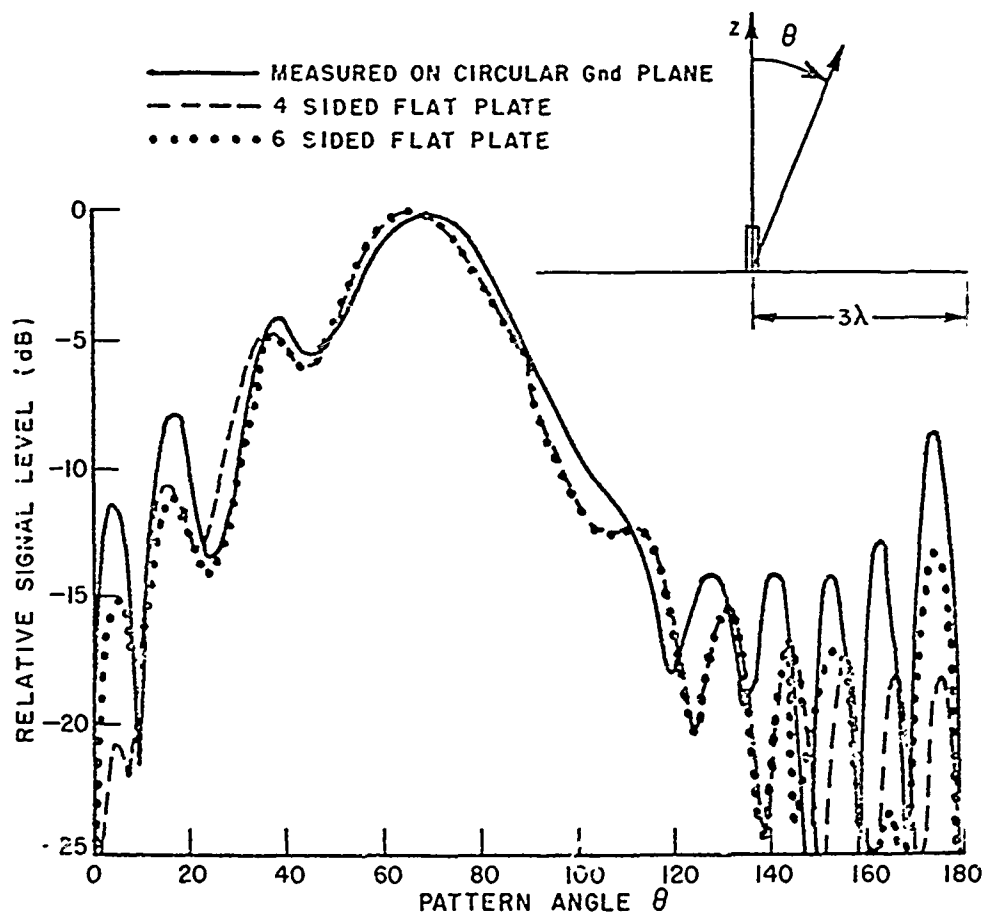


Fig. 20b--Radiation pattern of a stub on a ground plane.

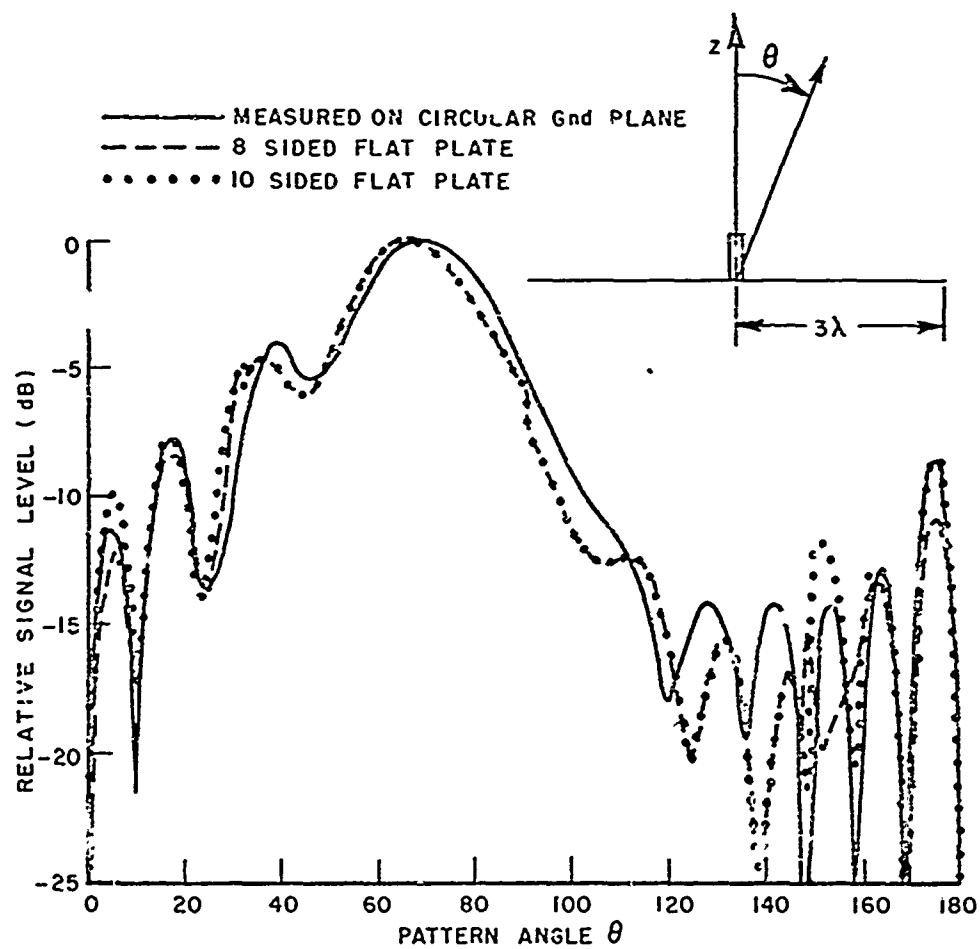


Fig. 20c--Radiation pattern of a stub on a ground plane.

This solution, of course, yields the radiation pattern for antennas mounted above flat plate reflectors. As stated earlier a large antenna or array can be handled simply by using the superposition principle and summing the scattered fields from delta function or array elements. As is shown in the next chapter, this solution can be modified somewhat and applied to the aircraft antenna problem in order to handle the scattering by wings and/or horizontal stabilizers which are approximated by "n" sided flat plates. Another possible application of this study is in solving the near field scattering of buildings. This is a problem of recent interest in terms of the overall airport/aircraft antenna system performance in that the scattering from buildings may adversely affect the desired antenna performance.

C. Near Field Scattering by a Finite Cylinder

Even though many authors [41,42] have previously studied the far field scattering properties of finite cylinders, the near field scattering of large finite cylinders has received little attention. It is this near field problem that is examined here basically to study the engine effect in the on-aircraft problem. The geometry of this near field scattering problem is illustrated in Fig. 21. The solution developed is basically an application of ray optics techniques.

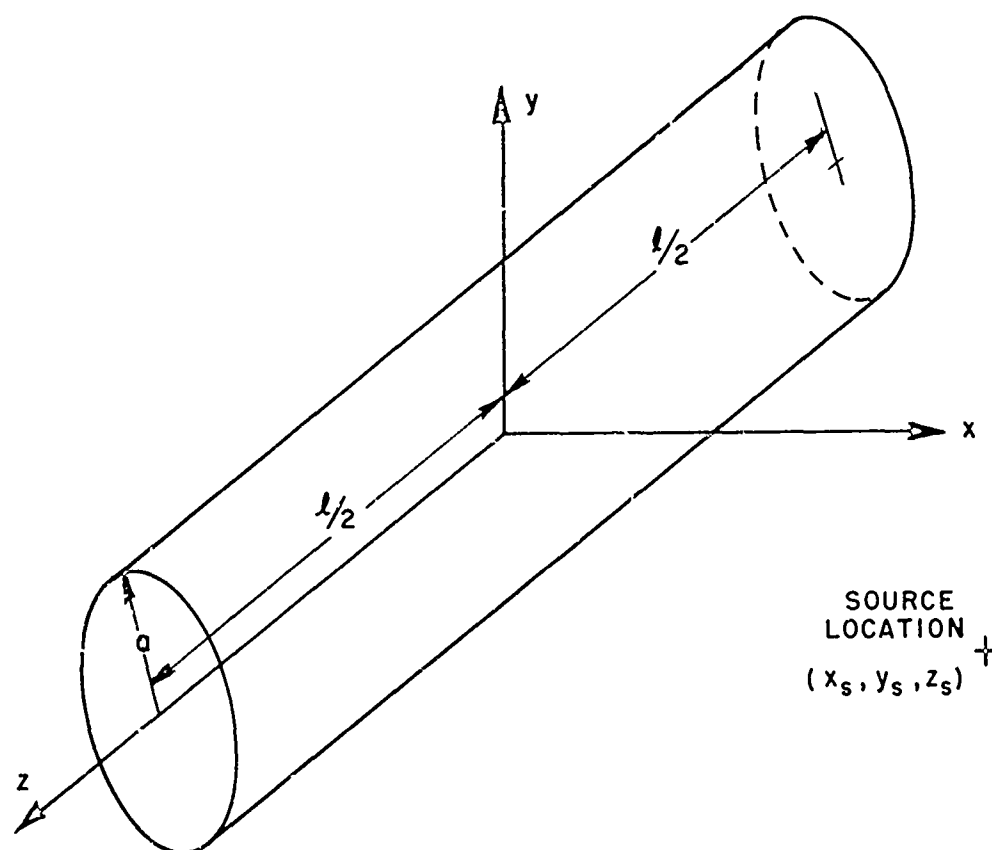


Fig. 21. Near field finite cylinder geometry.

The modal solution for the circular cylinder is used to determine the scattering properties of the cylinder portion, wedge diffraction is applied to the edges at the end caps and physical optics is used to determine the specular scatter from the end caps. In the process of developing the near field scattering properties, the far field problem is presented using similar solutions. Again this far field solution is obtained by applying several solutions which are known to be adequate in certain regions. Thus, this approach is not an attempt to extend a solution beyond its capability but only uses previously developed solutions which are known to be valid in certain sectors. The most interesting point is that there is an adequate overlap between the various regions in which each solution provides a good approximation thus giving complete coverage.

Let us first consider the physical optics solution applied to determine the specular scatter from the disc-shaped end caps. The geometry used for this analysis is illustrated in Fig. 22. In this solution as well as the ones to follow, the parallel and perpendicular components of the incident E-field are considered separately. Considering the perpendicular component of the incident field, one finds that

$$\vec{E}_\perp^i = \hat{y} e^{jk(z \cos \theta_i + x \sin \theta_i)}$$

and

$$\vec{H}_\perp^i = (\hat{x} \cos \theta_i - \hat{z} \sin \theta_i) \frac{1}{Z_0} e^{jk(z \cos \theta_i + x \sin \theta_i)}$$

The physical optics current is, then, given by [43]

$$\vec{J}_\perp = 2\hat{z} \times \vec{H}_\perp^i|_{z=0} = 2\hat{y} \cos \theta_i \frac{e^{jk x \sin \theta_i}}{Z_0}$$

This current is substituted into the radiation integrals to find the scattered far field as given by

$$E_{\perp\theta}^S = -Z_0 \cos \theta \sin \phi \int_0^a \int_0^{2\pi} J_{\perp y} e^{jk[\rho' \cos(\phi-\phi') \sin \theta]} \rho' d\phi' d\rho'$$

and

$$E_{\perp\phi}^S = -Z_0 \cos \phi \int_0^a \int_0^{2\pi} J_{\perp y} e^{jk[\rho' \cos(\phi-\phi') \sin \theta]} \rho' d\phi' d\rho'$$

with the factor $\left[\frac{jk}{4\pi r} e^{-jkr} \right]$ removed. This results in

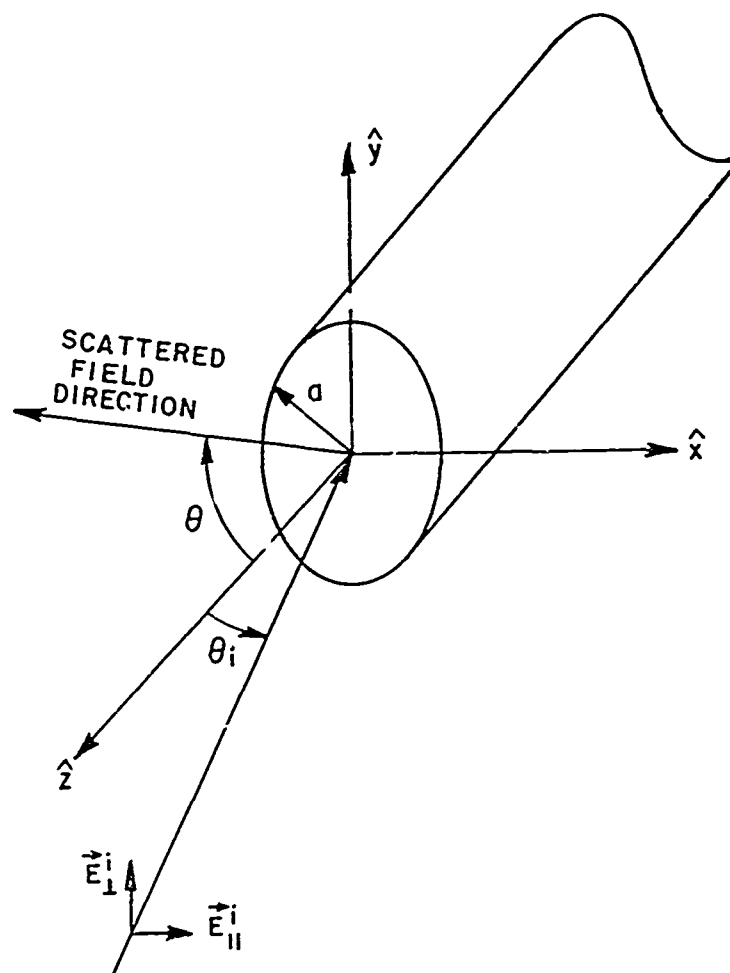


Fig. 22--Plane wave field incident on finite cylinder end cap.

$$(39) \quad E_{\perp i}^s = -2 \cos \epsilon \sin \phi \cos \theta_i \int_0^a \int_0^{2\pi} \rho' \cdot e^{jk\rho' [\sin \theta_i \cos \phi' + \sin \theta (\cos \phi \cos \phi' + \sin \phi \sin \phi')]} d\phi' d\rho'$$

and

$$(40) \quad E_{\perp \phi}^S = -2 \cos \phi \cos \theta_i \int_0^a \int_0^{2\pi} \rho' \cdot e^{jk\rho' [\sin \theta_i \cos \phi' + \sin \theta (\cos \phi \cos \phi' + \sin \phi \sin \phi')]} d\phi' d\rho'.$$

In order to simplify this solution let

$$\begin{aligned} \sin \theta_i \cos \phi' + \sin \theta_i (\cos \theta_i \cos \phi' + \sin \theta_i \sin \phi') \\ = \sin \theta_i (\cos \theta_i \cos \phi' + \sin \theta_i \sin \phi') = \sin \theta_i \cos(\theta_i - \phi') \end{aligned}$$

where

$$(41) \quad \gamma = \sqrt{\sin^2 \theta_i + 2 \sin \theta_i \sin \theta \cos \phi' + \sin^2 \theta}.$$

Substituting the above expression into Eq. (39) one finds that

$$E_{1\theta}^S = -2 \cos \theta \sin \phi \cos \theta_i \int_0^a \int_0^{2\pi} e^{jk\rho' \gamma \cos(\theta - \phi')} d\phi' d\rho'$$

$$E_{1\phi}^S = -4\pi \cos \theta \sin \phi \cos \theta_i \int_0^a \rho' J_0(k\rho' \gamma) d\rho'$$

or

$$(42) \quad E_{1\theta}^S = - \frac{4\pi a \cos \theta \cos \theta_i \sin \phi}{k_Y} J_1(ka_Y)$$

and similarly

$$(43) \quad E_{1\phi}^S = - \frac{4\pi a \cos \theta_i \cos \phi}{k_Y} J_1(ka_Y).$$

Let us now consider the parallel component of the incident field, which is given by

$$\vec{E}_u^i = \hat{e} e^{jk(z \cos \theta_i + x \sin \theta_i)},$$

and

$$\vec{H}_u^i = -\hat{y} \frac{e^{jk(z \cos \theta_i + x \sin \theta_i)}}{Z_0}.$$

Again the physical optics current is simply given by

$$\vec{J}_u = 2 \hat{z} \times \vec{H}_u^i \Big|_{z=0} = \hat{x} \frac{2}{Z_0} e^{jk\rho' \sin \theta_i \cos \phi'}$$

with the far scattered fields given by

$$(44) \quad E_{||\theta}^S = -2 \cos \theta \cos \phi \int_0^a \int_0^{2\pi} e^{jk_z' [\sin \theta_i \cos \phi_i + \sin \theta \cos(\phi - \phi_i)]} d\phi_i' d\phi_i'$$

$$(45) \quad E_{||\phi}^S = 2 \sin \phi \int_0^a \int_0^{2\pi} e^{jk_z' [\sin \theta_i \cos \phi_i + \sin \theta \cos(\phi - \phi_i)]} d\phi_i' d\phi_i'$$

These integrals can be evaluated using the same technique as applied earlier giving

$$(46) \quad E_{||\theta}^S = - \frac{4\pi a \cos \theta \cos \phi}{k_Y} J_1(ka_Y),$$

and

$$(47) \quad E_{||\phi}^S = \frac{4\pi a \sin \phi}{k_Y} J_1(ka_Y).$$

In order to consider the total scattered field, one must treat an arbitrary plane wave incident on the end cap. In so doing let us assume that the incident field is, in general, given in ray form by

$$(48) \quad \vec{R}^i|_{\text{at origin}} = R_{\perp}^i \hat{y} + R_{||}^i \hat{\theta}$$

Then the total scattered far field is simply given using the superposition principle and Eqs. (42), (43), (46), (47), (48) by

$$(49) \quad \vec{E}_{\text{end caps}}^{\text{far field}}(\theta, \phi) = \hat{\theta} (R_{\perp}^i E_{\perp\theta}^S + R_{||}^i E_{||\theta}^S) + \hat{\phi} (R_{\perp}^i E_{\perp\phi}^S + R_{||}^i E_{||\phi}^S).$$

Note that the phase of the above solution is referenced to the center of the end cap disc. If the above solution was for the rear end cap with its phase referenced to the center of the cylinder, then Eq. (49) must be multiplied by the additional phase factor

$$[e^{jk \ell/2 (\cos \theta_i + \cos \theta)}]$$

It is well-known that the physical optics solution is a very good approximation in the specular region of the scattered field. The center of this region is defined by setting Eq. (41) equal to zero ($r=0$). This region is bounded by the zeros of $J_1(ka_r)$ as discussed in Ref. (44). However, these bounds may change depending on the size of the disc which in turn varies the region of overlap between the physical optics solution for the end caps and the wedge diffraction solution for the circular edges of the finite cylinder. In any event, the validity of this approach is illustrated by the results presented later.

Now the question arises as to how this solution can be applied to the near field scattering problem. Note that this near field problem will ultimately be adapted to simulate the scattering from aircraft engines. Even though this flat structure does not simulate the ends of engines, it is a convenient means of closing off the surface. Further, as shown later the engine has very little effect on the over-all pattern. In general, aircraft type engines are inherently long in comparison to their diameter; thus, the source can be in the near field of the engine yet in the far field of the relatively small discs at the ends of the engine. As a result, the far field solution of Eq. (49) can be adapted to this problem simply by assuming that field intensity of the incident plane wave is that radiated by the source and incident at the center of the end cap. This simply implies that the field incident at any point across the end cap is very nearly the same as the field at the center of the end cap (or nearly a plane wave). The geometry for this situation is illustrated in Fig. 23 with the source located behind the cylinder.

As was done for the flat plate problem it is known that the far field pattern of a general source can be written as

$$\vec{E}_{\text{source}}(\theta_a, \phi_a) = [\hat{\theta}_a F(\theta_a, \phi_a) + \hat{\phi}_a G(\theta_a, \phi_a)] \frac{jke^{-jkr}}{4\pi r},$$

where $\frac{jke^{-jkr}}{4\pi r}$ is factored out as done earlier. This field is then decomposed into parallel and perpendicular components such that

$$(50) \quad \vec{E}_{\text{source}}(\theta_a, \phi_a) = [\hat{y}(F_{\perp} + G_{\perp}) + \hat{\theta}(F_{\parallel} + G_{\parallel})] \frac{jke^{-jkR_r}}{4\pi R_r},$$

which is the field incident on the rear end cap. The values of θ_a and ϕ_a are known once the center of the end cap is located in terms of the source coordinate system. The total near field scatter from the rear end cap is then given using Eqs. (42), (43), (46), (47), (50) by

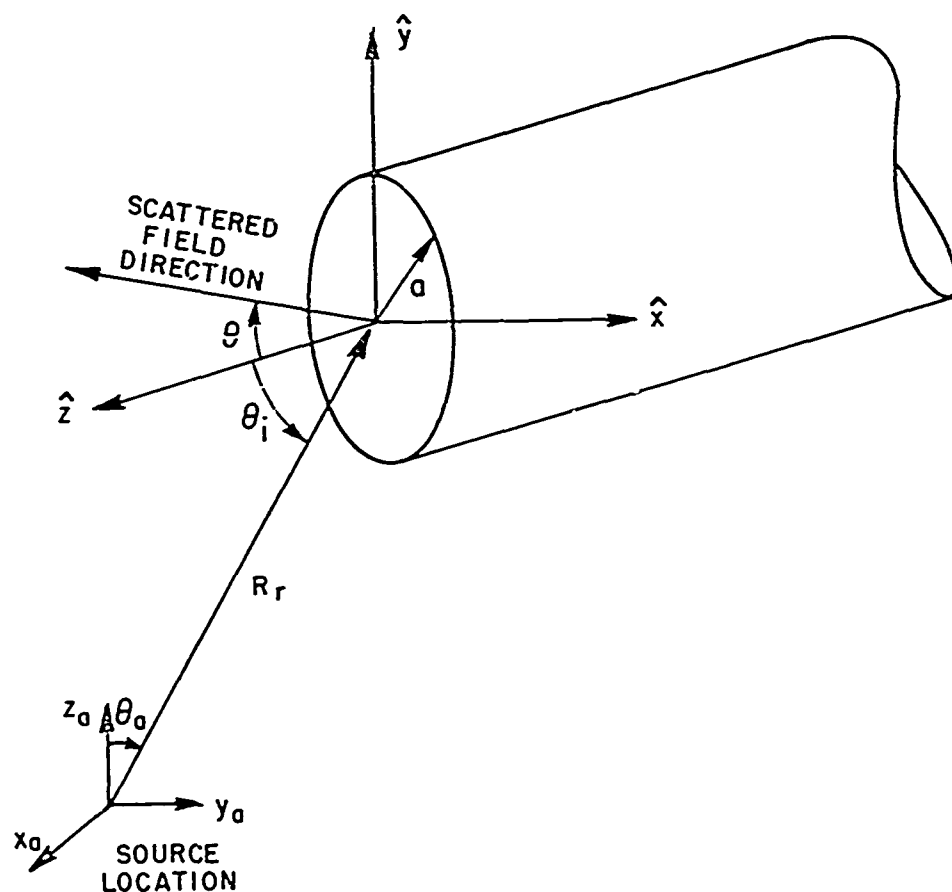


Fig. 23--Near field specular scatter by rear cylinder end cap.

$$(51) \quad \vec{E}_{\text{end cap}}^{\text{near field}}(\theta, \phi) = \{ \hat{\theta} [F_{\perp} + G_{\perp}] E_{\perp \theta}^S + (F_{\parallel} + G_{\parallel}) E_{\parallel \theta}^S \} +$$

$$\hat{\phi} [(F_{\perp} + G_{\perp}) E_{\perp \phi}^S + (F_{\parallel} + G_{\parallel}) E_{\parallel \phi}^S] \} \frac{j k e^{j k R_r}}{4 \pi R_r} e^{j k \ell / 2 \cos \theta_i}$$

for $k a \gamma \leq$ (approximately) 3.8317. Note that in this case the phase is referenced to the center of the cylinder. A similar expression can be written when the source is located in front of the cylinder where it is possible that the specular scatter from the front disc can dominate.

It is usually extremely difficult to analyze the more complex end shapes of actual engines. Thus, one must have a real need for such results to make a thorough investigation of that topic. As will be shown in the following chapter the engine has little effect on the principal plane patterns. Consequently, the flat plate end cap simply serves to close off the structure.

Once removed from the specular region of the end caps, the diffractions from the circular edges become dominant. In order to include these effects, the problem requires more sophistication than the straight-forward wedge diffraction problem of Section II-C. The curvature of the diffracting edges must be included in this solution by applying an equivalent current technique such as that presented in Ref. [45]. Using this approach an equivalent current is found on the diffracting edge using the appropriate two-dimensional diffraction solution. The resulting current is then used in the radiation integrals to find the far scattered field.

Let us first consider the perpendicular component of the incident plane wave on the back edge of the cylinder as illustrated in Fig. 22. This component is given by

$$\vec{E}_\perp^i = \hat{y} e^{jk(z \cos \theta_i + x \sin \theta_i)}$$

which results in giving

$$(52) \quad E_{\perp\phi}^i \Big|_{z=0} = \cos \phi' e^{jkx \sin \theta_i} \quad \text{and}$$

$$(53) \quad H_{\perp\phi}^i \Big|_{z=0} = - \frac{\cos \theta_i \sin \phi'}{Z_0} e^{jkx \sin \theta_i}.$$

The equivalent electric and magnetic currents are given, respectively, by Ref. [20] as

$$(54) \quad I_{\perp\phi}^e = \frac{2j G^e(\phi')}{Z_0 k \sin^2 \beta} E_{\perp\phi}^i \Big|_{z=0}, \quad \text{and}$$

$$(55) \quad I_{\perp\phi}^m = \frac{2j Z_0 G^h(\phi')}{k \sin^2 \beta} H_{\perp\phi}^i \Big|_{z=0},$$

which are related to the ray form of the diffraction function. The

various terms of the above expression are defined later in the discussion. In any event, these currents are given using Eqs. (52)-(55) by

$$I_{\perp\phi'}^e = \frac{2j G^e(\phi') \cos \phi'}{Z_0 k \sin^2 \beta} e^{jka \sin \theta_i \cos \phi'}, \text{ and}$$

$$I_{\perp\phi'}^m = \frac{2j G^h(\phi') \cos \theta_i \sin \phi'}{k \sin^2 \beta} e^{jka \sin \theta_i \cos \phi'}.$$

Substituting these currents into the radiation integrals one finds that

$$\begin{aligned} E_{\perp\theta}^e &= -a \cos \theta \int_0^{2\pi} J_{\perp\phi'}^e \sin(\phi - \phi') e^{jka[\sin \theta_i \cos \phi' + \sin \theta \cos(\phi - \phi')]} d\phi', \\ E_{\perp\phi}^e &= -a \int_0^{2\pi} J_{\perp\phi'}^e \cos(\phi - \phi') e^{jka[\sin \theta_i \cos \phi' + \sin \theta \cos(\phi - \phi')]} d\phi', \\ (56) \quad E_{\perp\phi}^m &= a \cos \theta \int_0^{2\pi} J_{\perp\phi'}^m \sin(\phi - \phi') e^{jka[\sin \theta_i \cos \phi' + \sin \theta \cos(\phi - \phi')]} d\phi', \\ E_{\perp\theta}^m &= -a \int_0^{2\pi} J_{\perp\phi'}^m \cos(\phi - \phi') e^{jka[\sin \theta_i \cos \phi' + \sin \theta \cos(\phi - \phi')]} d\phi' \end{aligned}$$

where

$$\begin{aligned} (57) \quad J_{\perp\phi'}^e(\phi') &= \frac{2j G^e(\phi') \cos \phi'}{k \sin^2 \beta} \quad \text{and} \\ J_{\perp\phi'}^m(\phi') &= \frac{2j G^h(\phi') \cos \theta_i \sin \phi'}{k \sin^2 \beta}. \end{aligned}$$

Note that the phase reference is at the center of the end cap and the factor $\left[\frac{jk}{4\pi r} e^{-jkr} \right]$ has been removed from the above expressions. Now using the method of stationary phase one can evaluate the previous integrals asymptotically using [46]

$$\int_0^{2\pi} F(\phi') e^{jka\phi(\phi')} d\phi' = F(\phi'_S) \sqrt{\frac{2\pi}{ka|\phi''(\phi'_S)|}} e^{j[ka\phi(\phi'_S) + \frac{\pi}{4} \text{sign } \phi''(\phi'_S)]}$$

where ϕ'_S is the stationary phase point or points defined by $\phi'(\phi'_S)=0$. All of the above integrals (Eq. (56)) are of this form with

$$\phi(\phi') = \sin \theta_i \cos \phi' + \sin \theta \cos(\phi - \phi')$$

giving the relation that

$$\phi'_S = \tan^{-1} \left(\frac{\sin \theta \sin \phi}{\sin \theta_i + \sin \theta \cos \phi} \right),$$

which has two solutions for $0 < \phi'_S < 360^\circ$ (ϕ_{S1}, ϕ_{S2}). Making the appropriate substitutions in the above integral expressions one finds that

$$(58) \quad E_{1\theta}^e(\theta, \phi) \sim -a \cos \theta \sum_{\phi_{S1}, \phi_{S2}} J_{1\phi}^e(\phi'_S) \sin(\phi - \phi'_S) X(\phi'_S)$$

$$E_{1\phi}^e(\theta, \phi) \sim -a \sum_{\phi_{S1}, \phi_{S2}} J_{1\phi}^e(\phi'_S) \cos(\phi - \phi'_S) X(\phi'_S)$$

$$E_{1\theta}^m(\theta, \phi) \sim a \cos \theta \sum_{\phi_{S1}, \phi_{S2}} J_{1\phi}^m(\phi'_S) \sin(\phi - \phi'_S) X(\phi'_S)$$

and

$$E_{1\theta}^m(\theta, \phi) \sim -a \sum_{\phi_{S1}, \phi_{S2}} J_{1\phi}^m(\phi'_S) \cos(\phi - \phi'_S) X(\phi'_S)$$

where

$$X(\phi'_S) = \sqrt{\frac{2\pi}{ka|\phi''(\phi'_S)|}} e^{j[ka\phi(\phi'_S) + \frac{\pi}{4} \text{sign } \phi''(\phi'_S)]}$$

and

$$\psi(\phi_S') = -\psi''(\phi_S') = \sin \theta_i \cos \phi_S' + \sin \theta \cos(\phi - \phi_S').$$

The total perpendicular component of the scattered far field for the circular diffracting edge is then the sum of the electric and magnetic components and is given using Eqs. (57) and (58) by

$$(59) \quad E_{\perp \phi}^d(\theta, \phi) = 2ja \sum_{\phi_{S1}, \phi_{S2}} \frac{X(\phi_S')}{k \sin^2 \beta_S} [-G^e(\phi_S') \cos \theta \cos \phi_S' \sin(\phi - \phi_S') + G^h(\phi_S') \cos \theta_i \sin \phi_S' \cos(\phi - \phi_S')]]$$

$$(60) \quad E_{\perp \psi}^d(\theta, \phi) = -2ja \sum_{\phi_{S1}, \phi_{S2}} \frac{X(\phi_S')}{k \sin^2 \beta_S} [G^e(\phi_S') \cos \phi_S' \cos(\phi - \phi_S') + G^h(\phi_S') \cos \theta \cos \theta_i \sin \phi_S' \sin(\phi - \phi_S')] .$$

The diffraction terms are yet to be defined in terms of the stationary phase points (ϕ_{S1}, ϕ_{S2}) . The geometry pertinent to this discussion is illustrated in Fig. 24. The ray forms of the diffracted field are given by

$$G_{\phi_S'}^e = R(\psi - \psi_0, 3/2) \mp R(\psi + \psi_0, 3/2)$$

where it is shown in Ref. [20] that

$$R(\phi, 3/2) = \frac{\frac{2}{3} \sin \frac{2\pi}{3}}{\cos \frac{2\pi}{3} - \cos \frac{2\phi}{3}} .$$

The values of the diffraction angles are based on the two-dimensional wedge problem and are given by

$$\psi_0 = \tan^{-1} \left(\frac{-\hat{I} \cdot \hat{y}_e}{-\hat{I} \cdot \hat{x}_e} \right) = \tan^{-1} \left(\frac{\cos \theta_i}{-\cos \phi_S' \sin \theta_i} \right)$$

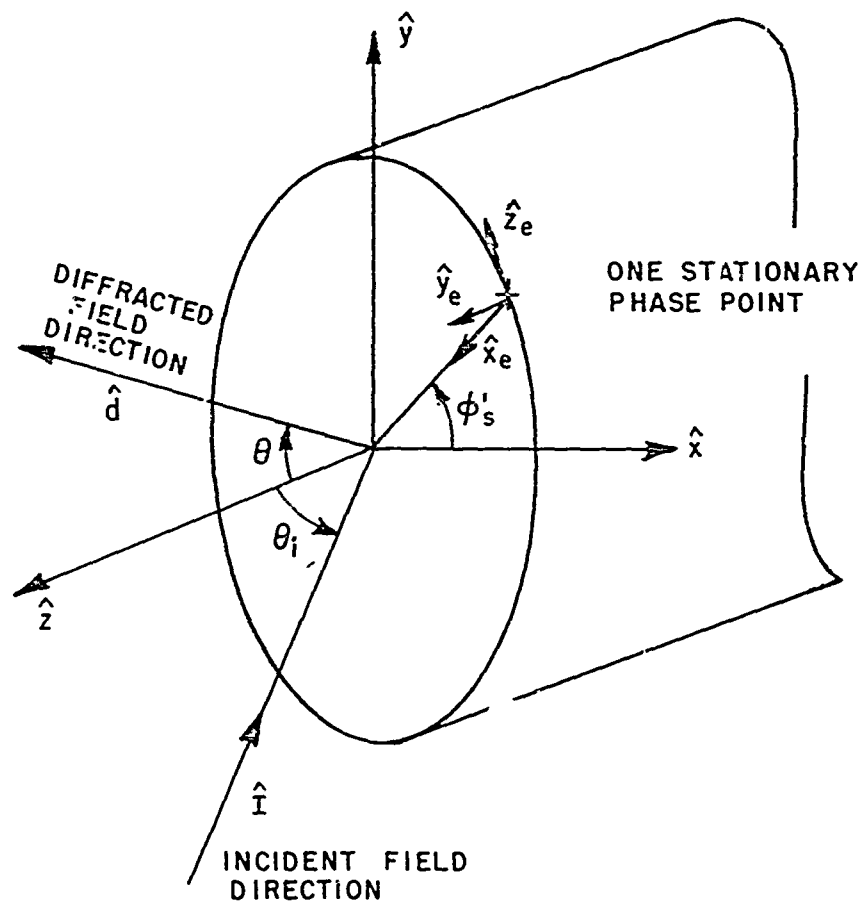


Fig. 24--Diffracted field geometry for finite cylinder edge.

$$\psi = \tan^{-1} \left(\frac{\hat{d} \cdot \hat{y}_e}{\hat{d} \cdot \hat{x}_e} \right) = \tan^{-1} \left(\frac{\cos \theta}{\sin \theta \cos(\phi - \phi'_s)} \right) .$$

The three-dimensional effect on the wedge diffraction problem is introduced by the angle β_S which is defined by

$$\beta_S = \tan^{-1} \left(\frac{\sqrt{(-\hat{I} \cdot \hat{x}_e)^2 + (-\hat{I} \cdot \hat{y}_e)^2}}{-\hat{I} \cdot \hat{z}_e} \right) = \tan^{-1} \left(\frac{\sqrt{(\hat{d} \cdot \hat{x}_e)^2 + (\hat{d} \cdot \hat{y}_e)^2}}{\hat{d} \cdot \hat{z}_e} \right)$$

where $0 \leq \beta_S \leq 180^\circ$. Finally, if the condition exists where $\beta_0 > n^-$, then diffractions do not occur from that stationary phase point in that the cylinder shadows that term

The parallel component of the incident field is given by

$$\vec{E}_{\parallel}^i = (\hat{x} \cos \theta_i - \hat{z} \sin \theta_i) e^{jk(z \cos \theta_i + x \sin \theta_i)}$$

which gives

$$E_{\parallel\phi}^i \Big|_{z=0} = -\cos \theta_i \sin \phi' e^{jkx \sin \theta_i}, \text{ and}$$

$$H_{\parallel\phi}^i \Big|_{z=0} = -\frac{\cos \theta_i}{Z_0} e^{jkx \sin \theta_i}.$$

Then using the same approach as before, the parallel component of the scattered field for the diffracting edge is given by

$$(61) \quad E_{\parallel\theta}^d(\theta, \phi) = 2ja \sum_{\phi_{S1}, \phi_{S2}} \frac{\chi(\phi_S')}{k \sin^2 \beta_S} [G^e(\phi_S') \cos \theta_i \sin \phi_S' \sin(\phi - \phi_S') \\ + G^h(\phi_S') \cos \phi_S' \cos(\phi - \phi_S')]$$

and

$$(62) \quad E_{\parallel\phi}^d(\theta, \phi) = 2ja \sum_{\phi_{S1}, \phi_{S2}} \frac{\chi(\phi_S')}{k \sin^2 \beta_S} [G^e(\phi_S') \cos \theta_i \sin \phi_S' \cos(\phi - \phi_S') \\ - G^h(\phi_S') \cos \theta \cos \phi_S' \sin(\phi - \phi_S')]$$

with the various terms being defined previously.

The total scattered far field from the rear diffracting edge is given using Eqs. (48), (59), (60), (61), (62) by

$$(63) \quad \vec{E}_{\text{edge diff.}}^{\text{far field}}(\theta, \phi) = \hat{\phi} (R_{\perp}^i E_{\perp\theta}^d + R_{\parallel}^i E_{\parallel\theta}^d) + \hat{\theta} (R_{\perp}^i E_{\perp\phi}^d + R_{\parallel}^i E_{\parallel\phi}^d) e^{jk(\lambda/2)(\cos\theta_1 + \cos\theta_2)}$$

Note that in this case the phase is referenced to the center of the cylinder. In addition, a similar expression can be generated for the scattered field which results from diffractions off the front edge of the finite cylinder. These two diffracted field solutions are then summed using the superposition principle and applied between the specular regions of the end caps and cylinder section. The cylinder specular term is presented later in the discussion.

It was assumed by using the stationary phase method that only two points around each of the cylindrical rims could contribute to the scattered field. However, there are certain regions (caustics) where diffractions from the complete rim contribute to the scattered field. In these regions one must carry out the complete integrations around the edges rather than using the stationary phase method. The expressions have been developed but are not included in our numerical computations in that this solution is applied only to simulate the engine near field scattering effect. Thus, a complete investigation of the finite cylinder is beyond the scope of our final objective. For this reason, our numerical solutions can tend to diverge near the caustic regions as is noted when the results are presented later.

As was done for the end cap specular region, it will be assumed that the edges of the finite cylinder are in the far field of the source for the near field scattering problem. With this being the case and using the geometry illustrated in Fig. 22, the diffracted field from the rear edge is given using Eqs. (50), (59), (60), (61), (62) by

$$(64) \quad \vec{E}_{\text{edge diff.}}^{\text{near field}}(\theta, \phi) = \hat{\theta} [(F_{\perp} + G_{\perp}) E_{\perp\theta}^d + (F_{\parallel} + G_{\parallel}) E_{\parallel\theta}^d] + \hat{\phi} [(F_{\perp} + G_{\perp}) E_{\perp\phi}^d + (F_{\parallel} + G_{\parallel}) E_{\parallel\phi}^d] \frac{jke^{-jkR_r}}{4\pi R_r} e^{jk(\lambda/2)\cos\theta}$$

A similar expression can be found for the diffracted field from the front edge of the cylinder. The total diffracted field is then the superposition of the diffracted fields from the two edges of the cylinder.

Since in this case the range of the source is not an infinite distance from the edge, one must apply the V_B form of the diffraction function in which

$$R(\cdot, 3/2) = V_B(R_r \sin^2 \theta_S, \cdot, 3/2) e^{j(kR_r \sin^2 \theta_S \pm \pi/4)} \sqrt{2-kR_r \sin \theta_S}$$

giving

$$G^e(\cdot, \theta_S) = V_B^{\pm} e^{j(kR_r \sin^2 \theta_S \pm \pi/4)} \sqrt{2-kR_r \sin \theta_S}.$$

One then simply substitutes this result for the terms E_L^d , E_{L+}^d , E_{L-}^d , and E_H^d for the near field scattering solution of Eq. (64). Otherwise the terms are the same as found previously. Finally, in the near field problem the diffracted fields from the two finite cylinder edges are included everywhere except in the specular region of the end caps. This is somewhat different from that of the far field solution where the diffracted fields are only present between the specular regions of the end cap and cylindrical sections.

The final region to be considered is the specular region of the long cylindrical section. The solution for this region is found similar to the physical optics solution used for the end caps; however in this case, the current used in the radiation integral is the exact current found on an infinitely long cylinder. This current is, then, integrated over the finite length of the cylinder as presented in Ref. [42]. This type of solution generally has good accuracy throughout the specular region of the cylindrical section much as the physical optics solution.

With a perpendicular component E-field incident on the cylinder, it is shown in Appendix I that

$$H_{1z}^t = -\frac{\sin \theta_i}{Z_0} e^{jkz \cos \theta_i} \sum_{n=-\infty}^{\infty} j^n \left[J_n(\beta a) - \frac{J_n'(\beta a)}{H_n^{(2)'}(\beta a)} H_n^{(2)}(\beta a) \right] e^{-jn\phi}$$

$$H_{1\phi}^t = -\frac{\cos \theta_i}{k_0 Z_0 \sin \theta_i} e^{jkz \cos \theta_i} \sum_{n=-\infty}^{\infty} nj^n \left[J_n(\beta a) - \frac{J_n'(\beta a)}{H_n^{(2)'}(\beta a)} H_n^{(2)}(\beta a) \right] e^{-jn\phi}$$

where $k_z = k \sin \theta_i$. The equivalent surface current density is given by

$$\vec{J}_s = \hat{n} \times (\vec{H}_{1z}^t \hat{z} + H_{1\phi}^t \hat{\phi})|_{r=a} = -\hat{z} H_{1z}^t(r=a) + \hat{\phi} H_{1\phi}^t(r=a)$$

The θ -component of the far scattered field is given by

$$E_{\theta}^C = Z_0 \int_{-\pi/2}^{\pi/2} [-J_z \sin(\phi-\phi') \cos \theta + J_z \sin \phi]$$

$$e^{jkz'} \cos(\phi-\phi') \sin \theta + z' \cos \phi] a dz' d\phi'$$

or

(65)

$$E_{\theta}^C = -\sin \theta_i \sum_{n=-\infty}^{\infty} j^n X_n(a) \int_{-\pi/2}^{\pi/2} e^{jkz'(\cos \theta_i + \cos \theta)} \sin(\phi-\phi') \cos \theta$$

$$e^{-jn\phi'} e^{jka \cos(\phi-\phi') \sin \theta} dz' d\phi'$$

$$- \frac{\cos \theta_i}{ka \sin \theta_i} \sum_{n=-\infty}^{\infty} nj^n X_n(a) \int_{-\pi/2}^{\pi/2} e^{jkz'(\cos \theta_i + \cos \theta)} \sin \theta$$

$$e^{-jn\phi'} e^{jka \cos(\phi-\phi') \sin \theta} dz' d\phi'$$

where $X_n(a) = J_n(ka) - \frac{J_n'(ka)}{H_n^{(2)'}(ka)} H_n^{(2)}(ka)$. These integrals can be evaluated using

$$\int_{-\pi/2}^{\pi/2} e^{jkz'(\cos \theta_i + \cos \theta)} dz' = \frac{\pi \sin \left[\frac{k\ell}{2} (\cos \theta_i + \cos \theta) \right]}{\frac{k\ell}{2} (\cos \theta_i + \cos \theta)}$$

$$\int_0^{2\pi} e^{-jn\phi'} e^{jka \cos(\phi-\phi') \sin \theta} \sin(\phi-\phi') d\phi' \\ = \frac{2\pi e^{jn(\phi+\pi/2)}}{ka \sin \theta} n J_n(ka \sin \theta)$$

and

$$e^{-jn\phi} e^{jka \sin \theta_i \cos(\phi - \phi_i)} d\phi_i = 2e^{jn(\phi - \phi_i/2)} J_n(ka \sin \theta_i).$$

Substituting these results into Eq. (65) one finds that

$$(66) \quad E_{\perp}^C(\phi, z) = \frac{-8j}{k^2 a} \left(\cot \theta_i + \frac{\cos \theta_i \sin \theta_i}{\sin^2 \theta_i} \right) \frac{\sin \left[\frac{k_z}{2} (\cos \theta_i + \cos \theta) \right]}{\frac{k_z}{2} (\cos \theta_i + \cos \theta)} \sum_{n=0}^{\infty} n(-1)^n \frac{J_n(ka \sin \theta_i)}{H_n^{(2)}(ka \sin \theta_i)} \sin n\phi.$$

Similarly the ϕ -component of the scattered field is given by

$$E_{\phi}^C(\phi, z) = -Z_0 a \int_{-\pi/2}^{\pi/2} J_0(\cos(\phi - \phi_i)) e^{jk[a \cos(\phi - \phi_i) \sin \theta + z' \cos \theta]} dz' d\phi_i$$

which can be evaluated as above to give

$$(67) \quad E_{\phi}^C(\phi, z) = \frac{4j}{k} \frac{\sin \left[\frac{k_z}{2} (\cos \theta_i + \cos \theta) \right]}{\frac{k_z}{2} (\cos \theta_i + \cos \theta)} \sum_{n=0}^{\infty} \epsilon_n (-1)^n \frac{J_n'(ka \sin \theta_i)}{H_n^{(2)'}(ka \sin \theta_i)} \cos n\phi.$$

For a parallel component E -field incident it is shown in Appendix I that

$$H_{\parallel z}^t = 0$$

$$H_{\parallel \phi}^t = \frac{j}{Z_0} e^{j k z \cos \theta_i} \sum_{n=-\infty}^{\infty} j^n \left[J_n'(\beta a) - \frac{J_n(\beta a)}{H_n^{(2)}(\beta a)} H_n^{(2)'}(\beta a) \right] e^{-jn\phi}.$$

In this case, the equivalent surface current density is given by

$$\mathbf{j}_s = \hat{\mathbf{z}} \wedge (\mathbf{H}_s^t|_{z=a}) = \hat{\mathbf{z}} \wedge \mathbf{H}_s^t(z=a).$$

Substituting this current into the radiation integrals one finds that

$$(69) \quad E_{\theta}^C = 0, \text{ and}$$

$$E_{\phi}^C = Z_0 a \int_{-\pi/2}^{\pi/2} \int_{-\pi/2}^{\pi/2} j_{\phi} \sin \theta' e^{jk[a \cos(\theta - \theta') \sin \theta + z' \cos \theta]} dz' d\theta'.$$

This integral can be evaluated as done previously giving

$$(70) \quad E_{\phi}^C = \frac{-4j \sin \theta}{k \sin^2 \theta_i} \frac{\sin \left[\frac{k}{2} (\cos \theta_i + \cos \theta) \right]}{\frac{k}{2} (\cos \theta_i + \cos \theta)}$$

$$\sum_{n=0}^{\infty} (-1)^n \frac{J_n(ka \sin \theta)}{H_n^{(2)}(ka \sin \theta_i)} \cos n\theta.$$

The total scattered field in this region is then given using the superposition principle and Eqs. (66), (67), (69), (70) by

$$(71) \quad \vec{E}_{\text{cyl}}^{\text{far field}}(\theta, \phi) = \hat{\mathbf{r}} [R_{\perp}(\theta_i, \phi_i) E_{\perp \theta}^C(\theta, \phi) + R_{\parallel}(\theta_i, \phi_i) E_{\parallel \theta}^C(\theta, \phi)]$$

$$+ \hat{\boldsymbol{\phi}} [R_{\perp}(\theta_i, \phi_i) E_{\perp \phi}^C(\theta, \phi) + R_{\parallel}(\theta_i, \phi_i) E_{\parallel \phi}^C(\theta, \phi)].$$

where R_{\perp} and R_{\parallel} are defined in Eq. (48). Note that in this case the phase is already referenced to the center of the finite cylinder.

As stated earlier this solution gives a good approximate solution for computing the specular scattered fields of the long cylindrical section. As was done earlier this region is normally defined between the first nulls about the main beam of the specular scatter direction. These boundaries are each defined by

$$\frac{kL}{2} (\cos \theta_i + \cos \theta) = n\pi$$

where $n=0$ gives the specular main beam direction and $n = -1$ defines the first null directions. This is the only term necessary through the cylindrical specular scatter region. However, as is shown later the edge diffracted fields must be included through this region for the near scattered field solution.

This solution completes our study of the scattered far field from a finite cylinder which is given using Eqs. (49), (63), (71) by

$$(72) \quad \bar{E}_{\text{far}}(\cdot, \cdot) = \begin{cases} \bar{E}_{\text{front cap}}^{\text{far field}}(\cdot, \cdot) & ka_{\text{front}} \leq (\cdot) 3.8317 \\ \bar{E}_{\text{rear cap}}^{\text{far field}}(\cdot, \cdot) & ka_{\text{rear}} \leq (\cdot) 3.8317 \\ \bar{E}_{\text{cyl.}}^{\text{far field}}(\cdot, \cdot) & \left| \frac{k_z}{2}(\cos \theta_i + \cos \theta) \right| \leq \pi \\ \bar{E}_{\text{front edge}}^{\text{far field}}(\cdot, \cdot) + \bar{E}_{\text{rear edge}}^{\text{far field}}(\cdot, \cdot) & \text{otherwise.} \end{cases}$$

In order to compare this solution with previously measured scattered far field data it was found that backscatter data was most readily available. In Fig. 25 the results of Eq. (72) are compared with measured backscatter data taken from Ref. [41]. It was extremely difficult to extract the measured data from their graphs in that the finite cylinder measured was quite large which resulted in much ripple. In any event, the agreement between the results for the points chosen does indicate the validity of our solution. Note that both incident polarizations were considered which covers the complete problem at least for the backscatter case.

The far field solutions could be applied to the near-field problem in the two other regions since the cylinder was assumed to be long and thin. However, that approximation can not be made for this cylindrical specular region unless the source is moved a large distance ($2\lambda^2/\lambda$) away from the cylinder. This implies that the spherical wave front radiated by the source must be considered in the approximating currents. This is a very difficult problem to solve except for cylinders short in terms of the wavelength. Thus, a different approach must be applied to solve for the scattered near field solution in this specular region.

This obstacle is overcome by applying a technique similar to that employed for the finite flat plate problem, in which the reflections from the plate are added only when the point of reflection falls within the limits of the finite plate. In this case, the modal solution can be used to obtain a similar scattered field term from an infinite cylinder which is only included when the origin of the scattered term falls within the limits of the finite cylinder.

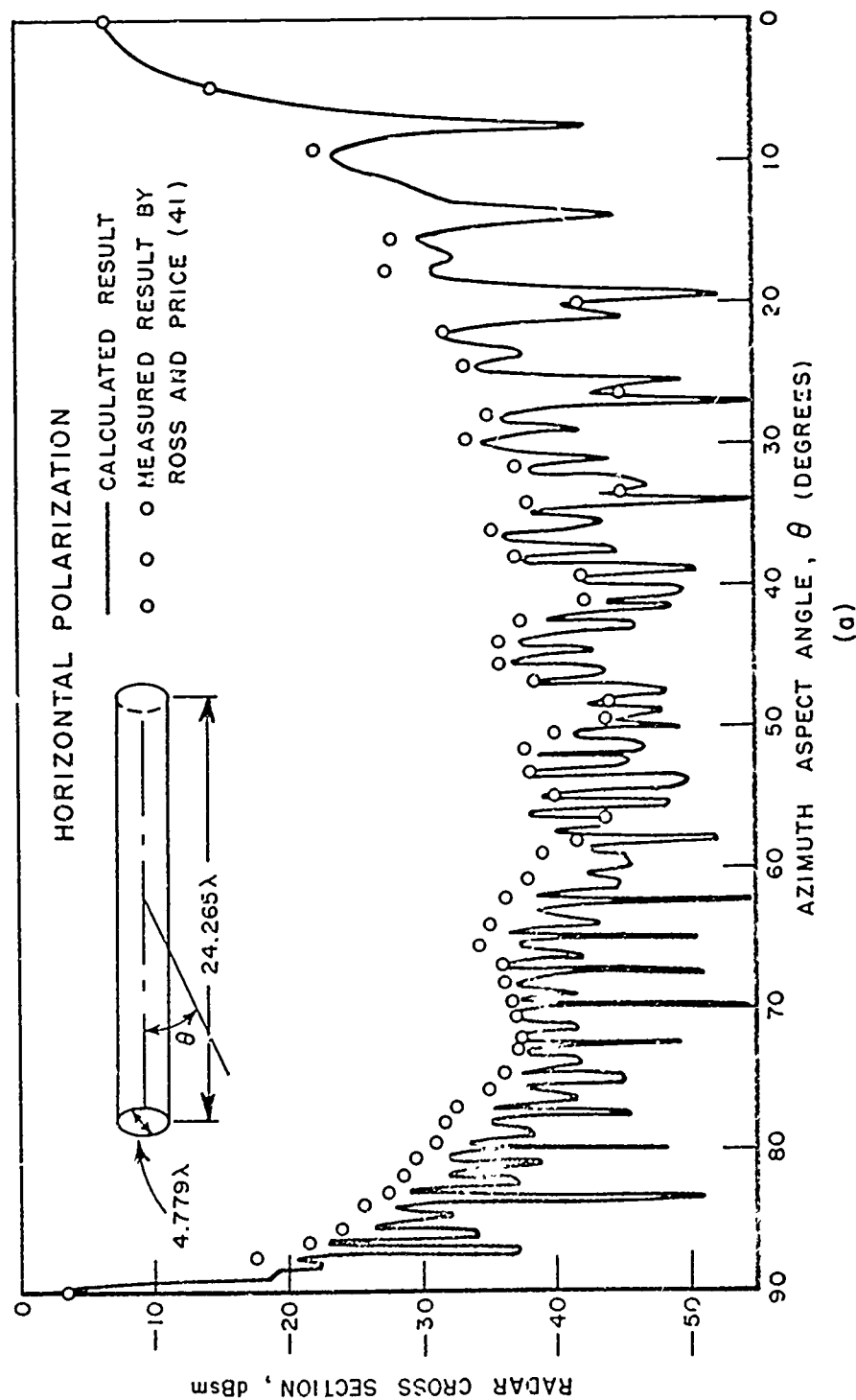


Fig. 25a--Far field radar cross-section from a finite cylinder.

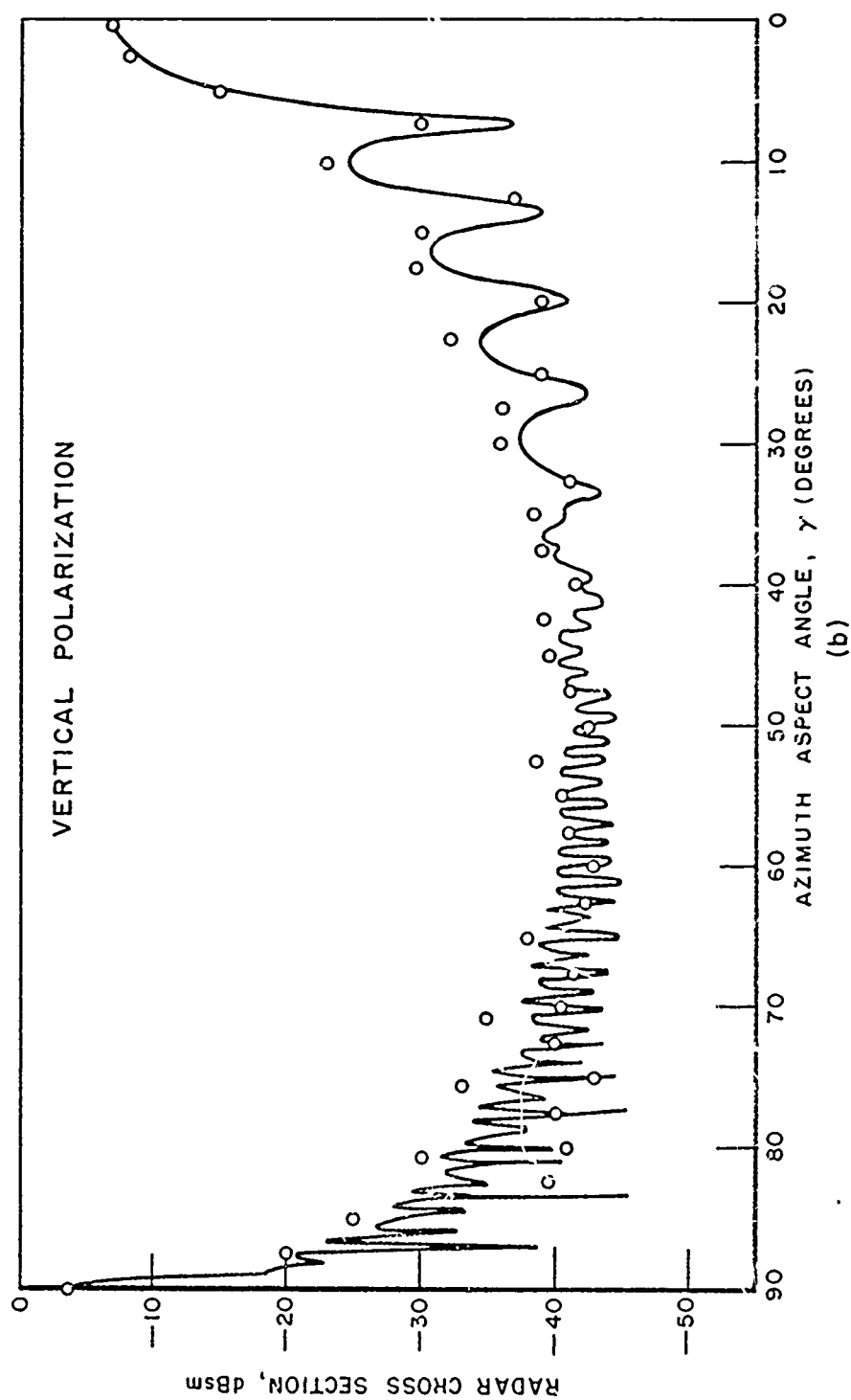


Fig. 25b. Far field radar cross-section from a finite cylinder.

Based on a ray optics description, it is known that for the reflected terms the angle of incidence (θ_i) is equal to the angle of reflection (θ_r). Secondly, it is known that the creeping wave terms attach to the cylindrical surface tangentially and propagate around the surface in a helical path with constant pitch, such that θ remains constant. For these reasons, one can affirm that to a good approximation the bounds of this region can be specified in terms of θ_i as shown in Fig. 26, for $\theta_r \leq \theta_i \leq \theta_f$.

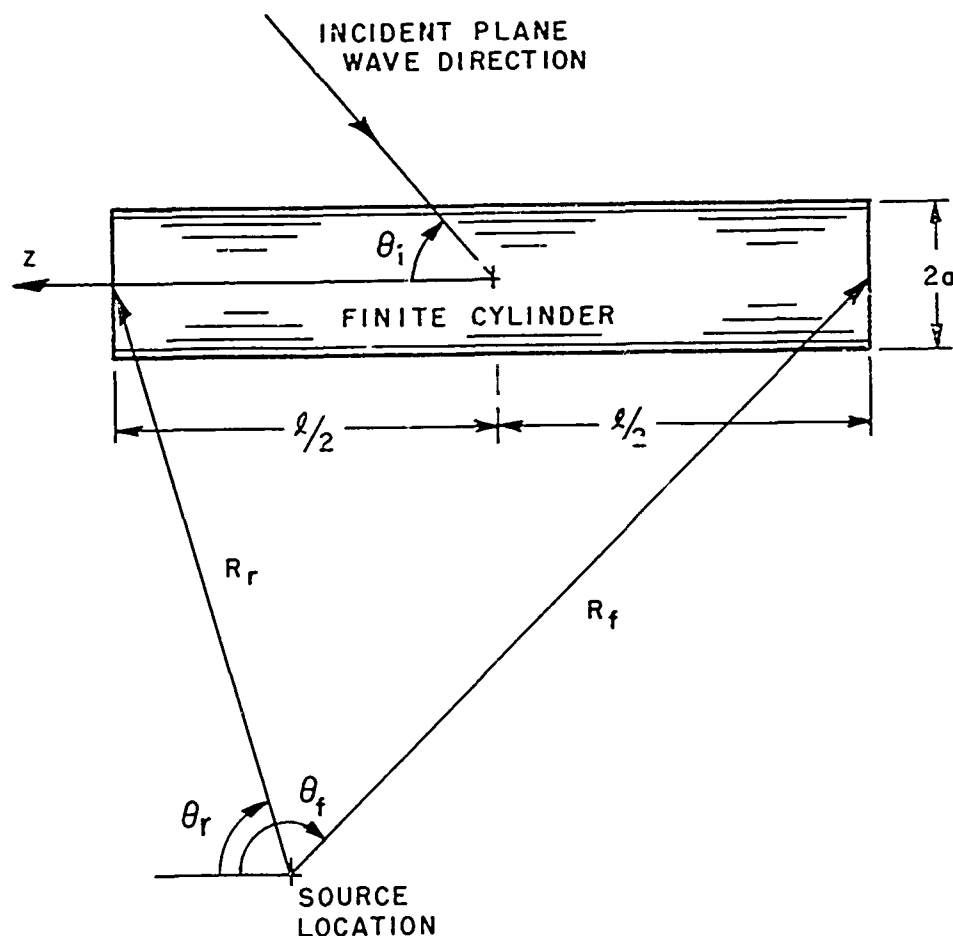


Fig. 26--Cylindrical specular region for near zone cylinder.

In order to apply the results of Appendix I one must use a reciprocity argument in that it is assumed there that a plane wave is incident. In this case, the source is in the near field and the scattered far field is desired which can be solved using

$$E_{\perp\phi}^{cly}(\theta, \phi) = \frac{2 \cos \theta_i}{k r \sin \theta_i} e^{jkz \cos \theta_i} \sum_{n=1}^{\infty} n j^{n+1} \frac{J_n'(\beta a)}{H_n^{(2)'}(\beta a)}$$

$$H_n^{(2)}(\beta \rho) \sin n(\phi - \phi_i)$$

$$E_{\perp\phi}^{cly}(\theta, \phi) = e^{jkz \cos \theta_i} \sum_{n=0}^{\infty} \epsilon_n j^{n+1} \frac{J_n'(\beta a)}{H_n^{(2)'}(\beta a)} H_n^{(2)'}(\beta \rho) \cos n(\phi - \phi_i) \quad (73)$$

$$E_{\parallel\theta}^{cly}(\theta, \phi) = e^{jkz \cos \theta_i} \sum_{n=0}^{\infty} \epsilon_n j^n \frac{J_n(\beta a)}{H_n^{(2)}(\beta a)} [-\sin \theta_i \sin \phi H_n^{(2)}(\beta \rho) + \cos \theta_i \cos \phi H_n^{(2)}(\beta \rho)] \cos n(\phi - \phi_i)$$

and

$$E_{\parallel\phi}^{cly}(\theta, \phi) = \frac{2 \cos \theta_i}{k r \sin \theta_i} e^{jkz \cos \theta_i} \sum_{n=1}^{\infty} n j^{n+1} \frac{J_n(\beta a)}{H_n^{(2)}(\beta a)} H_n^{(2)}(\beta \rho) \sin n(\phi - \phi_i)$$

where $\beta = k \sin \theta_i$. Note that the above equations give the θ and ϕ components of the field at the source position which is defined by (ρ, ϕ, z) .

The received signal by the antenna can be found using the far field pattern as defined by

$$\vec{E}_{\text{source}}(\theta_a, \phi_a) = [\hat{\theta}_a F(\theta_a, \phi_a) + \hat{\phi}_a G(\theta_a, \phi_a)] \frac{e^{-jkr}}{r}$$

Thus, the pattern function of the source can be expressed in terms of the θ and ϕ coordinates by

$$(74) \quad \vec{R}_{\text{source}}(\theta_a, \phi_a) = \hat{\theta}(F_{\theta} + G_{\theta}) + \hat{\phi}(F_{\phi} + G_{\phi})$$

where θ_a and ϕ_a are defined in terms of the incident field direction in the source coordinate system. The radiated field by the source using the reciprocity theorem is then given by

$$(75) \quad \vec{E}_{\text{cly}}^{\text{near field}}(\theta_i, \phi_i) = \hat{\theta}_i [(F_{\parallel\theta} + G_{\theta}) E_{\parallel\theta}^{cly}(\theta, \phi) + (F_{\perp\theta} + G_{\phi}) E_{\perp\theta}^{cly}(\theta, \phi)] \\ + \hat{\phi}_i [(F_{\theta} + G_{\theta}) E_{\perp\theta}^{cly}(\theta, \phi) + (F_{\phi} + G_{\phi}) E_{\perp\phi}^{cly}(\theta, \phi)]$$

for $r \leq r_f$ as defined in Fig. 26 and where θ_i and ϕ_i now define the scattered field direction. In this case the phase is already referred to the center of the finite cylinder. In addition, the diffractions from the edges of the cylinder must be included throughout this region. Note, also, that the directly radiated field by the source must be included in every region of the near field problem.

To illustrate the validity of this near field solution, it is compared with measured results for two cases. A vertical and horizontal dipole are, respectively, mounted in the near zone of a finite cylinder as shown in Fig. 27a and b. One should note that the agreement is quite good except near the caustic regions where our solution tends to diverge. The reason is that the diffractions from the circular edge are not coming from just two points but from the complete circular edge, which can be included in our solution by actually integrating Eq. (56). However, it is shown in Section IV-D that when this solution is used in solving for the azimuth principal plane pattern, the engine (finite cylinder) has very little effect. Thus, an extensive study of this topic is not necessary at present. In any event, the basic tools are presented in the previous discussion.

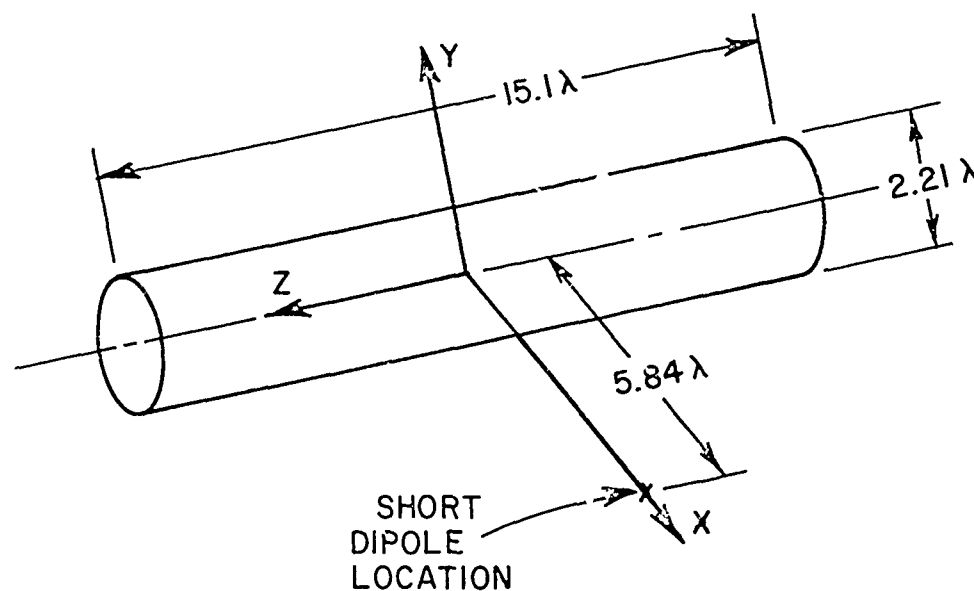


Fig. 27a--Short dipole illuminating a finite cylinder.

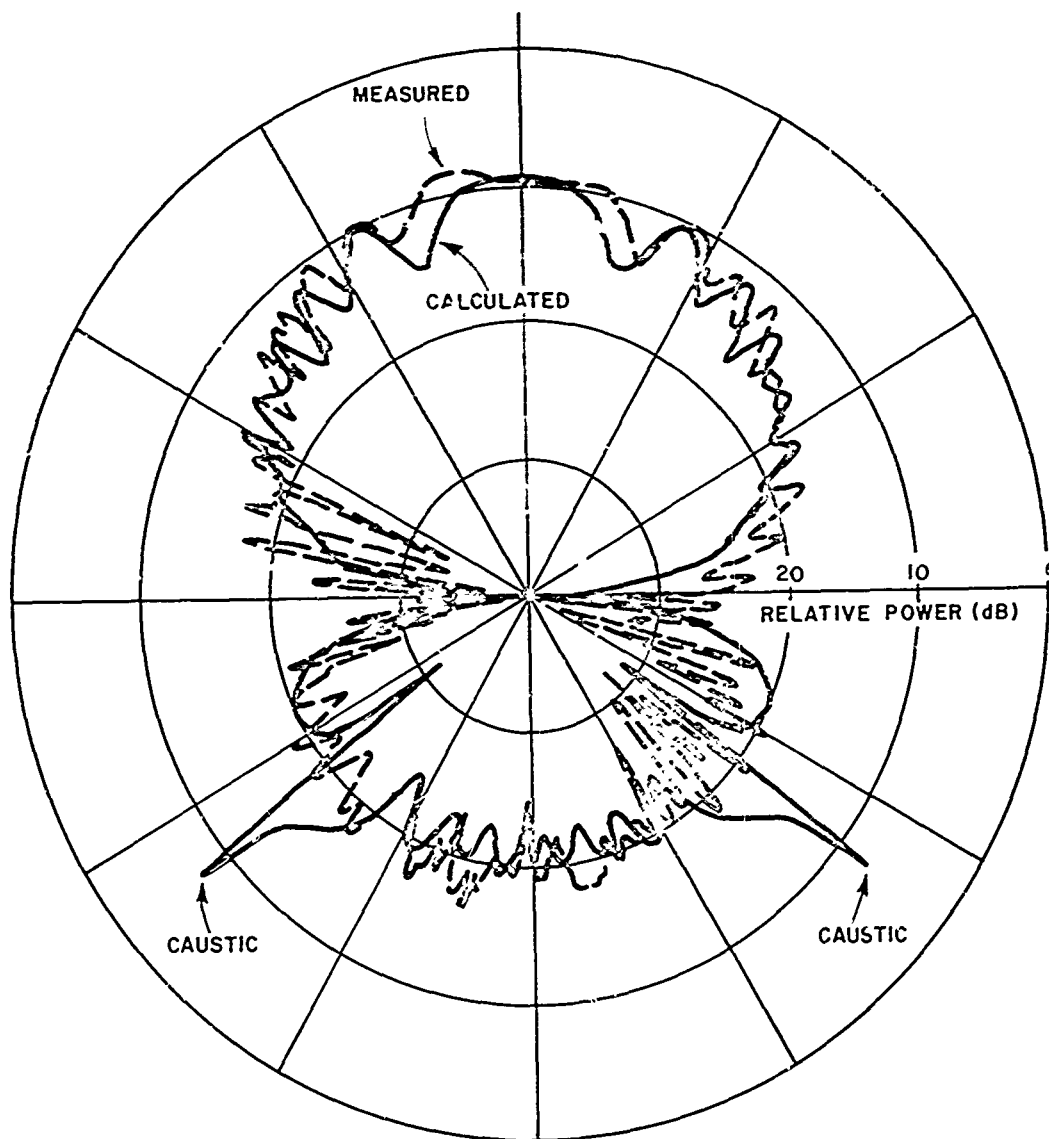


Fig. 27b--Radiation pattern of a horizontal dipole (E_θ)
with $-180^\circ \leq \theta < 180^\circ$.

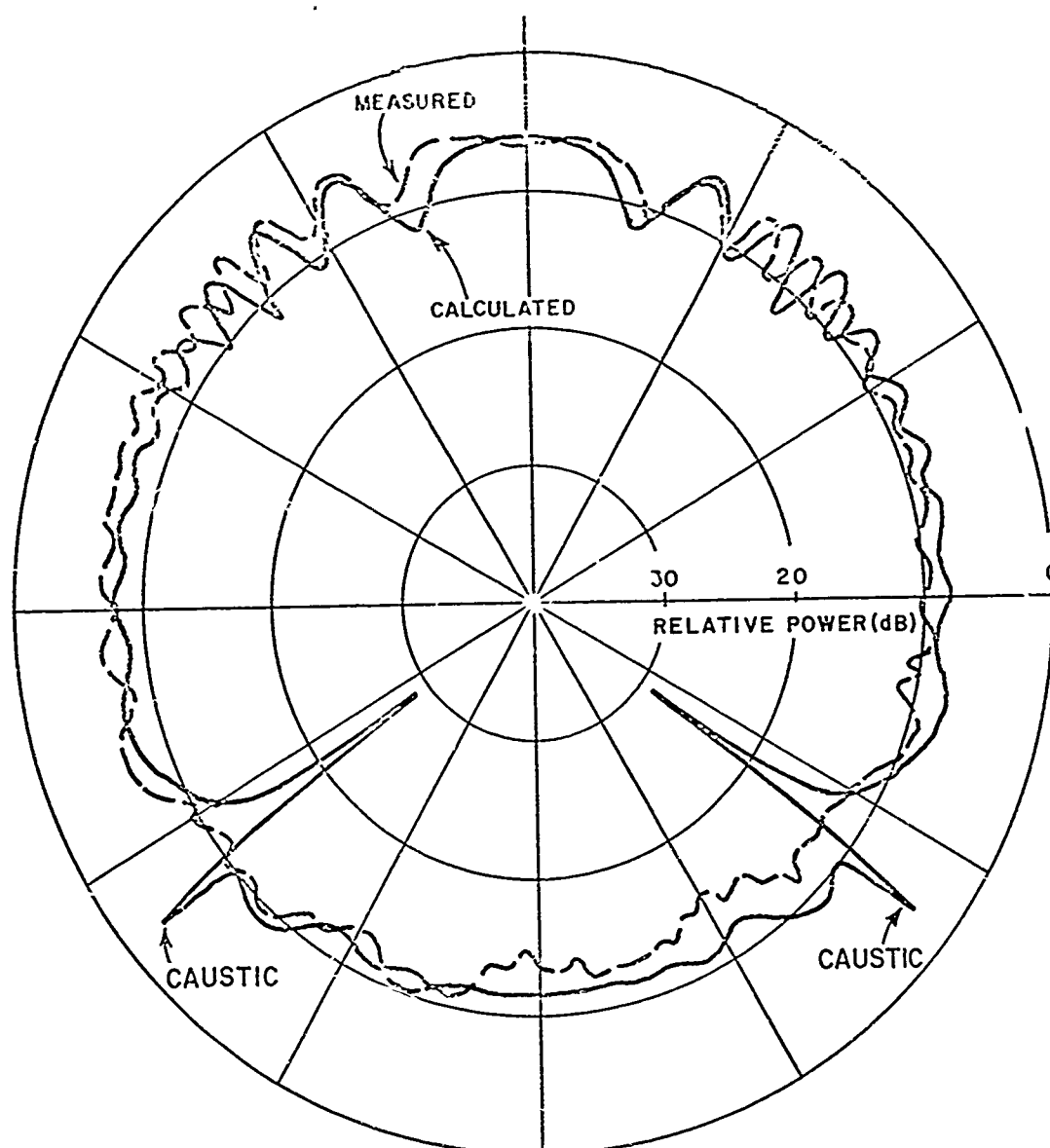


Fig. 27c--Radiation pattern of a vertical dipole (E_θ)
with $-180^\circ \leq \theta \leq 180^\circ$.

CHAPTER IV

ON-AIRCRAFT ANTENNA PRINCIPAL PLANE PATTERN STUDY

A. Introduction

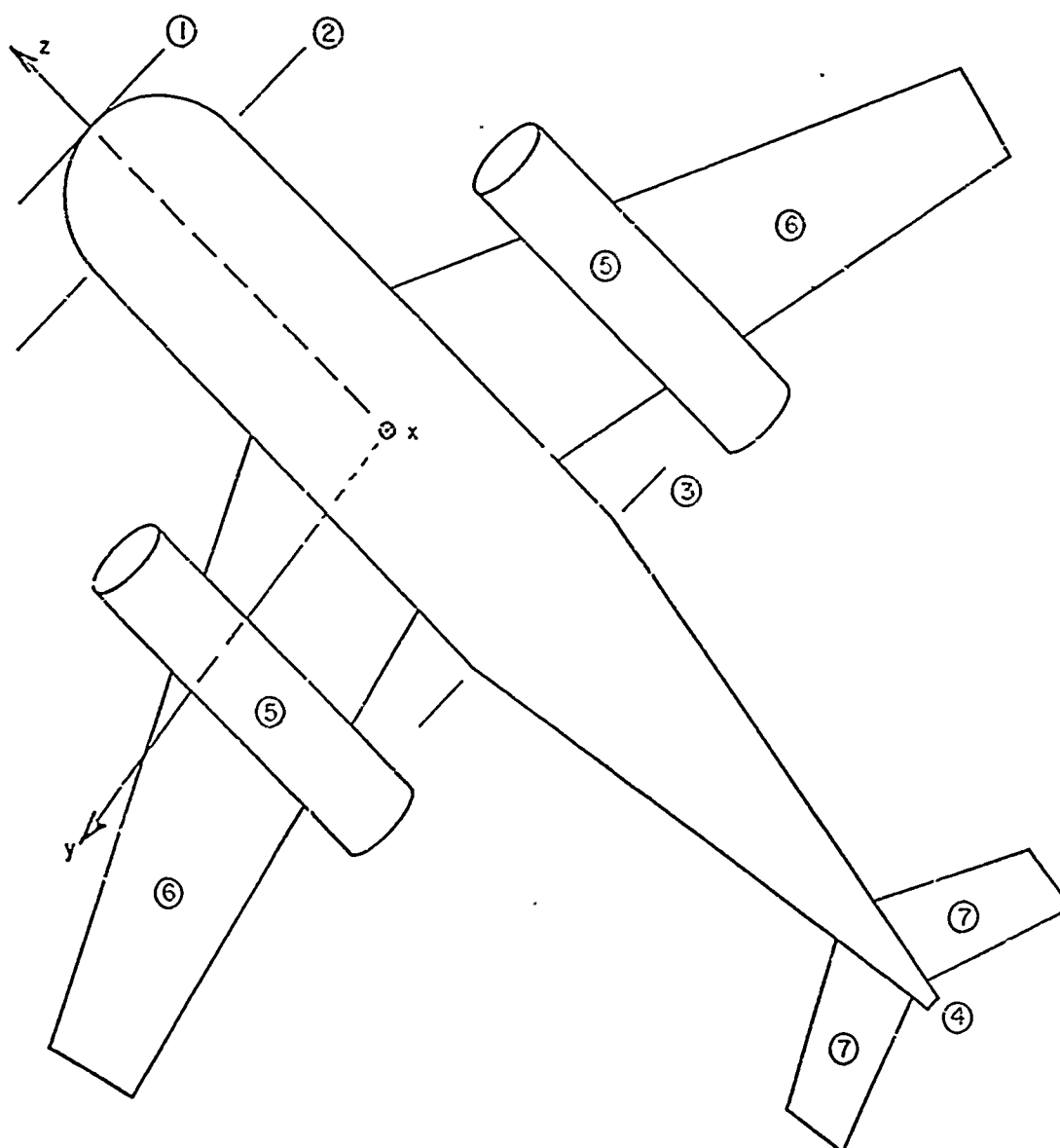
This chapter illustrates the application of solutions previously discussed to determine radiation patterns in three principal planes for fuselage mounted aircraft antennas. Most of these results have been presented elsewhere [47,48]; however, they are pertinent to the present discussion. Furthermore, several improvements have been made in the present work. The complete detailed equations for each solution will not be presented except in the cases where improvements have been made.

The basic aircraft to be analyzed in this study is shown in Fig. 28. It is composed of flat plates, cylinders, cones, and spheres. It is assumed that the source is mounted on the fuselage and restricted to the regions near the top or bottom of the aircraft. As is shown later in this discussion some of these restrictions and models are revised in order to obtain better approximate solutions for the desired pattern. In this way models are considered that approximate a wide variety of aircraft structures with the solutions derived in such a form that arbitrary antennas can be considered simply by integrating the equivalent aperture currents.

The lower frequency limit of these solutions is dictated by the ray optics format which requires that the various scattering bodies be no closer than approximately a wavelength with the overall aircraft being large in terms of the wavelength. The upper frequency limit is dictated by the model representation of the actual aircraft considered.

B. Roll Plane Analysis

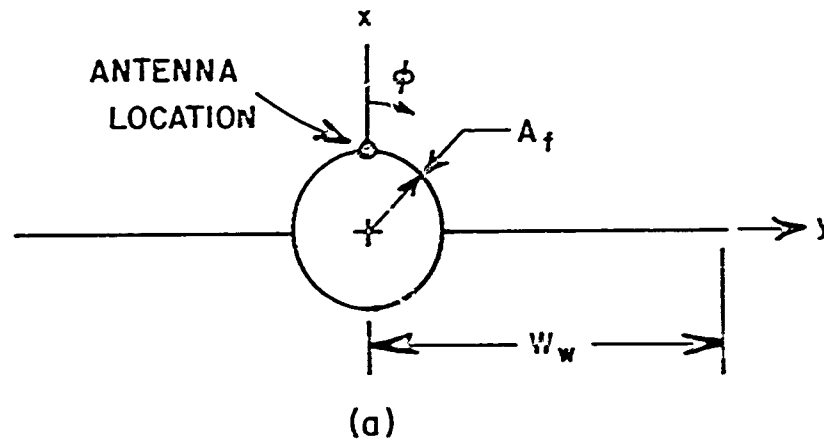
This section is a synopsis of the material presented in Ref. [47] along with recently developed improvements. The two-dimensional problem is considered initially in order to develop the necessary analytical tools to attack the much more difficult three-dimensional roll plane problem. The geometry of the two-dimensional problem is illustrated in Fig. 29 with and without the engines included. The fuselage and engines are assumed circular in cross-section and mounted symmetrically about the finite wing. Since wedge diffraction is applied to handle the finite length wing, the radiated field must



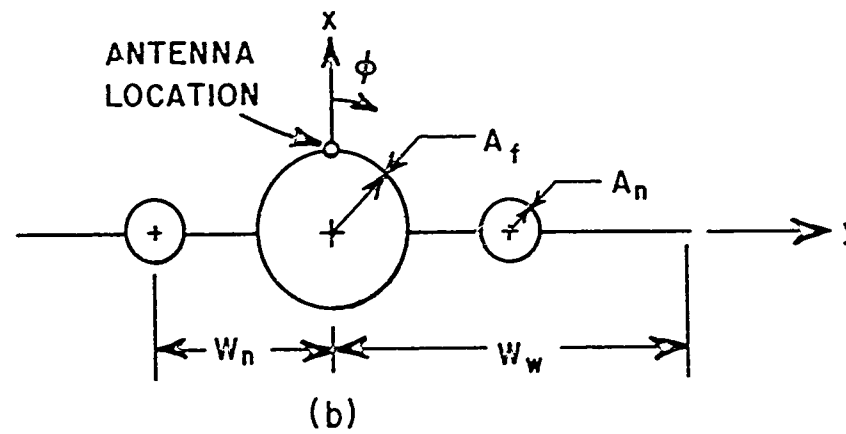
STATION

- 1-2 SPHERE
- 2-3 CIRCULAR CYLINDER
- 3-4 CONE
- 5 CIRCULAR CYLINDER
- 6 PLANAR CONDUCTOR
- 7 PLANAR CONDUCTOR

Fig. 28--Simplified aircraft model.



TWO DIMENSIONAL MODEL FOR THE ROLL PLANE W/O ENGINES.



TWO DIMENSIONAL MODEL FOR THE ROLL PLANE W/ ENGINES.

Fig. 29--Two-dimensional model for the roll plane.

be described in terms of rays. However, one of the nicer features of this approach is that other solutions such as modal solutions can be cast into a ray form and then applied to a diffraction problem. Consequently, it was found that the modal solutions (Eqs. (3) and (4)) for an arbitrary antenna mounted on an infinite circular cylinder was ideal for treating the antenna mounted on the fuselage. In fact, this solution has been applied in past years as the sole solution for high frequency on-aircraft antenna analyses.

Using image theory the wing reflections are analyzed using the geometry illustrated in Fig. 30. Note that due to the finite length wing the reflected field contributes only in a given region. The wedge diffraction solution is applied to include the effect of the wing tip. The field scattered by the engines is included using the modal solutions (Appendix I) for a near field source illuminating an infinitely long circular cylinder. In addition, a portion of the energy scattered by the engine is incident upon the wing tip which is included as a higher-order term. The phase of these various terms is then referenced to the center of the fuselage, and the terms summed to give the total radiated field. There were other higher-order terms considered in this study but found to be negligible so they are not included here or in the following numerical results. There are basically three infinitesimal sources considered in this analysis (monopole and axial and circumferential slots). These solutions allow for an arbitrary antenna to be considered using a numerical aperture integration as presented in Section II-B.

The radiation patterns for three finite sources are shown in Fig. 31 on a model without engines. The monopole is approximately $\lambda/4$ and the slots are simply open-ended X-band waveguides. These solutions compare very favorably with measured results taken on the two-dimensional aircraft model of Fig. 29. It is observed that the direct term from the antenna has the dominant effect on the pattern in the lit region. The reflected term adds the slowly varying ripple to the lit portion of the pattern. The scattering from the wing tips causes the rapidly varying backlobes in the pattern. The backlobes are not shown in these figures in that they were well below the noise level of our equipment and thus, the measured result was not accurate through that region. The radiation patterns for the same configurations with the engines added are illustrated in Fig. 32. Again very good agreement is obtained between our calculated and measured results. These results indicate that the scattering from the engines tend to smooth out the pattern by filling the nulls and lowering the peaks especially near $\phi = 90^\circ$ and 270° .

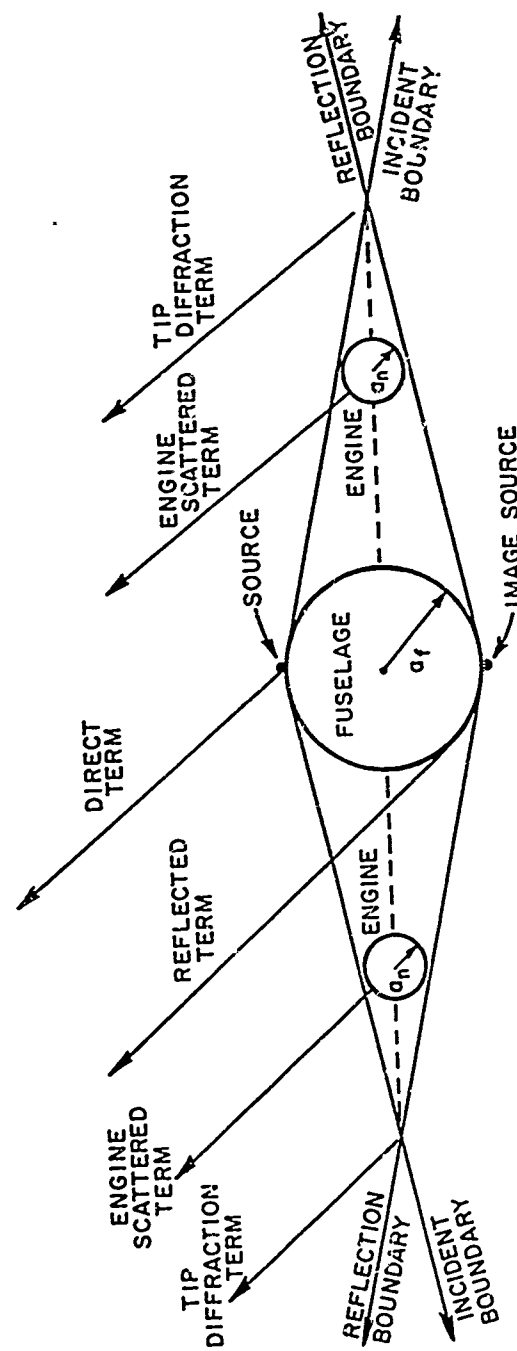


Fig. 30--Various scattering terms in two-dimensional problem.

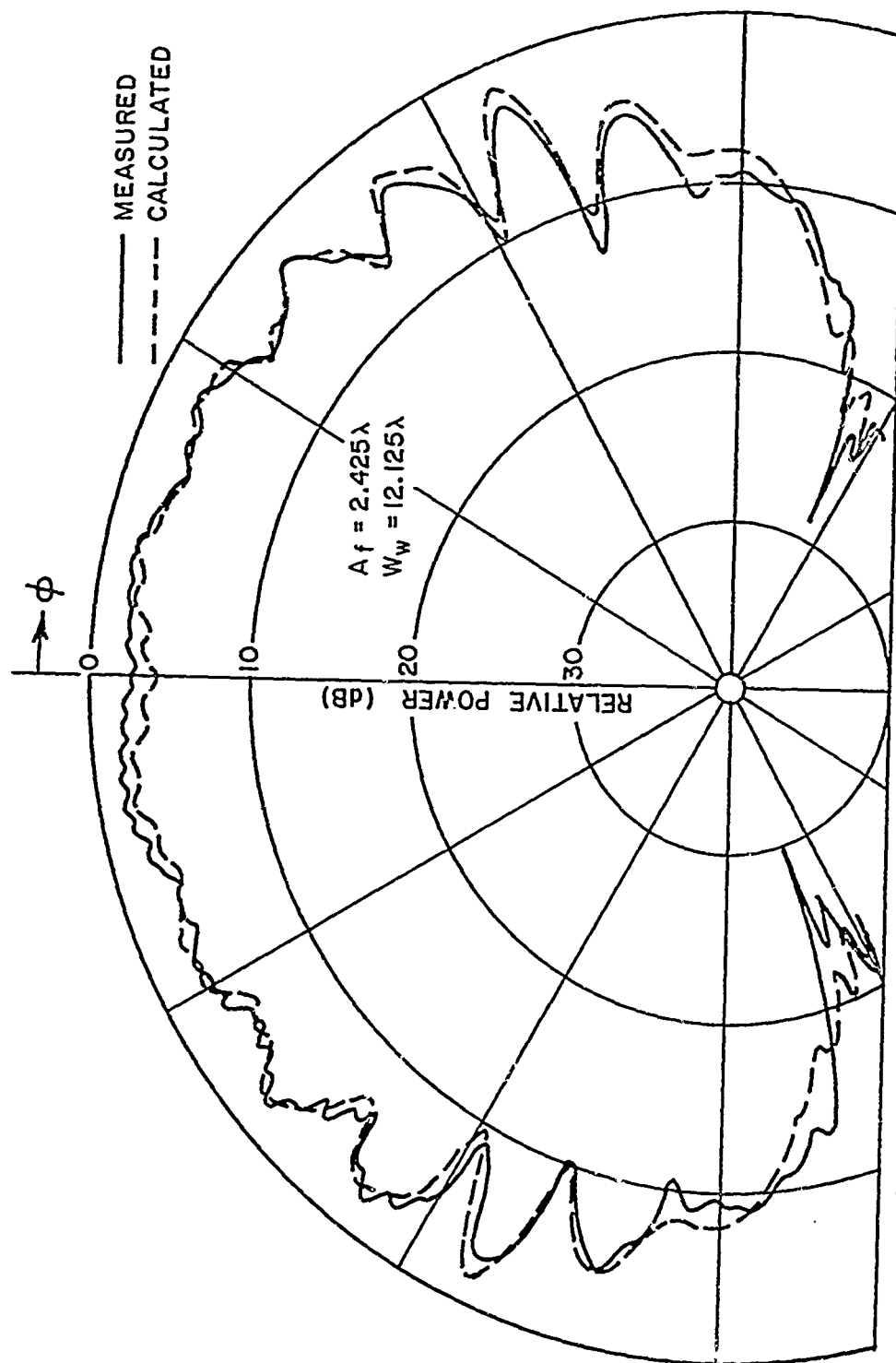


Fig. 31a--E_φ radiation pattern for an axial slot on a fuselage with finite length wing.

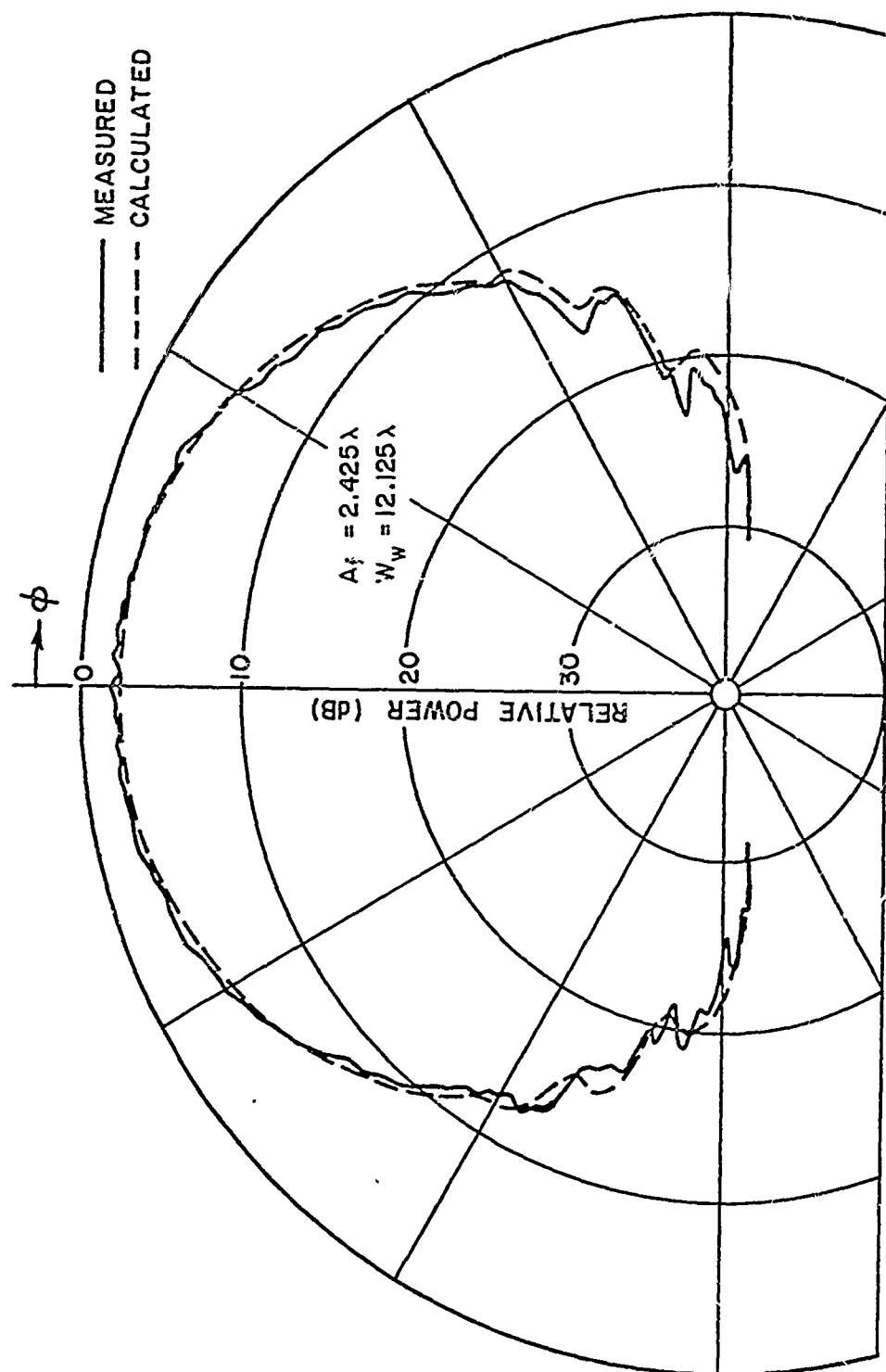


Fig. 31b-- E_θ radiation pattern for a circumferential slot on a fuselage with finite length wing.

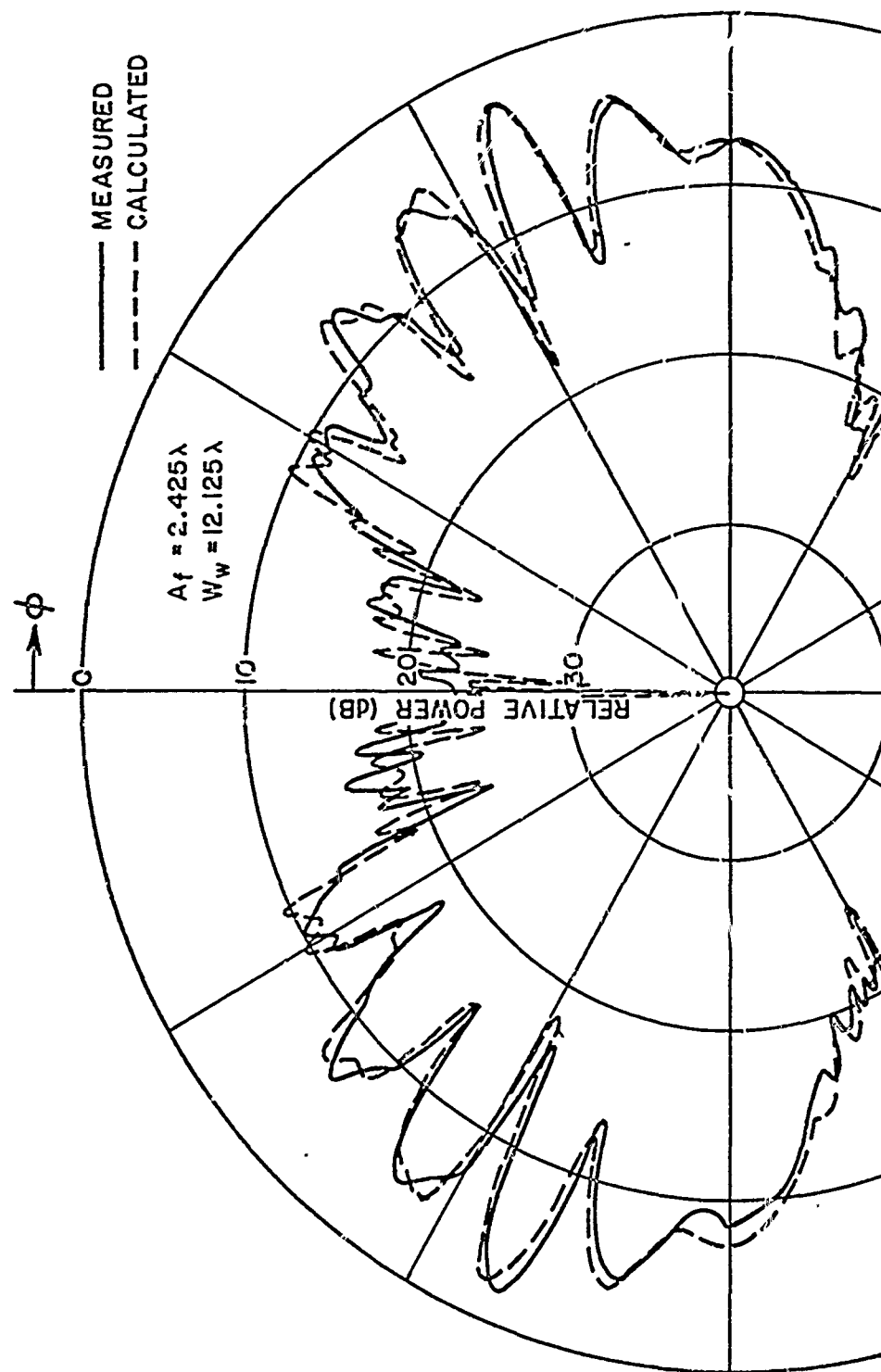


Fig. 31c-- E_ϕ radiation pattern for a $\lambda/4$ monopole on a fuselage with finite length wing.

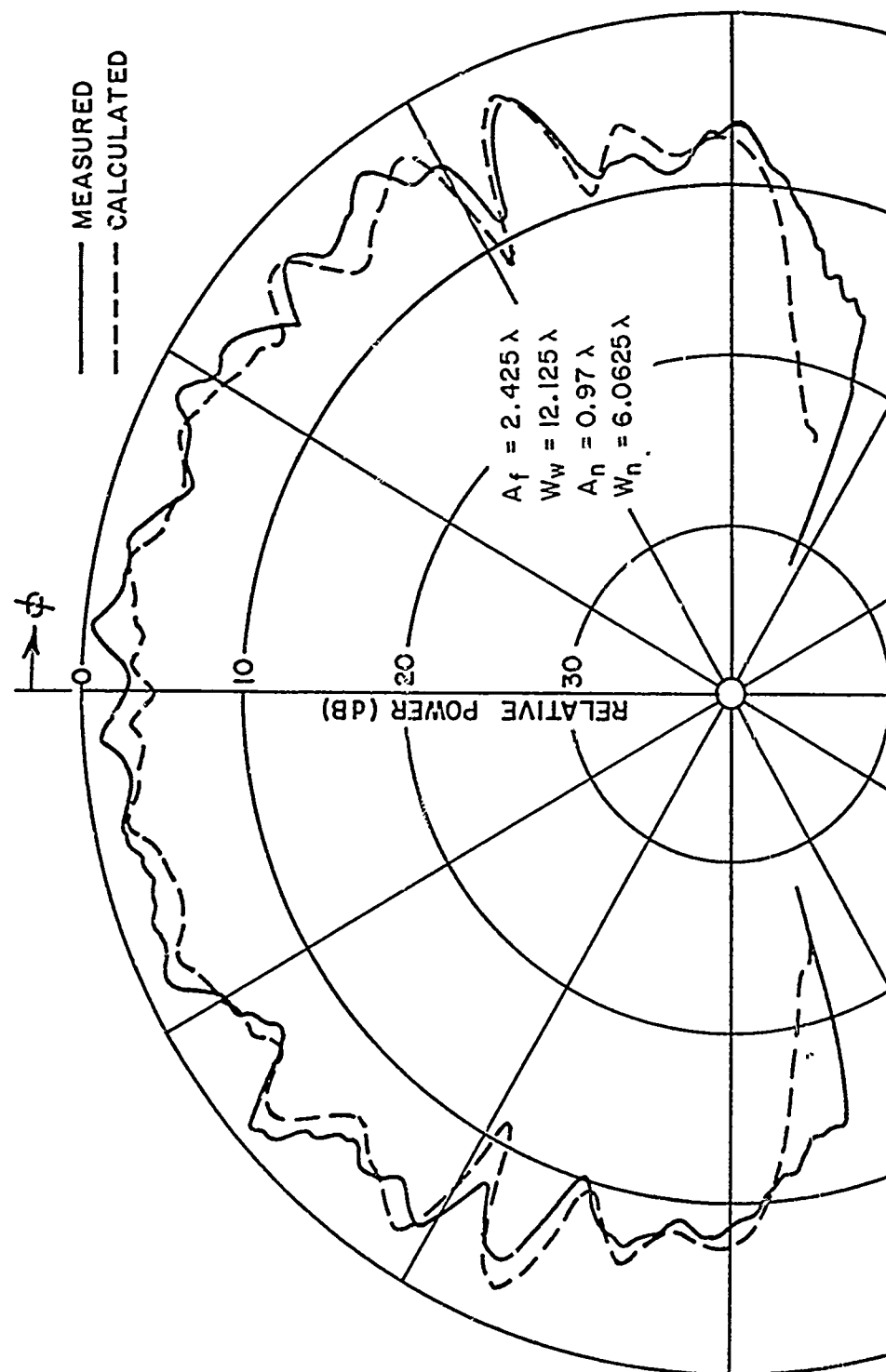


Fig. 32a-- E_ϕ radiation pattern for an axial slot on a fuselage with dominant engine and finite length wing.

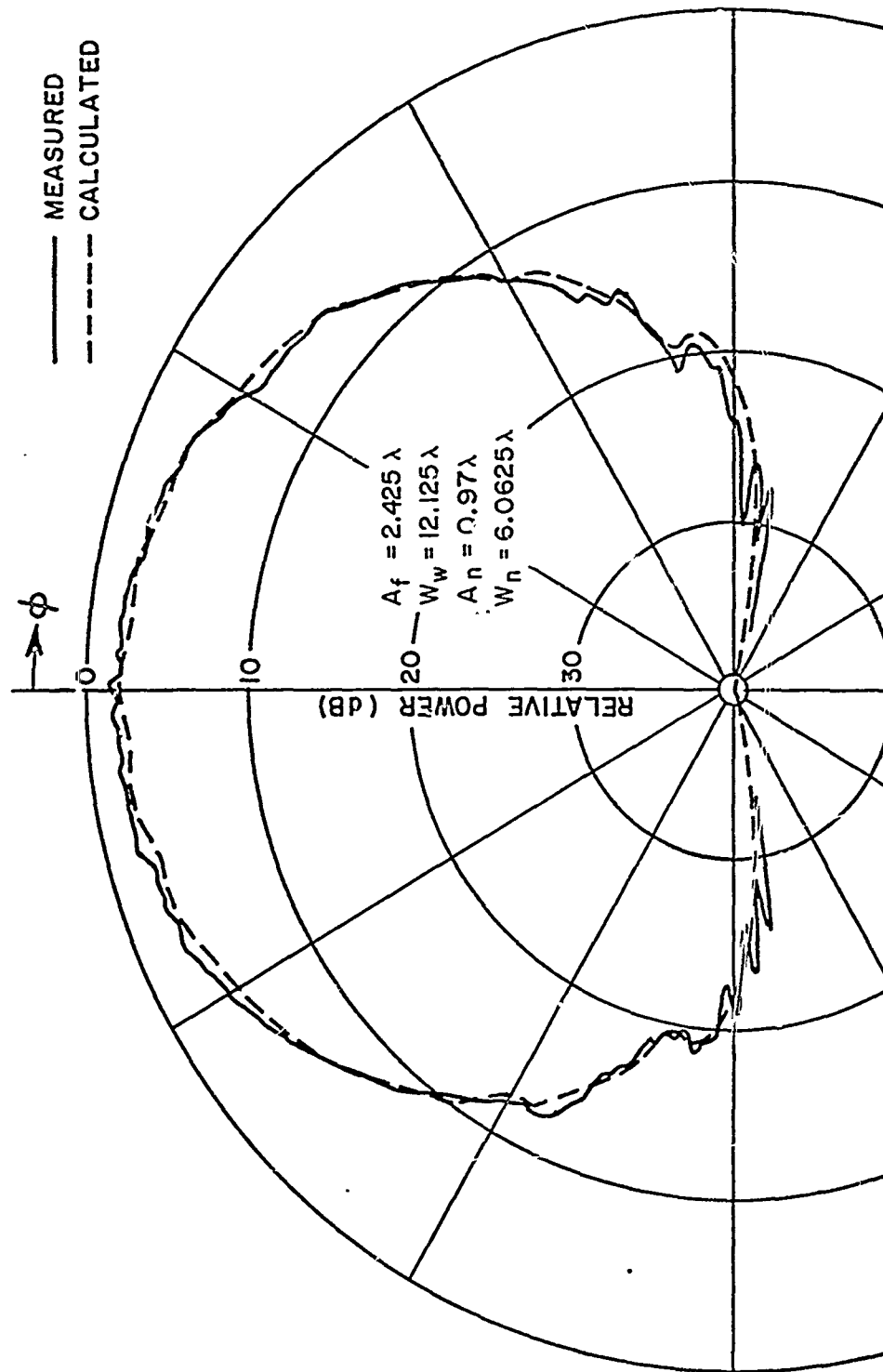


Fig. 32b-- E_θ radiation pattern for a circumferential slot on
with dominant engine and finite length wing.

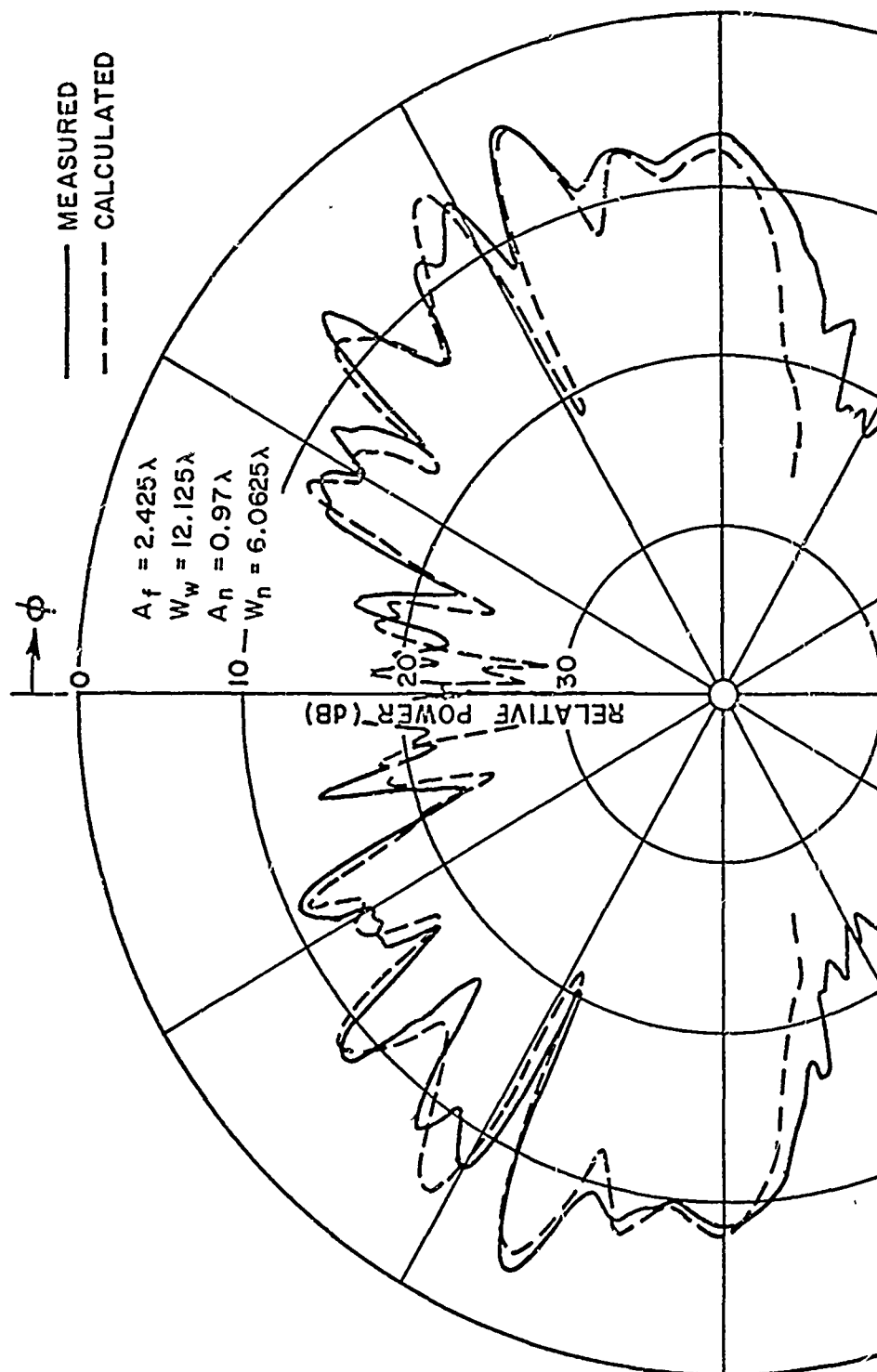


Fig. 32c-- E_θ radiation pattern for a $\lambda/4$ monopole on a fuselage with dominant engine and finite length wing.

Even though the two-dimensional solution should be more accurate in some cases than the previously used modal solutions which only models the fuselage, one must model the wing width as well as the length in order to make the solution really practical. In order to accomplish this feat, the near field flat plate scattering solution of Section III-B is adapted to this new model such as illustrated in Fig. 28. Note that each wing can be located arbitrarily with any number of edges provided only that the wings are flat and horizontal. The following discussion is presented with more detail in that selected improvements have been made over our previous solution as presented in Ref. [47].

Let us first find the effective source location for the reflected field. Recall that in our flat plate result the source was imaged and the reflected field added to the total solution provided the image ray passed through the finite flat plate (wing) limits. So one must initially determine the effective source position which in turn results in giving the desired reflected field. With the source mounted on an infinitely long circular cylinder one can easily show that the surface rays from the source propagate around the cylinder on helical paths (geodesics), which in turn diffract energy tangentially. Now let us assume that the source does not illuminate the right wing directly (as illustrated in Fig. 33) and proceed to determine the unique helical path that diffracts energy from a known tangent point which is then reflected off the wing in the desired radiation (or scatter) direction. This helical path can be specified in general by

$$x = a_f \cos \phi$$

$$y = a_f \sin \phi$$

$$z = b(\phi - \phi_{s0}) + z_{s0}$$

where $(a_f, \theta_{s0}, z_{s0})$ defines the actual source location on the fuselage. Let the desired radiation direction be given by (θ_s, ϕ_s) . Then using Fig. 33a one finds that the tangent direction at the effective source location is defined by

$$\left. \frac{dx}{d\phi} \right|_{(x_e, y_e, z_e)} = -a \sin \phi_e$$

$$\left. \frac{dy}{d\phi} \right|_{(x_e, y_e, z_e)} = a \cos \phi_e$$

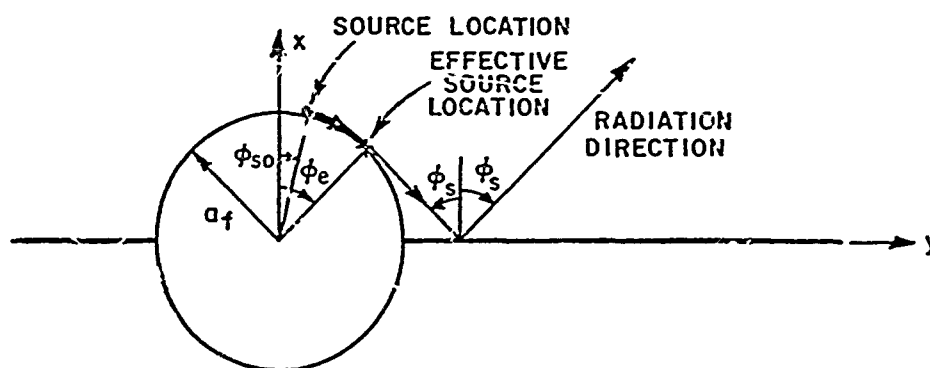


Fig. 33a--Reflection problem in x-y plane.

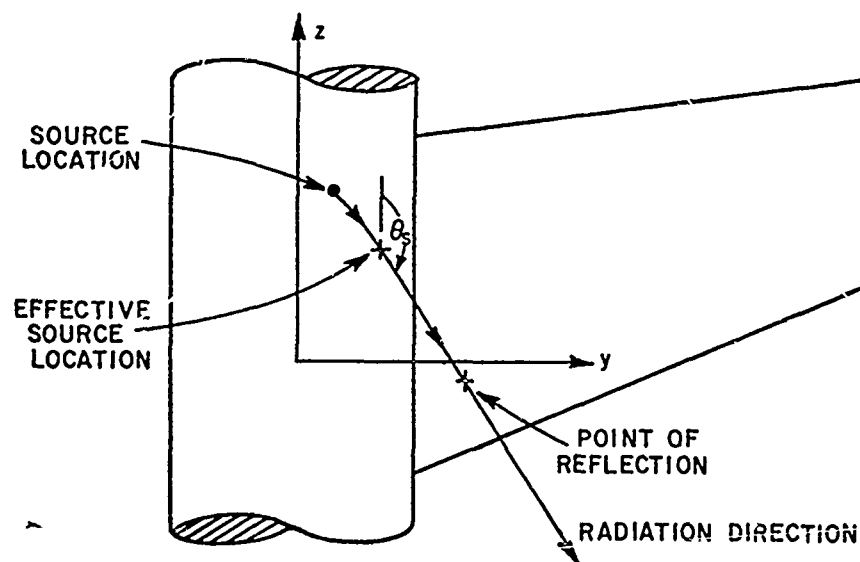


Fig. 33b--Reflection problem in y-z plane.

or

$$\left. \frac{dy}{dx} \right|_{(x_e, y_e, z_e)} = -\cot \phi_e = -\cot(90^\circ - \phi_s)$$

which result in $\phi_e = 90^\circ - \phi_s$. Using Fig. 33b the tangent direction is given by

$$\left. \frac{dz}{d\phi} \right|_{(x_e, y_e, z_e)} = b$$

$$\left. \frac{dy}{d\phi} \right|_{(x_e, y_e, z_e)} = a_f \cos \phi_e$$

or

$$\frac{dz}{dy} = \frac{b}{a_f \cos \phi_e} = \tan(90^\circ - \theta_s)$$

which gives $b = a_f \cos \phi_e \tan(90^\circ - \theta_s)$. The above equations uniquely specify the effective source position for reflections from the right wing in terms of the given radiation direction by

$$\begin{aligned} x_e &= a_f \cos(90^\circ - \phi_s) \\ (76) \quad y_e &= a_f \sin(90^\circ - \phi_s) \\ z_e &= a_f \cos(90^\circ - \phi_s) \tan(90^\circ - \theta_s) (\pi/2 - \phi_s - \phi_0) + z_{s0} \end{aligned}$$

which in turn can be used in the flat plate problem as the effective source location. Note that as the desired radiation direction is varied the effective source location changes. In addition, if the source directly illuminates the wing for a given reflection term then the effective source location is simply the actual source location. A result similar to Eq. (76) can be found for the reflections from the left wing. Finally, the actual source field value used to compute the reflected term is determined from the modal solutions of Appendix I.

Using a similar technique the effective source locations for the diffracted field components must be found. Recall that our flat plate solution used a search technique to find the diffraction point by computing the diffraction angles at selected test points along a given edge. Once a test point (x_d, y_d, z_d) is specified along the edge one

can find the effective source location (x_e, y_e, z_e) using the geometry illustrated in Fig. 34. Again it is assumed that the source does not directly illuminate the test point. Using Fig. 34a one finds that the tangent direction at the effective source is given by

$$\left. \frac{dx}{dz} \right|_{(x_e, y_e, z_e)} = -a_f \sin \tau_e = -y_e$$

$$\left. \frac{dy}{dz} \right|_{(x_e, y_e, z_e)} = a_f \cos \tau_e = x_e$$

or

$$\left. \frac{dx}{dy} \right|_{(x_e, y_e, z_e)} = \frac{(x_d - x_e)}{(y_d - y_e)} = -\frac{y_e}{x_e}$$

which gives $\frac{2}{x_e^2} = x_e^2 + y_e^2$ and $a_f^2 = x_e x_d + y_e y_d$. The value of (b) of the helical path on the cylindrical surface is defined using Fig. 34b by

$$\left. \frac{dz}{d\phi} \right|_{(x_e, y_e, z_e)} = b$$

$$\left. \frac{dy}{d\phi} \right|_{(x_e, y_e, z_e)} = a_f \cos \phi_e = x_e$$

or

$$\left. \frac{dz}{dy} \right|_{(x_e, y_e, z_e)} = \frac{b}{x_e} = \frac{z_d - z_e}{y_d - y_e}$$

which gives $b = x_e \left(\frac{z_d - z_e}{y_d - y_e} \right)$. Using the above relations one finds that for the wing on the right side the effective source location for the test diffraction point is given by

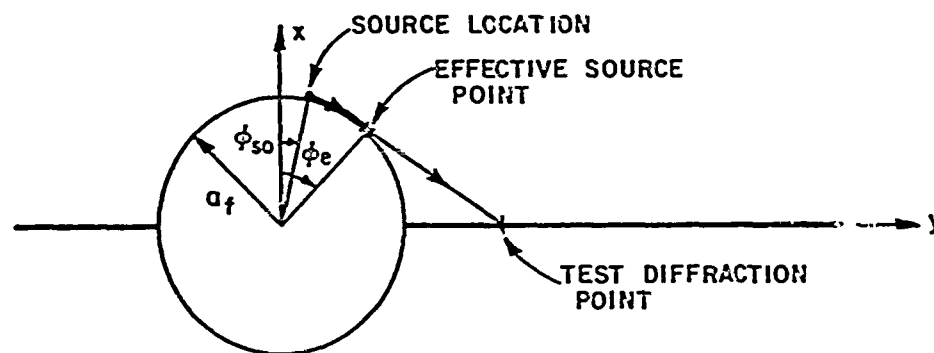


Fig. 34a--Diffraction problem in x-y plane.

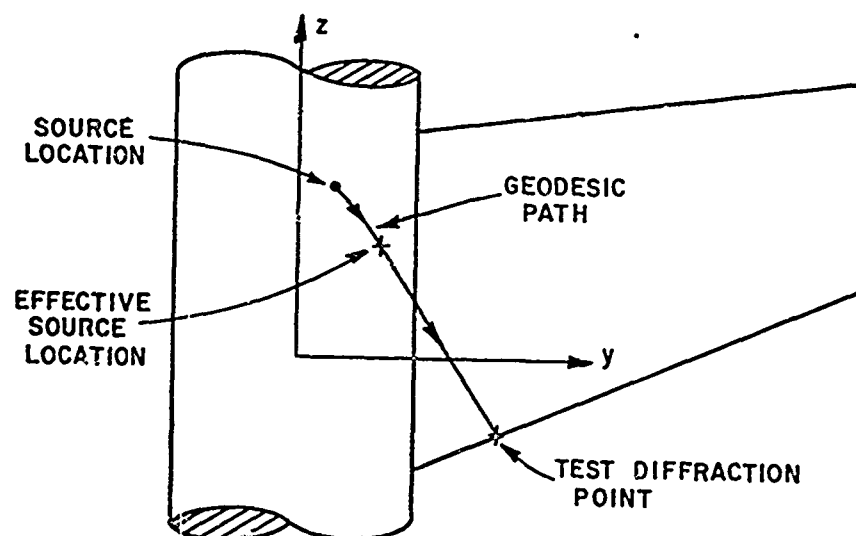


Fig. 34b--Diffraction problem in y-z plane.

$$\begin{aligned}
 x_e &= \frac{a_f}{(x_d^2 + y_d^2)} \left[a_f x_d + y_d \sqrt{y_d^2 + x_d^2 - a_f^2} \right] \\
 (77) \quad y_e &= \frac{a_f}{(x_d^2 + y_d^2)} \left[a_f y_d - x_d \sqrt{y_d^2 + x_d^2 - a_f^2} \right] \\
 z_e &= \frac{x_e z_d (\phi_e - \phi_{so}) + z_{so} (y_d - y_e)}{x_e (\phi_e - \phi_{so}) + (y_d - y_e)}
 \end{aligned}$$

where $\phi_e = \tan^{-1} \left(\frac{y_e}{x_e} \right)$. Given the effective source location for the chosen test point, the search technique of Section III-B is applied to find the actual diffraction point along a given edge. Note that once the actual diffraction point is determined, the effective source of the diffracted field is specified by Eq. (77), and the source field value is, again, computed using the modal solutions.

The total field is found by summing the directly radiated field with the scattered fields from the wings using the superposition principle. Several different configurations have been tested using this solution and compared with measured results. The roll plane radiation patterns for the three infinitesimal sources are shown in Fig. 35, when the antennas are mounted directly above the wings. The patterns are shown in Fig. 36 when the antennas are mounted on the fuselage over the back limit of the wing. In Fig. 37 the patterns are shown when the antennas are mounted over the wings but rotated 45° from the straight up direction. Only the monopole is considered for measured comparisons since it was the only source available at the time. In each of these cases, one can note the good agreement obtained between the calculated and measured results. The slight deviations being attributed to the assumptions made in solving the flat plate problem of Section III-B. For example, the jump in the calculated result of Fig. 36 near $\phi = 90^\circ$ and 270° can be attributed to the lack of doubly diffracted terms in the solution.

It was originally assumed in the aircraft model of Fig. 28 that the wings were attached such that they were contained in the horizontal plane which also contains the axis of the fuselage. This meant that no diffractions occurred from the junction edge in that image theory could be applied to handle the cylinder/plate junction problem. This is not the case when the wing is moved away from this location.

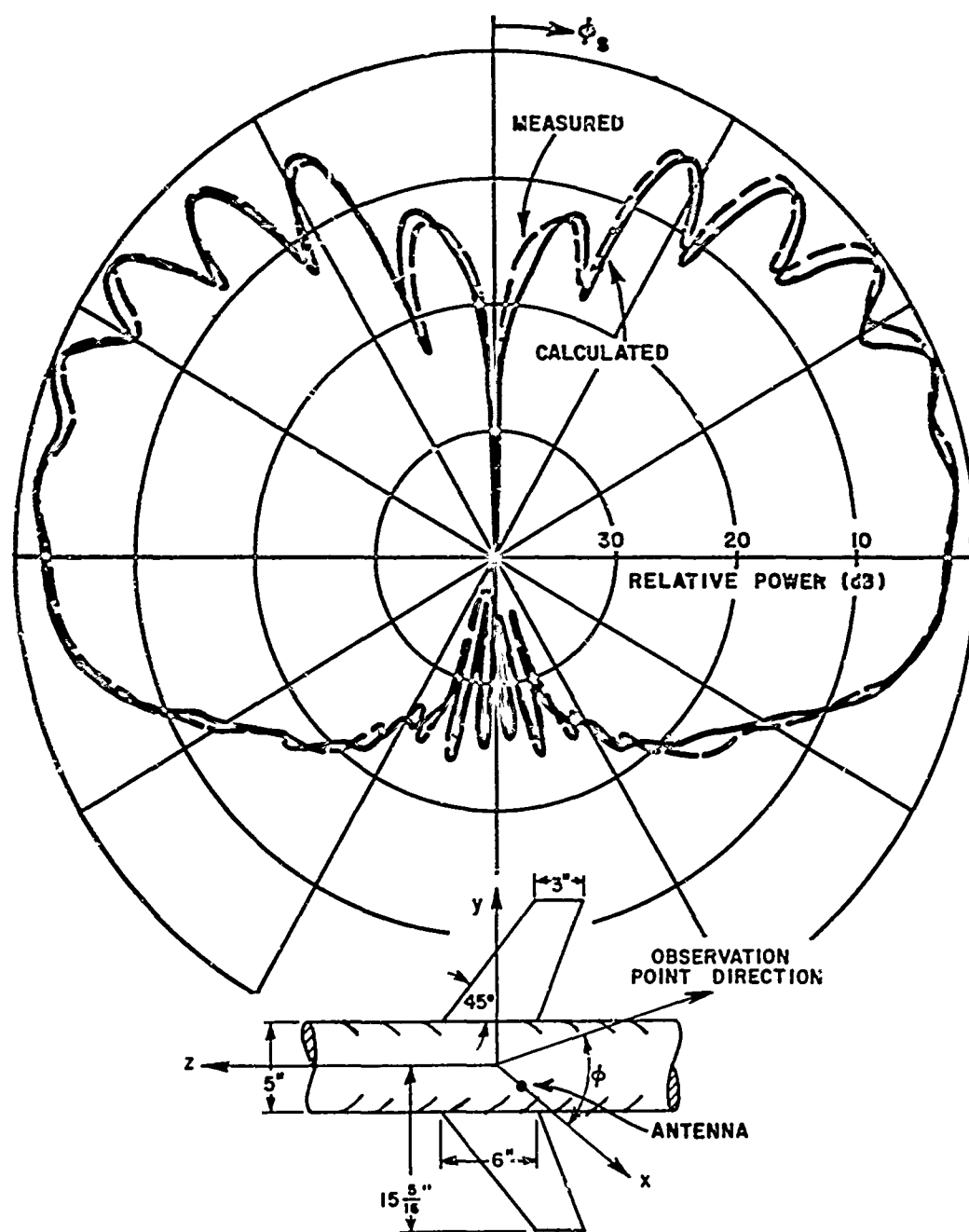


Fig. 35a--Roll plane pattern of monopole (E_ϕ).

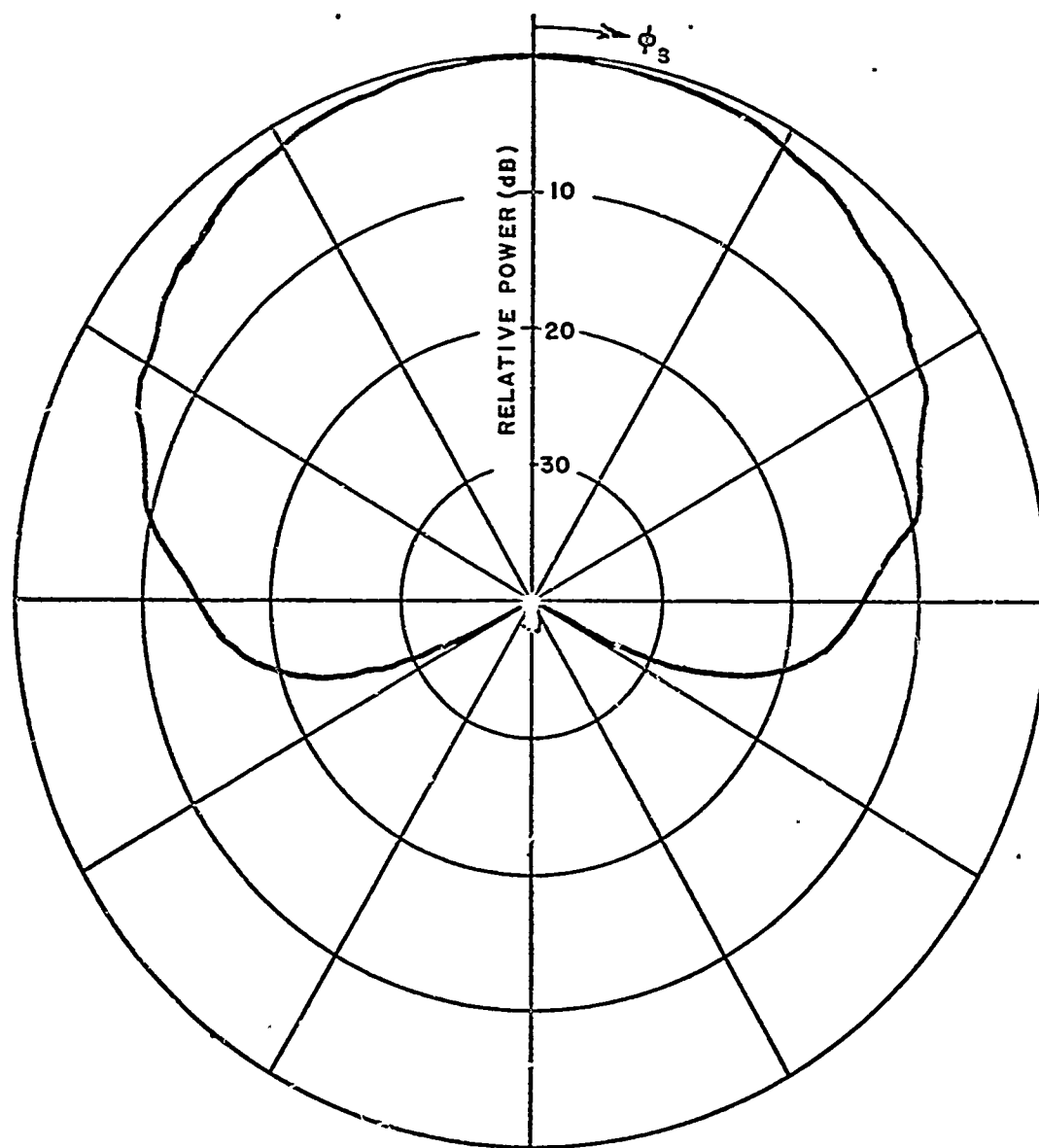


Fig. 35b--Roll plane pattern of circumferential slot (E_θ).

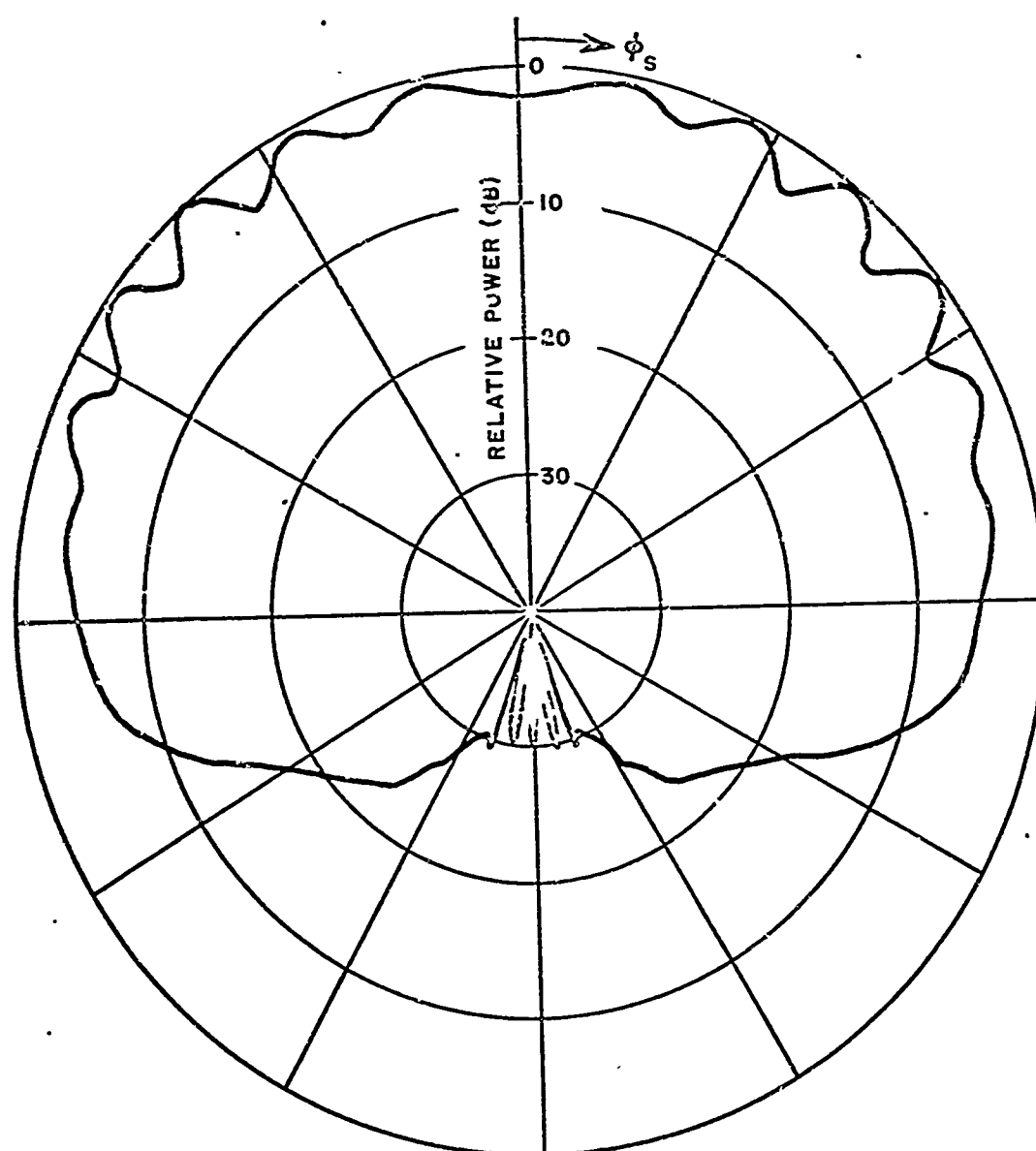


Fig. 35c--Roll plane pattern of axial slot (E_ϕ).

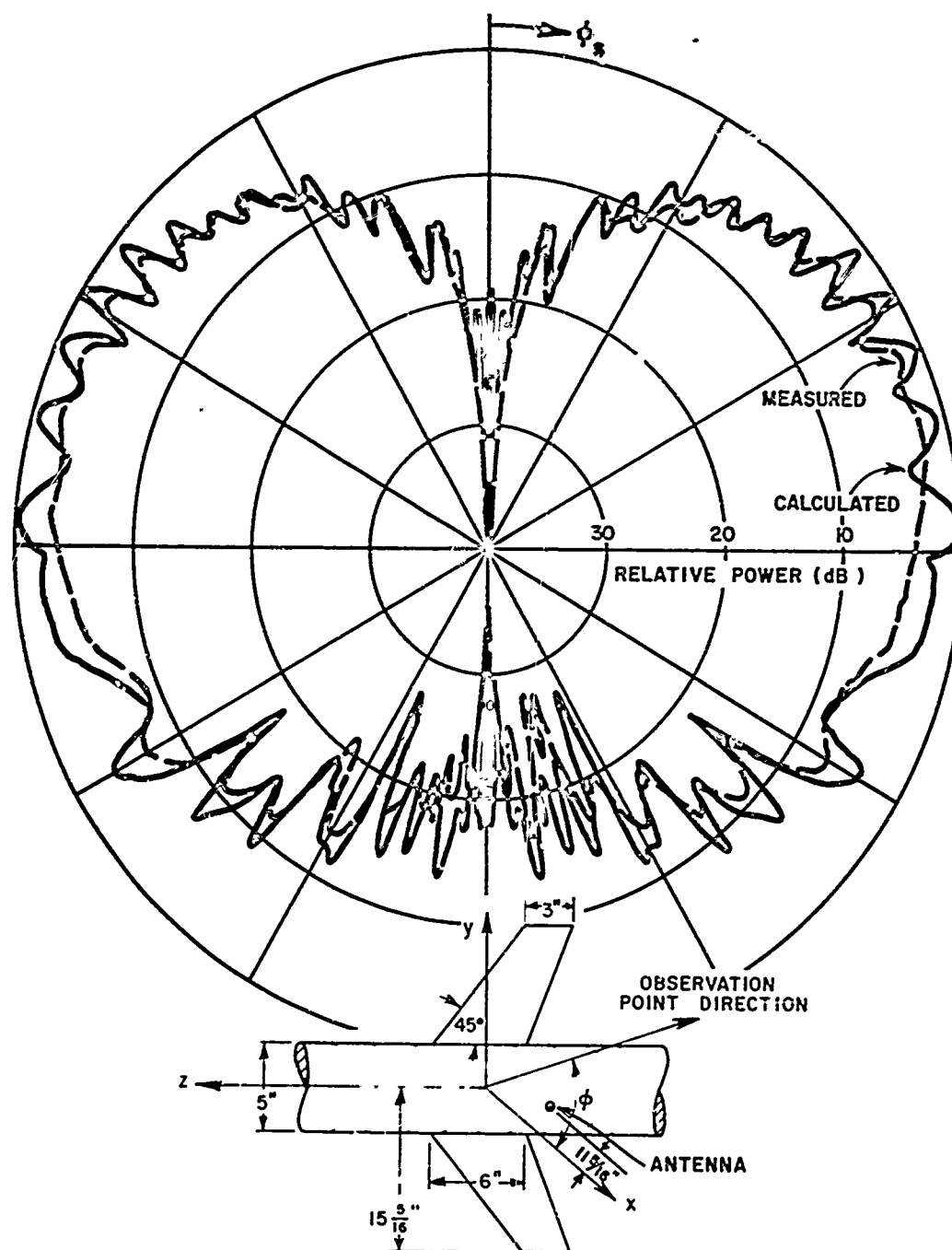


Fig. 36a--Roll plane pattern of monopole (E_ϕ).

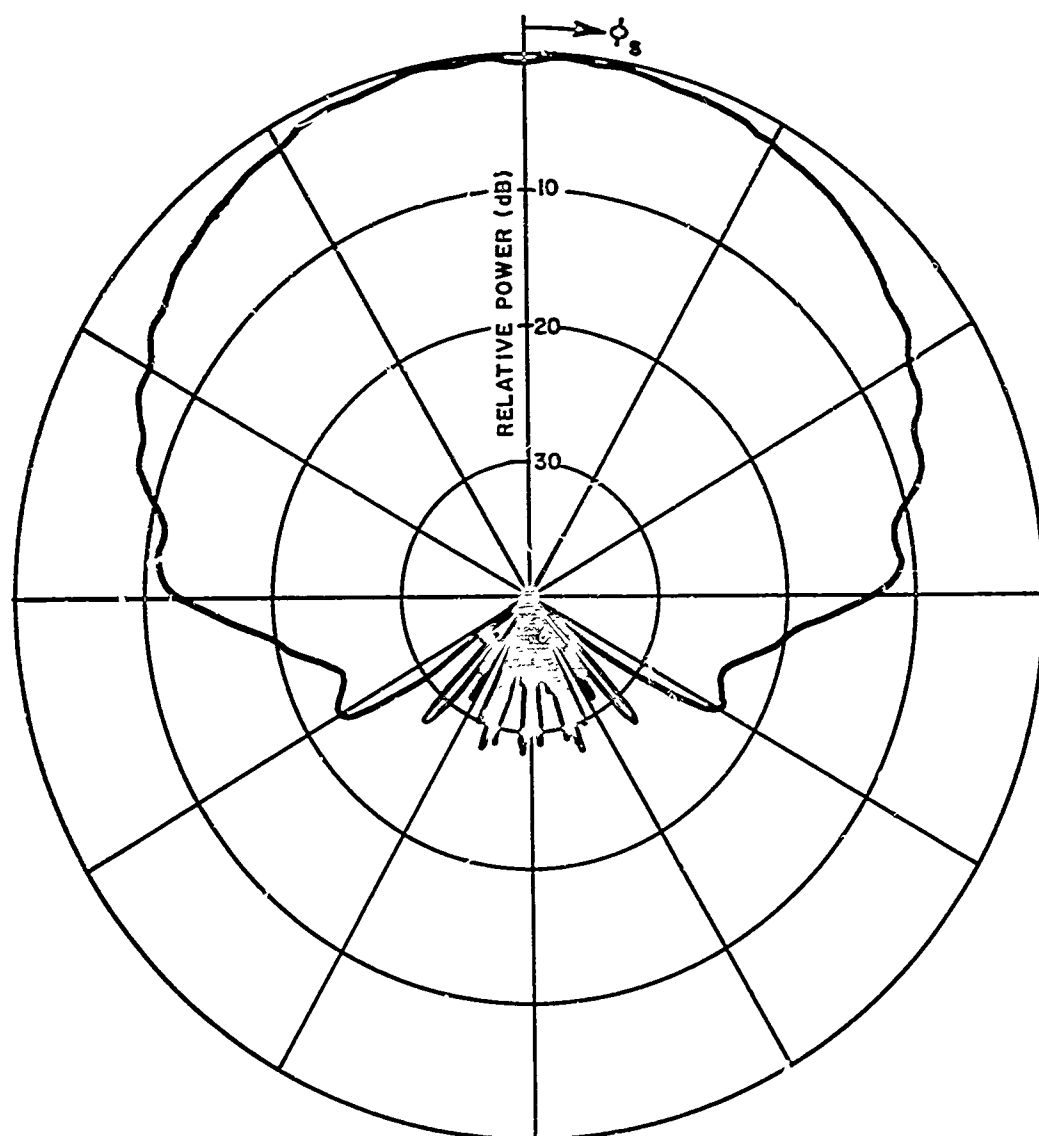


Fig. 36b--Roll plane pattern of circumferential slot (E_θ).

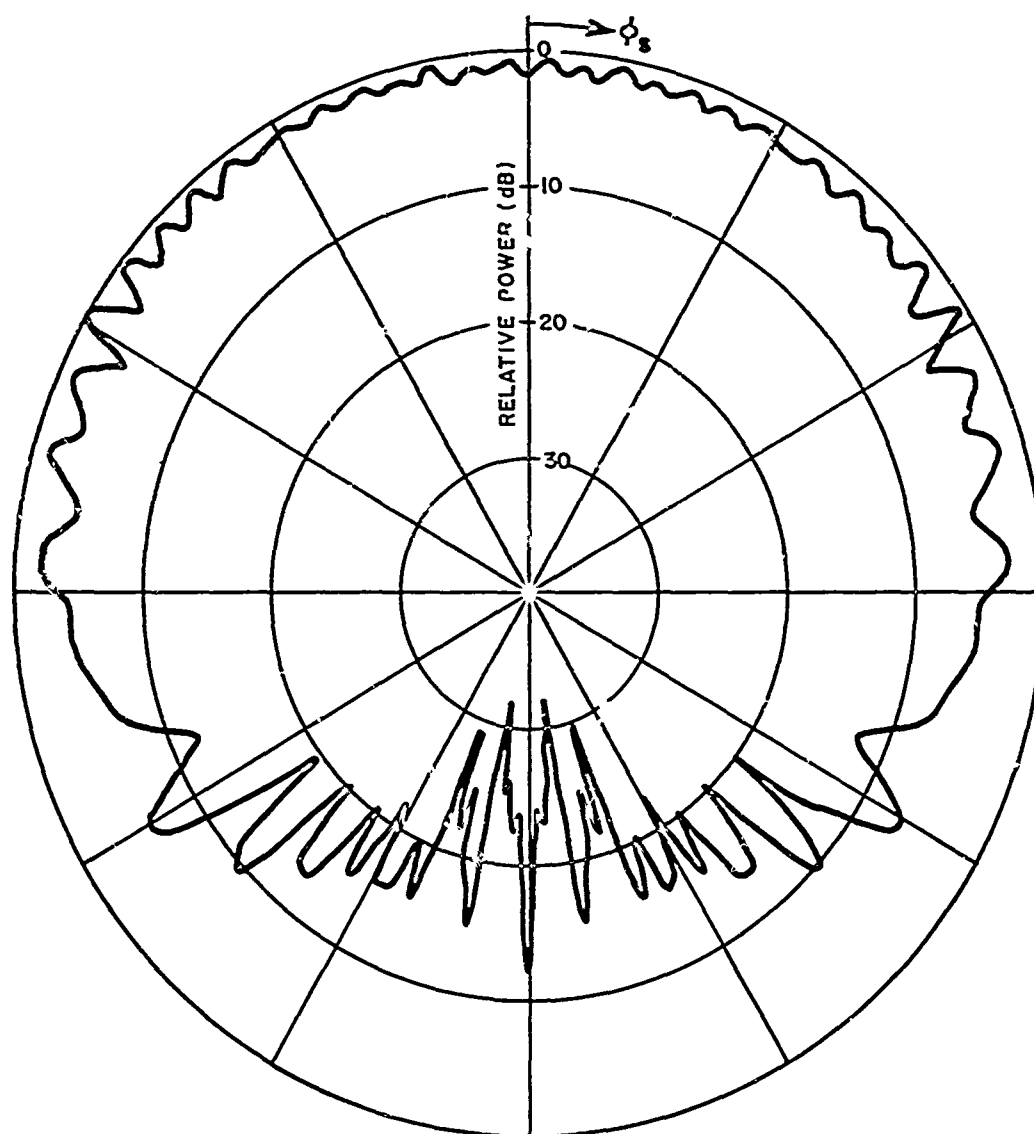


Fig. 36c--Roll plane pattern of axial slot (E_ϕ).

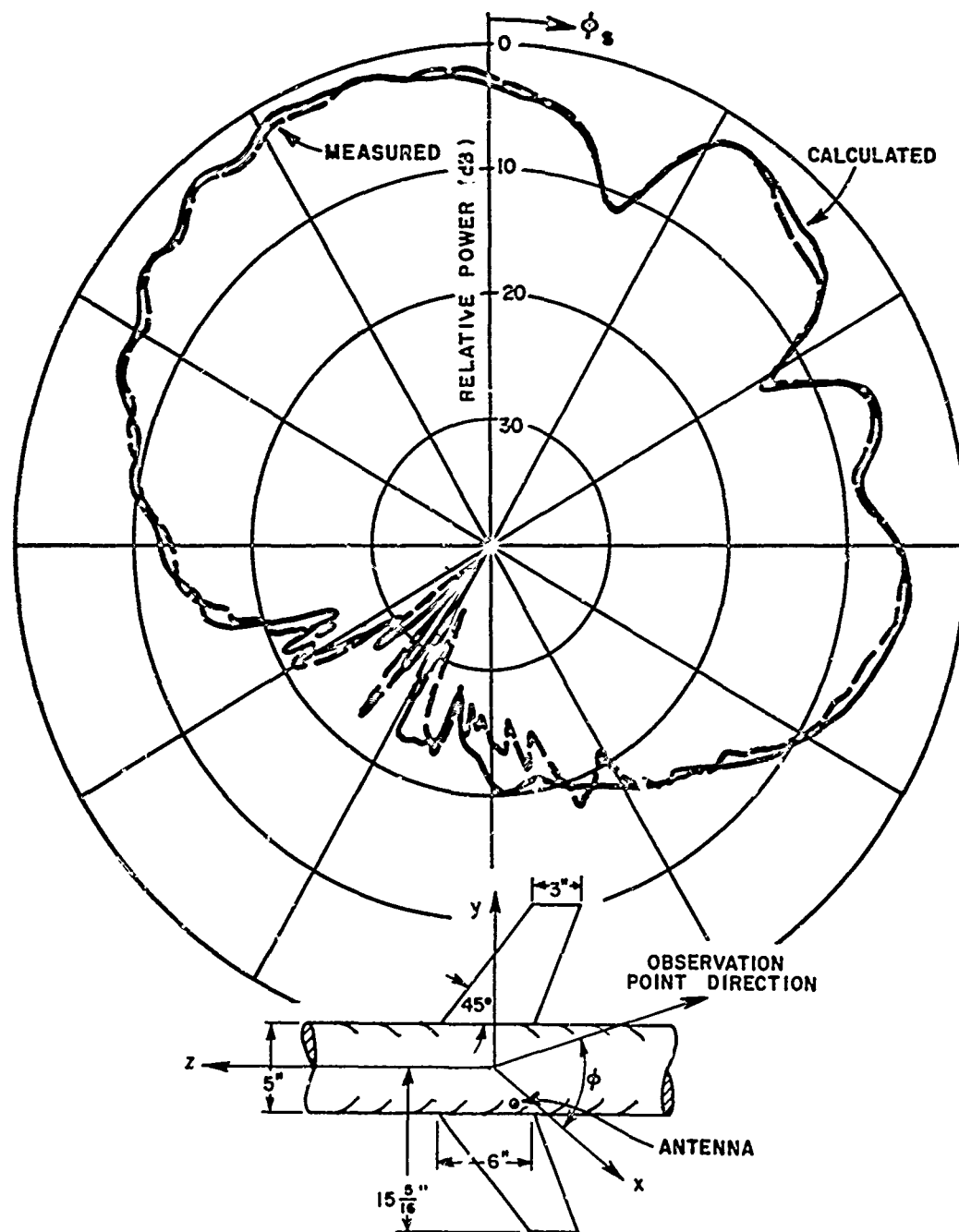


Fig. 37a--Roll plane pattern of monopole (E_ϕ).

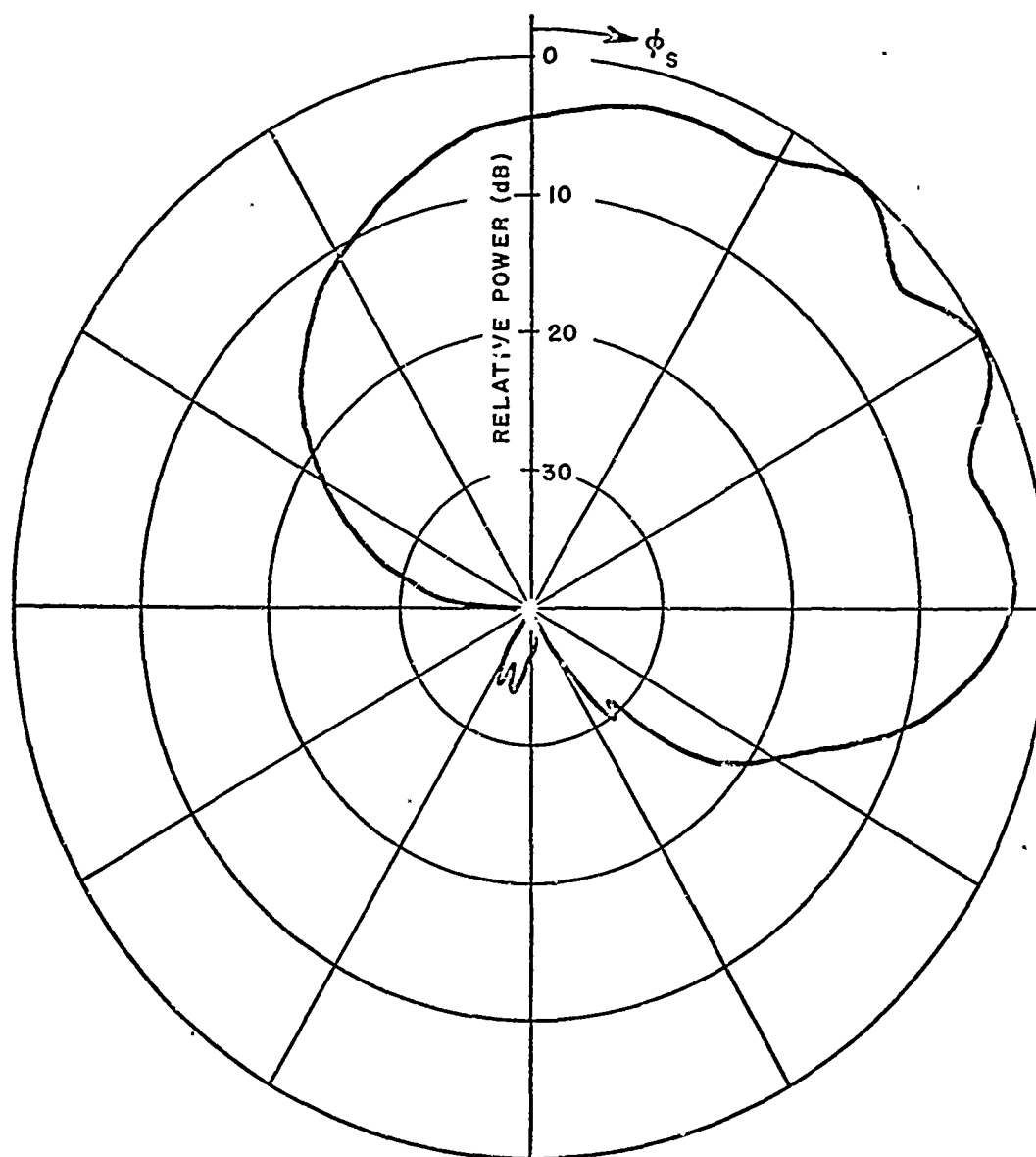


Fig. 37b--Roll plane pattern of circumferential slot (E_θ).

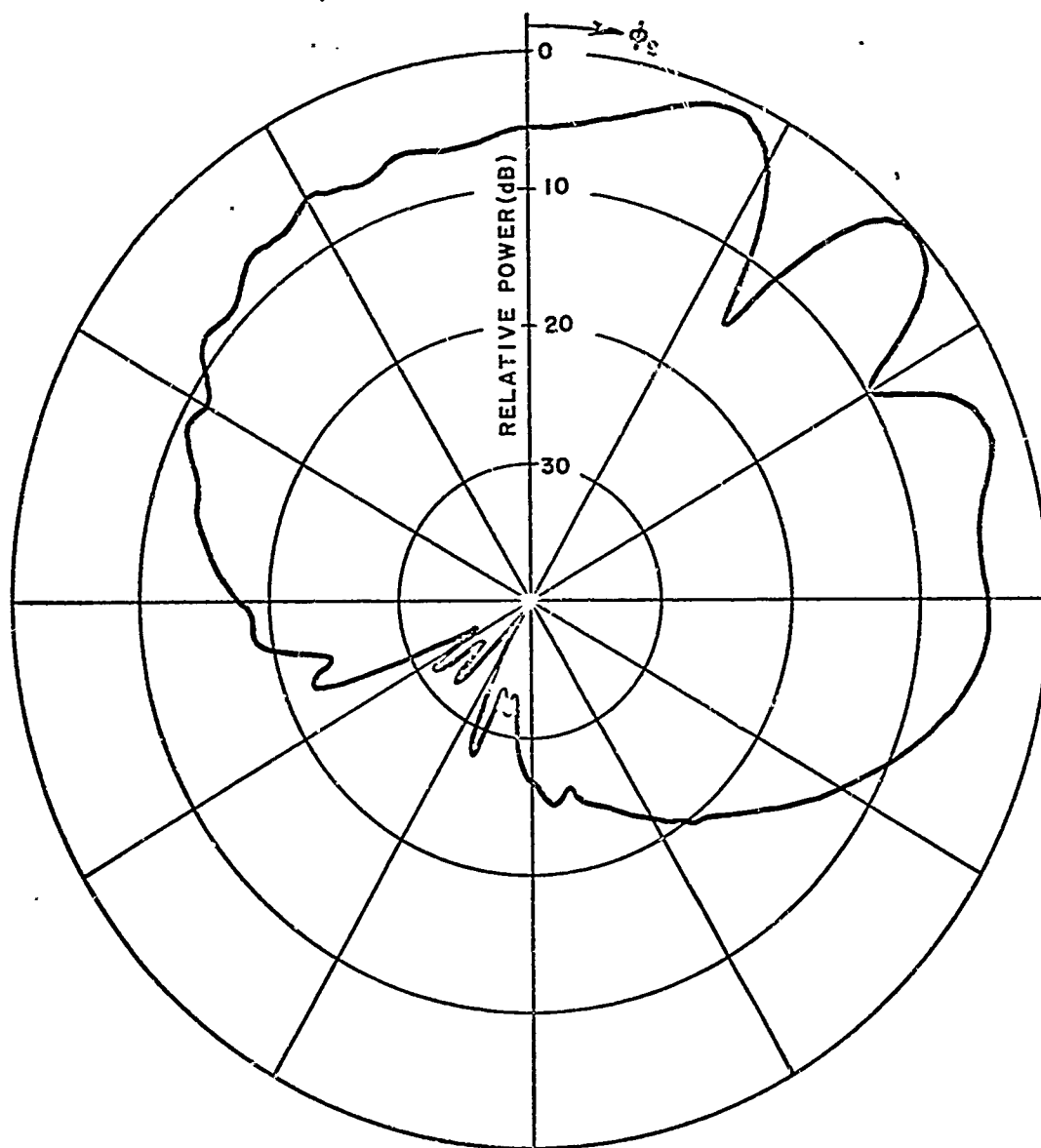


Fig. 37c--Roll plane pattern of axial slot (E_ϕ).

However, in order to make this solution even more practical one must be able to move the wing from its former central position. As a result, a technique has been developed to handle the case with the wing mounted above the central position or closer to the source location. Again the flat plate analysis of Section III-B is applied but in this case the edge formed by the junction of the wing and fuselage must be included. This is done by including the diffraction from the interior wedge illustrated in Fig. 38. Note that once the diffraction point is known only the wedge angle (which is defined by "n" in the diffraction function) is changed from the previous solution. In this case the effective source is found by using the helical path solution for the surface rays on the fuselage except now the path intersects the edge formed by the fuselage-wing junction. The tangent direction of the path at that point gives the incident field direction with the effective source location for the diffracted field calculation being shown in Fig. 38. Note again that the incident field values are actually given by the modal solutions of Section II-B. However, in this case the field is incident along the surface of the wedge; thus, the incident field for the diffracted field solution from this edge must be one half the value given by the modal solution as discussed in Ref. [49]. In Fig. 39 the radiation patterns for the three infinitesimal sources are shown with the wings moved up such that $\phi_w = 45^\circ$ as shown in Fig. 38. The validity of this solution is verified by the measured result taken for the monopole case of Fig. 39a.

Even though the previous results look good in comparison with the measured results, several improvements in the solution could be made. For example, it was assumed that the fuselage is an infinitely long cylindrical structure. This can be improved by including the three-dimensional effects of the fuselage as introduced in the following chapter. Nevertheless, based on data taken at the Naval Air Development Center the circular shaped fuselage appears to be adequate for present needs. Other possible changes that might be considered are tilting the wings, mounting the antenna off the fuselage, introducing other possible scattering structures in the analysis, etc.

C. Elevation Plane Analysis

This section is basically a synopsis of the material presented in Ref. [48]. It is presented here to illustrate the validity of the GTD approach for treating antennas mounted on a convex two-dimensional body. Note that this material is an essential step in determining the volumetric pattern of an antenna mounted on a three-dimensional surface as considered in the next chapter.

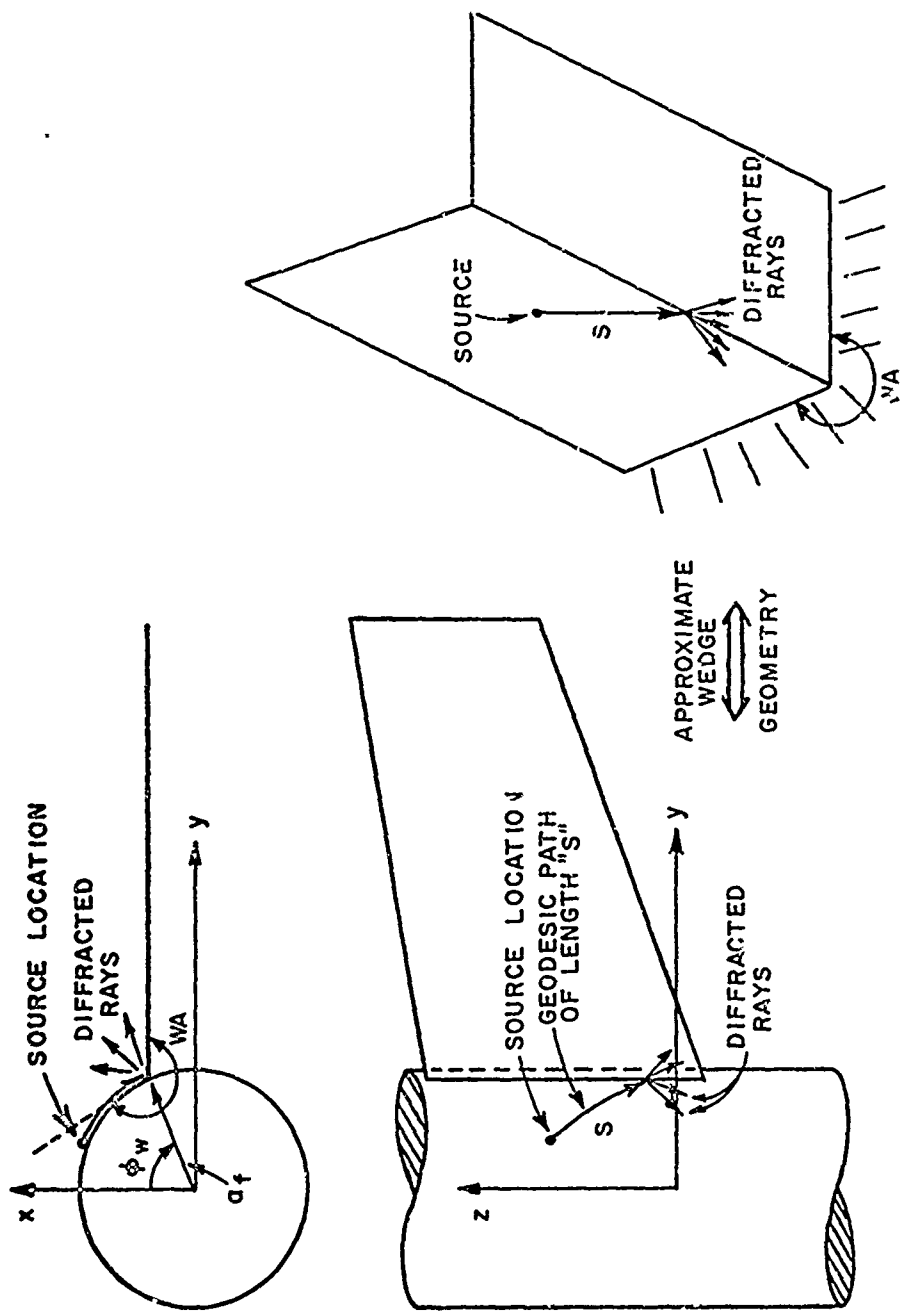


Fig. 38--Geometry used to find junction edge diffracted fields.

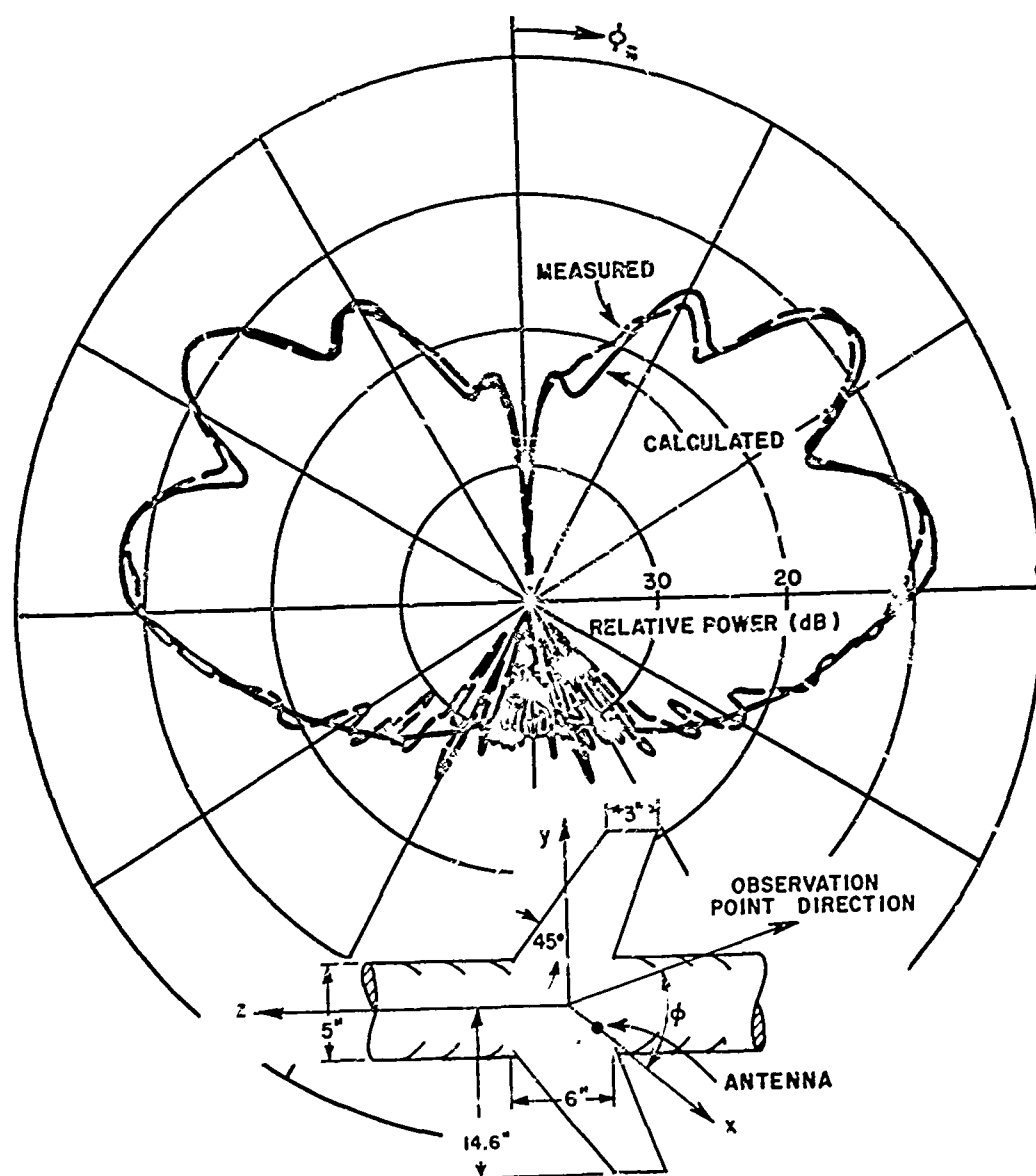


Fig. 39a--Roll plane pattern of monopole (E_{ϕ}).

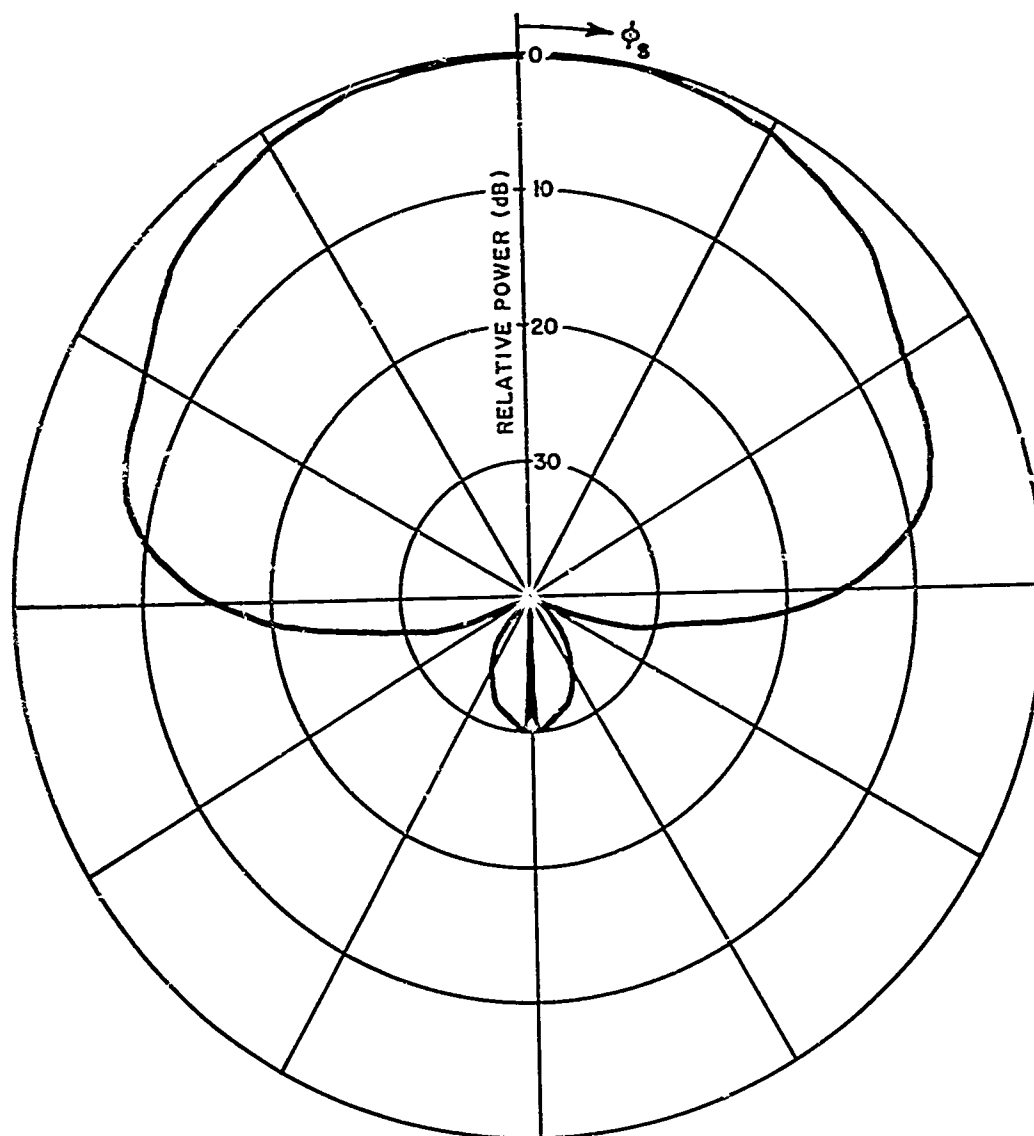


Fig. 39b--Roll plane pattern of circumferential slot (E_θ).

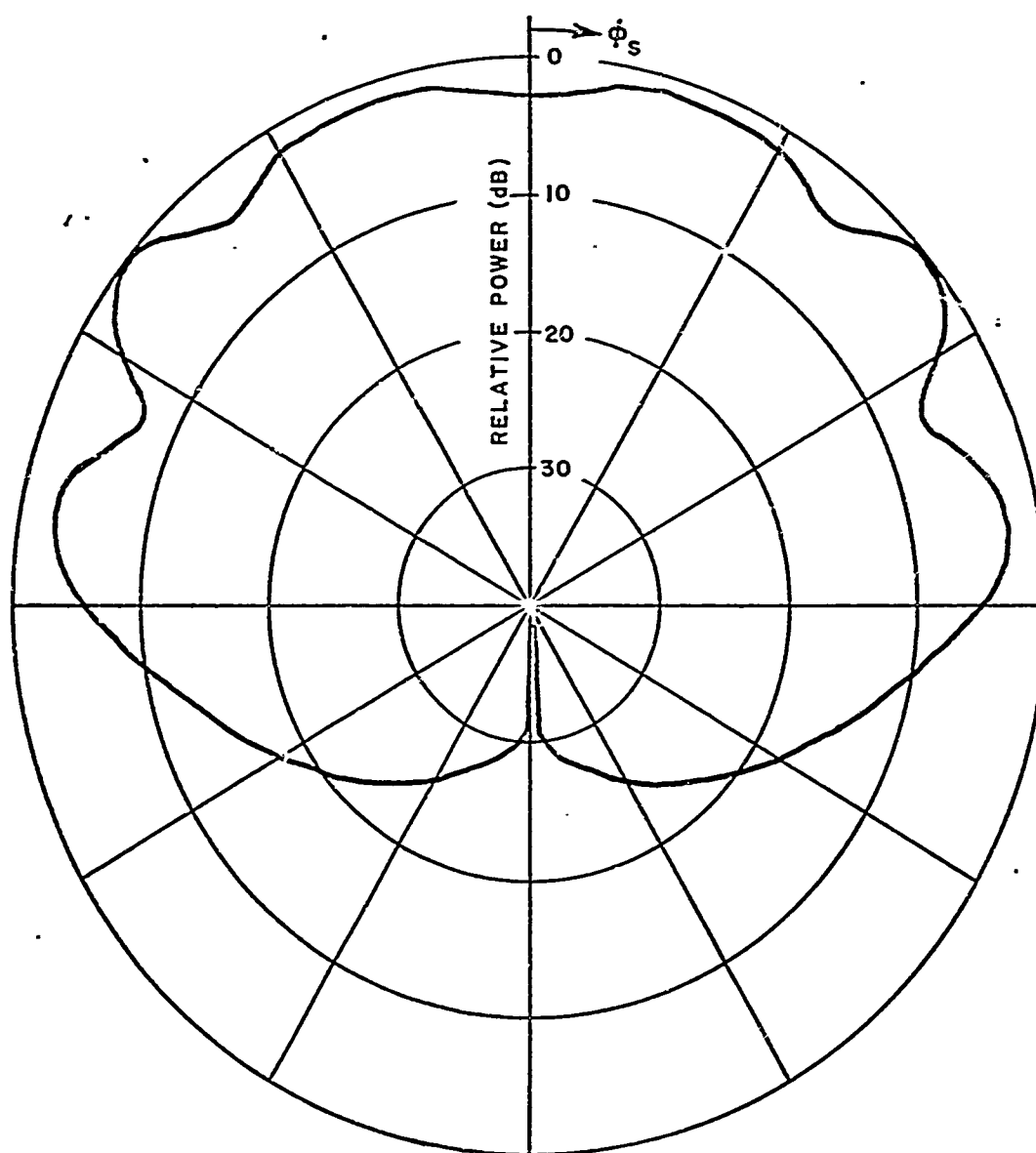


Fig. 39c--Roll plane pattern of axial slot (E_ϕ).

Based on our original aircraft model of Fig. 28, the fuselage is composed of cylinders, cones, and spheres. It was shown by Ryan in Ref. [20] that a two-dimensional diffraction analysis could be adapted to solve for the elevation plane pattern for an antenna mounted on a rocket model composed of cylinders and cones. With the antenna, in our problem, being mounted on the fuselage near the top or bottom of the aircraft one can to a good approximation just consider the fuselage effect in the elevation plane in that the other terms have normally a secondary effect. Thus, Ryan's approach is applied here with only the spherical nose cone being included in his solution in order to complete our analysis of the originally specified model.

Some of the results of the present study are illustrated in Fig. 40. In Fig. 40a Ryan's calculated result is compared with the the measured result for a circumferential slot mounted on the fuselage with good agreement obtained between the two results.

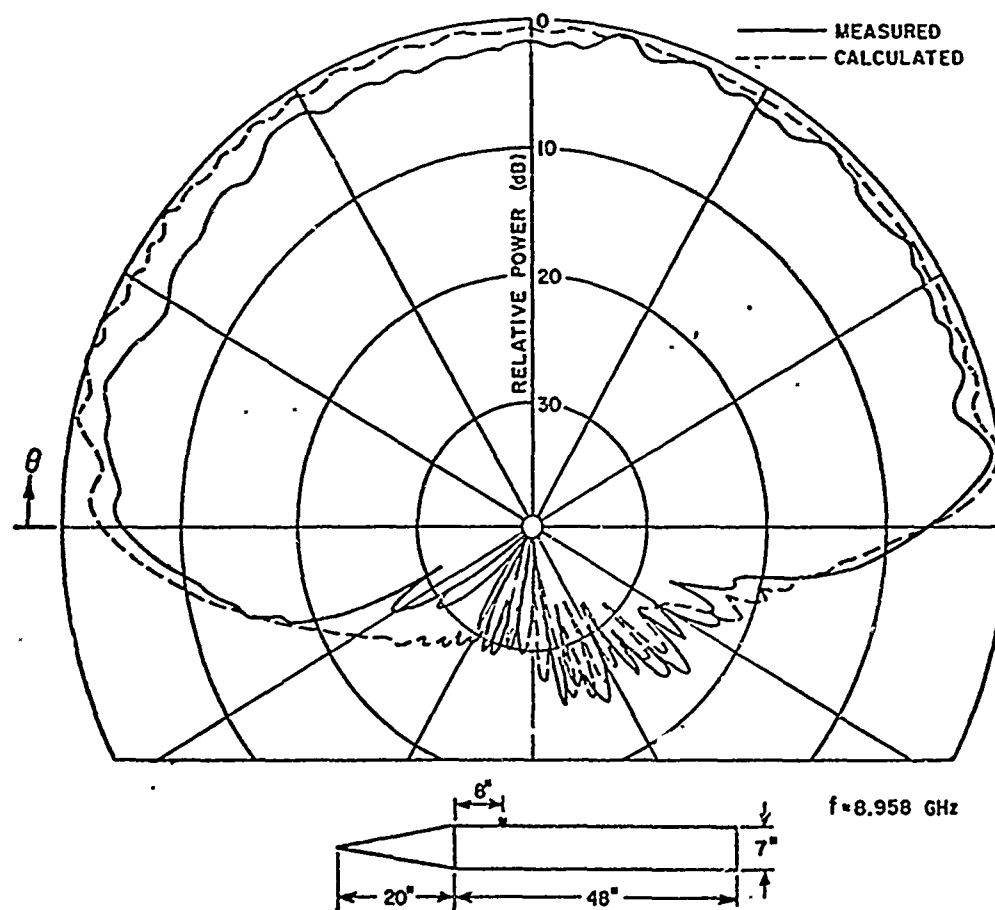


Fig. 40a--Elevation plane patterns.

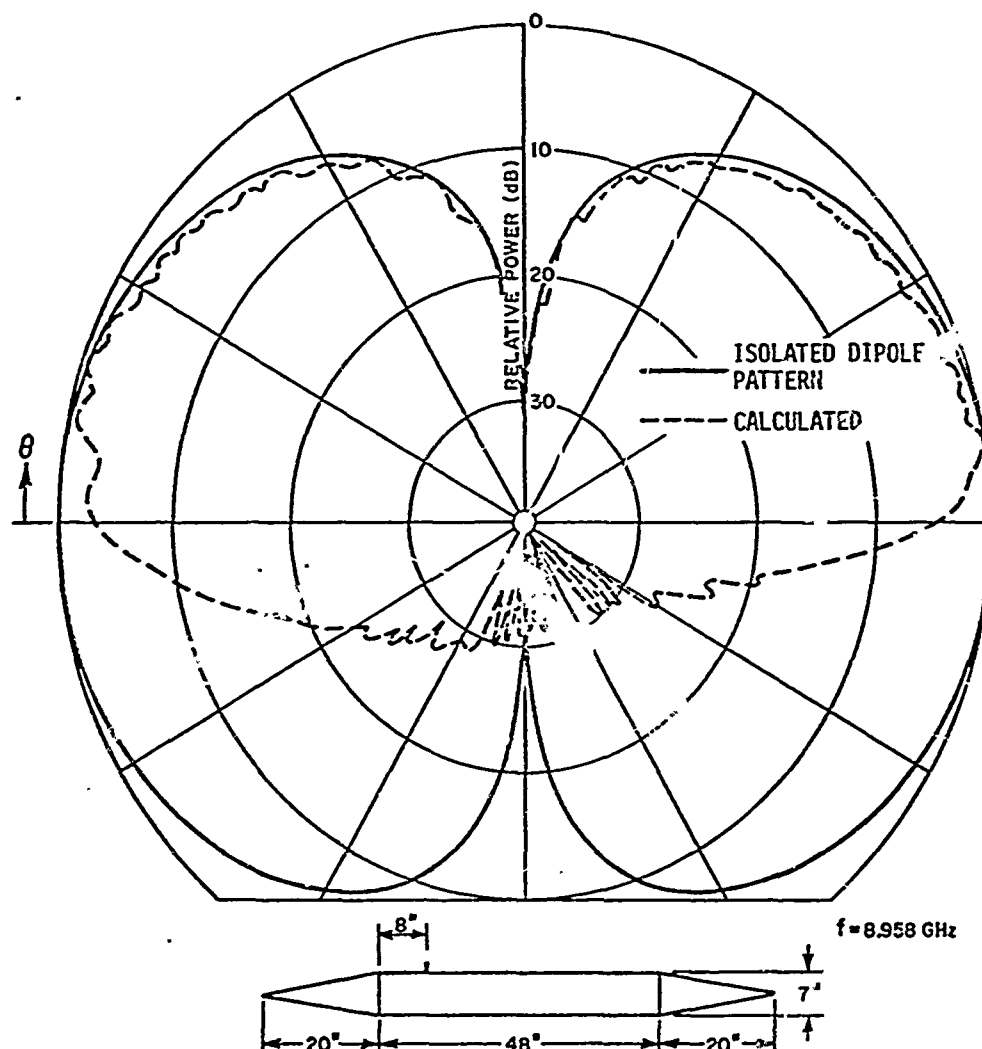


Fig. 40b--Elevation plane patterns.

In Fig. 40b a monopole is placed on the fuselage with the analytic results compared with the isolated dipole pattern showing that in the lit region the fuselage-mounted antenna radiates much like the isolated antenna. However, the on-aircraft antenna pattern deviates greatly outside the lit region. Thus, one must be careful when approximating the on-aircraft antenna performance using simply an isolated antenna pattern. Finally, in Fig. 40c the radiation patterns of monopoles mounted on different fuselages are considered to illustrate the effect of the fuselage shape on the resulting pattern. Note that with the spherical nose cone the ripple is greatly reduced with much more energy radiated in the forward direction.

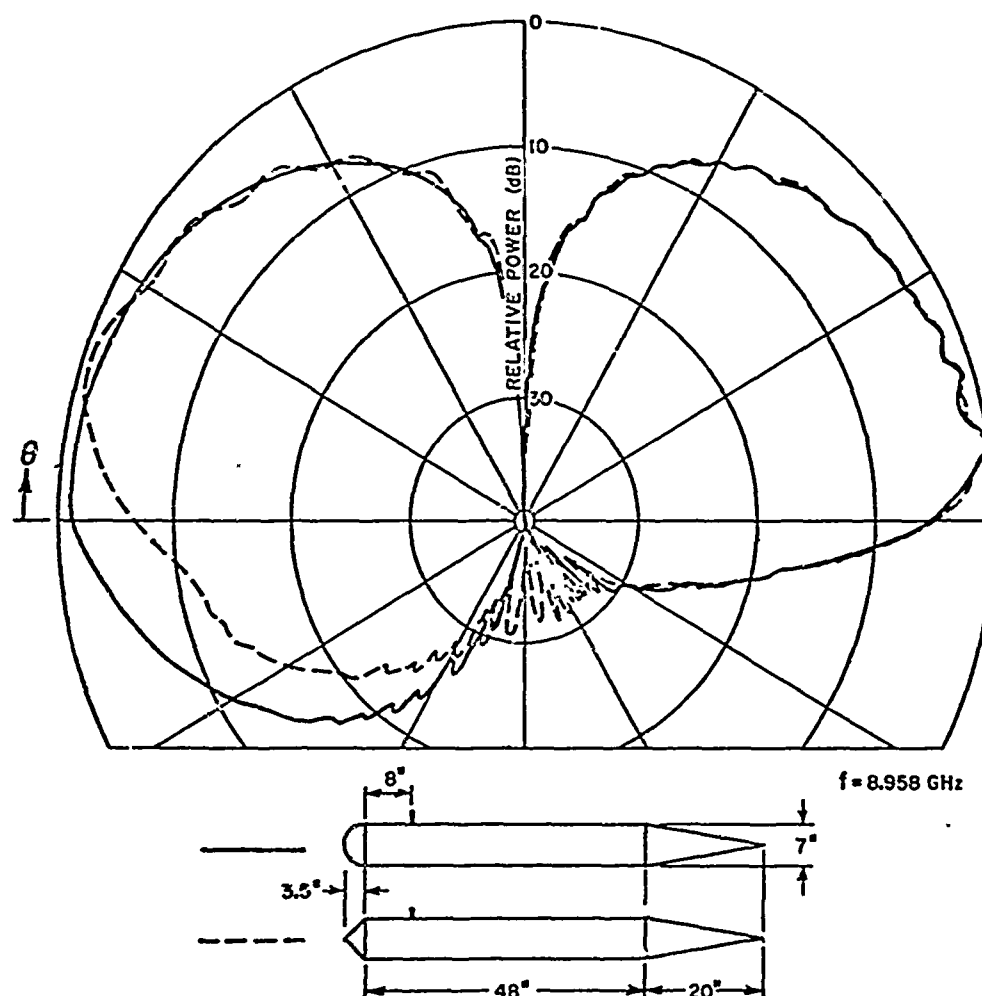


Fig. 40c--Elevation plane patterns.

In the previous fuselage models as well as the ones to follow, the nose radome has not been treated as a special case. In other words, it is assumed that the nose radome is a perfect conductor as is the rest of the fuselage. These solutions can be in error due to this approximation especially for dielectric radomes. However, it appears that metallic radomes will find widespread use in the future; in which case, our model could be a good approximation in the radome region especially outside its pass-band.

The simple models described above are not general enough to include the wide variety of aircraft fuselages encountered in practice. An aircraft fuselage is predominantly a convex body which can not be completely described by simple analytic equations. In practice, an aircraft fuselage is often specified by a set of points.

Consequently a new approach, called "Section Matching GTD Method," is developed in which a set of discrete points is used to outline the profile of the fuselage. In this way any convex fuselage shape can be included in our general solution in a straight-forward manner. Note that this solution is still two-dimensional but in many cases this is a good approximation in computing the three-dimensional elevation plane pattern. Nevertheless, the complete three-dimensional shape and volumetric pattern will be treated in the next chapter which will remove this present restriction.

It was shown in Section II-F that one can write high frequency asymptotic expressions for the far zone radiated fields of an antenna mounted on a general two-dimensional convex surface. This solution is broken up into solutions for the three regions which were illustrated in Fig. 7. The forms of these expressions are given in general terms by Eqs. (23), (24) and (25). Note that the solution in the lit region is just the geometrical optics field for the isolated antenna and is not affected by the surface geometry. On the other hand, the solution in the transition region is dependent on terms of the form

$$\xi = \int \left(\frac{k}{2\rho_g^2(s)} \right)^{1/3} ds \quad \text{and}$$

$e^{-j \int k ds}$ which are characteristic of the convex surface. Note that in the above equations $\rho_g(s)$ is the radius of curvature and s is the arclength along the appropriate geodesic path. If the surface is now approximated by a set of points, one can evaluate the above integrals numerically using

$$\xi \approx \sum_i \left(\frac{k}{2\rho_g^2(s_i)} \right)^{1/3} \Delta s_i \quad \text{and}$$

$$e^{-j \int k ds} \approx e^{-j \sum_i k \Delta s_i} = \prod_i e^{-jk \Delta s_i}.$$

These expressions require that the incremental arclength between points (Δs_i) and the radius of curvature at each point (ρ_g) be found based on the set of defining points. If the actual surface is given by $f(x)$ which is known only at a finite number of points, one can make a polynomial approximation to a segment of the surface which is given by

$$(78) \quad y(x) = \sum_{i=0}^{n-1} c_i x^i.$$

The geometry for this problem is illustrated in Fig. 41. Equating the above polynomial solution with the surface equation at "n" consecutive surface defining points one can find a matrix of the form

$$\begin{bmatrix} f(x_1) \\ f(x_2) \\ \vdots \\ f(x_n) \end{bmatrix} = \begin{bmatrix} 1 & x_1 & x_1^2 & \dots & x_1^{n-1} \\ 1 & x_2 & x_2^2 & \dots & x_2^{n-1} \\ \vdots & \vdots & \vdots & & \vdots \\ 1 & x_n & x_n^2 & \dots & x_n^{n-1} \end{bmatrix} \begin{bmatrix} c_0 \\ c_1 \\ \vdots \\ c_{n-1} \end{bmatrix}.$$

This matrix equation can then be inverted to solve for the values of the c 's. Substituting these values into Eq. (78) one obtains an equation which locally describes the surface and from which one can determine the radius of curvature and incremental arclength.

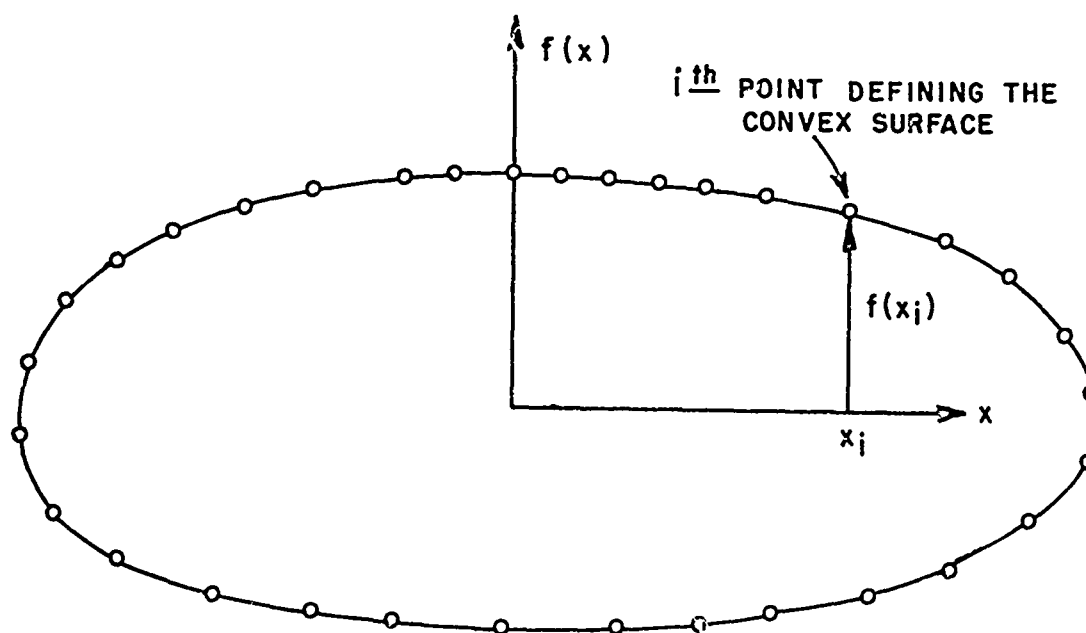


Fig. 41--Numerical description of convex surface.

The radius of curvature can be defined in many ways. In this case it is given by

$$(79) \quad \rho_g \equiv \left| \frac{\left[1 + \left(\frac{dy}{dx} \right)^2 \right]^{3/2}}{\frac{d^2y}{dx^2}} \right|$$

which is applied unless dy/dx approaches infinity in which case let x be defined in terms of y then

$$\rho_g \equiv \left| \frac{\left[1 + \left(\frac{dx}{dy} \right)^2 \right]^{3/2}}{\frac{d^2x}{dy^2}} \right|.$$

The values of the various derivatives are then found from the polynomial expression of Eq. (78) which is evaluated at the mid point (x_{n+1}) of the approximating section by

$$\left. \frac{dy}{dx} \right|_{x_{\frac{n+1}{2}}} = \sum_{i=1}^{n-1} i C_i x_{\frac{n+1}{2}}^{i-1} \quad \text{and}$$

$$\left. \frac{d^2y}{dx^2} \right|_{x_{\frac{n+1}{2}}} = \sum_{i=2}^{n-1} i(i-1) C_i x_{\frac{n+1}{2}}^{i-2}$$

giving

$$(80) \quad \rho_g(x_{\frac{n+1}{2}}) \equiv \left| \frac{\left[1 + \left(\sum_{i=1}^{n-1} i C_i x_{\frac{n+1}{2}}^{i-1} \right)^2 \right]^{3/2}}{\sum_{i=2}^{n-1} i(i-1) C_i x_{\frac{n+1}{2}}^{i-2}} \right|.$$

Using this technique the radius of curvature is defined at each surface defining point. Note, however, that this requires a new polynomial solution (Eq. (78)) for each ρ_g calculation. One should realize that the arclength as well as the radius of curvature must

be determined to a good approximation in that they will be used in the deep shadow region to find $d\rho_g/ds$ and $d^2\rho_g/ds^2$. Consequently, using the straight line distance between adjacent points is not the best method to find the incremental arclength based on our limited comparisons. These comparisons were made between various numerical solutions and the known solutions for s , ρ_g , $\dot{\rho}_g$, and $\ddot{\rho}_g$ along an elliptical surface. A better approximation appears to be one which takes into account the curved nature of the surface between points. One such approach is illustrated in Fig. 42 where

$$(81) \quad \Delta s_i = \frac{\rho_g(x_i) + \rho_g(x_{i+1})}{2} \Delta \phi_i =$$

$$[\rho_g(x_i) + \rho_g(x_{i+1})] \sin^{-1} \left(\frac{\Delta \ell_i}{\rho_g(x_i) + \rho_g(x_{i+1})} \right)$$

with

$$\Delta \ell_i \sim \sqrt{(y_{i+1} - y_i)^2 + (x_{i+1} - x_i)^2}.$$

This information can then be used in Eq. (24) to determine the values of the radiated field in the transition region. Recall that $g^*(\xi)$ and $\tilde{g}^*(\xi)$ are Fock functions which were defined in Section II-D and are tabulated in the literature[50]. These tabulated values can be applied to a simple interpolation procedure that can be employed to compute the complete set of values, which completes the approach used in the transition region.

In the deep shadow region additional information is needed about the surface. For the diffraction and attenuation constants one needs information about ρ_g , $d\rho_g/ds$, and $d^2\rho_g/ds^2$ at each point $[f(x_i)]$ along the surface. The values of the radius of curvature $\rho_g(x_i)$ and incremental arclength s_i have been defined by Eqs. (80) and (81). These values can now be used to compute the other terms using

$$(82) \quad \dot{\rho}_g(x_i) = \frac{\rho_g(x_i) - \rho_g(x_{i-1})}{\Delta s_{i-1}} + \frac{\rho_g(x_{i+1}) - \rho_g(x_i)}{\Delta s_i} -$$

$$\frac{\rho_g(x_{i+1}) - \rho_g(x_{i-1}))}{\Delta s_{i-1} + \Delta s_i}$$

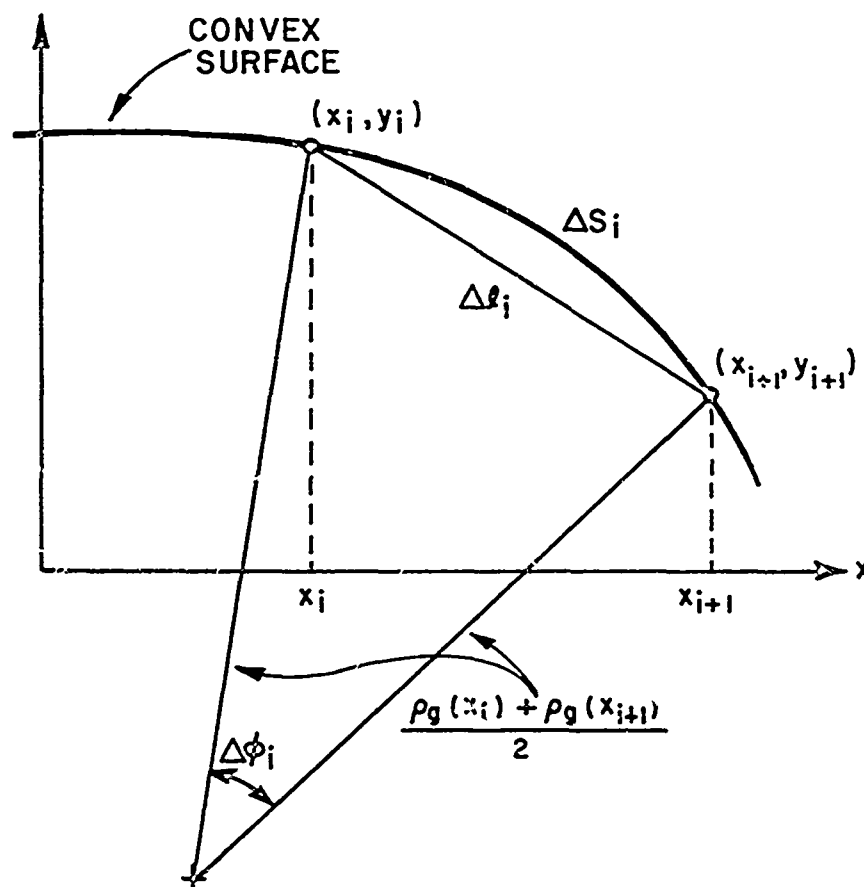


Fig. 42--Geometry describing the arc length computation.

and

$$(83) \quad \ddot{\rho}_g(x_i) = \frac{\dot{\rho}_g(x_i) - \dot{\rho}_g(x_{i-1})}{\Delta s_{i-1}} + \frac{\dot{\rho}_g(x_{i+1}) - \dot{\rho}_g(x_i)}{\Delta s_i} - \frac{\dot{\rho}_g(x_{i+1}) - \dot{\rho}_g(x_{i-1})}{\Delta s_{i-1} + \Delta s_i}$$

which are numerical averaging solutions specifically designed to compute derivatives based on discrete data as presented in Ref. [51].

The only undefined terms remaining are the values of $A_i(\bar{q}_m)$ and $A_i'(-q_m)$ which are tabulated Airy functions. In our solutions for the GTD fields in the deep shadow region only two modes are considered. The values of these terms for the first five modes are given in

Section II-D. Thus, it has been shown that the GTD solution in the deep shadow region can be completely defined in terms of our general two-dimensional convex surface which is only defined by a finite number of points.

For the actual computations, the tangent values at each of the defining points were determined using the polynomial approximation to a section of the surface. These tangent directions in turn specify the radiation direction of the fields diffracted from that point. Note that curved surface diffraction is a local surface phenomenon as shown in Ref. [52]. Thus, the points which define the surface must be spaced close enough together such that the tangent directions of adjacent points do not vary too rapidly. Otherwise, the pattern can only be determined for large angular changes, which means some of the pattern structure can be lost due to the large pattern change between data points.

It was found for the cases considered in this study that a 4th order polynomial was sufficient to locally describe the surface. This was based on a comparison of our numerical data with known results for various convex surfaces. Note that the values of ρ_g , $\dot{\rho}_g$, and $\ddot{\rho}_g$ could then be computed at the center point of each approximated section. It is this section approximation of the surface that leads to the term Section Matching GTD Solution. Actual numerical calculations are presented in Ref. [48] to show the validity of these various approximations.

In order to verify our solution, it was first compared with the modal solution (Eqs. (3) and (4)) for an antenna mounted on a circular cylinder. These solutions are compared for the infinitesimal antennas as shown in Figs. 43 for a one wavelength radius cylinder. In each case there is very good agreement between the two results. These results do tend to verify this approach. However, this fuselage profile is circular ($\rho_g = \dot{\rho}_g = 0$) and the circular case is not a true test for our more general solution.

This section matching GTD solution now is extended to obtain radiation patterns in the elevation plane for a simulated fuselage model with an elliptical profile. The calculated radiation patterns for infinitesimal antennas such as circumferential slot, axial slot and infinitesimal monopole mounted on an infinitely long elliptical cylinder with a semi-major axis $a = 0.637\lambda$ and semi-minor axis $b = 0.390\lambda$ are shown in Figs. 44 to 46. The comparison between the continuous GTD solution[37] and the section matching GTD solution, again, is very satisfactory. In addition these methods have been applied to more general fuselage models such as composite elliptical cylinders. The radiation patterns in the elevation plane for a circumferential slot mounted at various locations on a composite elliptical cylinder are shown in Fig. 47. The results, again, compare very favorably with the continuous GTD solution[37]. The elevation

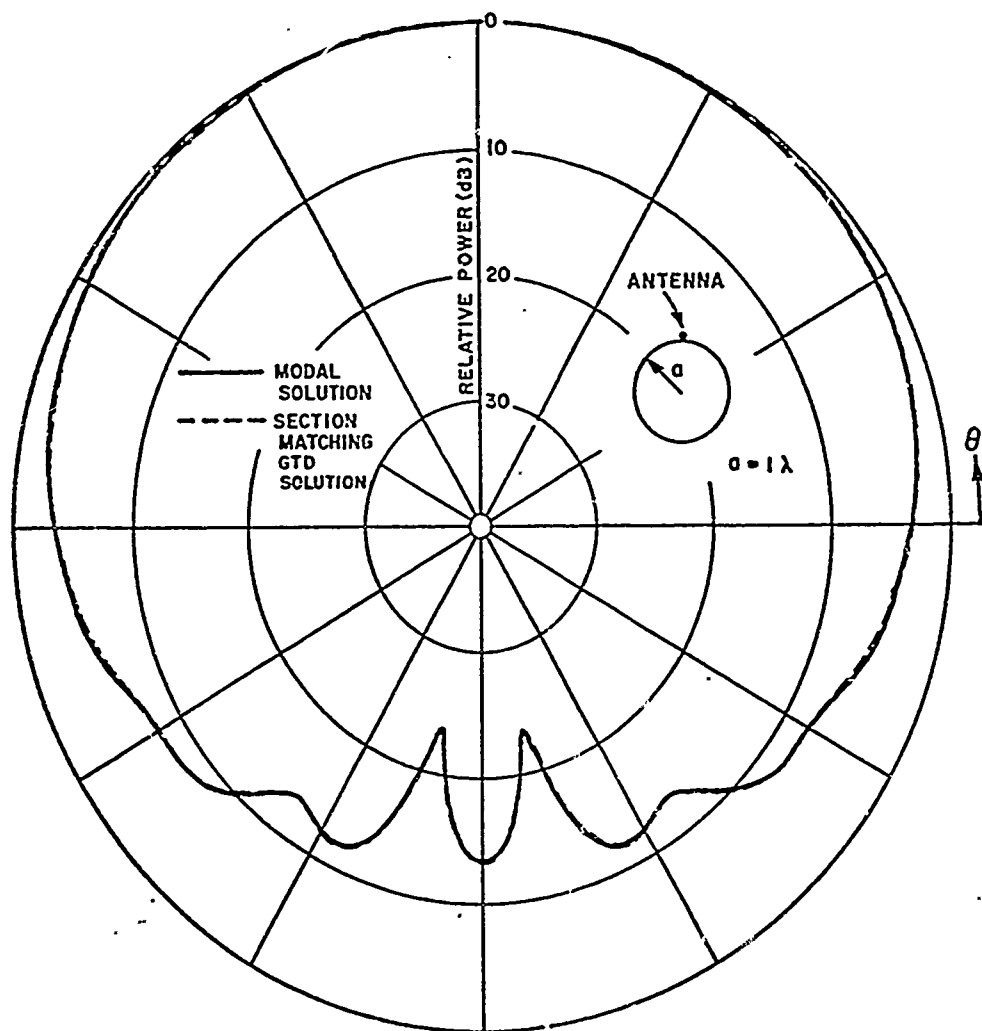


Fig. 43a--Principal plane patterns with a circumferential slot mounted on a circular cylinder.

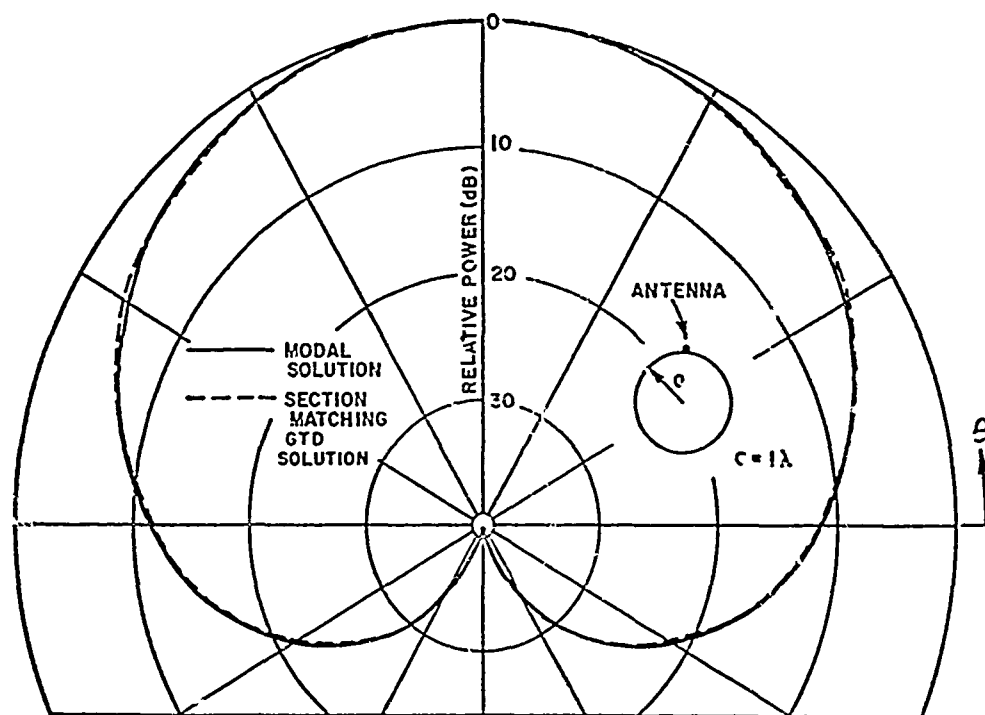


Fig. 43b--Principal plane patterns with an axial slot mounted on a circular cylinder.

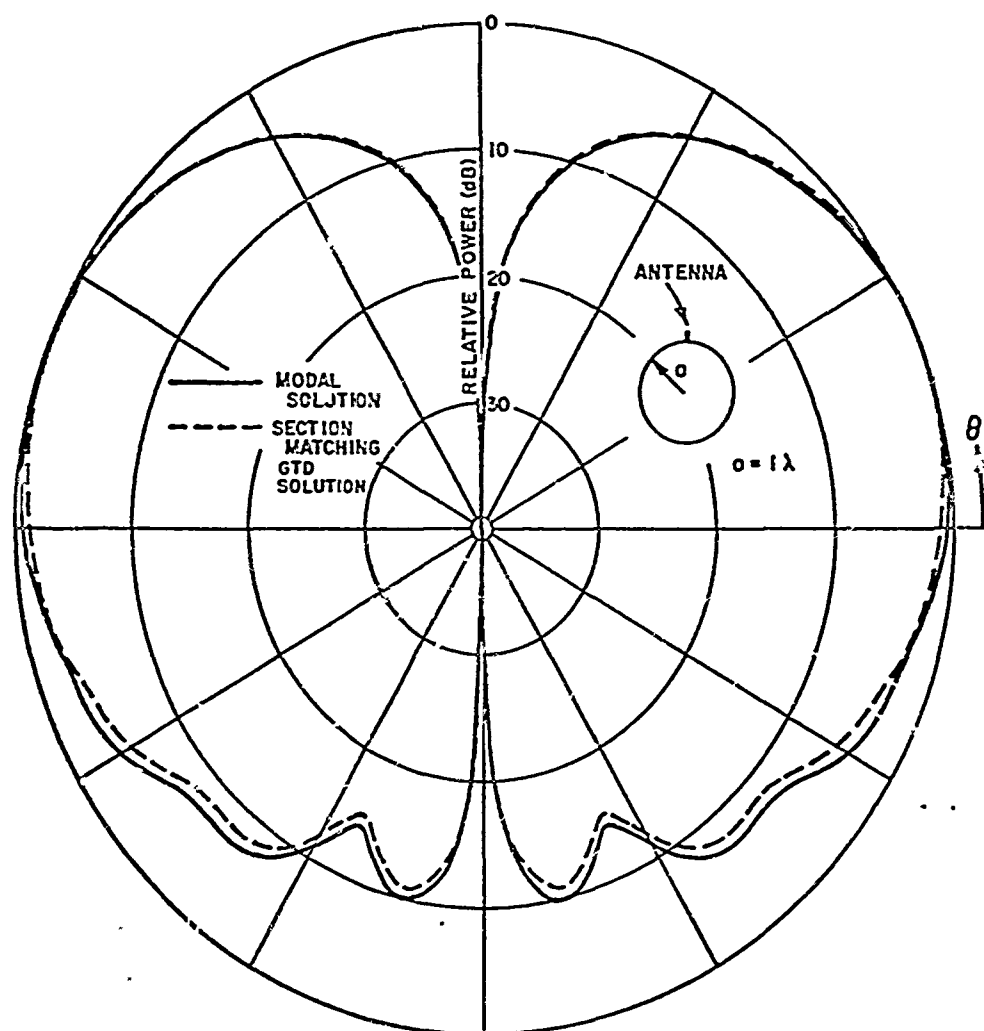


Fig. 43c--Principal plane patterns with an infinitesimal monopole mounted on a circular cylinder.

plane patterns for an axial slot and infinitesimal monopole are also shown in Figs. 48 and 49, respectively. Based on these results, the pattern in the lit region is simply the direct radiation by the antenna itself. On the other hand, the pattern in the shadow region is completely dominated by the fuselage structure through the diffraction mechanisms. Thus, the complete radiation pattern for an antenna mounted on a fuselage is greatly affected by the fuselage as one should expect. The location at which the antenna is mounted is also an important factor in determining the radiation pattern. The radiation patterns in the elevation plane for a smaller composite elliptical fuselage, with $a_1 = 1.5\lambda$ and $a_2 = 2.0\lambda$ and $b = 0.5\lambda$, are presented in Fig. 50. From the comparison between these figures one notices that there are fewer backlobes but more energy radiated in the shadow region for the smaller structure. The larger structure has more backlobes at a lower average energy level. This is simply due to the size of the fuselage and the interaction between the two surface waves propagating in opposite directions from the source; in which case, the two ray paths play a most important role. That is, the longer the ray path, the more the surface ray attenuates. Again, this shows the significant effect which the structure of the aircraft fuselage plays in terms of the antenna's performance.

D. Azimuth Plane Analysis

With an antenna mounted near the top or bottom of the fuselage, it is quite apparent that the dominant aircraft structure effect in the azimuth plane is the fuselage. However, in this case one is not dealing simply with the cross-sectional shape of the fuselage as in the roll-plane or the profile of the fuselage as in the elevation plane. In fact, in order to deal with this problem to a good approximation, a more complete three-dimensional study must be made of the fuselage as is considered in the next chapter. On the other hand, this section is concerned with characteristic features of the azimuth pattern in terms of the important secondary components. Two such contributors considered here are the engine and wing scattering effects.

In order to apply our previous solutions with only minor modifications it is again assumed that the antenna is mounted on an infinitely long circular cylinder (fuselage). As in the roll plane, the modal solutions are applied to determine the radiation pattern of the fuselage mounted antenna. Using this approach one can again consider an arbitrary antenna by integrating the equivalent aperture currents as discussed in Section II-B. These patterns will be compared with patterns including additional scattering structures. This should allow one to determine if these secondary scattering structures are important in the azimuth plane.

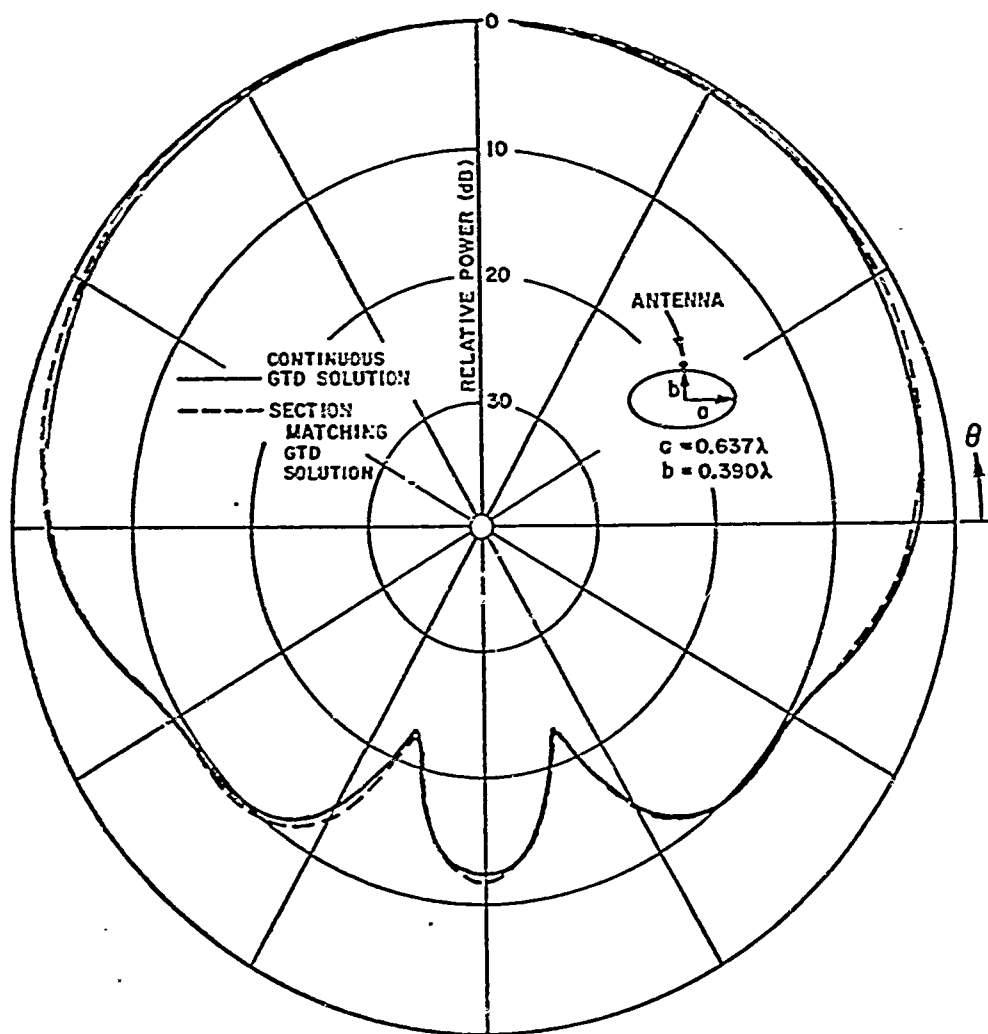


Fig. 44a--Elevation plane patterns with a circumferential slot mounted on an elliptical cylinder.

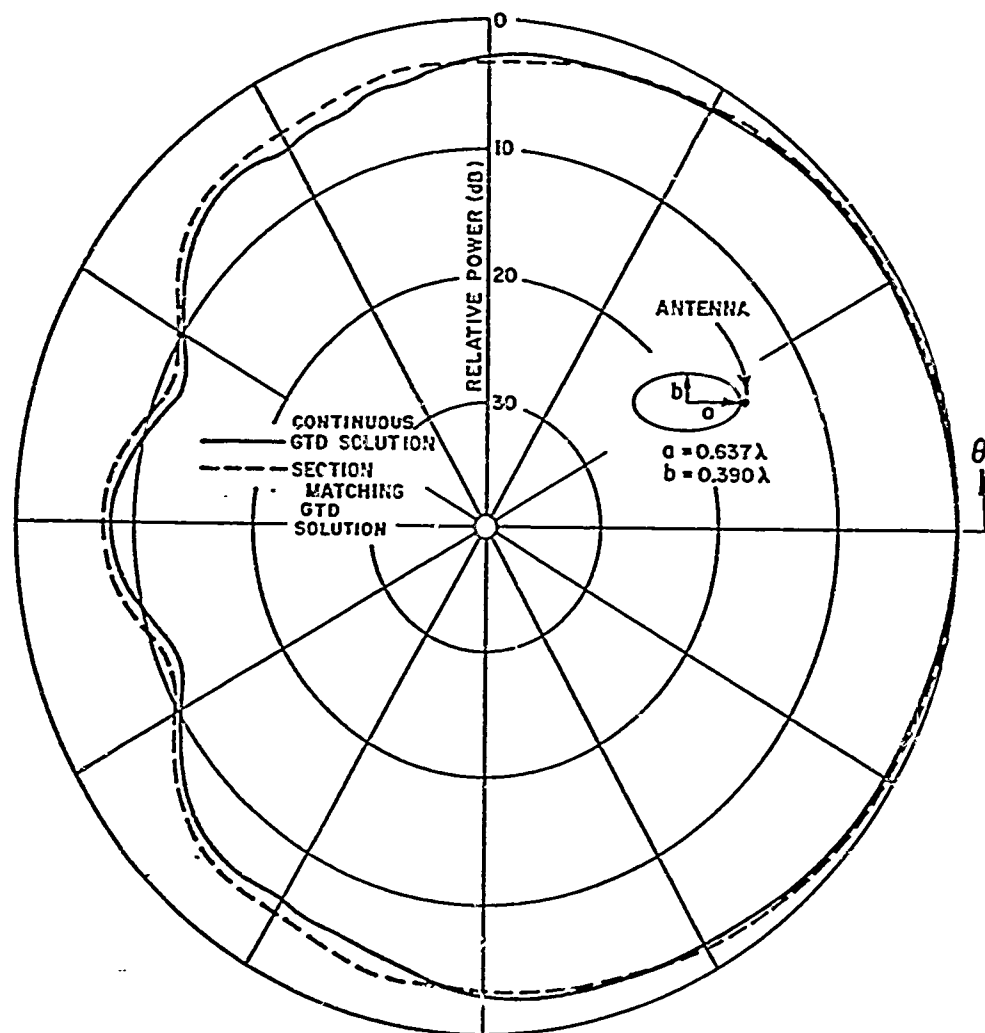


Fig. 44b--Elevation plane patterns with a circumferential slot mounted on an elliptical cylinder.

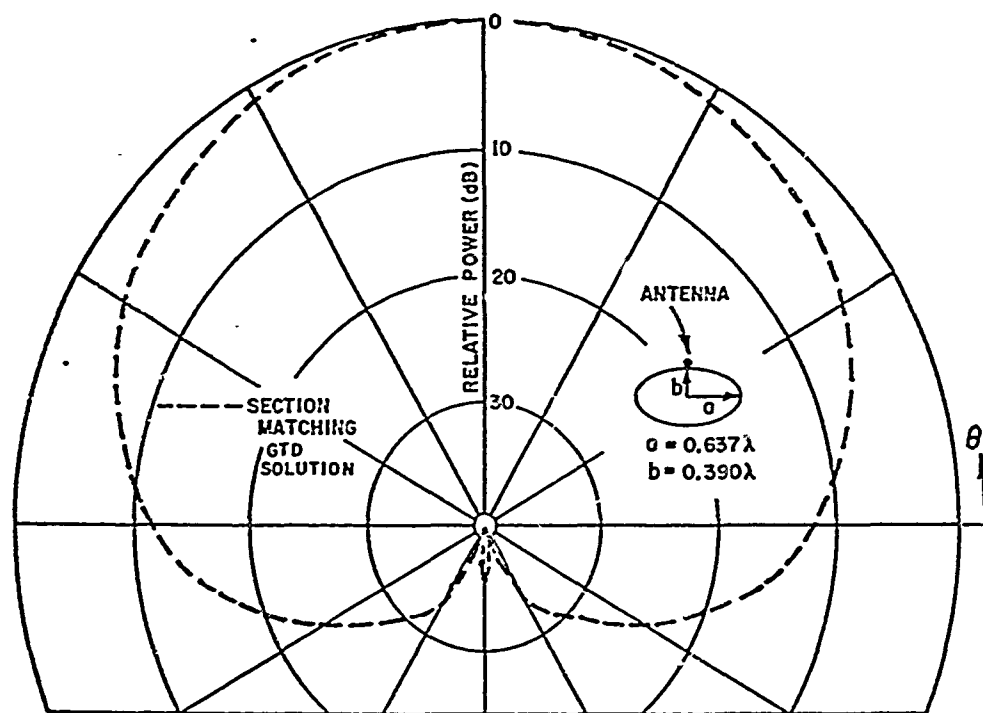


Fig. 45--Elevation plane patterns with an axial slot mounted on an elliptical cylinder.

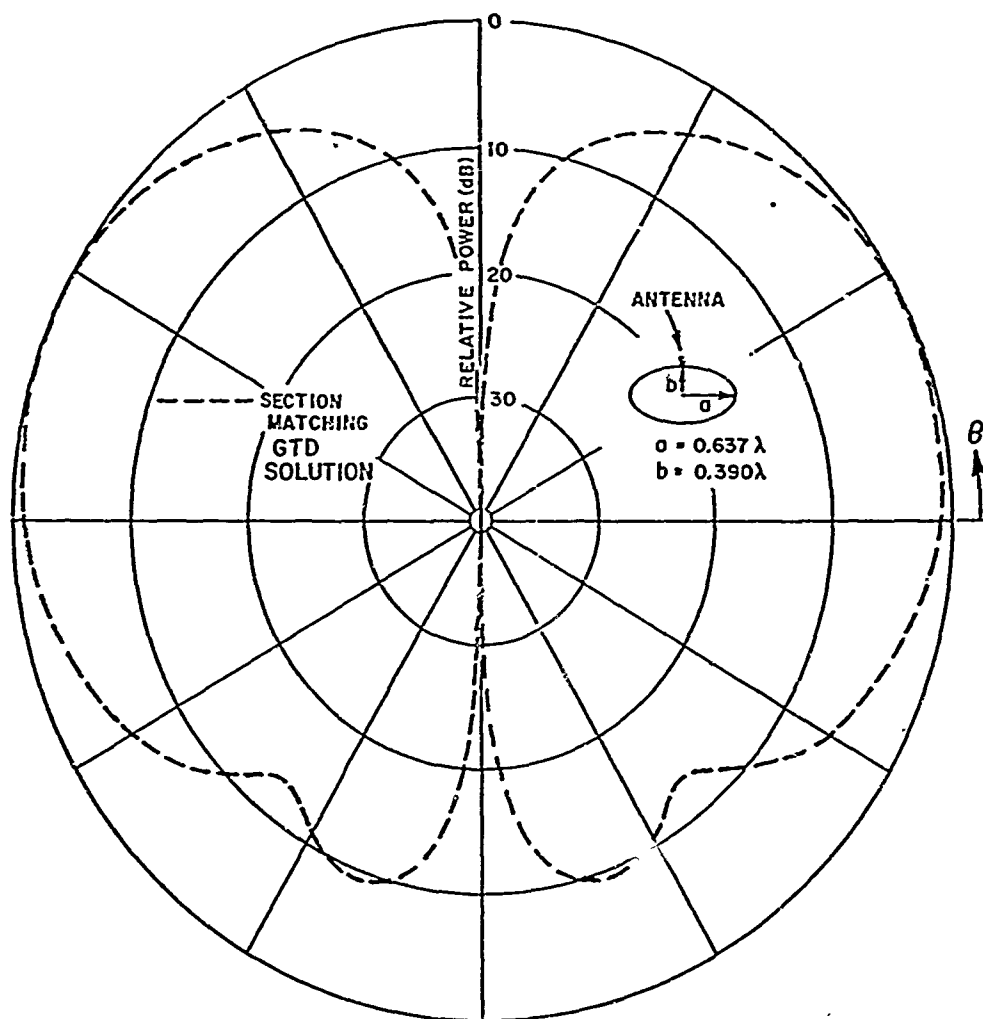


Fig. 46--Elevation plane pattern with an infinitesimal monopole mounted on an elliptical cylinder.

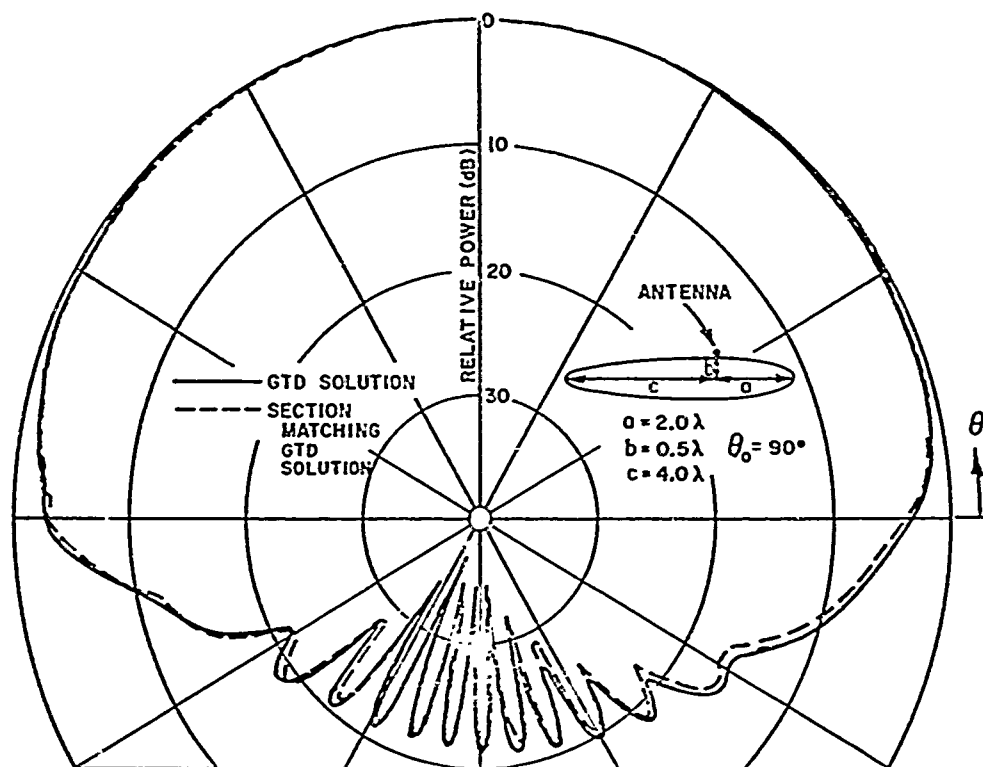


Fig. 47a--Elevation plane pattern with a circumferential slot mounted on a composite ellipse model.

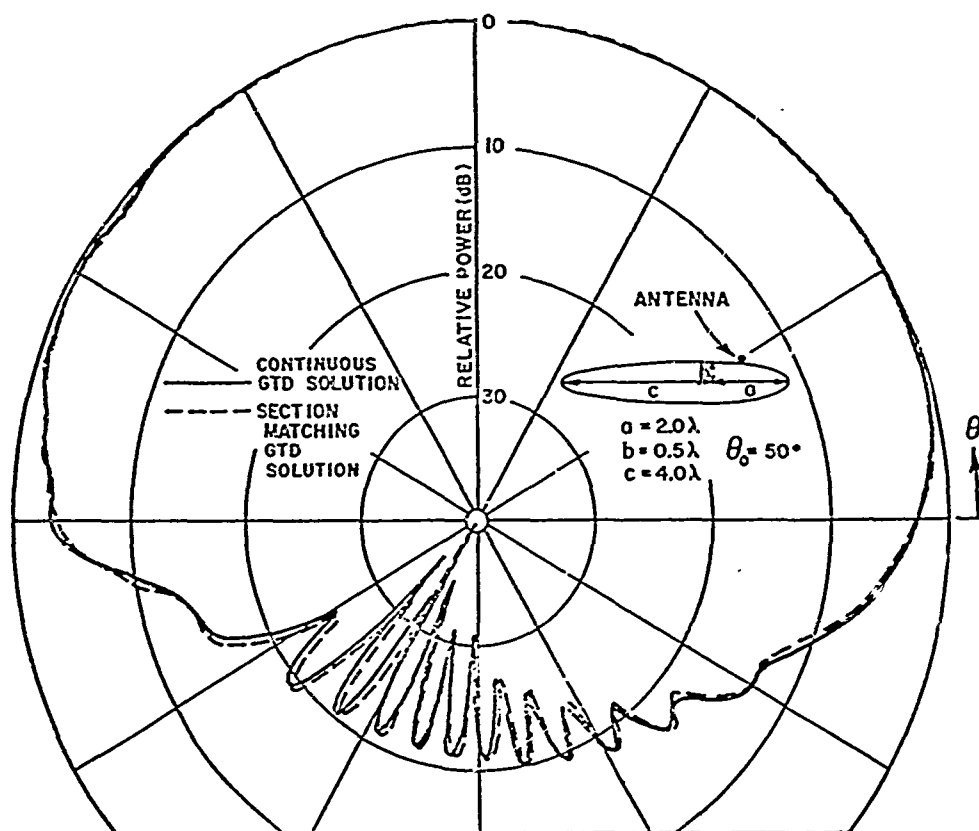


Fig. 47b--Elevation plane pattern with a circumferential slot mounted on a composite ellipse model.

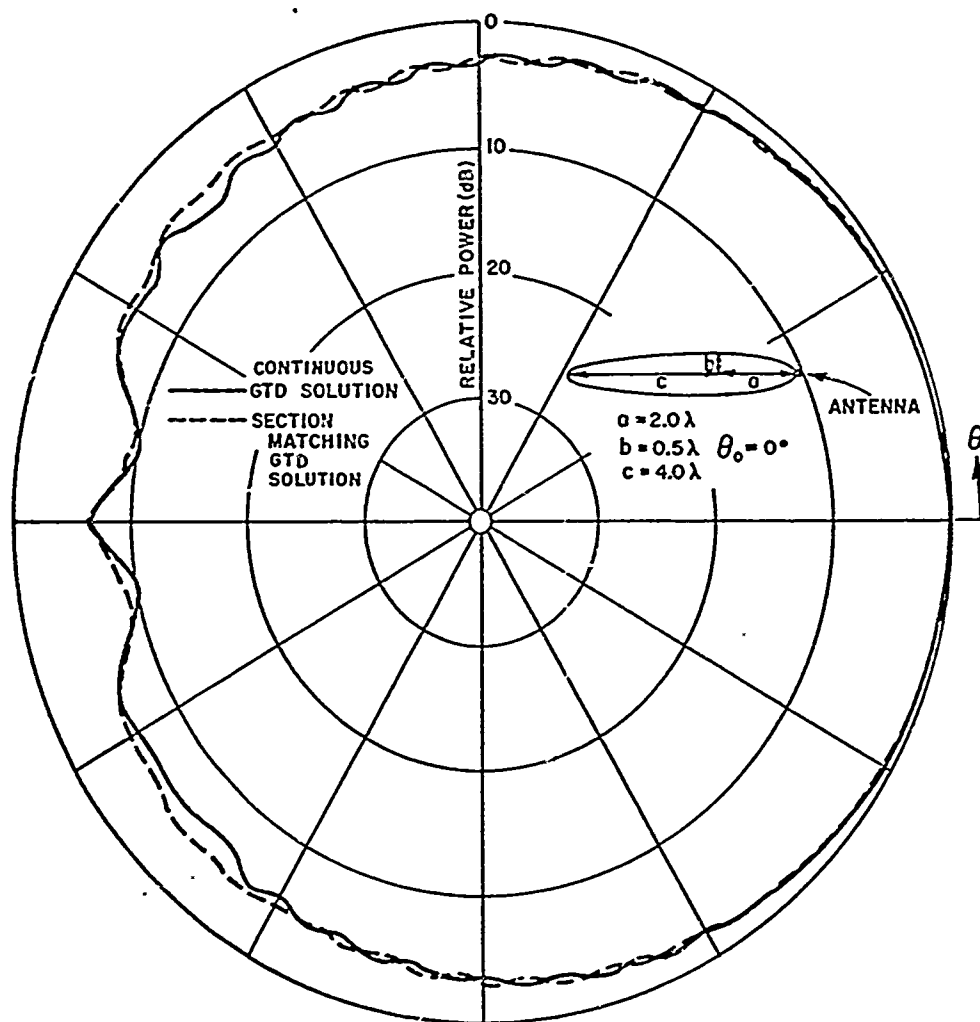


Fig. 47c---Elevation plane pattern with a circumferential slot mounted on a composite ellipse model.

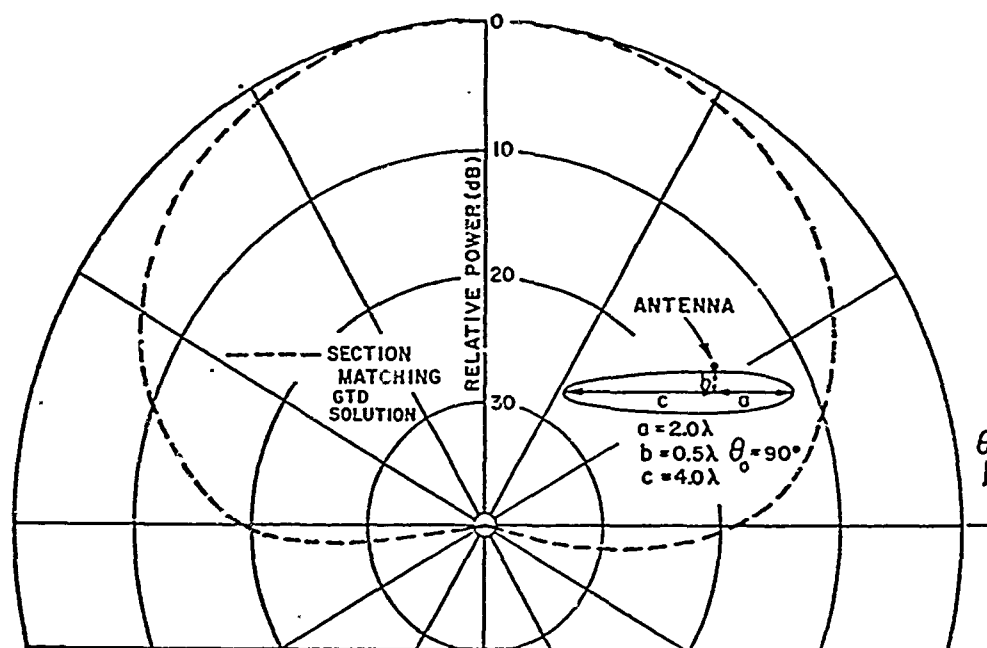


Fig. 48a--Elevation plane pattern with an axial slot mounted on a composite ellipse model.

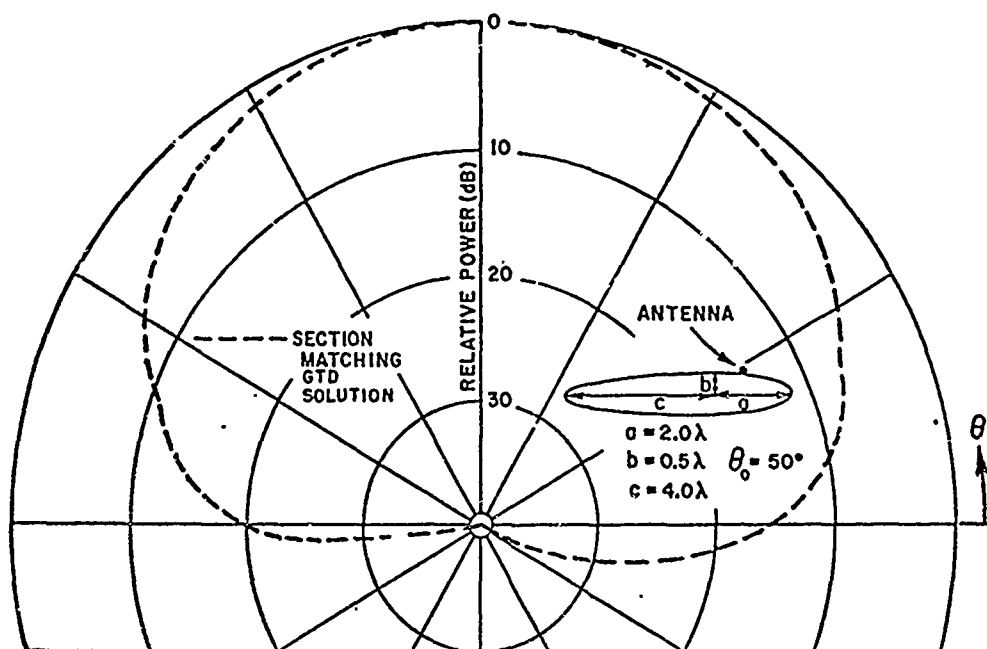


Fig. 48b--Elevation plane pattern with an axial slot mounted on a composite ellipse model.

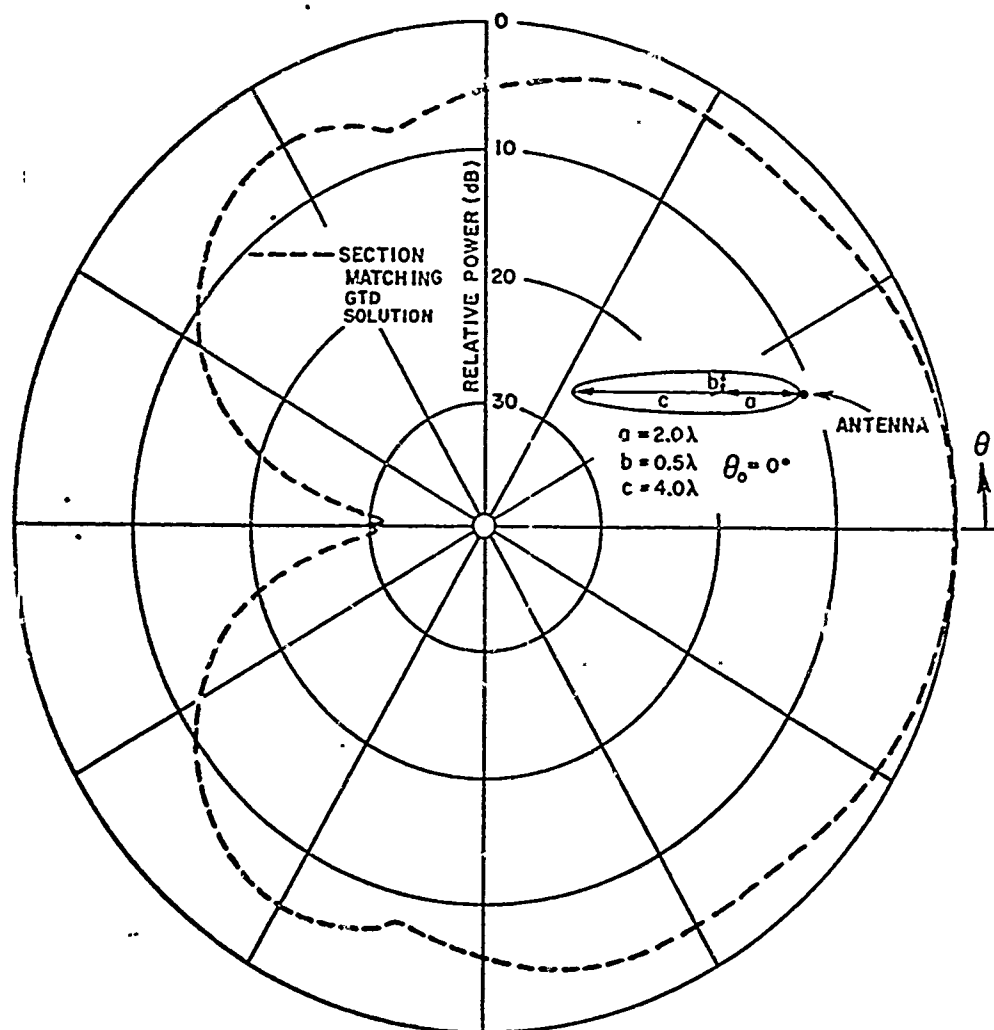


Fig. 48c--Elevation plane pattern with an axial slot mounted on a composite ellipse model.

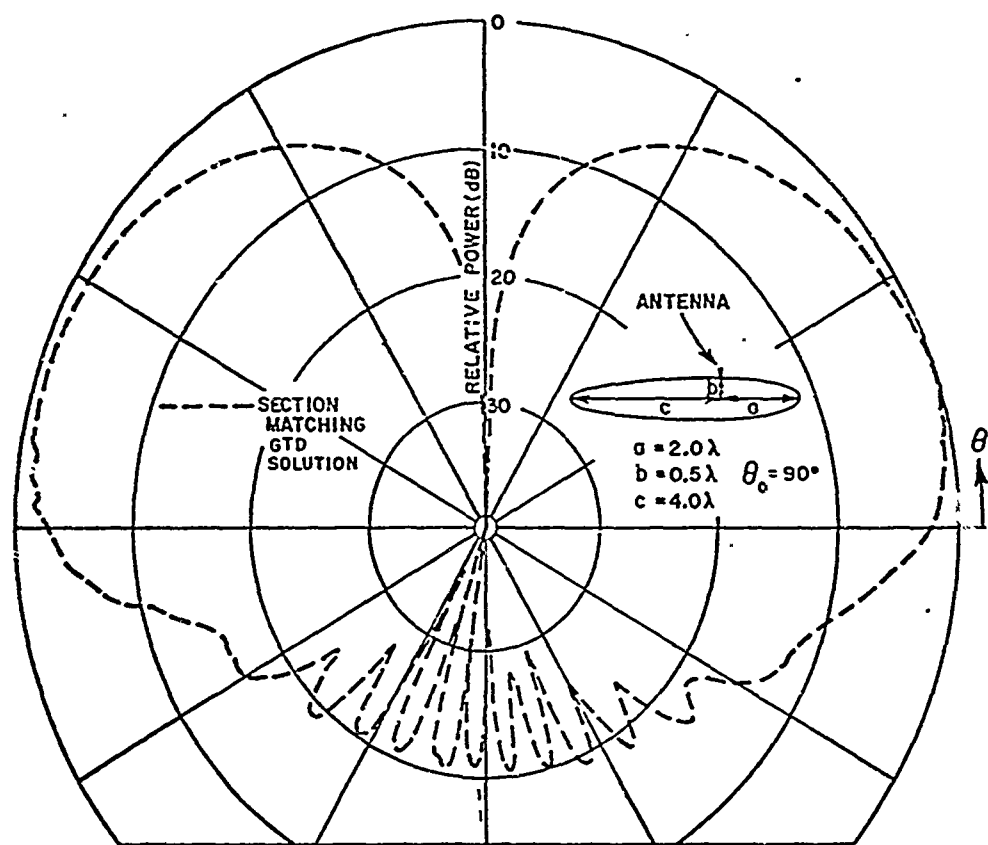


Fig. 49a--Elevation plane pattern with an infinitesimal monopole mounted on a composite ellipse model.

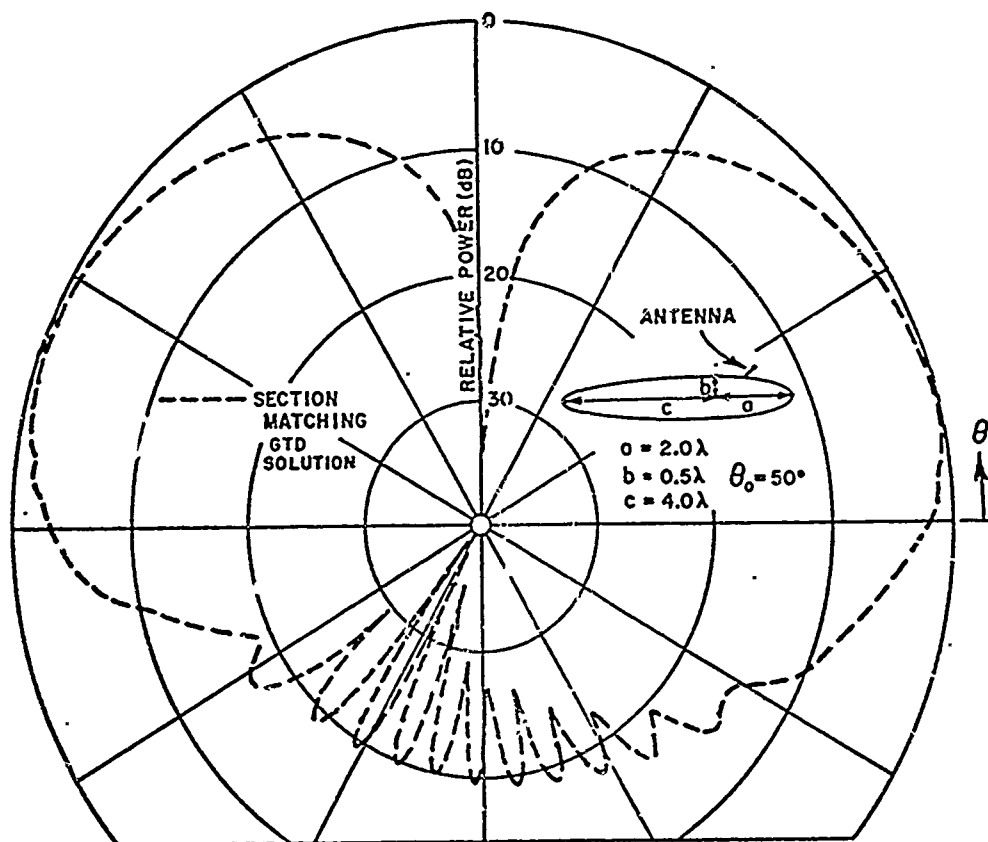


Fig. 49b--Elevation plane pattern with an infinitesimal monopole mounted on a composite ellipse model.

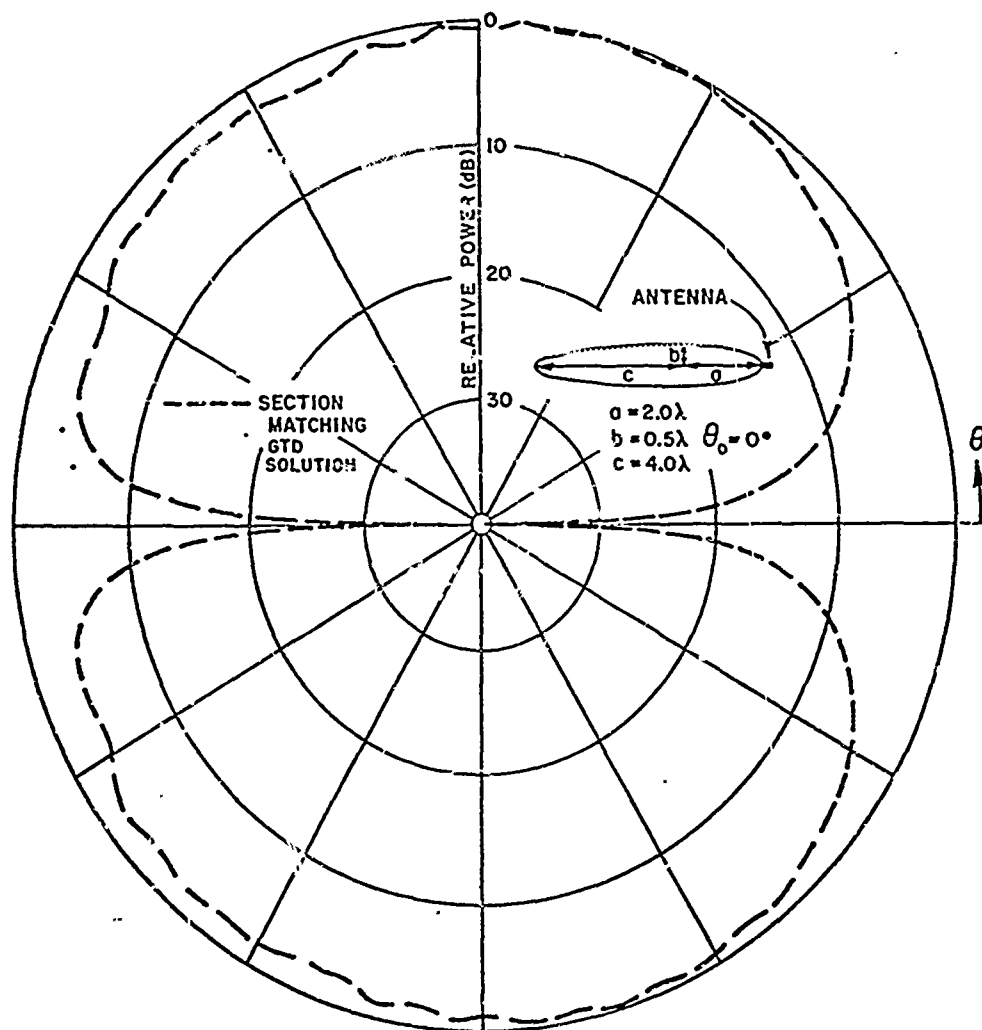


Fig. 49c--Elevation plane pattern with an infinitesimal monopole mounted on a composite ellipse model.

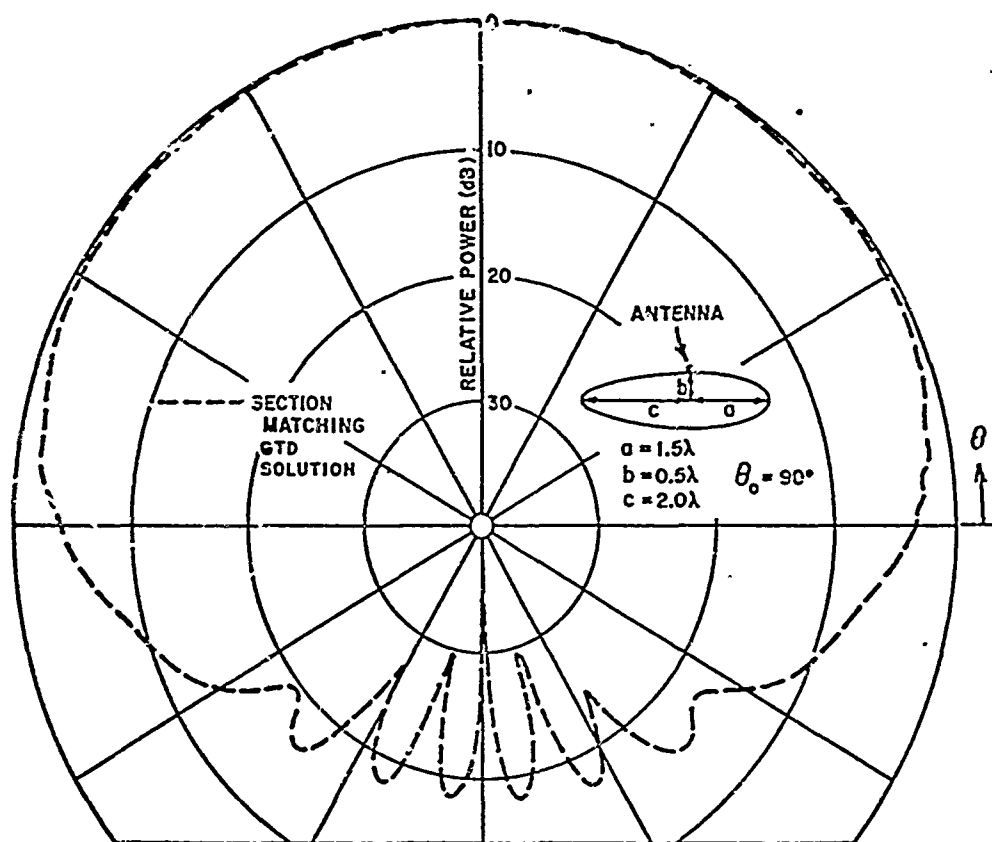


Fig. 50a--Elevation plane pattern with a circumferential slot mounted on a composite ellipse model.

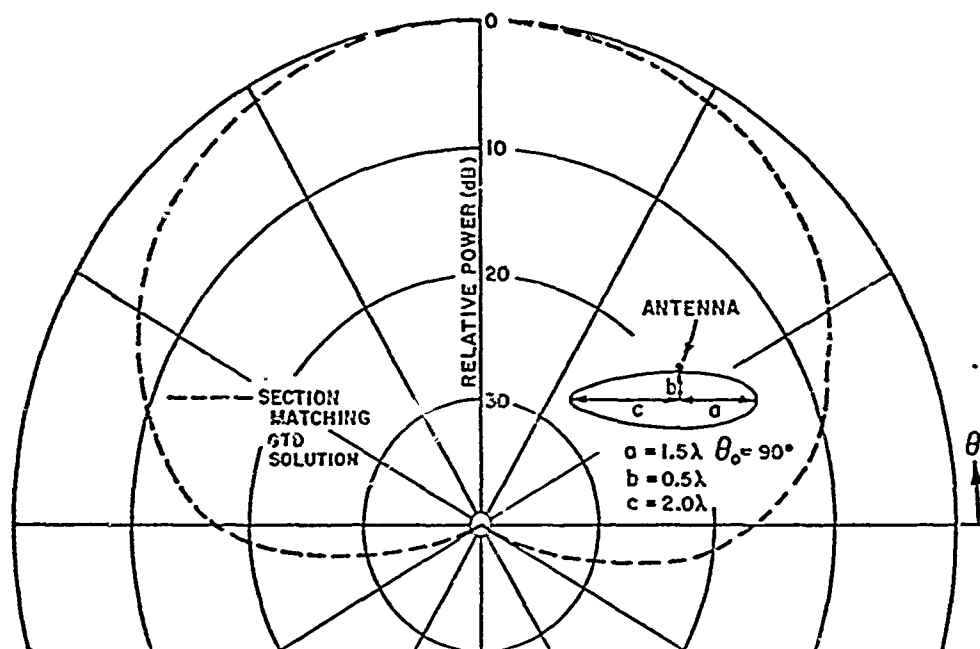


Fig. 50b--Elevation plane pattern with an axial slot mounted on a composite ellipse model.

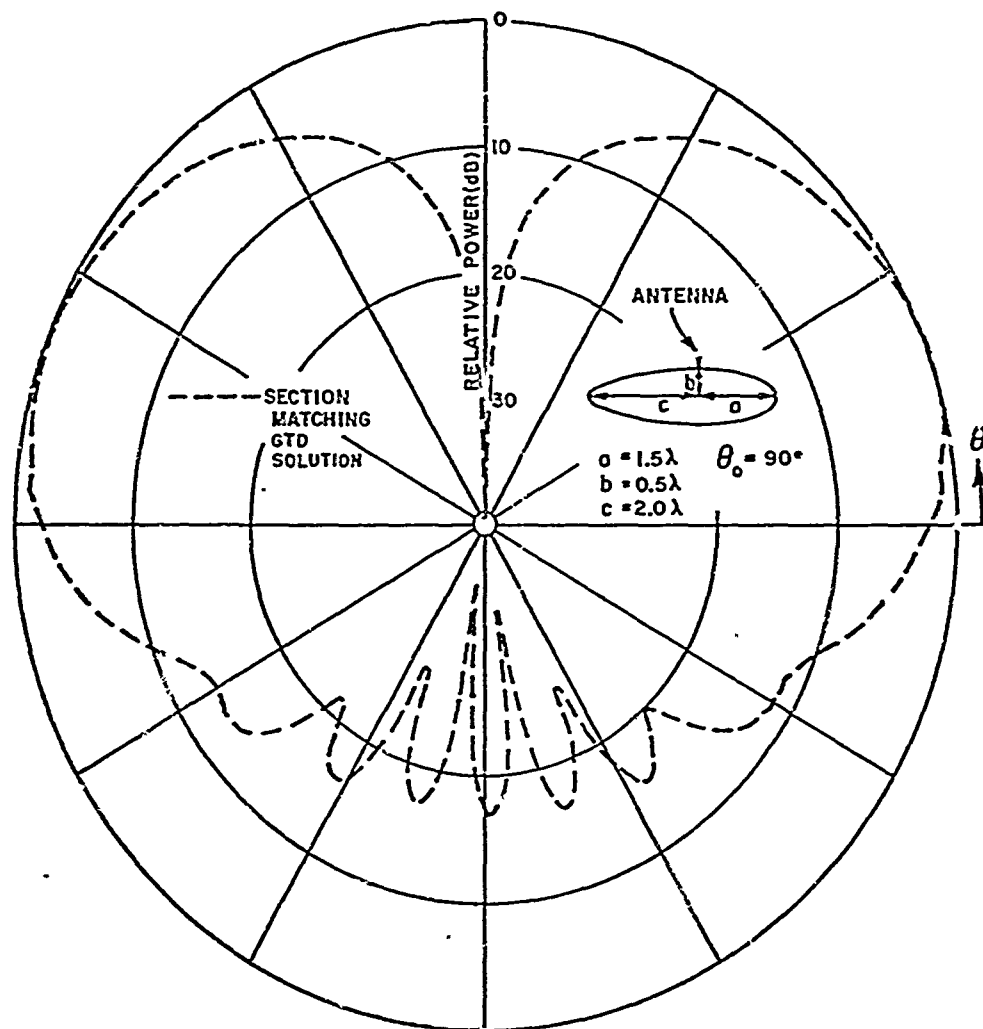


Fig. 50c--Elevation plane pattern with an infinitesimal monopole mounted on a composite ellipse model.

Let us first consider the engine effect, which is modelled as a finite circular cylinder. Recall that in the roll plane the engines had little effect and were neglected in the more general three-dimensional roll plane problem, which was a great simplification in the analysis. The solution of this problem is simply an extension of the finite cylinder scattering problem treated in Section III-C. The geometry used in this problem is illustrated in Fig. 51. Note that only the source fields incident on the engine have been modified in this situation which is accomplished using the techniques developed in the roll plane analysis of Section IV-B, in order to find the effective source locations. For example, the source field incident on the rear end cap of the engine is illustrated in Fig. 52. The location of the center of the cap is given by

$$(x_d = 0, y_d = d, z_d = -z' + \ell/2).$$

With this location known one can apply Eq. (76) to find the effective source location on the fuselage which is given by

$$x_e = \frac{a_f}{d} \sqrt{d^2 - a_f^2}$$

$$y_e = a_f^2/d$$

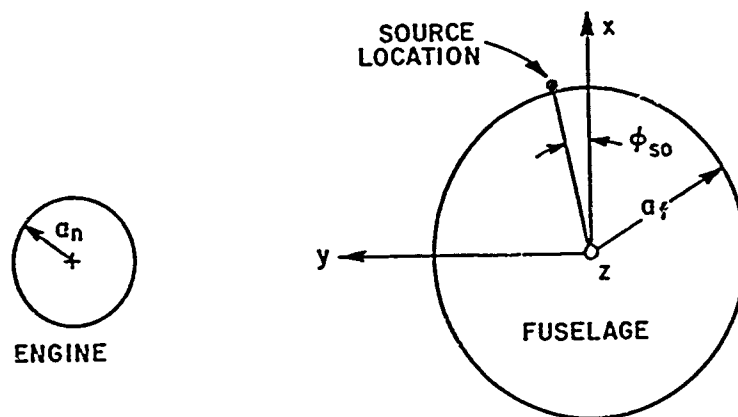
$$z_e = \frac{x_e(-z' + \ell/2)(\phi_e - \phi_{so})}{x_e(\phi_e - \phi_{so}) + (d - y_e)}$$

where $\phi_e = \tan^{-1} \left(\frac{a_f}{\sqrt{d^2 - a_f^2}} \right)$. With the effective source location

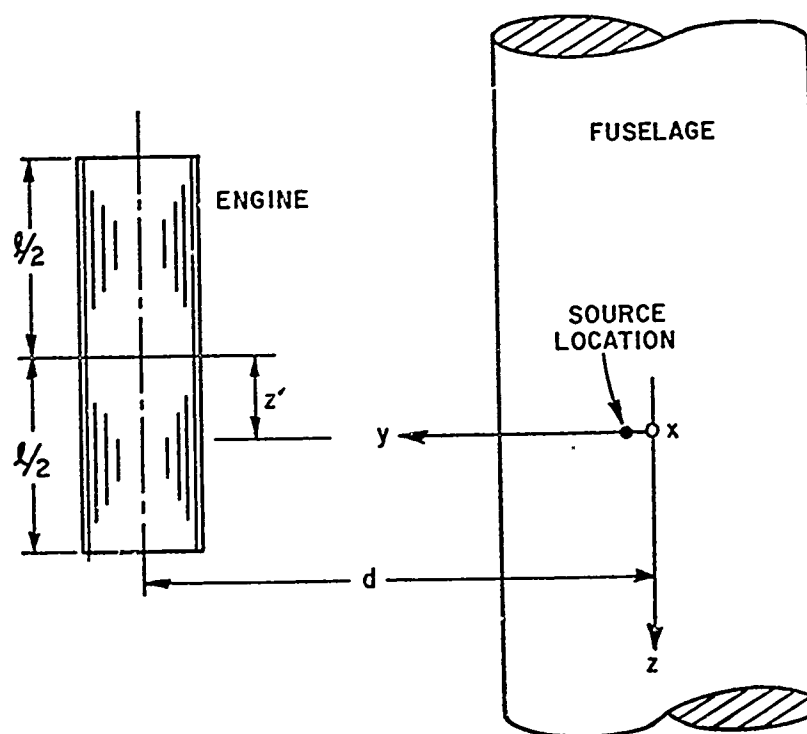
known one can apply the end cap scattering effects as given by Eqs. (51), (64). The source field value incident on the rear end cap is given by the modal solutions with the radiation direction defined by

$$\theta = \tan^{-1} \left(\frac{\sqrt{(-x_e)^2 + (d - y_e)^2}}{\ell/2 - z' - z_e} \right)$$

$$\phi = \tan^{-1} \left(\frac{d - y_e}{-x_e} \right)$$

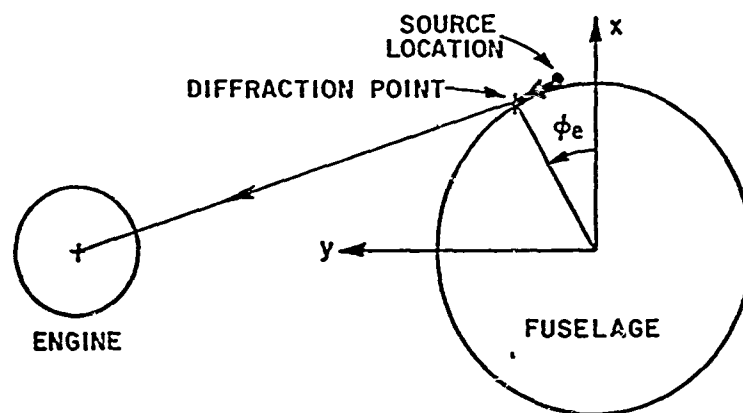


END VIEW

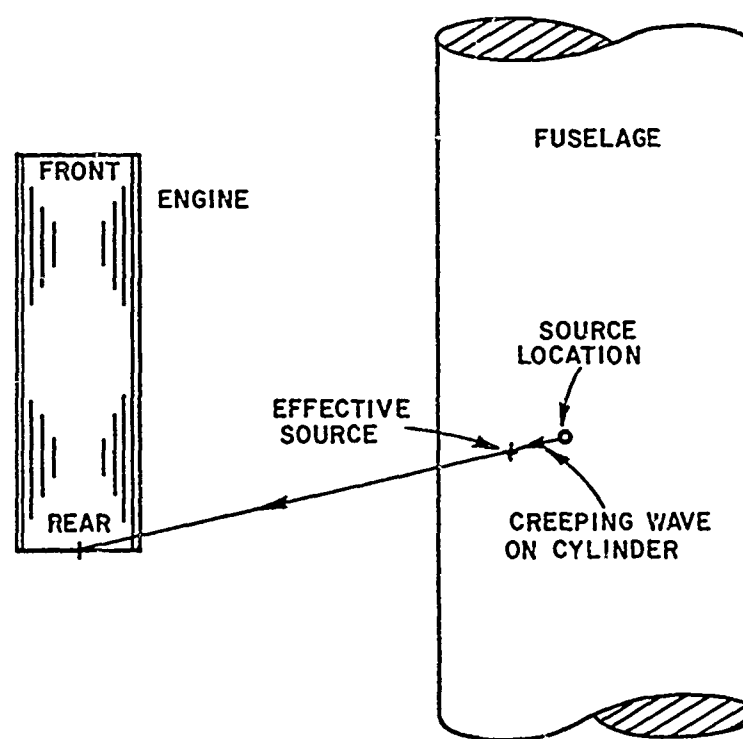


TOP VIEW

Fig. 51--Azimuth plane geometry with engine added.



END VIEW



TOP VIEW

Fig. 52--Geometry of source field incident on rear end cap.

Similar expressions can be developed for the effective source location and field value for the front end cap.

In order to include the effect of the cylindrical section one can apply the geometry illustrated in Fig. 53. The field incident on the engine is dependent on the desired radiation direction (θ_s , $\phi_s = 90^\circ$) and determined using the modal solutions with the direction given by

$$\theta = \theta_s$$

$$\phi = \tan^{-1} \left(\frac{\sqrt{d^2 - a_f^2}}{-1} \right)$$

Again the results of Section IV-B can be applied to determine the effective source position which in turn can be used in the near field cylinder problem. Using Eq. (77) one finds that

$$x_e = a_f \cos(90^\circ - \phi)$$

$$y_e = a_f \sin(90^\circ - \phi)$$

$$z_e = a_f \cos(90^\circ - \phi) \tan(90^\circ - \theta)(\pi/2 - \phi - \phi_{s0}).$$

with the actual source location on the fuselage defined by ($a_f, \phi_{s0}, z_{s0} = 0$). Note that this term is only included over the finite limits of the cylindrical section as shown in Fig. 53. This discontinuity in the cylinder scattered field should be compensated for by the edge diffracted field contributions from the ends of the finite engine. The engine scattered field is then added to the directly radiated source field using the superposition principle to obtain the total radiation pattern.

Some of the results of this study are presented in Figs. 54. Note that in each case the engine has very little effect on the total solution. The maximum deviation, for the cases considered, is less than 2 dB between the above solution and the solution that considers only the directly radiated term. This implies that one can to a good approximation leave the engine effect out of the solution in the azimuth plane provided that the source is limited to the region originally assumed. Finally, measured patterns were taken for the monopole case in Fig. 54a in which it was found that the engine played such a little effect that it was difficult to observe the measured pattern changes with and without the engine (finite cylinder).

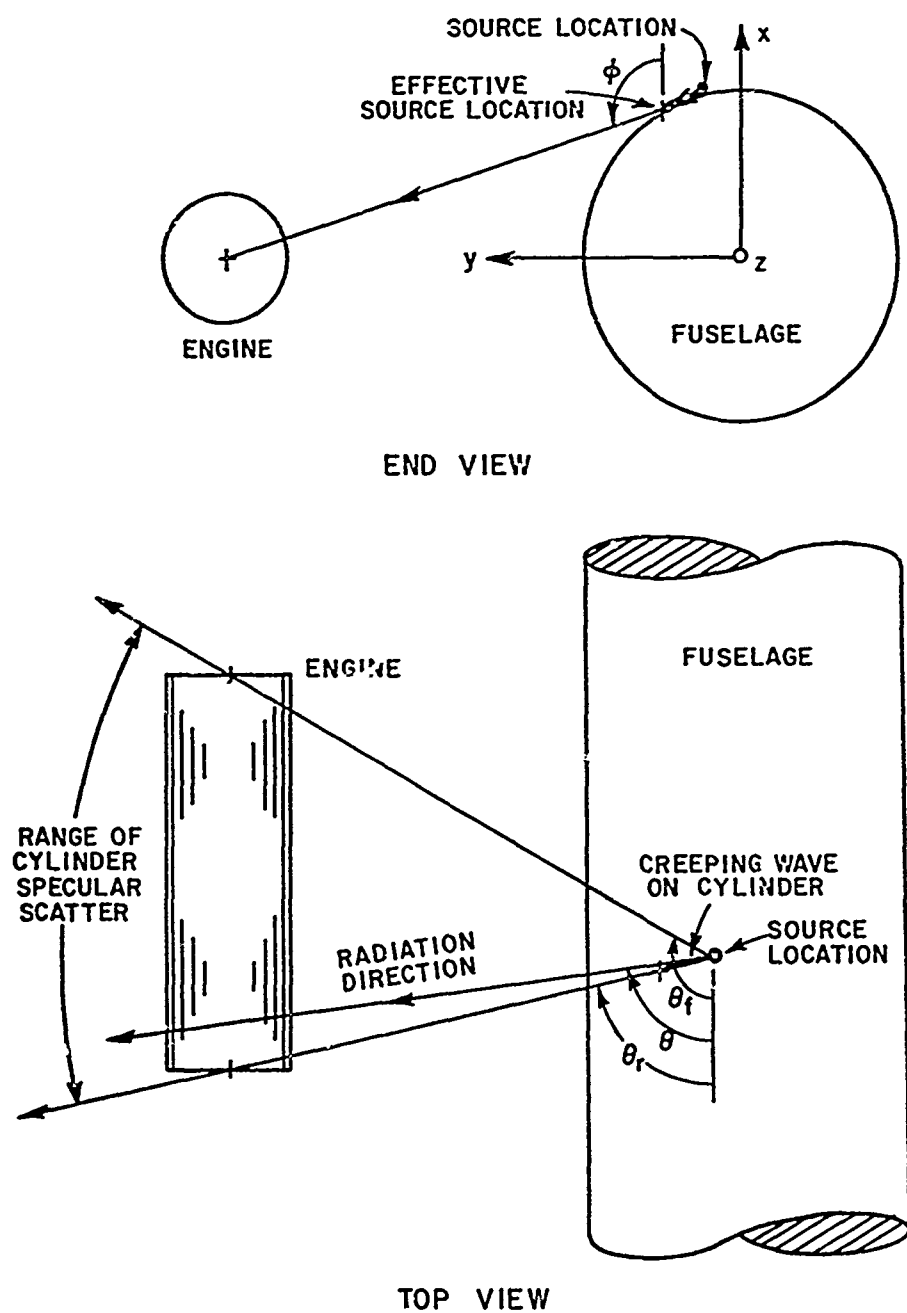


Fig. 53--Cylinder section scattered field.

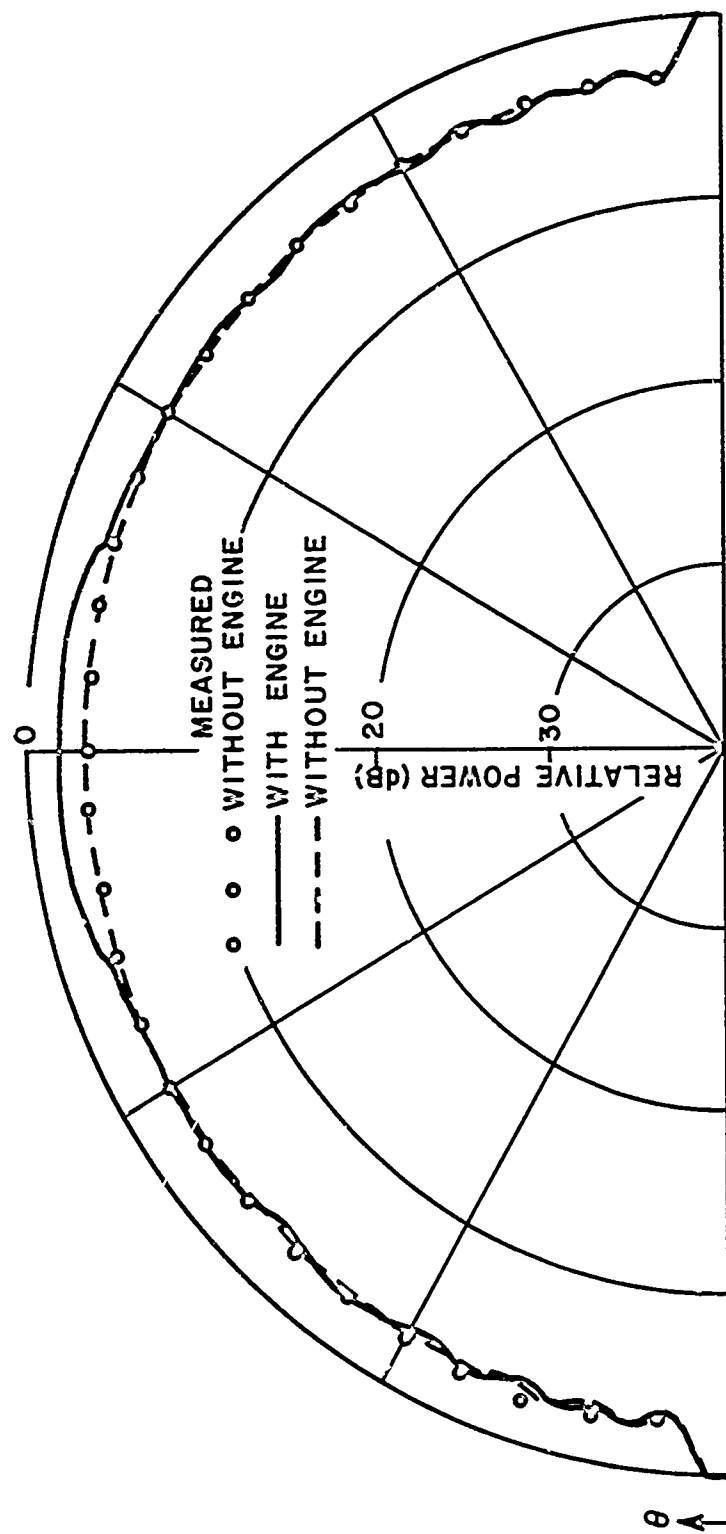


Fig. 54a--Azimuth plane pattern of monopole (E_ϕ) with and without engine.

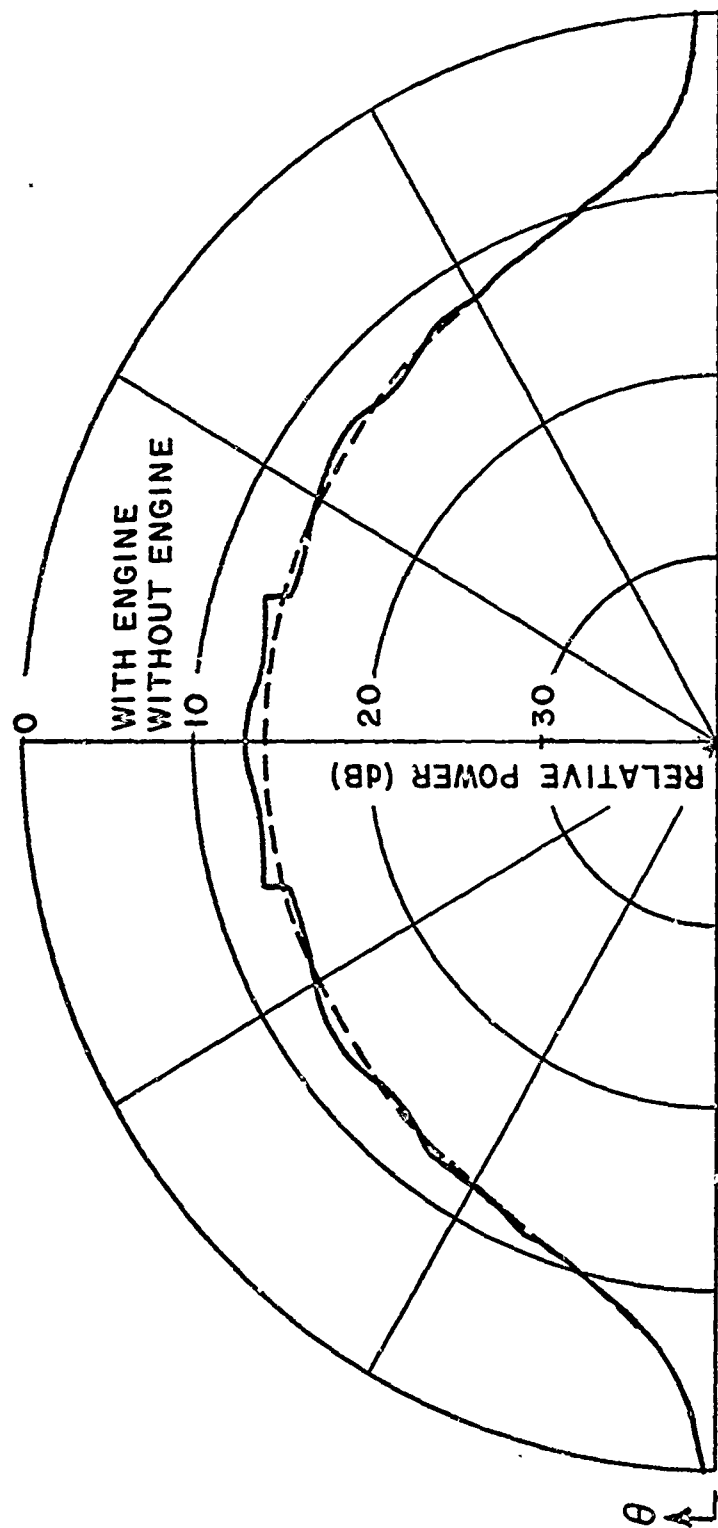


Fig. 54b--Azimuth plane pattern of circumferential slot (E_{θ}) with and without engine.

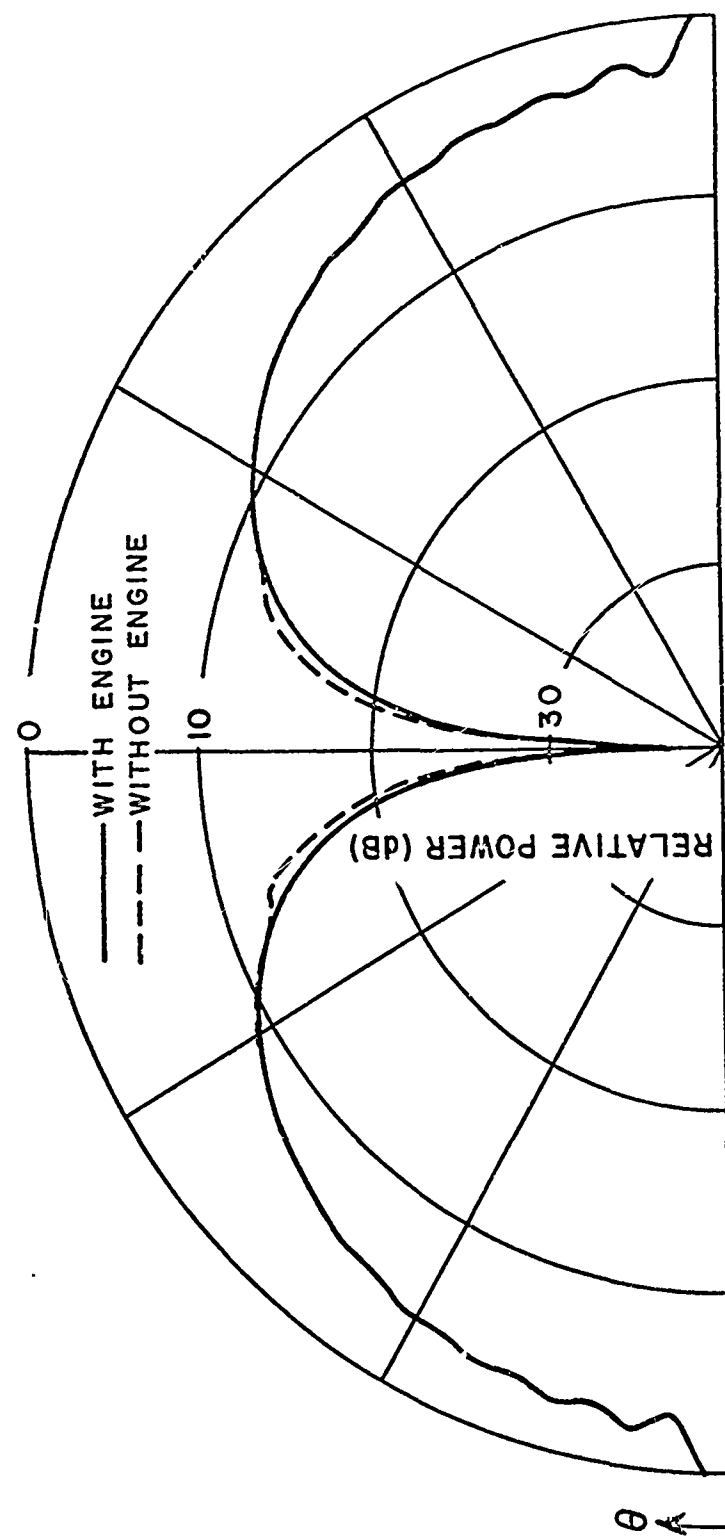


Fig. 54c--Azimuth plane pattern of circumferential slot (E_ϕ) with and without engine.

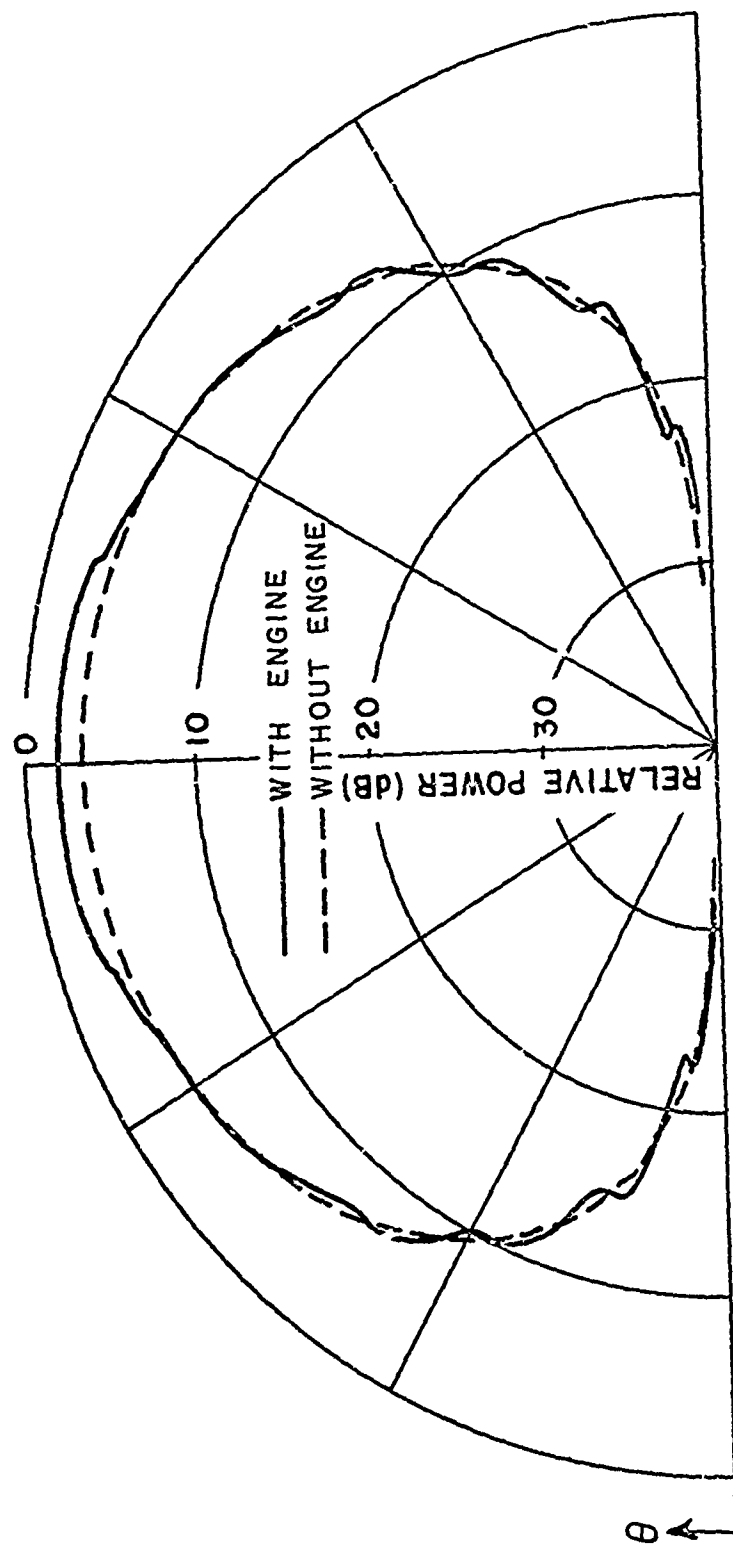


Fig. 54d--Azimuth plane pattern of axial slot (E_ϕ) with and without engine.

The wing and possibly horizontal stabilizer effect in the azimuth plane must also be considered. To analyze these structures one can simply apply the solutions presented for the three-dimensional roll plane problem of Section IV-B with only the desired radiation direction (θ_s, ϕ_s) being changed to those angles dictated by the desired azimuth pattern. Again these results are compared with and without the finite wing effect in order to ascertain their significance in the overall azimuth plane pattern.

Some of the results of this study are presented in Figs. 55. Again it is observed in each case that the wing has little effect on the azimuth plane patterns. In fact, what little effect it does have occurs in the small sector aft of the aircraft which might only be significant for our assumed infinite cylinder model. Thus, the wing can be neglected to a good approximation in the azimuth plane provided that the assumed geometry and source location are adequate to represent the actual on-aircraft antenna problem.

As a result of this study, it is apparent that the dominant scatterer in the azimuth plane is the fuselage. This effect must be taken into account in terms of a three-dimensional model of the fuselage if the resulting pattern is to be representative of actual on-aircraft antenna patterns. This problem is considered in the next chapter. Nevertheless, based on the results of this section one can to a good approximation compute the azimuth plane pattern simply by treating the antenna mounted on a reasonable model of the fuselage without analyzing the other secondary scattering effects.

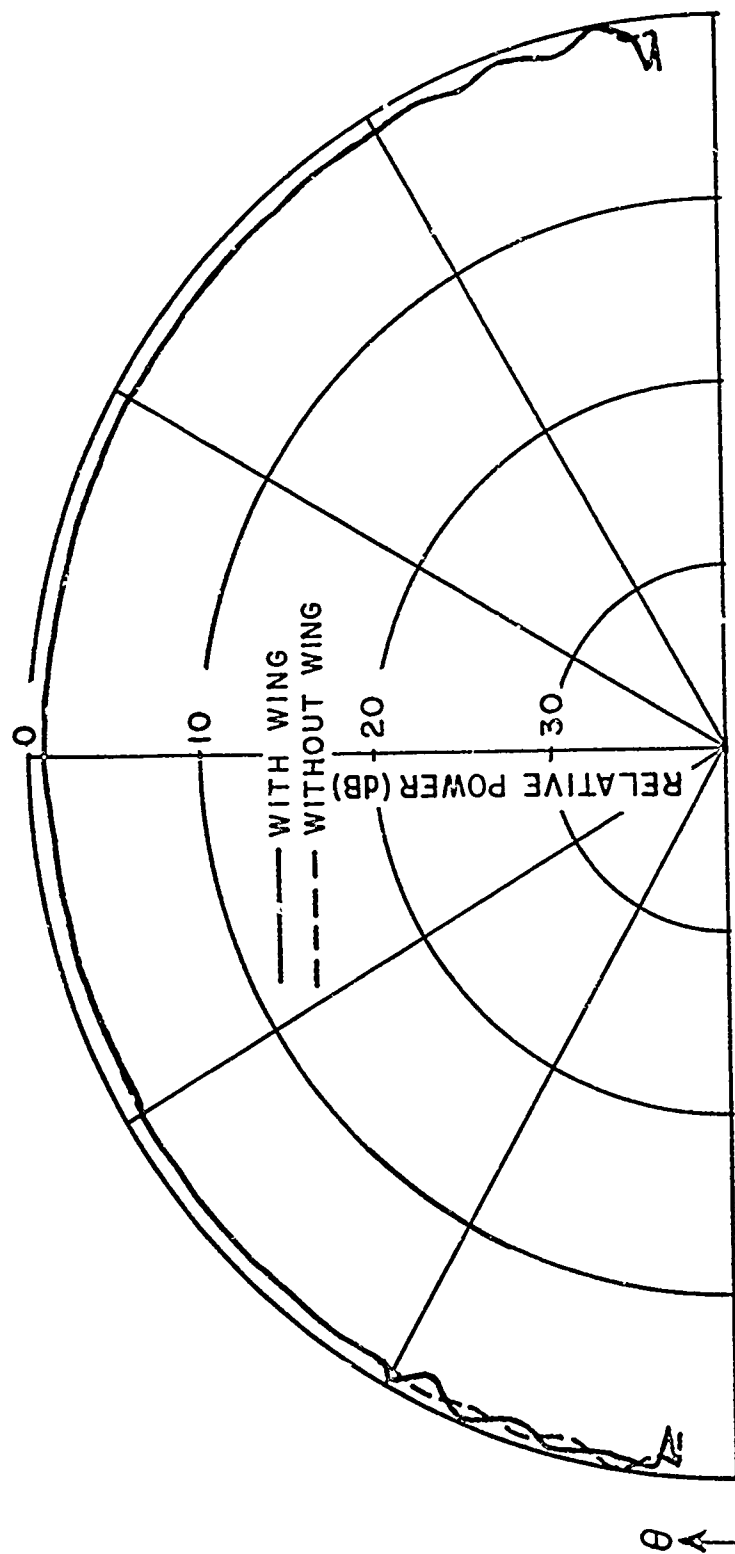


Fig. 55a--Azimuth plane pattern of monopole (E_ϕ)
with and without wing.

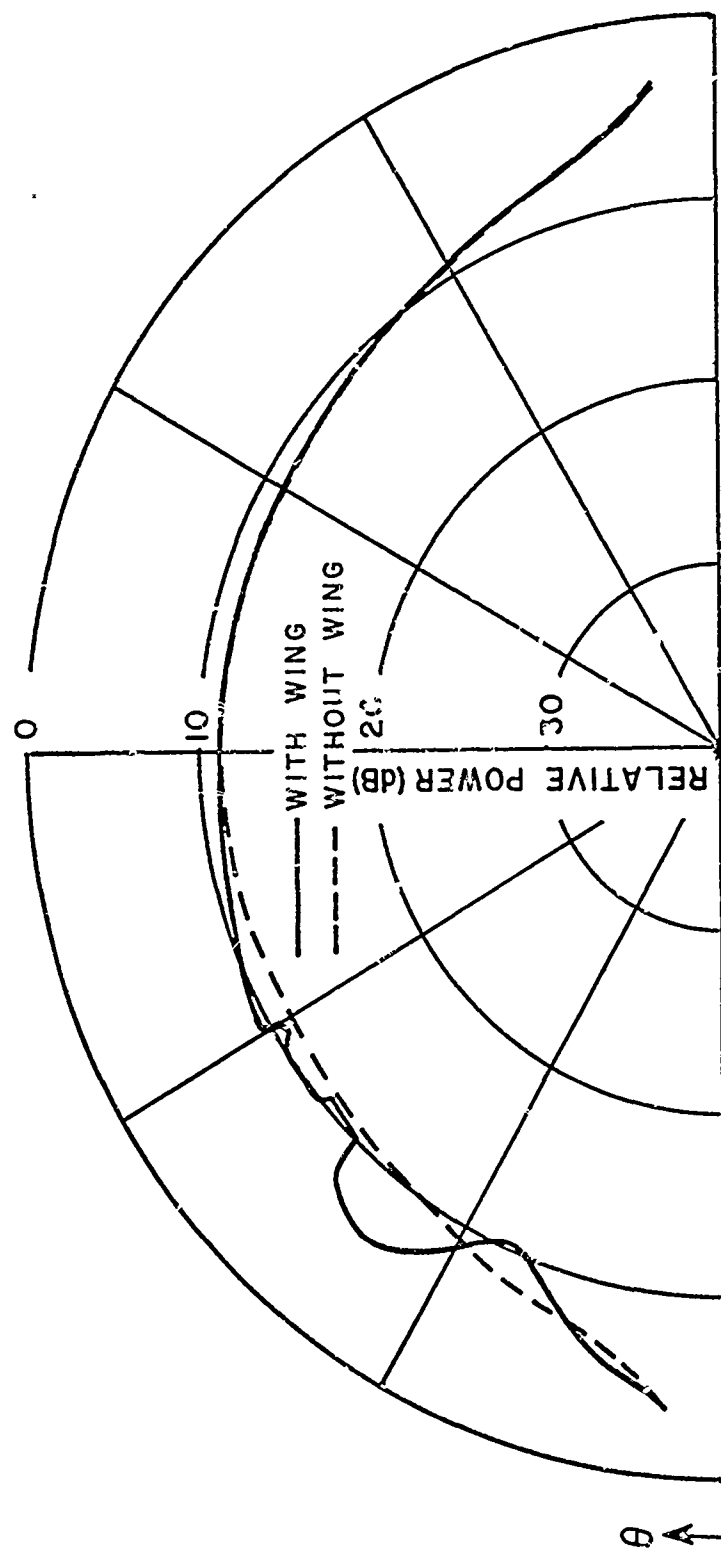


Fig. 55b--Azimuth plane pattern of circumferential slot (E_θ) with and without wing.

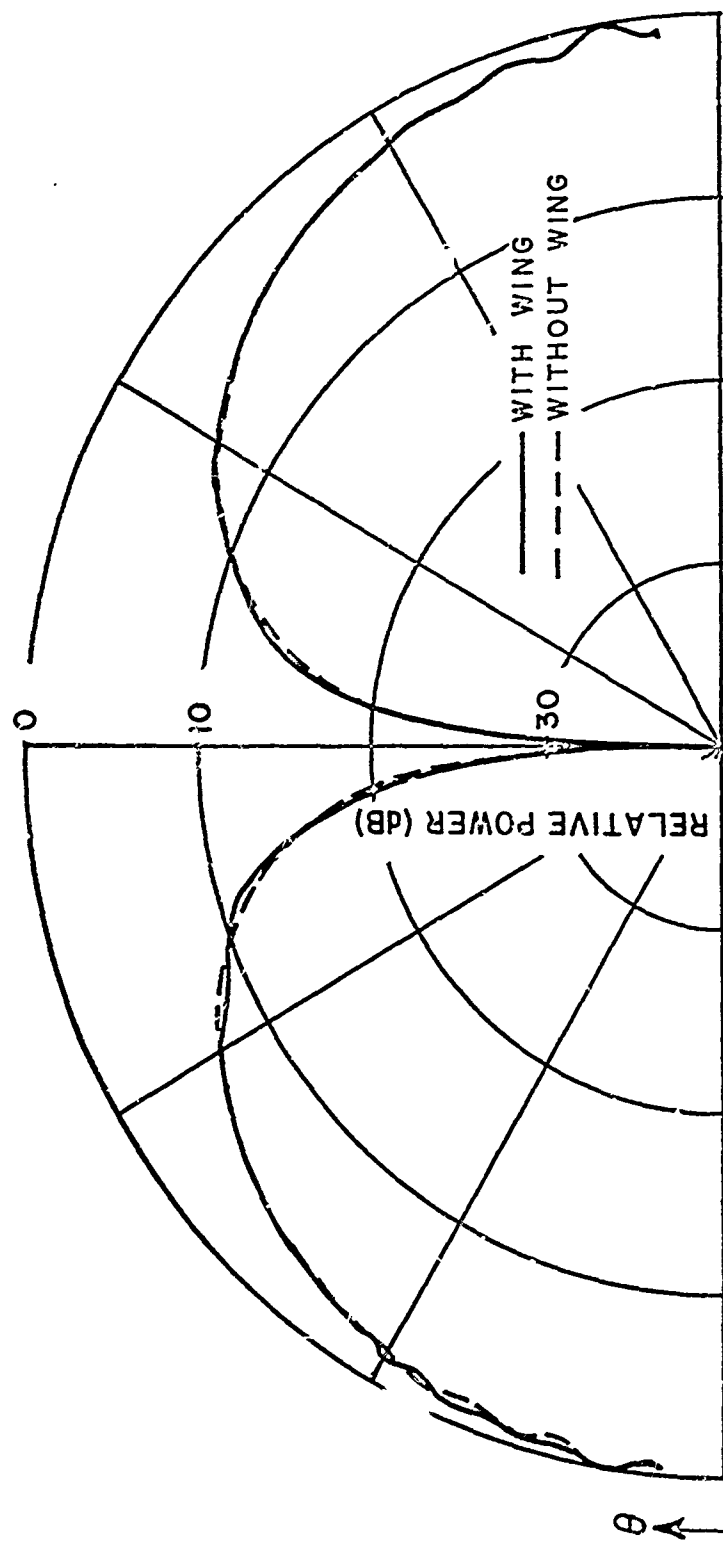


Fig. 55c--Azimuth plane pattern of circumferential slot (E_ϕ) with and without wing.

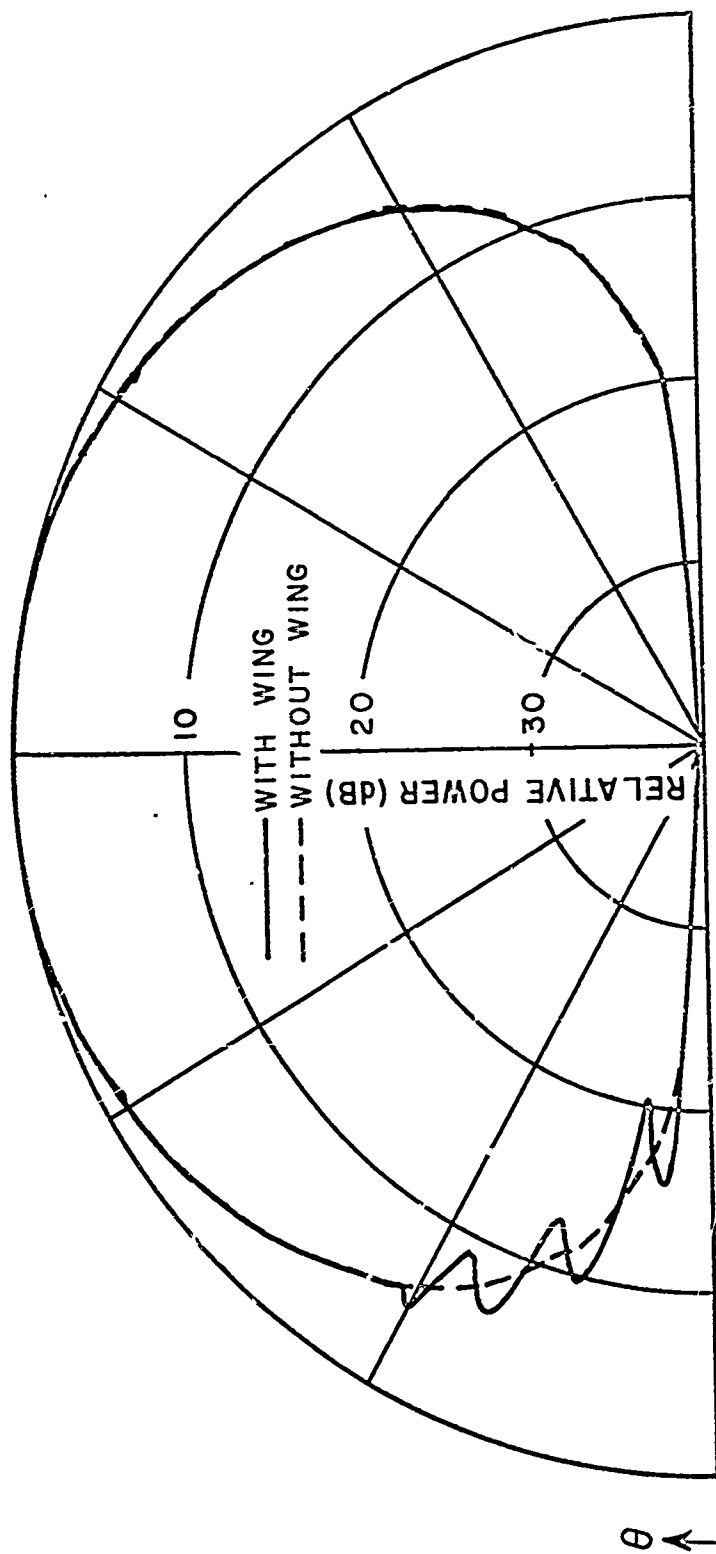


Fig. 55d--Azimuth plane pattern of axial slot (E_{ϕ})
with and without wing.

CHAPTER V

VOLUMETRIC PATTERNS OF ANTENNAS MOUNTED ON CONVEX SURFACES OF REVOLUTION

As stated earlier, for a source mounted on the fuselage of an arbitrary aircraft near the extreme top or bottom the fuselage shape has the dominant effect on the resulting antenna pattern. The wings and other flat plate structures can have strong effects in certain sectors of the pattern but they are not as dominant as the fuselage especially when the complete volumetric pattern is considered. For these reasons the volumetric pattern of an antenna mounted on a three-dimensional isolated fuselage is analyzed by the method presented in this chapter. Nevertheless, the wings and various other structures could be added to this solution in the future as was done in the three-dimensional roll plane problem.

In the previous chapter, aircraft models were considered that would resemble a wide variety of aircraft shapes and yet could also be analyzed with reasonable accuracy. In this case, it is quite obvious that the three-dimensional nature of the fuselage must be modelled if one is to adequately determine volumetric patterns. In the elevation plane it was found that the profile of the fuselage had to be accurately represented. This resulted in the development of the Section Matching GTD solution in which the profile was described by a finite number of points. Whereas in the roll plane, the circular cross-section was found to be adequate. One obvious extension of these observations is to consider a fuselage which is analytically described by a surface of revolution. In this case the profile is again described by a set of points which in turn are revolved about the axis of the fuselage. In this way the important features of our past studies in the three principal planes are incorporated in this new three-dimensional study. Not only is this shape quite versatile but it can also be analyzed by extending the techniques that were developed previously. This will become apparent in the following discussion.

As presented in Section II-D the rays which propagate outward from a source travel around the surface along geodesic paths while energy is continually being diffracted in the tangent direction at each point along the path. Thus, the first obstacle in computing the volumetric pattern of an antenna mounted on a three-dimensional convex body is finding a numerical technique to specify the geodesic paths. One such solution is based on tensor analysis from which two differential equations are given in Appendix II as

$$(84) \quad \frac{d^2 \theta}{d\lambda^2} + \frac{\frac{dR}{d\theta} \left(\frac{d^2 R}{d\theta^2} + R \right)}{\left(\frac{dR}{d\theta} \right)^2 + R^2} \left(\frac{d\theta}{d\lambda} \right)^2 - \frac{R \sin \theta (R \cos \theta + \frac{dR}{d\theta} \sin \theta)}{\left(\frac{dR}{d\theta} \right)^2 + R^2} \left(\frac{d\phi}{d\lambda} \right)^2 = 0$$

$$\frac{d^2 \phi}{d\lambda^2} + \frac{2(R \cos \theta + \frac{dR}{d\theta} \sin \theta)}{R \sin \theta} \frac{d\theta}{d\lambda} \frac{d\phi}{d\lambda} = 0$$

where λ is the arclength of the geodesic path. The geometry of this problem is illustrated in Fig. 56. Note that the surface is defined by a set of points, which are used to specify $R(\theta)$ for $0 < \theta < 180^\circ$. For the cases considered here $R(\theta)$ is defined every $\frac{1}{2}^\circ$ which requires a total of 361 points to define the surface.

Consider a point on the surface defined by θ and ϕ which is a function of the arclength (λ). Using a power series expansion one finds that

$$\theta(\lambda) = \sum_{n=0}^{\infty} \frac{\theta^{(n)}(0)}{n!} \lambda^n, \text{ and}$$

$$\phi(\lambda) = \sum_{m=0}^{\infty} \frac{\phi^{(m)}(0)}{m!} \lambda^m.$$

If it is assumed that one moves a very short distance ($\Delta\lambda$) along a given geodesic path then

$$(85) \quad \theta(\lambda + \Delta\lambda) \simeq \theta(\lambda) + \left. \frac{d\theta}{d\lambda} \right|_{\lambda} \Delta\lambda + \frac{1}{2} \left. \frac{d^2 \theta}{d\lambda^2} \right|_{\lambda} \Delta\lambda^2, \text{ and}$$

$$\phi(\lambda + \Delta\lambda) \simeq \phi(\lambda) + \left. \frac{d\phi}{d\lambda} \right|_{\lambda} \Delta\lambda + \frac{1}{2} \left. \frac{d^2 \phi}{d\lambda^2} \right|_{\lambda} \Delta\lambda^2.$$

Now referring back to the differential equations of Eq. (84) one must define the source location and starting direction in order to completely specify a geodesic path. However, with this knowledge one can use Eq. (84) to find the second derivatives of θ and ϕ with respect

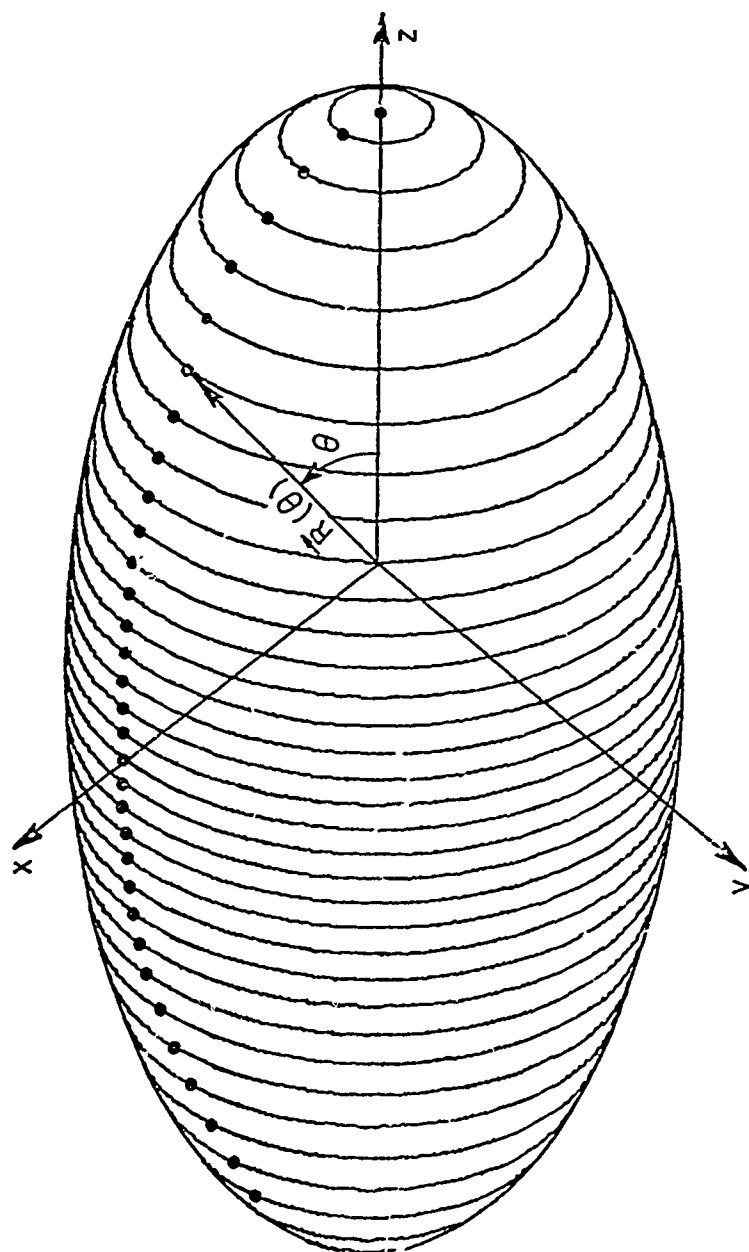


Fig. 56--Surface of revolution described by a finite set of points.

to λ at the point (θ, ϕ) as given by

$$(86) \quad \left. \frac{d^2 \theta}{d\lambda^2} \right|_{\lambda} = - \left[\frac{\frac{dR}{d\theta} \left(\frac{d^2 R}{d\theta^2} + R \right)}{\left(\frac{dR}{d\theta} \right)^2 + R^2} \left(\frac{d\theta}{d\lambda} \right)^2 - \frac{R \sin \theta \left(R \cos \theta + \frac{dR}{d\theta} \sin \theta \right)}{\left(\frac{dR}{d\theta} \right)^2 + R^2} \left(\frac{d\phi}{d\lambda} \right)^2 \right]_{\lambda}$$

$$\left. \frac{d^2 \phi}{d\lambda^2} \right|_{\lambda} = - \left[2 \frac{R \cos \theta + \frac{dR}{d\theta} \sin \theta}{R \sin \theta} \frac{d\theta}{d\lambda} \frac{d\phi}{d\lambda} \right]_{\lambda}$$

Thus by defining the initial conditions of the differential equation θ , $\frac{d\theta}{d\lambda}$, ϕ , and $\frac{d\phi}{d\lambda}$, one can solve for $\frac{d^2 \theta}{d\lambda^2}$ and $\frac{d^2 \phi}{d\lambda^2}$ using the above expressions. Substituting these results into Eq. (85), the values of $\theta(\lambda + \Delta\lambda)$ and $\phi(\lambda + \Delta\lambda)$ are located approximately which in turn defines a new point along the geodesic path. The derivatives of θ and ϕ at the new point are given by

$$(87) \quad \left. \frac{d\theta}{d\lambda} \right|_{\lambda + \Delta\lambda} = \left. \frac{d\theta}{d\lambda} \right|_{\lambda} + \left. \frac{d^2 \theta}{d\lambda^2} \right|_{\lambda} \Delta\lambda, \text{ and}$$

$$\left. \frac{d\phi}{d\lambda} \right|_{\lambda + \Delta\lambda} = \left. \frac{d\phi}{d\lambda} \right|_{\lambda} + \left. \frac{d^2 \phi}{d\lambda^2} \right|_{\lambda} \Delta\lambda.$$

Knowing these terms one can again use Eq. (86) to find $\left. \frac{d^2 \theta}{d\lambda^2} \right|_{\lambda + \Delta\lambda}$ and $\left. \frac{d^2 \phi}{d\lambda^2} \right|_{\lambda + \Delta\lambda}$ which can be used to locate a third point along the given geodesic path. By continuing this process one can completely trace out a geodesic ray path on an arbitrary surface of revolution. Some examples of geodesic paths on surfaces of revolution are illustrated in Figs. 57 and 58. Note that the geodesics on a sphere are great circles as is found to be the case in checking our formulation and is shown in Fig. 57.

An important question yet to answer is just how large can $\Delta\lambda$ be without causing our solution to be inaccurate. This is a difficult question to answer; however, some knowledge of the error can be found using Clairaut's theorem[53] which states that

$$r \sin \alpha = \text{constant}$$

for a given geodesic curve on a surface of revolution. Note that r

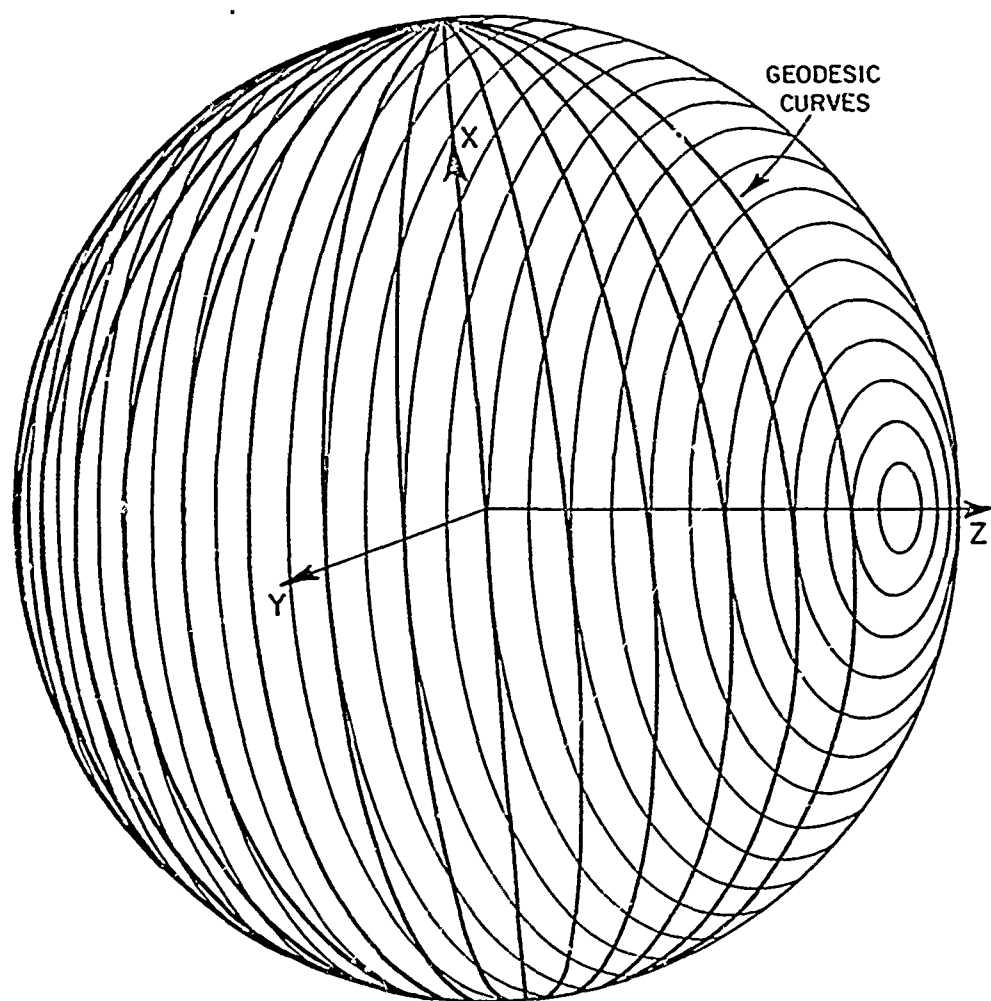


Fig. 57--Geodesic curves on a sphere with the source
at $\theta_0 = 90^\circ$, $\phi_0 = 0^\circ$.

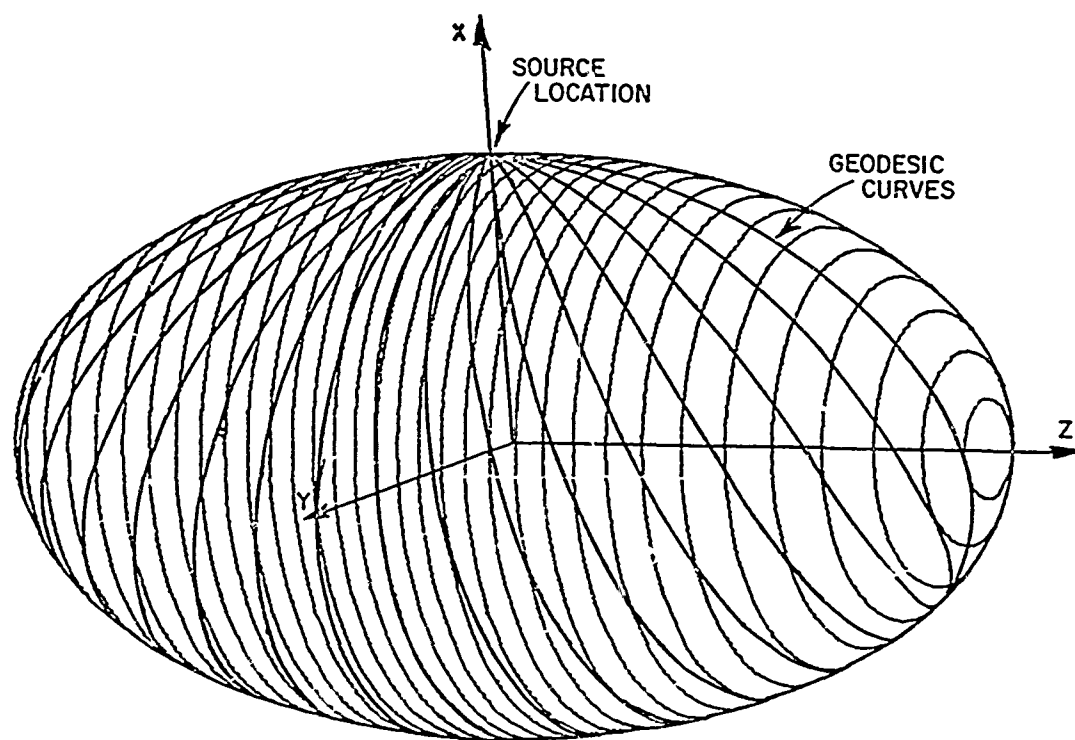


Fig. 58a--Geodesic curves on a $4\lambda \times 2\lambda$ prolate spheroid with the source at $\theta_0 = 90^\circ$, $\phi_0 = 0$.

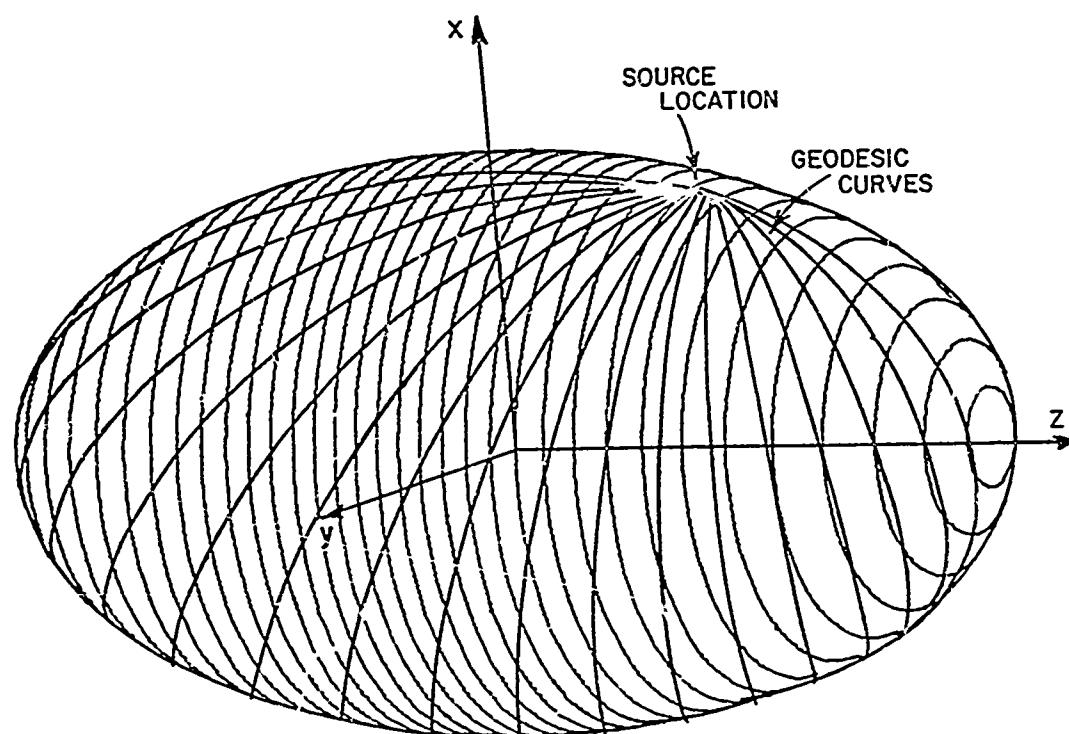


Fig. 58b--Geodesic curves on a $4\lambda \times 2\lambda$ prolate spheroid with the source at $\theta_0 = 45^\circ$, $\phi_0 = 0^\circ$.

is the radius of the parallel passing through the given point on the geodesic path and α is the solid angle between the geodesic direction and the meridian passing through that point, the meridian being the profile shaped curve that is revolved about the fuselage axis. Thus, one can examine the error by the variance of the constant defined above as he progresses along a given geodesic path. For example, on a prolate spheroid with semi-major and semi-minor dimensions given, respectively, by 4λ and 2λ and with $\Delta\lambda = 0.005\lambda$ it was found that Clairaut's theorem was satisfied to within 3 significant figures for several geodesic paths as illustrated in Table IV.

As stated earlier $R(\theta)$ is defined every $\frac{1}{2}^\circ$ for $0 < \theta < 180^\circ$; however, as observed in the previous equation, not only $R(\theta)$ but $\frac{dR}{d\theta}$ and $\frac{d^2R}{d\theta^2}$ must be known over the complete surface. To determine this information a simple 4th order polynomial was found that passed through 5 consecutive points defining the surface. The derivatives of $R(\theta)$ are then determined at the center point of each section using the same approach presented in Section IV-C. The values of these terms between the surface defining points are found using

$$R(\theta) \sim R(\theta_1) + \left. \frac{dR}{d\theta} \right|_{\theta_1} (\theta - \theta_1) + \left. \frac{d^2R}{d\theta^2} \right|_{\theta_1} \frac{(\theta - \theta_1)^2}{2}$$

$$\frac{dR(\theta)}{d\theta} \sim \left. \frac{dR}{d\theta} \right|_{\theta_1} + \left. \frac{d^2R}{d\theta^2} \right|_{\theta_1} (\theta - \theta_1)$$

$$\frac{d^2R(\theta)}{d\theta^2} \sim \left. \frac{d^2R}{d\theta^2} \right|_{\theta_1} + \frac{\left. \frac{d^2R}{d\theta^2} \right|_{\theta_2} - \left. \frac{d^2R}{d\theta^2} \right|_{\theta_1}}{(\theta_2 - \theta_1)} (\theta - \theta_1),$$

where θ is an arbitrary position parameter, θ_1 is the closest $\frac{1}{2}^\circ$ value to θ which is also less than θ and $\theta_2 = \theta_1 + \frac{1}{2}^\circ$.

A second solution for the geodesic paths is found using the calculus of variations. Using this approach one forms an integral of the arclength along a path on the surface which can be solved for an extremum. This extremum curve is simply the geodesic path. In this case, the integral of the arclength is given by

$$L = \int \sqrt{\left(\frac{dR}{d\theta} \right)^2 + R^2 + R^2 \sin^2 \theta \left(\frac{d\phi}{d\theta} \right)^2} d\theta$$

which has an extremum given by[53]

$$\phi = \int \sqrt{\frac{C \left[\left(\frac{dR}{d\theta} \right)^2 + R^2 \right]}{R^4 \sin^4 \theta - CR^2 \sin^2 \theta}} d\theta$$

with C being a constant. One can then relate C to the initial direction of a given geodesic curve and compare this result with the previous solution.

TABLE IV
CLAIRAUT'S CONSTANT ON A SPHEROID
USING TENSOR ANALYSIS SOLUTION

$\gamma = 100^\circ$			$\gamma = 120^\circ$		
θ	ϕ	Clairaut Constant	θ	ϕ	Clairaut Constant
89.97513	0.14106	1.96962	89.92838	0.12405	1.73205
87.00310	17.07253	1.96961	85.07056	8.56457	1.73199
85.01104	28.65405	1.96961	80.00671	17.53570	1.73193
84.01189	34.59238	1.96960	75.03504	26.70357	1.73188
82.00377	46.91133	1.96960	70.04465	36.49352	1.73184
80.01470	59.82879	1.96960	65.02831	47.23272	1.73181
79.00000	66.80015	1.96960	60.02371	59.28953	1.73178
78.01033	73.92622	1.96959	55.03424	73.37006	1.73177
76.01345	89.65047	1.96959	51.51429	85.24570	1.73176
$\gamma = 140^\circ$			$\gamma = 160^\circ$		
θ	ϕ	Clairaut Constant	θ	ϕ	Clairaut Constant
89.89027	0.09207	1.28557	89.86540	0.04899	0.68404
80.08774	8.39953	1.28533	79.97284	3.68367	0.68382
69.99167	17.49768	1.28513	70.08763	7.52630	0.68362
60.03110	27.70494	1.28496	60.02801	11.92162	0.68247
55.04909	33.58741	1.28491	50.06772	17.15761	0.68336
45.00158	48.15512	1.28483	40.02862	24.04913	0.68325
40.04995	57.48482	1.28479	30.02665	34.07472	0.68300
35.04354	69.43960	1.28473	25.04869	41.34835	0.68273
33.00055	75.42781	1.28470	20.13786	51.48320	0.68226

As illustrated in Fig. 59 the values of the position parameters (θ, ϕ) for the given curves compare extremely well for the two solutions. Note that the above integral solution is evaluated simply using Simpson's rule. In addition, it is shown in Fig. 60 that the tangent directions (θ_t, ϕ_t) of the various geodesic curves found using the two solutions compare very favorably. Recall that the radiation direction is specified by the tangent to the geodesic path. The actual solutions used to compute the tangent directions will be presented later.

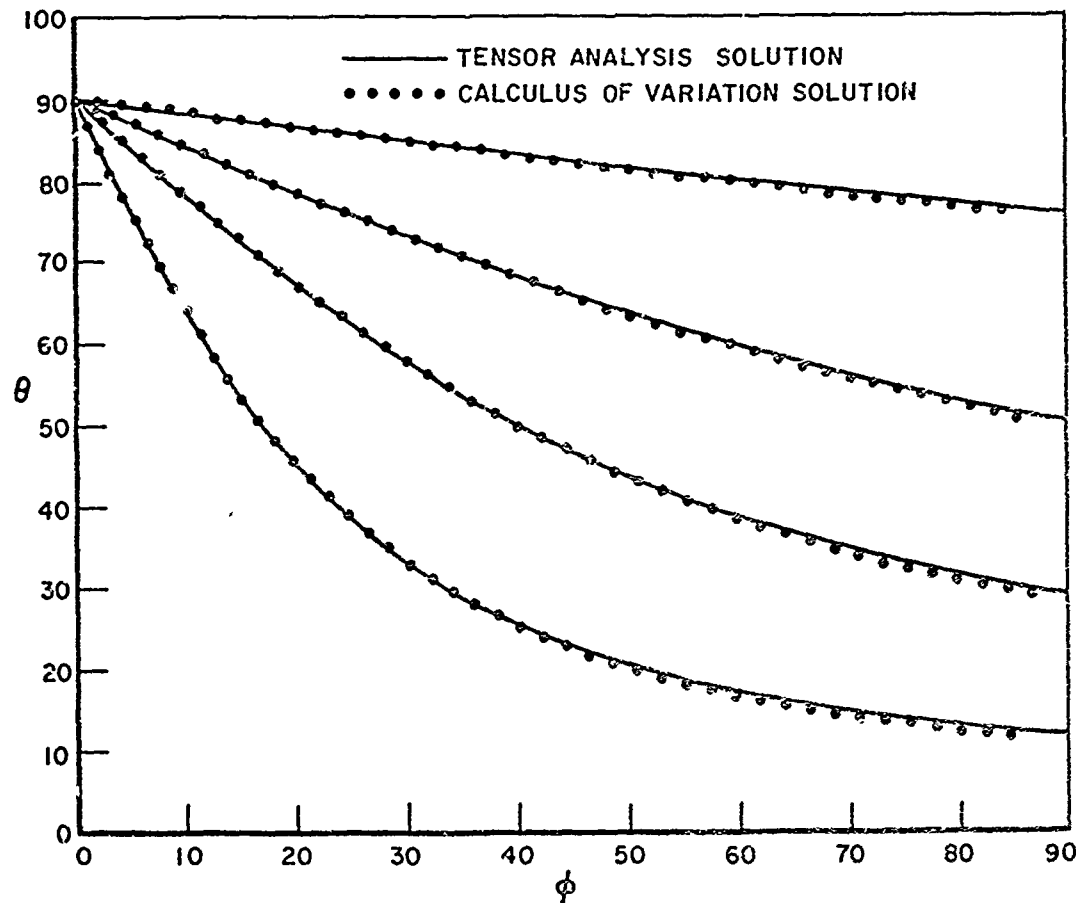


Fig. 59--Comparison of geodesic paths using tensor analysis and calculus of variations solutions.

Finally, in Table V the values of Clairaut's constants are shown for various values of C using the above integral solution for the geodesic path. Again this constant remains unchanged through 3 significant figures for the cases considered.

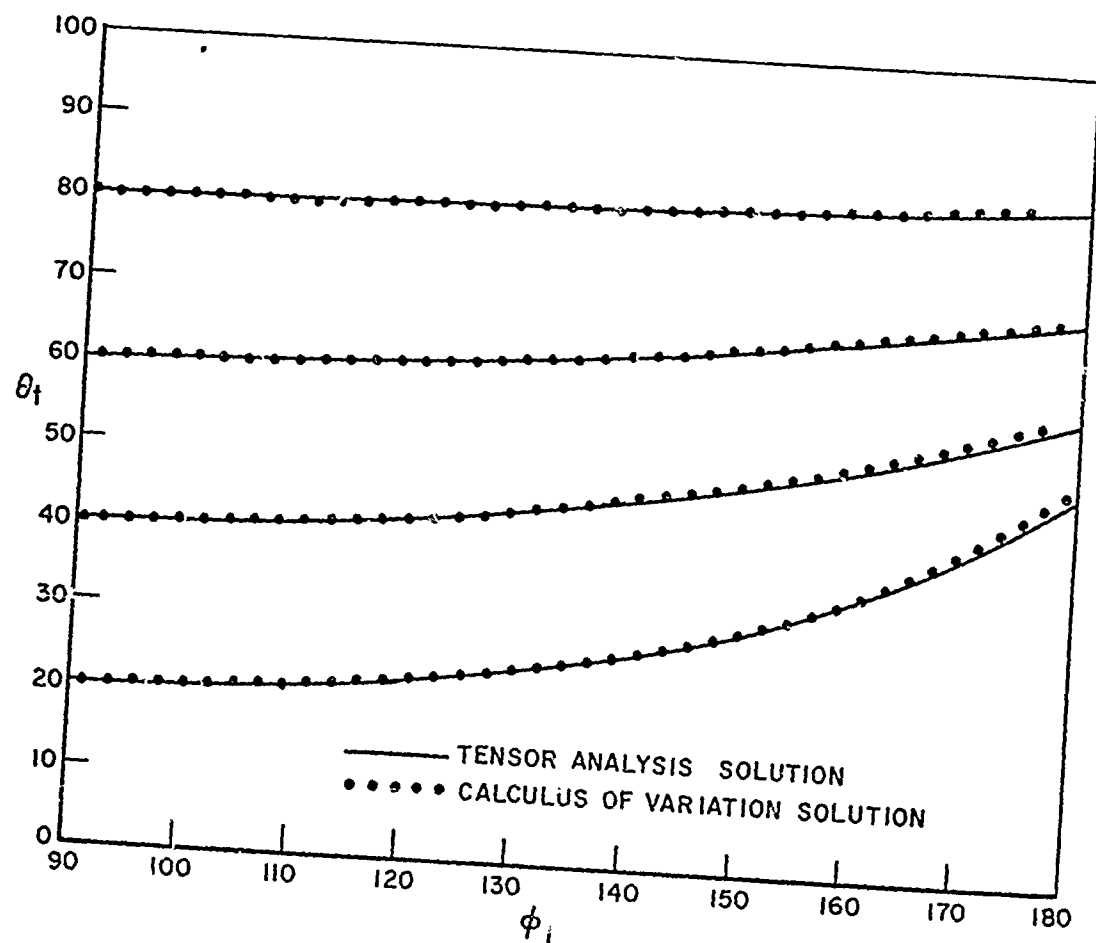


Fig. 6C--Comparison of tangent direction (θ_t, ϕ_t) using the geodesic solutions.

Now that the geodesic paths are known to a good approximation on an arbitrary surface of revolution, the radiation direction (or geodesic tangent) must be found for each path. In other words, if the radiated field in a given direction is desired one must know the appropriate geodesic path or paths to take in order that the tangent be in the desired radiation direction. To obtain this information one must first generate a set of test curves which are formed using known geodesic paths and plotting the resulting tangent angles (θ_t, ϕ_t). In order to get a uniform set of test curves one must consider rays which propagate outward from the source in all directions.

TABLE V
CLAIRAUT'S CONSTANT ON A SPHEROID
USING CALCULUS OF VARIATION SOLUTION

$\gamma = 100^{\circ}$			$\gamma = 120^{\circ}$		
θ	ϕ	Clairaut Constant	θ	ϕ	Clairaut Constant
89.97513	0.00000	1.96962	89.92838	0.00000	1.73205
87.00370	16.98105	1.96961	85.07056	8.67377	1.73199
85.01104	28.38179	1.96961	80.00671	17.48598	1.73193
84.01189	34.15925	1.96960	75.03504	26.62195	1.73188
82.00377	45.96819	1.96960	70.04465	36.30131	1.73184
80.01470	58.27634	1.96960	65.02831	46.80939	1.73181
79.00000	64.69234	1.96960	60.02371	58.55346	1.73178
78.01033	71.33482	1.96959	55.03424	72.18228	1.73177
76.01345	85.51688	1.96959	51.51429	83.44494	1.73176
$\gamma = 140^{\circ}$			$\gamma = 160^{\circ}$		
θ	ϕ	Clairaut Constant	θ	ϕ	Clairaut Constant
89.89027	0.00000	1.28557	89.86540	0.00000	0.68404
80.08774	8.46014	1.28533	79.97284	3.66851	0.68382
69.99167	17.42221	1.28513	70.08763	7.54001	0.68362
60.03110	27.56524	1.28496	60.02801	11.87875	0.68347
55.04909	33.38832	1.28491	50.96772	17.07832	0.68336
45.00158	47.60200	1.28483	40.02862	23.33207	0.68325
40.04995	56.76927	1.28479	30.02665	33.60774	0.68300
35.04354	68.30339	1.28473	25.04869	40.67232	0.68273
33.00055	73.91109	1.28470	20.13786	50.59393	0.68226

Using the geometry illustrated in Fig. 61 a set of test curves is defined as a function of the starting direction angle (γ) where $0 \leq \gamma \leq 180$. Note that the source position is defined by $[R(\theta_0), \phi_0, \psi_0 = 0]$. The vectors \hat{e}_1 and \hat{e}_2 are the unit tangent vectors to the surface which are defined in the $\psi = 0$ plane by

$$\hat{e}_1 = \frac{\left[\frac{dR}{d\theta} \sin \theta + R \cos \theta \right] \hat{x} + \left[\frac{dR}{d\theta} \cos \theta - R \sin \theta \right] \hat{z}}{\sqrt{\left(\frac{dR}{d\theta} \right)^2 + R^2}}$$

$$\hat{e}_2 = \hat{y}.$$

The starting direction of any arbitrary ray path is defined by

$$\hat{s} = \cos \gamma \hat{e}_1 + \sin \gamma \hat{e}_2,$$

where these terms can be related to $d\theta/d\lambda$ and $d\phi/d\lambda$ by

$$\left. \frac{d\theta}{d\lambda} \right|_{\theta_0} \approx \frac{\cos \gamma}{\sqrt{\left(\frac{dR}{d\theta} \right)^2 + R^2}} \Big|_{\theta_0}$$

$$\left. \frac{d\phi}{d\lambda} \right|_{\theta_0} \approx \frac{\sin \gamma}{R \sin \theta} \Big|_{\theta_0}$$

These expressions give the initial conditions used to solve the differential equations of Eq. (84).

Based on our results, solving for the test curves with $\Delta\gamma = 2\frac{1}{2}^\circ$ was satisfactory to find adequate values for the actual curves used in the pattern calculation. For example, the test curves are shown in Fig. 62 for a source mounted at the top of a prolate spheroid. Then any desired radiation direction can be plotted on this graph, which in turn can be used through an interpolation procedure to determine the value or values of the starting directions (γ) from the source. In this way all the dominant ray paths can be traced out with the associated field values summed in the far field to give the complete radiation pattern. Note that the test curves need only be determined for $0 \leq \gamma < 180^\circ$, since for a surface of revolution the results in the other half space are simply the mirror image.

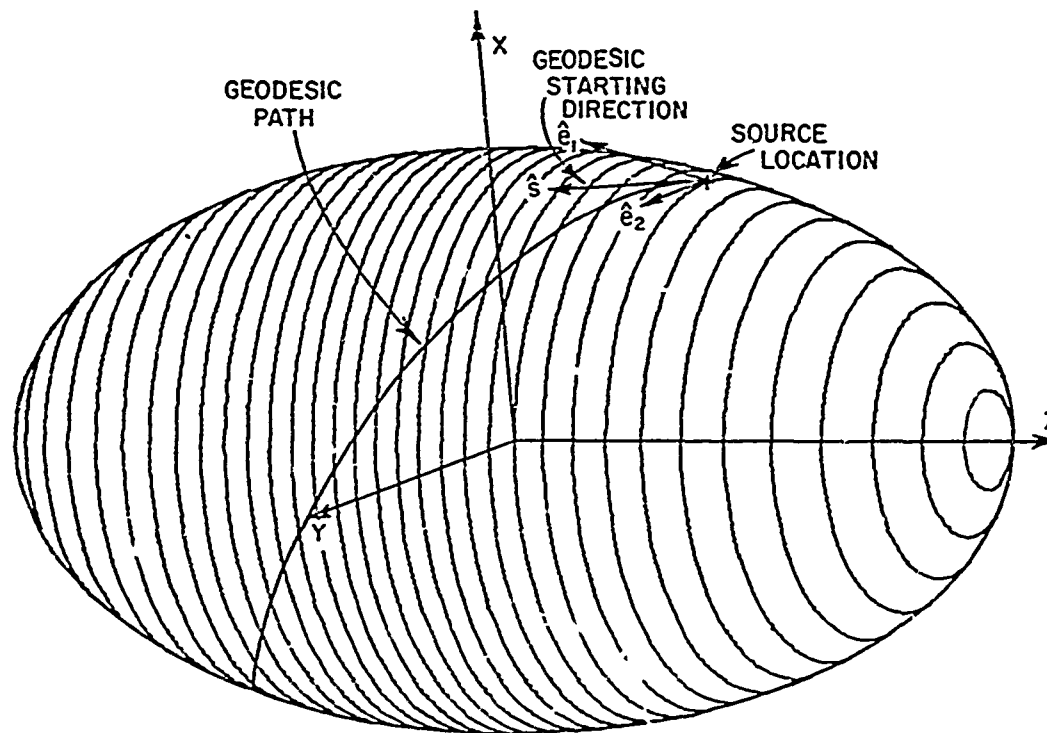


Fig. 61--Starting direction of geodesic path which is defined by the angle (γ).

To illustrate the validity of this technique the resulting radiating angles are presented in Table VI for various desired radiation directions. Note that as the errors increase, the resulting amplitudes of the field values are decreasing which tends to reduce the total error in the final result. This results from the fact that the error increases with path length (ℓ) due to the numerical computations but the longer the path the more the field is attenuated due to $e^{-\alpha\ell}$ in the GTD field expressions.

Now that the various geodesic paths are identified, one must determine the various parameters necessary for the field calculations using the GTD approach presented in Section II-C. First, let us consider the longitudinal and transverse radius of curvature. In order to define these terms consider the curvilinear coordinates given by \hat{t} , \hat{n} , and \hat{b} as illustrated in Fig. 63. Note that \hat{t} is the unit tangent vector, \hat{n} is the unit normal vector, and \hat{b} is the unit binormal vector ($\hat{b} = \hat{t} \times \hat{n}$). The radius of curvature is defined by

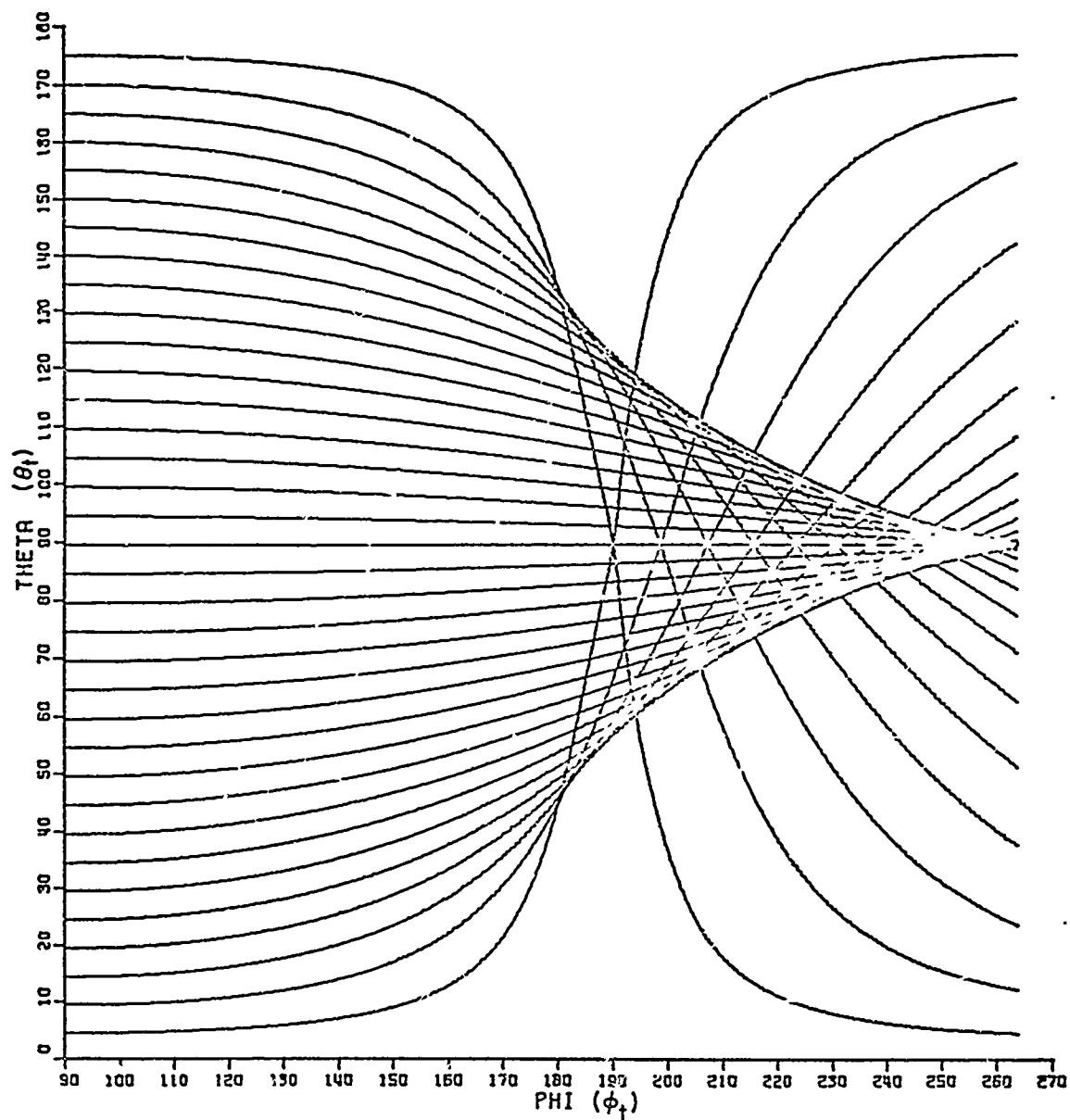


Fig. 62--Set of test geodesic tangent direction curves
on a prolate spheroid.

TABLE VI

RADIATION DIRECTIONS DESIRED VERSUS ACTUALLY COMPUTED TANGENT
DIRECTION OF GIVEN GEODESIC CURVE USING INTERPOLATION PROCEDURE

$\theta_{\text{desired}} = 90^\circ$			$\theta_{\text{desired}} = 70^\circ$		
$\theta_{\text{comp.}}$	ϕ_{desired}	$\phi_{\text{comp.}}$	$\theta_{\text{comp.}}$	ϕ_{desired}	$\phi_{\text{comp.}}$
90.000 ⁰	100 ⁰	99.969 ⁰	70.002 ⁰	100 ⁰	100.011 ⁰
90.000	110	110.053	69.998	110	110.019
90.000	120	120.023	70.002	120	120.016
90.000	130	129.992	70.007	130	130.001
90.000	140	139.962	69.990	140	139.960
90.000	150	150.046	70.004	150	150.059
90.000	160	160.015	69.997	160	159.945
90.000	170	169.985	69.969	170	169.925

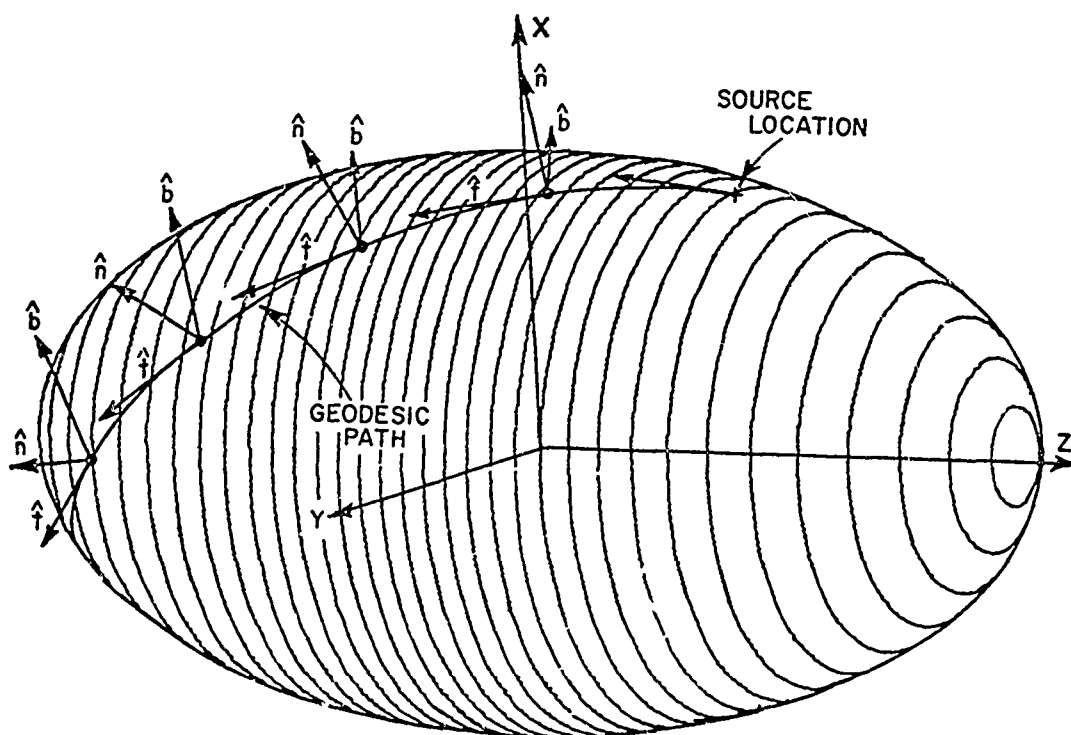


Fig. 63--Curvilinear coordinate along a geodesic path.

$$(88) \quad \rho = \frac{1}{|\dot{\hat{t}}(\lambda)|},$$

where $\dot{\hat{t}}(\lambda)$ is the derivative of \hat{t} with respect to the arclength (λ). The unit tangent vector to the geodesic path is given by

$$(89) \quad \hat{t}(\lambda) = \frac{d\vec{C}(\theta, \phi)}{d\lambda} = \frac{d\vec{C}(\theta, \phi)}{d\theta} \frac{d\theta}{d\lambda} + \frac{d\vec{C}(\theta, \phi)}{d\phi} \frac{d\phi}{d\lambda}$$

where $\vec{C}(\theta, \phi)$ is the position vector which defines the geodesic path. The values of $d\theta/d\lambda$ and $d\phi/d\lambda$ are defined at each point along the path; however, $d\vec{C}/d\theta$ and $d\vec{C}/d\phi$ must be found using

$$\vec{C}(\theta, \phi) = R(\theta) \sin \theta \cos \phi \hat{x} + R(\theta) \sin \theta \sin \phi \hat{y} + R(\theta) \cos \theta \hat{z}$$

or

$$\frac{d\vec{C}}{d\theta} = \left(\frac{dR}{d\theta} \sin \theta \cos \phi + R \cos \theta \cos \phi \right) \hat{x} + \left(\frac{dR}{d\theta} \sin \theta \sin \phi + R \cos \theta \sin \phi \right) \hat{y} + \left(\frac{dR}{d\theta} \cos \theta - R \sin \theta \right) \hat{z}$$

and

$$\frac{d\vec{C}}{d\phi} = -R \sin \theta \sin \phi \hat{x} + R \sin \theta \cos \phi \hat{y}.$$

Thus, the tangent vector is defined at each point (θ, ϕ) along a given geodesic path by substituting the above expressions in Eq. (89). Since the diffracted rays radiate in the tangent direction, this solution defines the radiation direction at every point along a given path.

The derivative of the unit tangent vector is given by

$$(90) \quad \dot{\hat{t}}(\lambda) = \frac{d^2\vec{C}}{d\theta^2} \left(\frac{d\theta}{d\lambda} \right)^2 + 2 \frac{d^2\vec{C}}{d\theta d\phi} \frac{d\theta}{d\lambda} \frac{d\phi}{d\lambda} + \frac{d^2\vec{C}}{d\phi^2} \left(\frac{d\phi}{d\lambda} \right)^2 + \frac{d\vec{C}}{d\theta} \frac{d^2\theta}{d\lambda^2} + \frac{d\vec{C}}{d\phi} \frac{d^2\phi}{d\lambda^2}.$$

The terms found in the above equation have all been defined earlier except for

$$\begin{aligned}\frac{d^2\vec{C}}{d\theta^2} = & \left(\frac{d^2R}{d\theta^2} \sin \theta \cos \phi + 2 \frac{dR}{d\theta} \cos \theta \cos \phi - R \sin \theta \cos \phi \right) \hat{x} \\ & + \left(\frac{d^2R}{d\theta^2} \sin \theta \sin \phi + 2 \frac{dR}{d\theta} \cos \theta \sin \phi - R \sin \theta \sin \phi \right) \hat{y} \\ & + \left(\frac{d^2R}{d\theta^2} \cos \theta - 2 \frac{dR}{d\theta} \sin \theta - R \cos \theta \right) \hat{z},\end{aligned}$$

$$\frac{d^2\vec{C}}{d\phi^2} = -R \sin \theta \cos \phi \hat{x} - R \sin \theta \sin \phi \hat{y}, \text{ and}$$

$$\frac{d^2\vec{C}}{d\theta d\phi} = -\sin \phi \left(\frac{dR}{d\theta} \sin \theta + R \cos \theta \right) \hat{x} + \cos \phi \left(\frac{dR}{d\theta} \sin \theta + R \cos \theta \right) \hat{y}.$$

All of these terms are then determined once the geodesic path is traced out to the point $\vec{C}(\theta, \phi)$ on the surface. The longitudinal radius of curvature is then simply obtained by substituting these quantities into Eq. (88).

In order to solve for the transverse radius of curvature, one must find similar relations for the curve on the surface of revolution which is orthogonal to our given geodesic path at the point $\vec{C}(\theta, \phi)$. In so doing the geodesic path orthogonal to our original path must first be found. This will allow us to use the previously derived equations which in this case give us the transverse radius of curvature. The unit tangent vectors at any point on the surface are given by

$$\begin{aligned}\hat{e}_1 = & \frac{1}{\sqrt{\left(\frac{dR}{d\theta}\right)^2 + R^2}} \left[\left(\frac{dR}{d\theta} \sin \theta + R \cos \theta \right) \cos \phi \hat{x} + \right. \\ (91) \quad & \left. \left(\frac{dR}{d\theta} \sin \theta + R \cos \theta \right) \sin \phi \hat{y} + \left(\frac{dR}{d\theta} \cos \theta - R \sin \theta \right) \hat{z} \right], \text{ and} \\ \hat{e}_2 = & -\sin \phi \hat{x} + \cos \phi \hat{y}.\end{aligned}$$

The unit tangent vector to the original geodesic path (\hat{t}) and the transverse path (\hat{b}) can be written, respectively, as

$$\hat{t} = t_1 \hat{e}_1 + t_2 \hat{e}_2, \quad \text{and}$$

$$\hat{b} = b_1 \hat{e}_1 + b_2 \hat{e}_2$$

Since $\hat{t} \cdot \hat{b} = 0$, one finds that

$$\hat{b} = -t_2 \hat{e}_1 + t_1 \hat{e}_2 = \frac{d\vec{C}_t}{d\ell}(\theta, \phi)$$

where $\vec{C}_t(\theta, \phi)$ is the position vector of the transverse geodesic path. Substituting Eq. (91) into the above expression it is seen that

$$\begin{aligned} \frac{-t_2}{\sqrt{\left(\frac{dR}{d\theta}\right)^2 + R^2}} & \left[\left(\frac{dR}{d\theta} \sin \theta + R \cos \theta \right) \cos \phi \hat{x} + \left(\frac{dR}{d\theta} \sin \theta + R \cos \theta \right) \sin \phi \hat{y} \right. \\ & \left. + \left(\frac{dR}{d\theta} \cos \theta - R \sin \theta \right) \hat{z} \right] + t_1 \left[-\sin \phi \hat{x} + \cos \phi \hat{y} \right] = \frac{d\vec{C}_t}{d\ell} \end{aligned}$$

However, $d\vec{C}_t/d\ell$ is defined by Eq. (89) which when substituted into the above equation gives

$$\begin{aligned} \left. \frac{d\theta}{d\ell} \right|_{\text{trans}} &= \frac{-t_2}{\sqrt{\left(\frac{dR}{d\theta}\right)^2 + R^2}}, \quad \text{and} \\ \left. \frac{d\phi}{d\ell} \right|_{\text{trans}} &= \frac{t_1}{R \sin \theta} \end{aligned}$$

Note that the values of t_1 and t_2 are defined at each point along the original geodesic path by Eq. (89). With these quantities known one can find $d^2\theta/d\ell^2|_{\text{trans}}$ and $d^2\phi/d\ell^2|_{\text{trans}}$ using the geodesic solutions of Eq. (86). Knowing this information the transverse radius of curvature is simply found as before using Eq. (88) with the transverse path terms being used in this case.

The accuracy of this approach is illustrated by a comparison with various analytic solutions for the longitudinal and transverse radii of curvature. Our approximate values were compared with the known values for a sphere and found to be in agreement through 5 significant figures. Our values are compared with the analytic solutions on a prolate spheroid along a meridian geodesic path in Table VII. Good agreement is obtained between the two solutions for the cases considered. Note that the derivatives of the radius of curvature are not included in this study to date in that the numerical complexity would be too great to warrant its insertion at this time. However, a method of computing such quantities has been presented in Section IV-C so that it could be introduced if desired at a later date.

TABLE VII
COMPARISON OF ACTUAL AND COMPUTED VALUES OF LONGITUDINAL AND TRANSVERSE RADII OF CURVATURE

θ	Prolate Spheroid ($4\lambda \times 2\lambda$)			
	ρ_t actual	ρ_t comp.	ρ_g actual	ρ_g comp.
0.0	1.00	1.00	1.00	1.00
10.0	1.15	1.15	1.54	1.54
20.0	1.43	1.43	2.91	2.93
30.0	1.65	1.66	4.47	4.58
40.0	1.79	1.80	5.76	5.85
50.0	1.88	1.89	6.69	6.78
60.0	1.94	1.94	7.32	7.36
70.0	1.98	1.98	7.71	7.75
80.0	1.99	2.00	7.93	7.97
90.0	2.00	2.00	8.00	8.02

Another quantity necessary in our calculations is the spread factor ($\sqrt{d\psi_0/d\psi}$), which is representative of the amount of separation between adjacent geodesic paths as they propagate around the surface. This type of separation is illustrated in Fig. 64. This parameter is obtained numerically by considering two adjacent rays initially separated by d_0 , then determine d which is the included angle between the adjacent tangent vectors at the point of diffraction. Thus, if tangent directions at the point of diffraction are given by \hat{t}_1 and \hat{t}_2 , then

$$d\psi = \cos^{-1} (\hat{t}_1 \cdot \hat{t}_2).$$

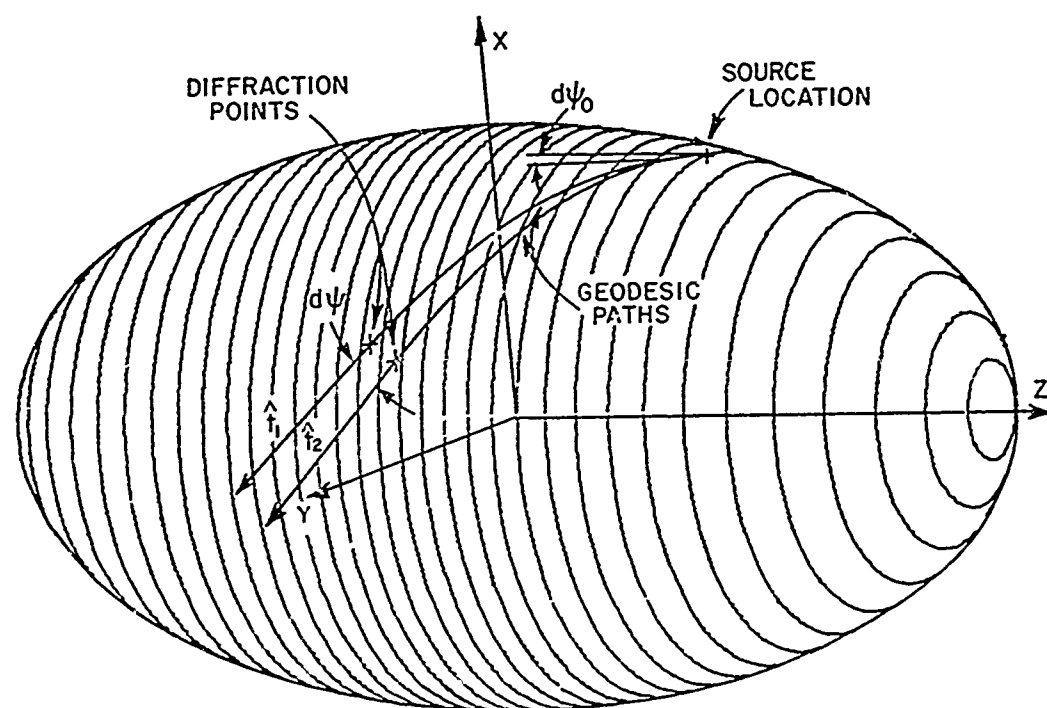


Fig. 64--Illustration of the spread factor ($\sqrt{d\psi_0/d\psi}$) terms.

A study was made to determine just how large $d\psi_0$ could be made without greatly distorting the value of $\sqrt{d\psi_0/d\psi}$ at the diffraction point. It was found that $d\psi_0$ could be as large as $2\frac{1}{2}^\circ$ which meant that the values of $\sqrt{d\psi_0/d\psi}$ could be computed and stored along with the test curves. Consequently, one need only specify the radiation direction which in turn specifies the initial directions (γ) of the geodesic paths and the associated spread factors ($\sqrt{d\psi_0/d\psi}$). These data are stored at the beginning of the program in that they are characteristic of the body and source location being considered.

The far field patterns can now be computed using the previously defined terms which provide information about the convex surface of revolution under consideration. Since the antenna is assumed to be mounted on the fuselage of the aircraft, one needs only consider two general types of antennas. These being the monopole type which has a normal component electric current with respect to the surface and a slot type antenna which has a tangential component magnetic current. It is assumed that the fields launched by infinitesimal antennas follow the solutions specified for the two-dimensional problem of Section II-D. Note that in this case the three-dimensional geometry is introduced in terms of the geodesic paths and associated

longitudinal and transverse radii of curvature which appear in the diffraction and attenuation coefficients. It is further assumed that the normal and tangential component boundary layer fields propagate around the surface independently. This approximation might be rather poor if the torsion along the geodesic curve varies too greatly; however, this point is not well understood at this time. In any event, the results presented here will be compared with actual measurements to illustrate the validity of these assumptions. On the other hand, torsion is a surface-curve relation which can be computed using techniques similar to the previously derived relations.

At this time only a convex body is considered in order that the radiation direction can be simply defined by the geodesic tangent direction as was indicated earlier. However, the study of a concave body is an important topic worthy of future consideration.

Let us first investigate the monopole antenna type whose surface rays propagate outward in all directions from the source with a normal component E-field (or follow the hard boundary condition). The following is a summary of the solutions in the three different regions for the monopole case using the geometry illustrated in Fig. 65:

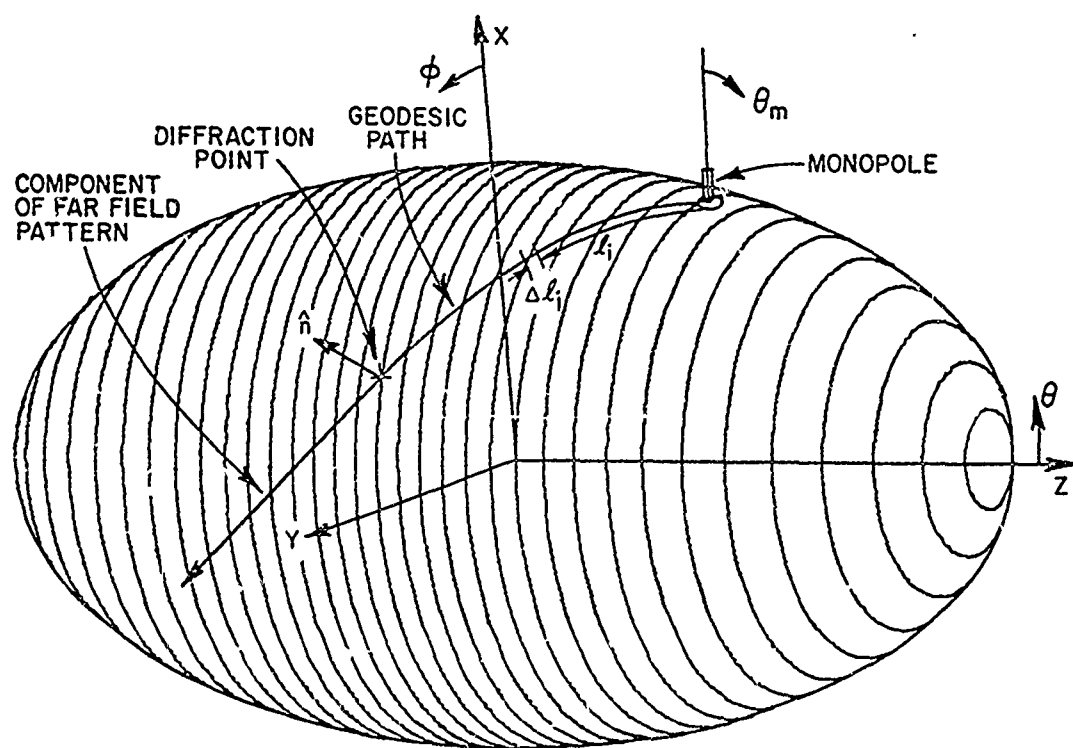


Fig. 65--Geometry of monopole problem.

Lit Region

$$(92) \quad \vec{E}(0, \psi) = -\sin \theta_m \hat{n}_m F(\text{source})$$

Transition Region

a) Lit side

$$(93) \quad \vec{E} = \hat{n} \left\{ \sin \theta_m \right\}^{1/2} e^{jk\ell} g^* \left[- \sum_i \left(\frac{k}{2\rho_g^2(\ell_i)} \right)^{1/3} \Delta \ell_i \right] \cdot F(\text{tangent})$$

b) Shadow side

$$(94) \quad \vec{E} = \hat{n} \left\{ \frac{1}{2} \sqrt{\frac{d\psi_0}{d\psi}} \right\} e^{-jk\ell} g^* \left[\sum_i \left(\frac{k}{2\rho_g^2(\ell_i)} \right)^{1/3} \Delta \ell_i \right] \cdot F(\text{tangent})$$

Deep Shadow

$$(95) \quad \vec{E} = \sum_j \hat{n}_j E_j^h F_j(\text{tangent})$$

where

$$E_j^h = \sqrt{\frac{d\psi_0}{d\psi}} \sum_{m=0}^1 D_m^h L_m^h \prod_i e^{-\gamma_m(\ell_i) \Delta \ell_i}$$

Note that the summation over "j" in the above expression indicates that several terms can contribute in the deep shadow. An example of this situation is illustrated in Fig. 66 where four rays contribute to the far field pattern. The only term in the above expressions that is yet to be defined is the launch coefficient which is given by [35]

$$(96) \quad L_m^h = \left[\pi e^{j \frac{\pi}{2}} D_m^h \left(\frac{2}{k\rho_g} \right)^{1/3} \right] A_i(-\bar{q}_m) \text{ at source location.}$$

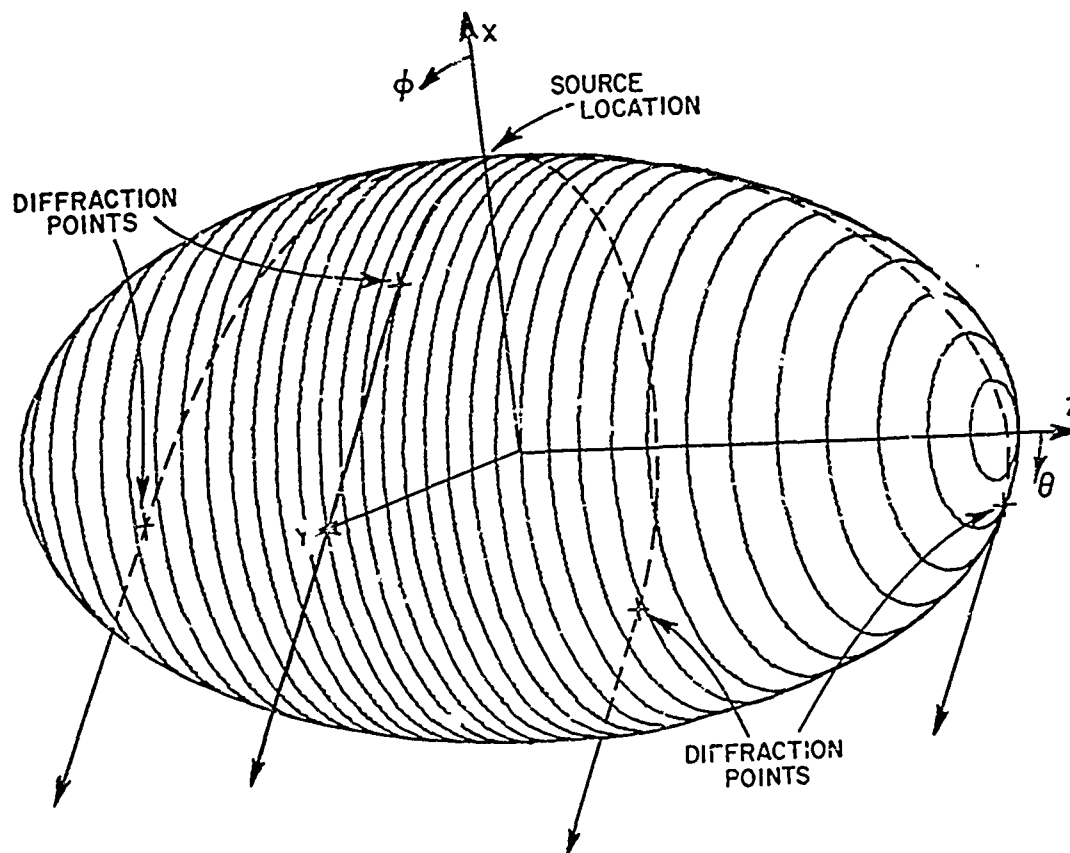


Fig. 66--The four dominant GTD terms that radiate at $(\theta=90^\circ, \phi=145^\circ)$.

Note that \hat{n} is the unit normal at the tangent (or diffraction) point of a given component of the far field pattern, and $F(\)$ is a phase factor used to reference the phase to the center of the surface of revolution.

In order to obtain measured patterns off the principal planes using a conventional pattern range, which only revolves about a vertical axis, the body is first rotated by an angle (ξ) as shown in Fig. 67. Thus, as the body turns about the z' -axis, one obtains the θ' and ϕ' components of the radiated field. In Fig. 68 the ϕ' -component of the field is illustrated with $\xi = 0^\circ$ for a short monopole mounted on a $4\lambda \times 2\lambda$ prolate spheroid. For this principal plane pattern the comparison between the measured and calculated results is quite good. The θ' and ϕ' components of the radiated field for the same body are illustrated in Figs. 69 and 70 for $\xi = 20^\circ$ and 40° , respectively. In these off-principal planes cases the agreement between the results is again quite good.

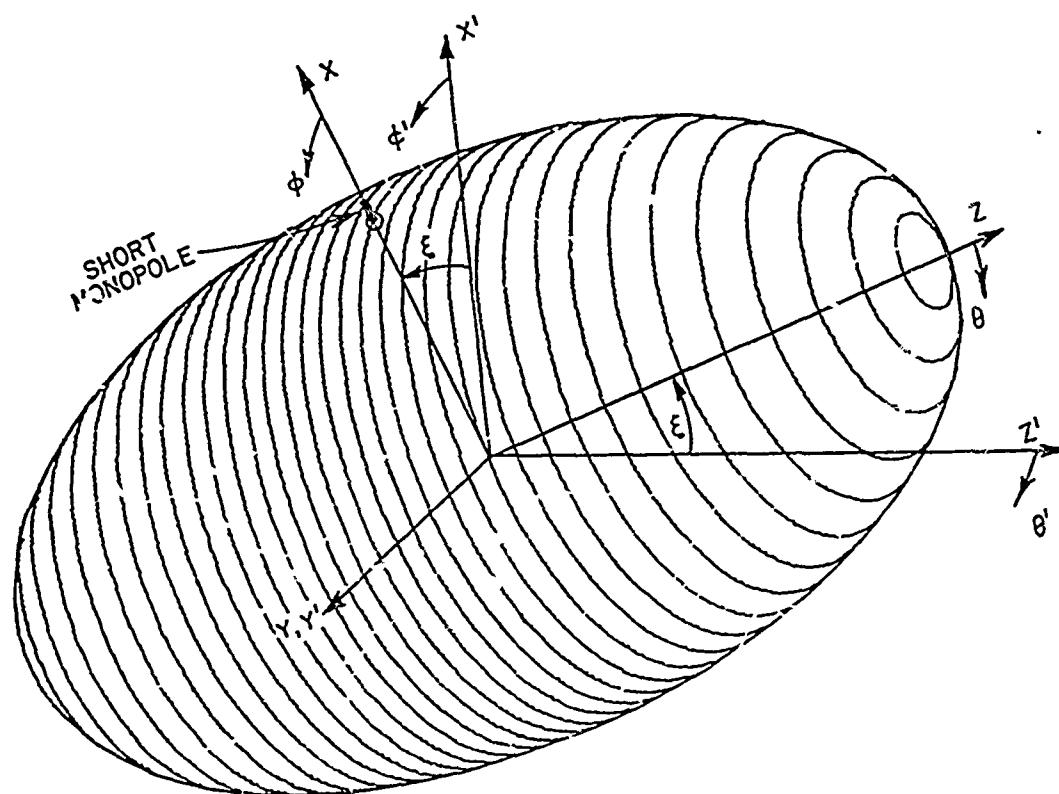


Fig. 67--Rotation of convex surface in order to obtain off-principal plane patterns.

Even though the above problems considered seem to be rather special cases of the more general problem originally treated at the outset, the results are encouraging especially for the off-principal plane cases. They do tend to verify this approach and the associated approximations at least for the monopole cases considered.

The next case to be considered is that of an arbitrary oriented slot mounted on a convex surface of revolution. It was shown in Section II-D that for the two-dimensional problem with the slot mounted parallel (orthogonal) to the cylinder axis that the slot radiated according to the hard (soft) boundary condition in the principal plane. If an arbitrary orientation of the slot were considered then one could assume that the pattern is given in the principal plane by

$$(97) \quad \vec{E} = \vec{E}_{\text{soft}} \sin \beta + \vec{E}_{\text{hard}} \cos \beta$$

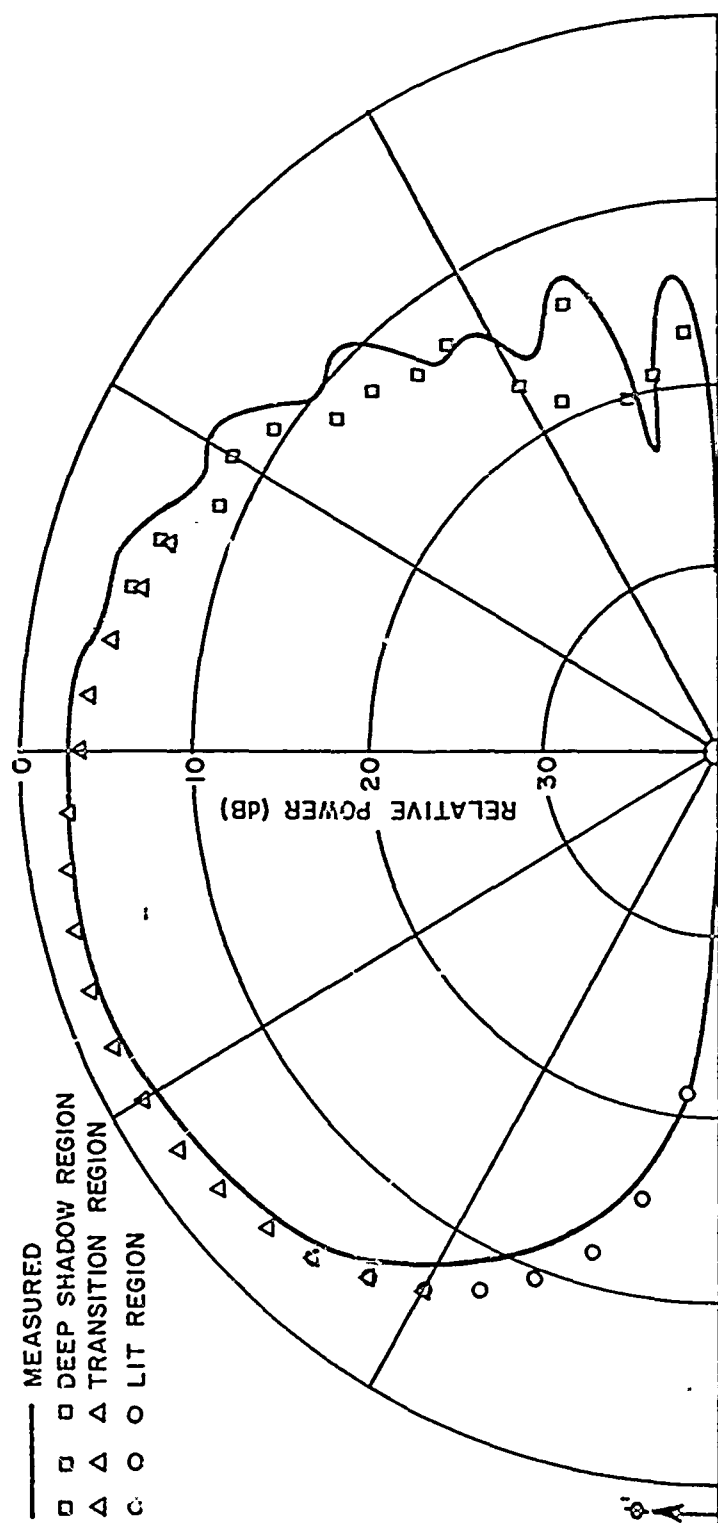


Fig. 68--Principal plane pattern of monopole (E_{ϕ_1})
with $\zeta=0^\circ$.

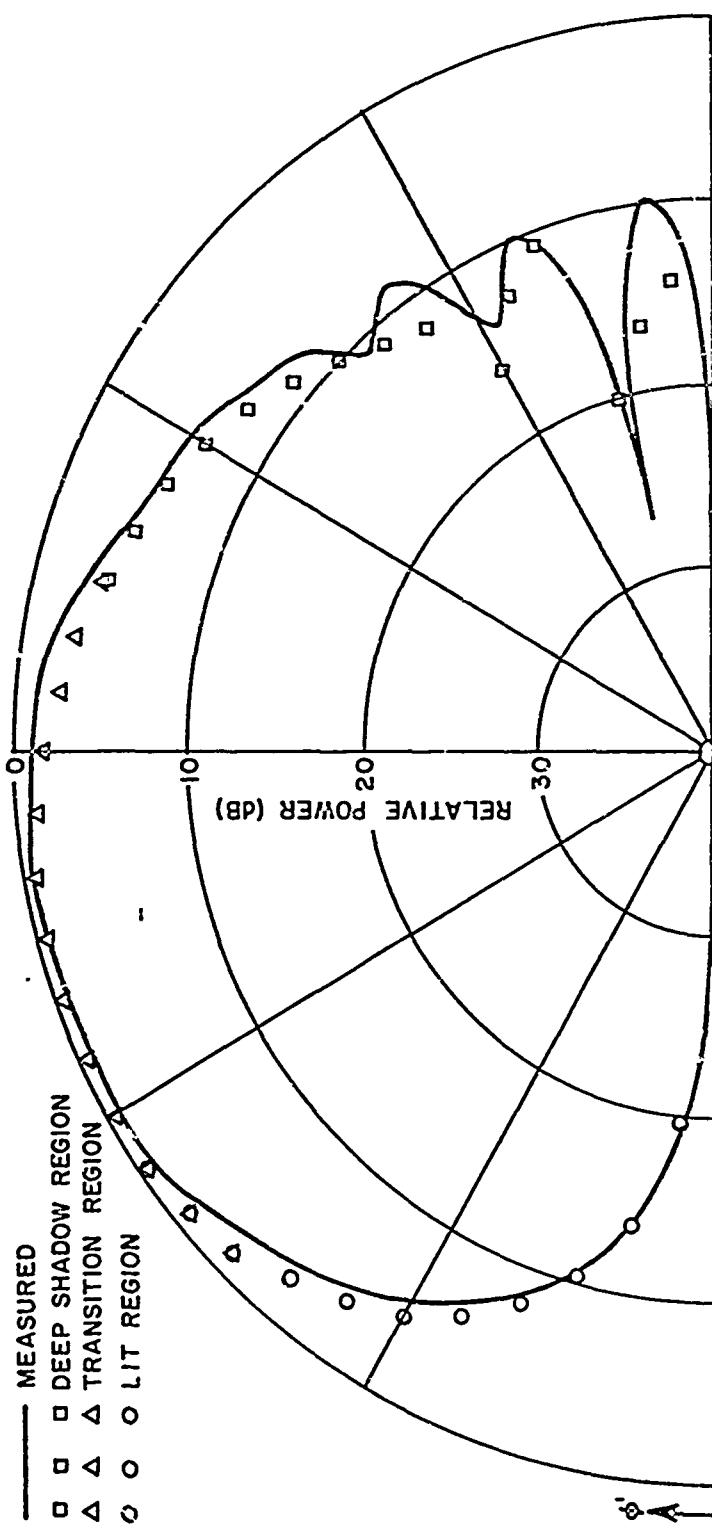


Fig. 69a--Off-principal plane pattern of monopole (E_{ϕ}) with $\epsilon=200$.

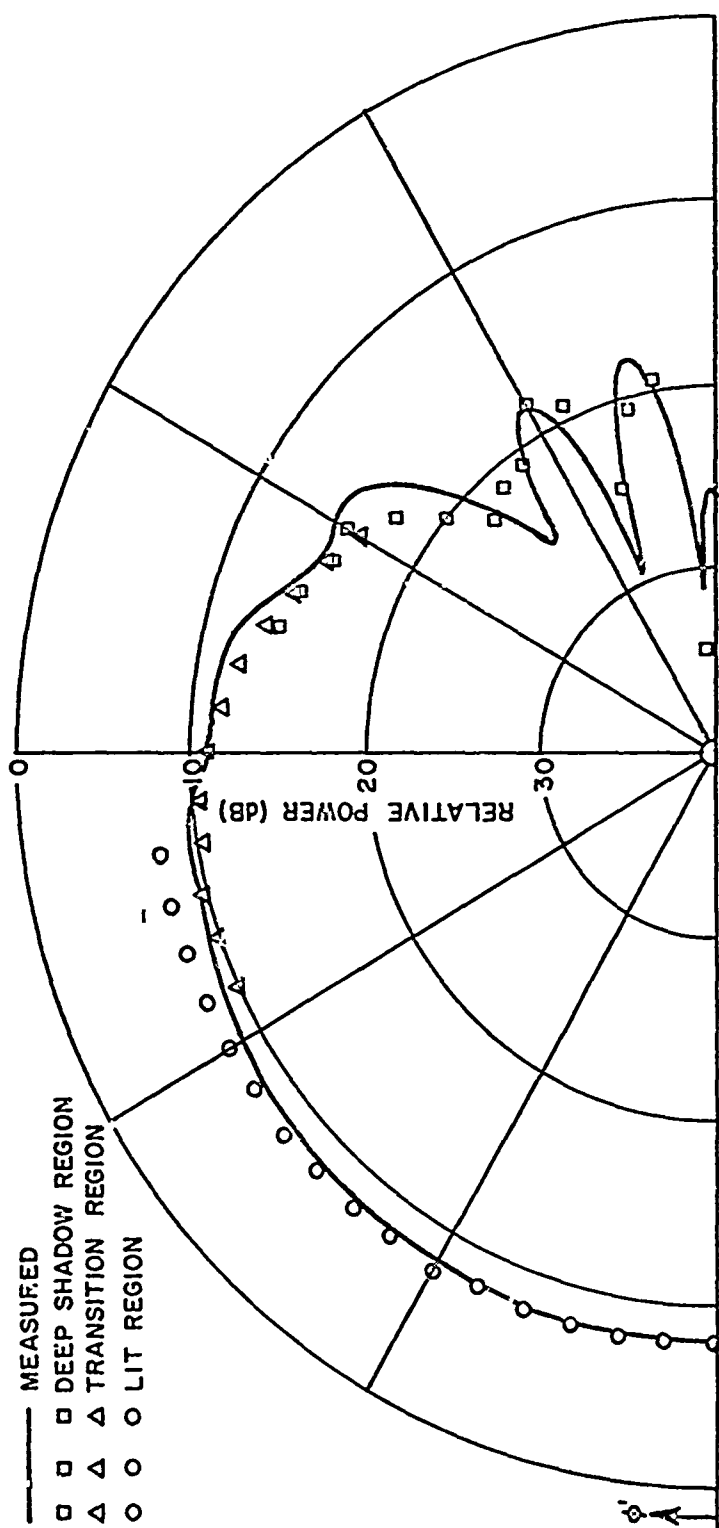


Fig. 69b--Off-principal plane pattern of monopole (E_{θ}) with $\xi=20^\circ$.

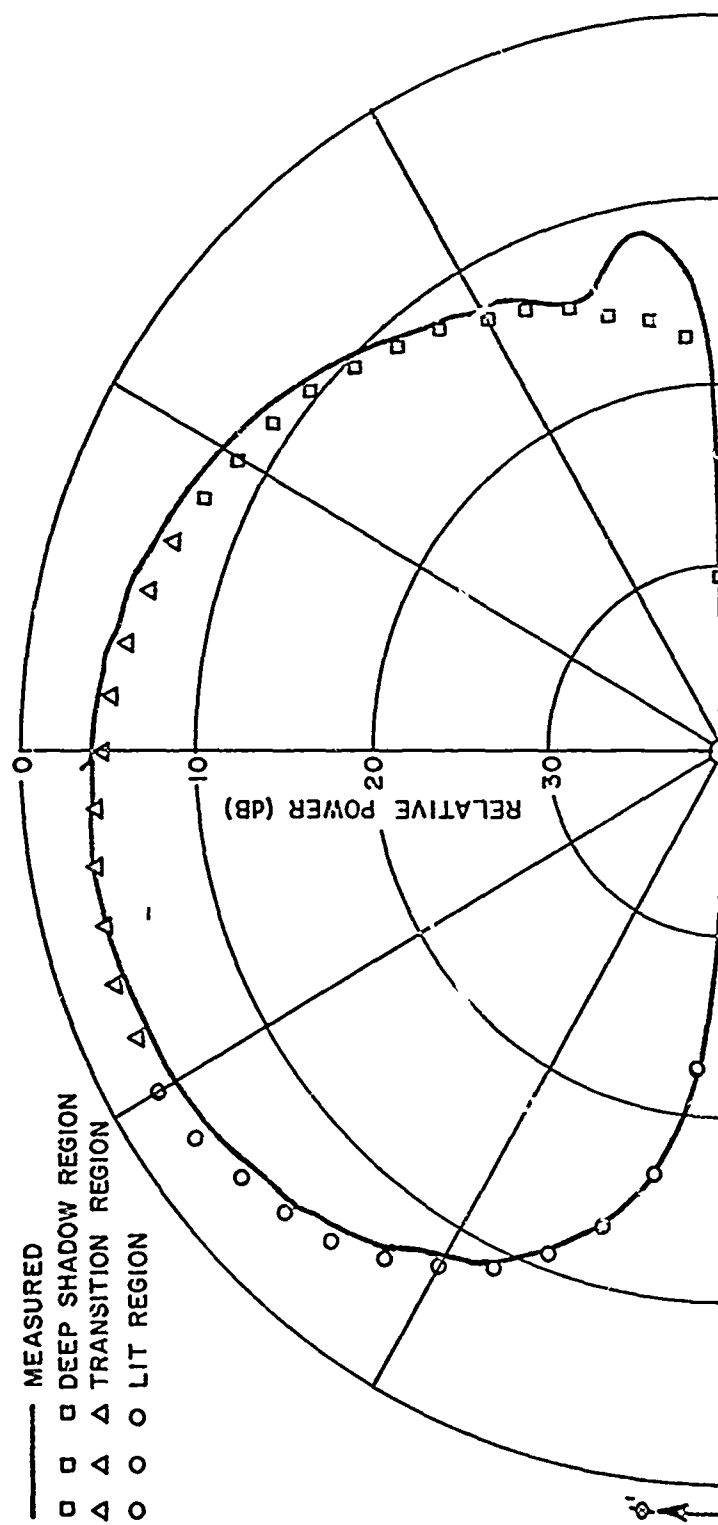


Fig. 70a--Off-principal plane pattern of monopole (E_{ϕ})
 with $\xi=40^\circ$.

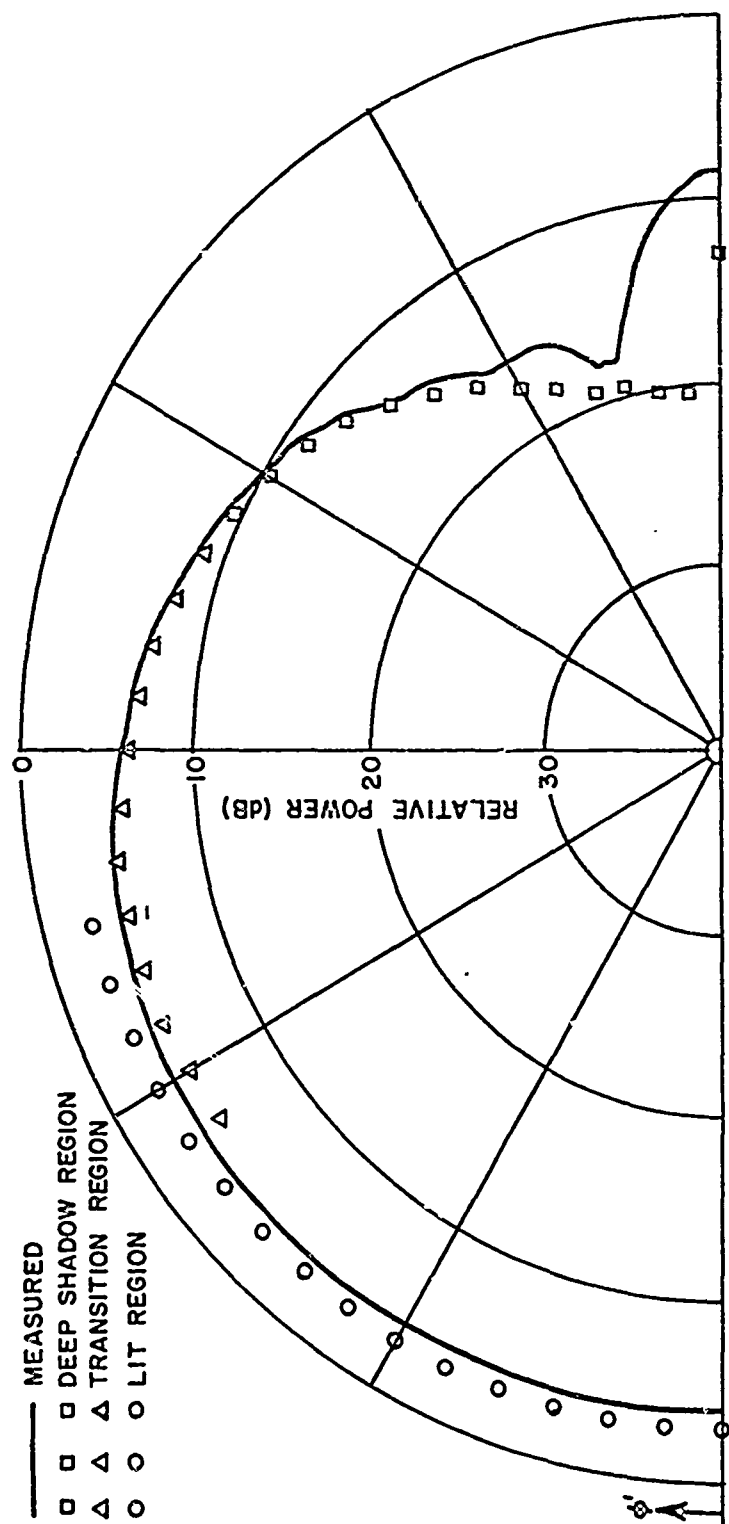


Fig. 70b--Off-principal plane pattern of monopole (E_{θ})
with $\xi=40^\circ$.

using the geometry illustrated in Fig. 71. Thus, for a slot antenna mounted arbitrarily on a three-dimensional surface with a volumetric pattern desired one can extend this approach by considering that the boundary layer field has a tangential component given by

$$\vec{E}_{\text{tang}} = \vec{E}_{\text{soft}} \cos(\gamma - \beta) = E_{\text{soft}} \cos(\gamma - \beta) \hat{b}$$

and a normal component given by

$$\vec{E}_{\text{normal}} = \vec{E}_{\text{hard}} \sin(\gamma - \beta) = E_{\text{hard}} \sin(\gamma - \beta) \hat{n}$$

where γ is the starting direction of the geodesic path defined earlier. Note that the above solutions agree with Eq. (97) in the principal plane ($\gamma = 90^\circ$). It is then assumed that these two components propagate around the surface independent of one another according to the formulas specified in Section II-D.

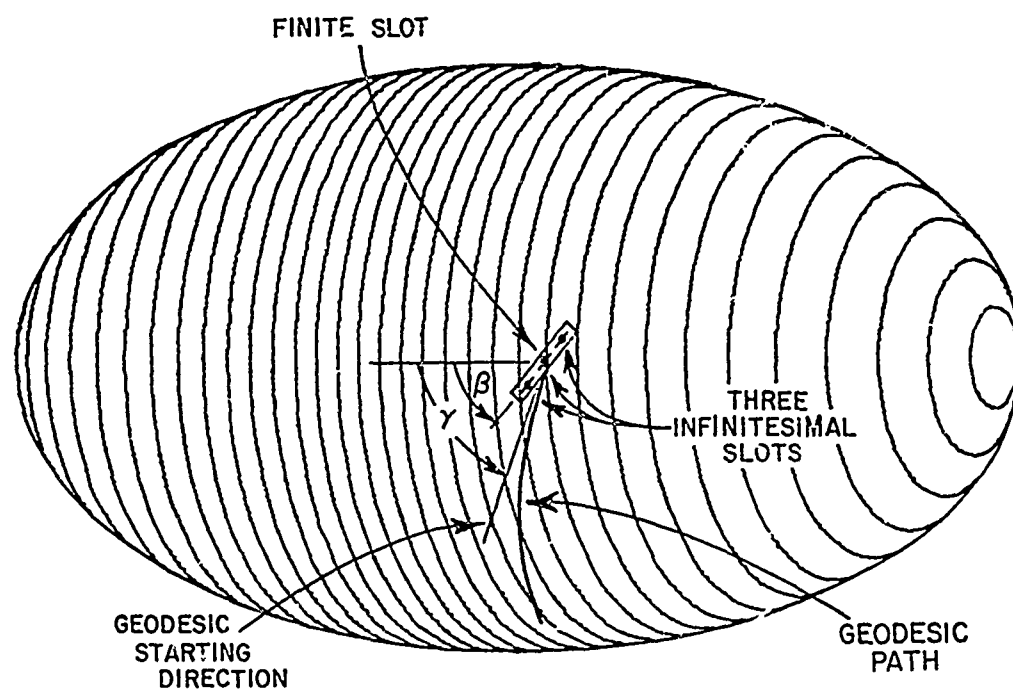


Fig. 71--Finite slot geometry.

Using these results one can define the slot far field pattern in terms of the three regional solutions by:

Lit region

$$(98) \quad \vec{E} = [\hat{\theta}(\cos \phi \sin \beta) + \hat{\phi}(\sin \beta \cos \theta \sin \phi - \sin \theta \cos \beta)] \cdot F(\text{source})$$

Transition region

a) Lit side

$$(99) \quad \vec{E} = \left\{ \hat{n} \left[\frac{1}{2} e^{jk\ell_g} \left(- \sum_i \left(\frac{k}{2\rho_g^2(\ell_i)} \right)^{1/3} \Delta \ell_i \right) \sin(\gamma + \beta) \right] + \right. \\ \left. \hat{b} \left[\frac{j}{2} e^{jk\ell_g^*} \left(- \sum_i \left(\frac{k}{2\rho_g^2(\ell_i)} \right)^{1/3} \Delta \ell_i \right) \left(\frac{2}{k\rho_g} \right)^{1/3} \cos(\gamma + \beta) \right] \right\} \cdot F(\text{tangent})$$

b) Shadow side

$$(100) \quad \vec{E} = \left\{ \hat{n} \left[\frac{1}{2} \sqrt{\frac{d\psi_0}{d\psi}} e^{-jk\ell_g} \left(\sum_i \left(\frac{k}{2\rho_g^2(\ell_i)} \right)^{1/3} \Delta \ell_i \right) \sin(\gamma - \beta) \right] + \right. \\ \left. \hat{b} \left[-\frac{j}{2} \sqrt{\frac{d\psi_0}{d\psi}} e^{-jk\ell_g^*} \left(\sum_i \left(\frac{k}{2\rho_g^2(\ell_i)} \right)^{1/3} \Delta \ell_i \right) \left(\frac{2}{k\rho_g} \right)^{1/3} \cos(\gamma - \beta) \right] \right\} \cdot F(\text{tangent})$$

Deep Shadow Region

$$(101) \quad \vec{E} = \sum_j [\hat{n}_j E_j^h \sin(\gamma - \beta) + \hat{b}_j E_j^s \cos(\gamma - \beta)] F(\text{tangent})$$

where

$$E^h = \sqrt{\frac{d\psi_0}{d\psi}} \sum_{m=0}^1 D_m^h L_m^h \prod_i e^{-\gamma_m(\lambda_i) \Delta \lambda_i}$$

$$E^s = \sqrt{\frac{d\psi_0}{d\psi}} \sum_{m=0}^1 D_m^s L_m^s \prod_i e^{-\gamma_m(\lambda_i) \Delta \lambda_i}.$$

Again the summation over "j" in the above expression indicates that several terms can contribute in the deep shadow region as shown previously in Fig. 66. The launch coefficient for the hard boundary condition is given by Eq. (96); whereas, the soft boundary condition launch coefficient is given by [35]

$$(102) \quad L_m^s = \left[\pi \left(\frac{2}{k \rho_g} \right)^{2/3} e^{-j \frac{\pi}{12}} D_m^s A_i^s(-q_m) \right]_{\text{at source location}}.$$

Note that \hat{n} and \hat{b} are, respectively, the normal and binormal to the geodesic curve at the point of diffraction and $F(\cdot)$ is simply a phase factor to refer the phase to the center of the surface of revolution.

In order to measure the pattern of a slot antenna, a finite length slot is considered. Actually for our measured patterns an open-ended waveguide is used except the width is cut down to approximately one-tenth of the wavelength. For this antenna one can compute the pattern by numerically integrating the patterns from three infinitesimal slot antennas which approximate the aperture fields as shown in Fig. 71. This approach is described in Ref. [22] and successfully applied in Ref. [47]. Using this solution the computed principal plane pattern [$\xi=0^\circ$ in Fig. 67] is compared with the measured result as shown in Fig. 72 for a circumferential slot ($\beta=90^\circ$). Note that these results are again taken on a prolate spheroid. The calculated and measured off-principal plane patterns for $\xi=20^\circ$ and 40° are shown, respectively, in Figs. 73 and 74. In each case, good agreement is obtained between the measured and calculated results.

Again the slot cases treated are rather idealized as compared to the more general problem originally outlined. However, off-principal plane radiation patterns from antennas mounted on three-dimensional surface which are large in terms of the wavelength have not been analytically computed with much success to date. Thus, one must begin by treating specific cases which are easily modelled and computed. In this way one is able to ascertain the validity of his solution. The above results, then, indicate that the high

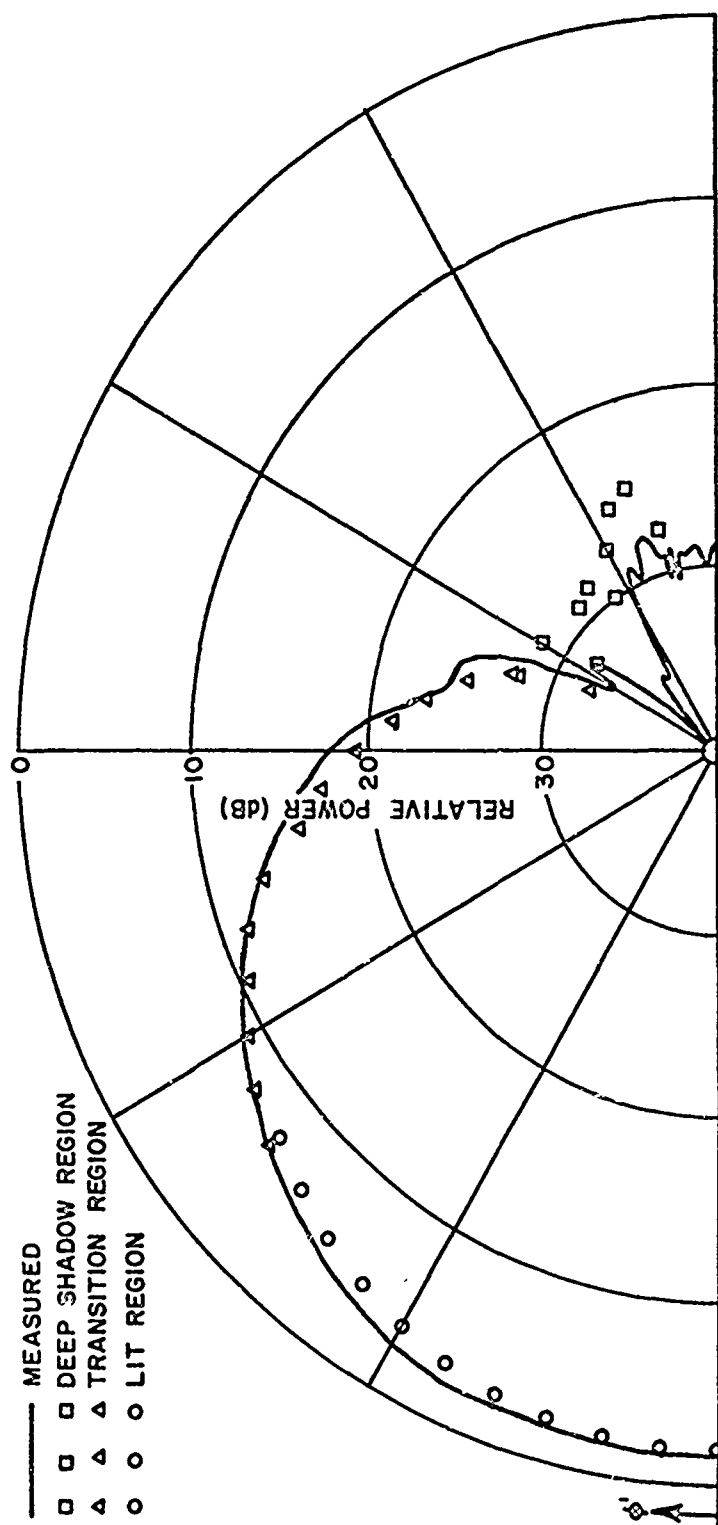


Fig. 72--Principal plane pattern of circumferential slot (E_{θ}) with $\xi=0^\circ$.

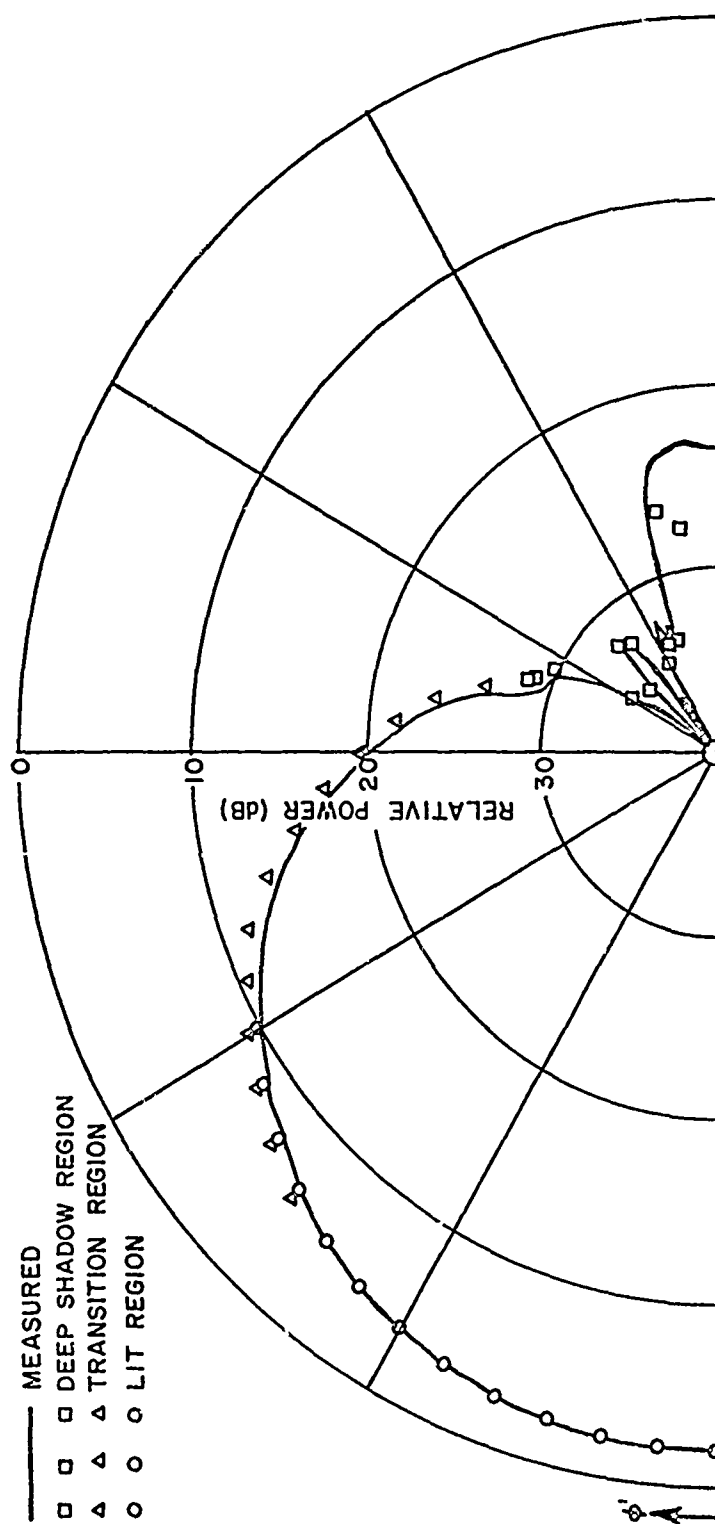


Fig. 73--Off-principal plane pattern of circumferential slot (E_{θ}) with $\xi = 20^\circ$.



THE
OFFICE OF
THE
SECRETARY OF
THE
NAVY
WASHINGTON
D. C.



THE
OFFICE OF
THE
SECRETARY OF
THE
NAVY
WASHINGTON
D. C.



frequency solutions of Kouyoumjian[35] can be applied at least to this idealized problem. One must, now, extend these solutions to determine for what type fuselage models they tend to break-down if in fact they do.

CHAPTER VI

CONCLUSIONS

High frequency solutions for the radiation patterns of general-type on-aircraft antennas mounted on the fuselage is the object of this research. It has been shown previously that the modal solutions are quite adequate for computing these patterns provided the structure is not illuminated too strongly. However, modern applications require antennas which can strongly interact with the aircraft structure. Thus, improved analytic models must be applied in order to develop useful theoretical solutions. These solutions can then be used to compute the antenna design and location for a given application.

The basic approach applied here is to add to the modal solutions by including additional structural components in the analytic model. This is accomplished using a ray optics technique in which the modal solutions are written in a ray form. Using this scheme, one is able to consider isolated structural components, which have been removed from the aircraft, and then add it to the model simply by adjusting the field incident on the structural scatterer.

Two near field scattering problems are initially studied in Chapter III. These are a finite flat plate, which is used to simulate the wing, and a finite cylinder, which is used to approximate the jet engines. The flat plate scattering is solved using three-dimensional wedge diffraction techniques. Various measured results are presented to verify our theoretical solutions. The finite cylinder scattering is solved using physical optics, the Geometrical Theory of Diffraction, and modal solutions. Again measured results are presented to illustrate the validity of this solution.

These near field scattering solutions are then added to analytic aircraft models to compute the principal plane patterns in Chapter IV. In the roll plane, it is found that the jet engine has little effect for a two-dimensional model and is, thus, neglected in the more general three-dimensional study. The resulting roll plane model is basically an infinitely long circular cylinder to which wings and horizontal stabilizers can be attached. Note that the wings and horizontal stabilizers are approximated by arbitrarily many sided flat plates. The elevation plane model approximates the profile of the fuselage by a set of discrete points with the resulting surface being convex. The fuselage is found to be the dominant

scatterer in the elevation plane. Finally, the azimuth plane model consists of an infinitely long circular cylinder to which wings and engines can be added. However, it is shown the wings and engines have such a small effect that they can be neglected to a good approximation in the azimuth plane. In each case, measured results were taken in order to verify the various solutions.

These solutions provide a high-speed analytic tool for determining the design and location of antennas based on their principal plane performance. For example, the programs delivered to the Naval Air Development Center typically run a pattern in 30 seconds or less on their CDC 6600 digital computer.

An additional feature of these solutions, which can be very important in certain critical cases, is that one can trace out the dominant pattern terms as they are scattered by the various aircraft structures. In this way one can quickly ascertain which structural scatterers are distorting the pattern in a critical region. This gives him the option of taking corrective action by changing the structure or by properly placing absorber. So these solutions not only provide fast pattern computations, but they, also, provide the antenna designer with a means of analytically considering several alternatives to improve the antenna's performance.

The final problem considered in Chapter V is the volumetric pattern analysis of an antenna mounted on a convex surface of revolution. This model describes the fuselage profile by a set of points which are revolved about the fuselage axis in order to analytically approximate a complete surface. The wings and jet engines are not, presently, considered in this study in that the fuselage scattered fields tend to dominate the overall pattern as determined by the principal plane studies. Nevertheless, these structural components can be considered in the future as was done in the principal planes. The volumetric patterns of monopoles and slots using the asymptotic high frequency solutions of Kouyoumjian[35] are numerically derived. The geodesic paths are found and verified as well as the radii of curvature, etc. The principal and off-principal plane patterns are computed and compared with measurements made on a prolate spheroid. In each case, good agreement is obtained which tends to verify the numerical solutions.

REFERENCES

1. Sinclair, G., "The Patterns of Antennas Located Near Cylinders of Elliptical Cross Section," Proc. IRE, Vol. 39, No. 6, June 1951.
2. Carter, P.S., "Antenna Arrays Around Cylinders," Proc. IRE, Vol. 31, December, 1943, pp. 671-693.
3. Carter, P.S., "Antennas and Cylindrical Fuselage," Report No. 895-11, RCA Laboratories, Rocky Point, N.Y.; December 24, 1943.
4. Richards, G.A., "A Boundary-Value Technique for Computing the Patterns of an Antenna Near a Conducting Body of Arbitrary Shape," Report 2235-2, 11 September 1967, ElectroScience Laboratory, Department of Electrical Engineering, The Ohio State University; prepared under Contract No. N10019-67-C-0063 for Naval Air Systems Command.
5. Richmond, J.R., "Computer Analysis of Three-Dimensional Wire Antennas," Report 2708-4, 22 December 1969, ElectroScience Laboratory, Department of Electrical Engineering, The Ohio State University; prepared under Contract No. DAAD 05-69-C-0031 for Ballistic Research Laboratory.
6. Lin, Y. T. and Ksienski, A.K., "Computation of Low Frequency Scattering from Airplanes," Report 2768-9, July 1972, ElectroScience Laboratory, Department of Electrical Engineering, The Ohio State University; prepared under Grant AFOSR 69-1710 for Air Force Office of Scientific Research.
7. Ryan, C.E., Jr. and Rudduck, R.C., "Calculation of the Radiation Pattern of a General Parallel-Plate Waveguide Aperture for the TEM and TE₀₁ Waveguide Modes," Report 1693-4, 10 September 1964, ElectroScience Laboratory, Department of Electrical Engineering, The Ohio State University; prepared under Contract N62269-2184 for U.S. Naval Air Development Center, Johnsville, Pennsylvania.
8. Ryan, C.E., Jr. and Rudduck, R.C., "A Wedge Diffraction Analysis of the Radiation Patterns of Parallel-Plate Waveguides," IEEE Trans. on Antennas and Propagation Comm., Vol. AP-16, No. 4, July 1968.

9. Wu, D.C.F., Rudduck, R.C., and Pelton, E.L., "Application of a Surface Integration Technique to Parallel-Plate Waveguide Radiation Pattern Analysis," IEEE Trans. Antennas and Propagation, Vol. AP-17, (May 1969), pp. 280-285.
10. Burnside, W.D. and Pelton, E.L., "Wedge Diffraction Theory Analysis of Parallel-Plate Waveguide Arrays," Report 2382-14, 25 September 1969, ElectroScience Laboratory, Department of Electrical Engineering, The Ohio State University; prepared under Contract F336150-67-C-1507 for the Air Force Avionics Laboratory at Wright-Patterson Air Force Base, Ohio.
11. Burnside, W.D., Pelton, E.L., and Peters, L., Jr., "Analysis of Finite Parallel-Plate Waveguide Arrays," to be published as a Communication in IEEE Trans. Antennas and Propagation.
12. Yu, J.S., Rudduck, R.C., and Peters, L., Jr., "Comprehensive Analysis for E-plane of Horn Antennas for Edge Diffraction Theory," IEEE Trans. Antennas and Propagation, Vol. AP-14, (March 1966), pp. 138-149.
13. Yu, J.S. and Rudduck, R.C., "H-Plane Pattern of a Pyramidal Horn," IEEE Trans. on Antennas and Propagation Comm., Vol. AP-17, No. 5, September 1969.
14. Ratnasiri, P.A.J., Kouyoumjian, R.G., and Pathak, P.H., "The Wide Angle Side Lobes of Reflector Antennas," Report 2183-1, 23 March 1970, ElectroScience Laboratory, Department of Electrical Engineering, The Ohio State University; prepared under Contract No. AF 19(628)-5929 for Air Force Cambridge Research Laboratories.
15. Mentzer, C.A., Pathak, P.H., and Peters, L., Jr., "Pattern Analysis of an Offset Fed Parabolic Reflector Antenna," Report 3220-2, June 1972, ElectroScience Laboratory, Department of Electrical Engineering, The Ohio State University; prepared under Contract No. N60178-71-C-0264 for U. S. Naval Weapons Laboratory.
16. Ryan, C.E., Jr. and Rudduck, R.C., "Radiation Patterns of Rectangular Waveguides," IEEE Trans. Antennas and Propagation Comm., Vol. AP-16, (July 1968), pp. 488-489.
17. Balanis, C.A. and Peters, L., Jr., "Analysis of Aperture Radiation from an Axially Slotted Circular Conducting Cylinder Using Geometrical Theory of Diffraction," IEEE T-AP-17, January 1969, pp. 93-97.

18. Balanis, C.A. and Peters, L., Jr., "Aperture Radiation from an Axially Slotted Elliptical Conducting Cylinder using Geometrical Theory of Diffraction," IEEE T-AP-17, July 1969, pp. 507-513.
19. Balanis, C.A. and Peters, L., Jr., "Radiation from TE₁₀ Mode Slots on Circular and Elliptical Cylinders," IEEE T-AP-18, No. 3, May 1970, pp. 400-403.
20. Ryan, C.E., Jr., "Analysis of Radiation Patterns of Antennas on Finite Circular Cylinders and Conically-Capped Cylinders," Report 2805-2, 25 September 1970, ElectroScience Laboratory, Department of Electrical Engineering, The Ohio State University; prepared under Contract DAA21-69-C-0535 for Picatinny Arsenal.
21. "Low-Profile Scanned-Beam IFF Antenna System Development Study," Final Report 2836-4, 11 August 1970, ElectroScience Laboratory, Department of Electrical Engineering, The Ohio State University; prepared under Contract N62269-69-C-0533 for Naval Air Development Center.
22. Walter, C.H., Traveling Wave Antennas, Dover Publications, Inc., New York, 1970, pp. 15-16.
23. Sommerfeld, A., Optics, Academic Press, Inc., New York, (1954), pp. 245-265.
24. Keller, J.B., "Geometrical Theory of Diffraction," Journal of the Optical Society of America, 52, (February 1962), pp. 116-130.
25. Rudduck, R.C., "Application of Wedge Diffraction to Antenna Theory," Report 1691-13, 30 June 1965, ElectroScience Laboratory, Department of Electrical Engineering, The Ohio State University; prepared under Grant No. NsG-448 for National Aeronautics and Space Administration, Washington, D.C. Also published as NASA Report CR-372.
26. Pauli, W., "An Asymptotic Series for Functions in the Theory of Diffraction of Light," Phys. Rev., 54, (1 December 1938), pp. 924-931.
27. Hutchins, D.L. and Kouyoumjian, R.G., "A New Asymptotic Solution to the Diffraction by a Wedge," URSI 1967 Spring Meeting, Ottawa, Canada, pp. 154-155.

28. Hutchins, D.L., "Asymptotic Series Describing the Diffraction of a Plane Wave by a Two-Dimensional Wedge of Arbitrary Angle," Ph.D. Dissertation, The Ohio State University, Dept. of Electrical Engineering. (1967).
29. Pathak, P.K. and Kouyoumjian, R.G., "The Dyadic Diffraction Coefficient for a Perfectly Conducting Wedge," Scientific Report No. 5, Report 2183-4, 5 June 1970, ElectroScience Laboratory, Department of Electrical Engineering, The Ohio State University; prepared under Contract AF19(628)-5929 for Air Force Cambridge Research Laboratories.
30. Levy, B.R. and Keller, J.B., "Diffraction by a Smooth Object," Institute of Mathematical Sciences, New York University, published under Contract Number AF 19(604)-1717; December 1957. Also in Comm. Pure Appl. Math., 12, 1959, pp. 159-209.
31. Franz, W. and Depperman, K., "Theorie der Beugung Am Zylinder unter Berucksichtigung der Kriechwelle," Ann. Physik, Vol. 10, June 1952, pp. 361-373.
32. Franz, W. and Depperman, K., "Theorie der Beugung der Kugel unter Berucksichtigung der Kriechwelle," Ann Physic. Vol. 14, June 1954, pp. 253-264.
33. Kouyoumjian, R.G., "Asymptotic High-Frequency Methods," Proceedings of the IEEE, Vol. 53, No. 8, August 1965, pp. 864-876.
34. Voltmer, D.V., "Diffraction by Doubly Curved Convex Surfaces," Ph.D. Dissertation, The Ohio State University, 1970.
35. Kouyoumjian, R.G., Notes in preparation for publication.
36. Fock, V.A., Electromagnetic Diffraction and Propagation Problems, Pergamon Press, 1965.
37. Donn, C., "Radiation Patterns of Narrow Slots on Cylindrical Surfaces," Internal Memorandum, July 1971, ElectroScience Laboratory, The Ohio State University.
38. Lentz, R. and Peters, L., Jr., "Near-Zone Scattering," IEEE Transactions on Antennas and Propagation, Vol. AP-19, No. 5, September 1971, pg. 695.

39. Wu, D.C.F., "Electromagnetic Analysis of Three-Dimensional Antenna-Radomes Using the Plane Wave Spectrum-Surface Integration Techniques," Report 2969-4, ElectroScience Laboratory, Department of Electrical Engineering, The Ohio State University; prepared under Contract No. N00019-70-C-0252 for the Navy, Washington, D.C.
40. Lopez, A.R., "The Geometrical Theory of Diffraction Applied to Antenna Pattern and Impedance Calculations," IEEE Transactions on Antennas and Propagation, Vol. AP-14, No. 1, January 1966, p. 40.
41. Ross, R.A. and Price, E.L., "Radar Cross Section of Finite Right-Circular Cylinders," Report ER/RIS-11, October 1966, Cornell Aeronautical Laboratory.
42. Sloan, R.W., "Echo Area of Wires and Hollow Cylinders," Report 444-2, 1 September 1951, Antenna Laboratory, Department of Electrical Engineering, The Ohio State University; prepared under Contract No. DA 36-039 sc5506 for Signal Corps Supply Agency Laboratory Procurement Office.
43. DeVore, R.V. and Kouyoumjian, R.G., "The Back-Scattering from a Circular Disc," presented at the 1961 URSI-IRE Spring Meeting, Washington, D.C.
44. Ryan, C.E., "A Geometrical Theory of Diffraction Analysis of the Radar Cross Section of a Sectionally Continuous Second-Degree Surface of Revolution," Report 2430-4, March 1968, ElectroScience Laboratory, Department of Electrical Engineering, The Ohio State University; prepared under Contract No. AF 19(628)-67-C-0308 for Electronic Systems Division of Air Force Systems Command.
45. Ryan, C.E. and Peters, L., Jr., "Evaluation of Edge Diffracted Fields Including Equivalent Currents for the Caustic Regions," IEEE Transactions on Antennas and Propagation, May 1969.
46. Silver, S., Microwave Antenna Theory and Design, New York; McGraw-Hill, 1949.
47. Marhefka, R.J., "Roll Plane Analysis of On-Aircraft Antennas," Report 3188-1, December 1971, ElectroScience Laboratory, Department of Electrical Engineering, The Ohio State University; prepared under Contract N62269-71-C-0296 for Naval Air Development Center.

48. Yu, C.L. and Burnside, W.D., "Elevation Plane Analysis of On-Aircraft Antennas," Report 3188-2, January 1972, Electro-Science Laboratory, Department of Electrical Engineering, The Ohio State University; prepared under Contract N62269-71-C-0296 for Naval Air Development Center.
49. Burnside, W.C. and Peters, L., Jr., "Axial Radar Cross Section of Finite Cones by the Equivalent Current Concept with Higher Order Diffraction," (to be published in Radio Science).
50. National Bureau of Standards, Handbook of Mathematical Functions, 1964.
51. Hildebrand, F.B., Introduction to Numerical Analysis, McGraw-Hill, New York/Toronto/London, 1956, pp. 64-68.
52. Kouyoumjian, R.G. and Burnside, W.D., "The Diffraction by a Cylinder-Tipped Half Plane," IEEE, AP-18, No. 3, May 1970, pp. 424-426.
53. Struik, D.G., Differential Geometry, Addison-Wesley Press, Inc., Cambridge, Mass., 1950, pp. 127-134.
54. Richmond, J.R. (private communication).
55. Harrington, R.F., Time Harmonic Electromagnetic Field, McGraw Hill Book Co., New York, 1961.

[illegible][illegible][illegible]

Journal of Management Education 30(6)

Journal of Management Studies, 19(1), 67-80.

Journal of Management Studies, 19(1), 67-80.

11 12 13 14 15

THE UNIVERSITY OF CHICAGO

Now using the cylindrically separable fields[54] from Table VIII one finds that

$$E_{\perp\phi}^i = -j e^{jkz \cos \theta_i} \sum_{n=-\infty}^{\infty} j^n J_n'(k\rho \sin \theta_i) e^{-jn\phi}.$$

The form of the scattered field can now be postulated giving

$$E_{\perp\phi}^s = j e^{jkz \cos \theta_i} \sum_{n=-\infty}^{\infty} a_n H_n^{(2)'}(k\rho \sin \theta_i) e^{-jn\phi}$$

where the a_n 's are unknowns. Using the boundary conditions at the surface of the cylinder, at which the tangential component of the E -field must vanish, one finds that

$$E_{\perp\phi}^t(\rho=a) = j e^{jkz \cos \theta_i} \left\{ \sum_{n=-\infty}^{\infty} [-j^n J_n'(ka \sin \theta_i) + a_n H_n^{(2)'}(ka \sin \theta_i)] e^{-jn\phi} \right\} = 0$$

which implies

$$a_n = j^n \frac{J_n'(ka \sin \theta_i)}{H_n^{(2)'}(ka \sin \theta_i)}.$$

The total field is now specified by the above relations in conjunction with Table VIII and is given by

$$E_{\perp \rho}^t = \frac{e^{jkz \cos \theta_i}}{k_\rho \sin \theta_i} \sum_{n=1}^{\infty} 2nj^{n+1} \left[J_n(k_\rho \sin \theta_i) - \frac{J'_n(ka \sin \theta_i)}{H_n^{(2)'}(ka \sin \theta_i)} \right.$$

$$\left. H_n^{(2)}(k_\rho \sin \theta_i) \right] \sin n\phi$$

$$E_{\perp \phi}^t = -j e^{jkz \cos \theta_i} \sum_{n=0}^{\infty} \epsilon_n j^n \left[J'_n(k_\rho \sin \theta_i) - \frac{J'_n(ka \sin \theta_i)}{H_n^{(2)'}(ka \sin \theta_i)} \right.$$

$$(104) \quad \left. H_n^{(2)'}(k_\rho \sin \theta_i) \right] \cos n\phi$$

$$E_{\perp z}^t = 0$$

$$H_{\perp \rho}^t = - \frac{j \cos \theta_i e^{jkz \cos \theta_i}}{Z_0} \sum_{n=0}^{\infty} \epsilon_n j^n \left[J'_n(k_\rho \sin \theta_i) - \frac{J'_n(ka \sin \theta_i)}{H_n^{(2)'}(ka \sin \theta_i)} \right.$$

$$\left. H_n^{(2)'}(k_\rho \sin \theta_i) \right] \cos n\phi$$

$$H_{\perp \phi}^t = - \frac{\cos \theta_i e^{jkz \cos \theta_i}}{k_\rho Z_0 \sin \theta_i} \sum_{n=1}^{\infty} 2n j^{n+1} \left[J_n(k_\rho \sin \theta_i) - \frac{J'_n(ka \sin \theta_i)}{H_n^{(2)'}(ka \sin \theta_i)} \right.$$

$$\left. H_n^{(2)}(k_\rho \sin \theta_i) \right] \sin n\phi$$

$$H_{\perp z}^t = - \frac{\sin \theta_i}{Z_0} e^{jkz \cos \theta_i} \sum_{n=0}^{\infty} \epsilon_n j^n \left[J_n(k_\rho \sin \theta_i) - \frac{J'_n(ka \sin \theta_i)}{H_n^{(2)'}(ka \sin \theta_i)} \right.$$

$$\left. H_n^{(2)}(k_\rho \sin \theta_i) \right] \cos n\phi ,$$

where

$$\epsilon_n = \begin{cases} 1 & n=0 \\ 2 & \text{otherwise.} \end{cases}$$

Note that these solutions give the total field at every point in space for a plane wave with a perpendicular component E-field incident on an infinitely long cylinder of radius (a).

The total field for the parallel component E-field incident is found in the same way. In this case, the incident field is given by

$$\vec{E}_{||}^i = (\hat{x} \cos \theta_i - \hat{z} \sin \theta_i) e^{jk(z \cos \theta_i + x \sin \theta_i)}.$$

Using Eq. (103) it is easily shown that

$$E_{||z}^i = -\sin \theta_i e^{jkz \cos \theta_i} \sum_{n=-\infty}^{\infty} j^n J_n(k\rho \sin \theta_i) e^{-jn\phi}.$$

Again the form of the scattered field can be postulated as

$$E_{||z}^s = -\sin \theta_i e^{jkz \cos \theta_i} \sum_{n=-\infty}^{\infty} a_n j^n H_n^{(2)}(k\rho \sin \theta_i) e^{-jn\phi}.$$

The total tangential E-field must vanish on the perfectly conducting cylindrical surface in which case

$$E_{||z}^s(\rho=a) = -\sin \theta_i e^{jkz \cos \theta_i} \sum_{n=-\infty}^{\infty} j^n [J_n(ka \sin \theta_i) + a_n H_n^{(2)}(ka \sin \theta_i)] e^{-jn\phi} = 0$$

which implies

$$a_n = -\frac{J_n(ka \sin \theta_i)}{H_n^{(2)}(ka \sin \theta_i)}.$$

Using these results along with the separable fields of Table VIII one finds that

$$\begin{aligned}
 E_{\parallel \rho}^t &= -j \cos \theta_i e^{jkz \cos \theta_i} \sum_{n=0}^{\infty} \epsilon_n j^n [J_n'(k\rho \sin \theta_i) - \\
 &\quad - \frac{J_n(ka \sin \theta_i)}{H_n^{(2)}(ka \sin \theta_i)} H_n^{(2)'}(k\rho \sin \theta_i)] \cos n\phi \\
 E_{\parallel \theta}^t &= - \frac{\cos \theta_i e^{jkz \cos \theta_i}}{k\rho \sin \theta_i} \sum_{n=1}^{\infty} 2n j^{n+1} [J_n(k\rho \sin \theta_i) - \\
 (105) \quad &\quad \frac{J_n(ka \sin \theta_i)}{H_n^{(2)}(ka \sin \theta_i)} H_n^{(2)}(k\rho \sin \theta_i)] \sin n\phi \\
 E_{\parallel z}^t &= -\sin \theta_i e^{jkz \cos \theta_i} \sum_{n=0}^{\infty} \epsilon_n j^n [J_n(k\rho \sin \theta_i) - \\
 &\quad \frac{J_n(ka \sin \theta_i)}{H_n^{(2)}(ka \sin \theta_i)} H_n^{(2)}(k\rho \sin \theta_i)] \cos n\phi \\
 H_{\parallel \rho}^t &= - \frac{e^{jkz \cos \theta_i}}{k\rho Z_0 \sin \theta_i} \sum_{n=1}^{\infty} 2n j^{n+1} [J_n(k\rho \sin \theta_i) - \frac{J_n(ka \sin \theta_i)}{H_n^{(2)}(ka \sin \theta_i)} \\
 &\quad H_n^{(2)}(k\rho \sin \theta_i)] \sin n\phi \\
 H_{\parallel \phi}^t &= \frac{j}{Z_0} e^{jkz \cos \theta_i} \sum_{n=0}^{\infty} \epsilon_n j^n [J_n'(k\rho \sin \theta_i) - \frac{J_n(ka \sin \theta_i)}{H_n^{(2)}(ka \sin \theta_i)} \\
 &\quad H_n^{(2)'}(k\rho \sin \theta_i)] \cos n\phi \\
 H_{\parallel z}^t &= 0.
 \end{aligned}$$

Note that these solutions give the total fields at any point in space for a parallel component plane wave field incident.

The solution for an arbitrary plane wave field incident can be easily found by decomposing the field incident into its perpendicular and parallel components multiplying these values by the above solutions and summing the terms.

It was assumed for convenience in the above modal solutions that the plane wave was incident at $\phi_i = 0$; however, this restriction is simply removed by replacing ϕ in Eqs. (104) and (105) by $\phi - \phi_i$ where ϕ_i is the general incident ϕ direction.

TABLE VIII
TE AND TM FIELDS SEPARABLE IN THE CYLINDRICAL COORDINATE SYSTEM

The harmonic electromagnetic fields listed below satisfy Maxwell's equations in a homogeneous source-free region.

<u>TE Fields</u>	<u>TM Fields</u>
$E_\rho = - (j\omega\mu/\rho) R P' Z$	$E_\rho = R' P Z'$
$E_\phi = j\omega\mu R' P Z$	$E_\phi = (1/\rho) R P' Z'$
$E_z = 0$	$E_z = \beta^2 R P Z$
$H_\rho = R' P Z'$	$H_\rho = (j\omega\epsilon/\rho) R P' Z$
$H_\phi = (1/\rho) R P' Z'$	$H_\phi = -j\omega\epsilon R' P Z$
$H_z = \beta^2 R P Z$	$H_z = 0$

The time dependence $e^{j\omega t}$ is understood. R is a function of ρ only, P is a function of ϕ only, and Z is a function of z only. Primes indicate differentiation with respect to ρ , ϕ or z . The functions satisfy the following differential equations:

$$\rho \frac{d}{d\rho} \left(\rho R' \right) + (\beta^2 \rho^2 - m^2) R = 0$$

$$P'' = -m^2 P$$

$$Z'' = -h^2 Z$$

where

$$\beta^2 + h^2 = \omega^2 \mu \epsilon, \text{ and } \beta \text{ and } h \text{ are constants.}$$

Some solutions of these differential equations are listed below.

$R(\rho) = J_m(\beta\rho)$	$P(\phi) = \cos m\phi$	$Z(z) = \cos hz$
$N_m(\beta\rho)$	$\sin m\phi$	$\sin hz$
$H_m^{(1)}(\beta\rho)$	$e^{jm\phi}$	e^{jhz}
$H_m^{(2)}(\beta\rho)$	$e^{-jm\phi}$	e^{-jhz}

APPENDIX II

The geodesic differential equations for an arbitrary surface of revolution are developed in this section using tensor analysis. Using the geometry illustrated in Fig. 56, any point on this surface is defined by

$$\begin{aligned}
 x(\theta, \phi) &= R(\theta) \sin \theta \cos \phi \\
 (106) \quad y(\theta, \phi) &= R(\theta) \sin \theta \sin \phi \\
 z(\theta, \phi) &= R(\theta) \cos \theta.
 \end{aligned}$$

The unit tangent vectors on the surface are given by

$$\begin{aligned}
 \hat{e}_1(\theta, \phi) &= \left[\hat{x} \left(\frac{dR}{d\theta} \sin \theta + R \cos \theta \right) \cos \phi + \hat{y} \left(\frac{dR}{d\theta} \sin \theta + R \cos \theta \right) \sin \phi \right. \\
 (107) \quad &\quad \left. \hat{z} \left(\frac{dR}{d\theta} \cos \theta - R \sin \theta \right) \right] / \sqrt{\left(\frac{dR}{d\theta} \right)^2 + R^2}
 \end{aligned}$$

and

$$\hat{e}_2(\phi, \phi) = -\hat{x} \sin \phi + \hat{y} \cos \phi.$$

The metric tensor is given by

$$g = \begin{pmatrix} \frac{\left(\frac{dR}{d\theta} \right)^2 + R^2}{\sqrt{\left(\frac{dR}{d\theta} \right)^2 + R^2(1 + \sin^2 \theta)}} & 0 \\ 0 & \frac{R^2 \sin^2 \theta}{\sqrt{\left(\frac{dR}{d\theta} \right)^2 + R^2(1 + \sin^2 \theta)}} \end{pmatrix}.$$

Using the above information, the christoffel symbols are given by

$$r_{11}^1 = \frac{\frac{dR}{d\theta} \left(\frac{d^2R}{d\theta^2} + R \right)}{\left(\frac{dR}{d\theta} \right)^2 + R^2}$$

$$r_{22}^1 = \frac{-R \sin \theta \left(R \cos \theta + \frac{dR}{d\theta} \sin \theta \right)}{\left(\frac{dR}{d\theta} \right)^2 + R^2}$$

$$r_{21}^2 = r_{12}^2 = \frac{R \cos \theta + \frac{dR}{d\theta} \sin \theta}{R \sin \theta}$$

$$r_{12}^1 = r_{21}^1 = r_{11}^2 = r_{22}^2 = 0 .$$

Substituting these results into the geodesic differential equations[53], one finds that the geodesics paths are defined by

$$\frac{d^2\theta}{d\lambda^2} + \frac{\frac{dR}{d\theta} \left(\frac{d^2R}{d\theta^2} + R \right)}{\left(\frac{dR}{d\theta} \right)^2 + R^2} \left(\frac{d\theta}{d\lambda} \right)^2 - \frac{R \sin \theta \left(R \cos \theta + \frac{dR}{d\theta} \sin \theta \right)}{\left(\frac{dR}{d\theta} \right)^2 + R^2} \left(\frac{d\theta}{d\lambda} \right)^2 = 0$$

$$(108) \quad \frac{d^2\phi}{d\lambda^2} + \frac{2 \left(R \cos \theta + \frac{dR}{d\theta} \sin \theta \right)}{R \sin \theta} \frac{d\theta}{d\lambda} \frac{d\phi}{d\lambda} = 0 ,$$

where λ is the arclength along the geodesic path. Note that these solutions are valid only for a surface of revolution such that the z-axis coincides with the axis of revolution.